SANDIA REPORT
SAND2005-6838
Unlimited Release
Printed November 2005

Micro Mass Spectrometer on a Chip

Matthew G. Blain, Dolores Cruz, James G. Flemming

Prepared by
Sandia National Laboratories
Albuquerque, New Mexico 87185 and Livermore, California 94550

Sandia is a multiprogram laboratory operated by Sandia Corporation,
a Lockheed Martin Company, for the United States Department of Energy's
National Nuclear Security Administration under Contract DE-AC04-94AL85000.

Approved for public release; further dissemination unlimited.

Issued by Sandia National Laboratories, operated for the United States Department of Energy by Sandia Corporation.

NOTICE: This report was prepared as an account of work sponsored by an agency of the United States Government. Neither the United States Government, nor any agency thereof, nor any of their employees, nor any of their contractors, subcontractors, or their employees, make any warranty, express or implied, or assume any legal liability or responsibility for the accuracy, completeness, or usefulness of any information, apparatus, product, or process disclosed, or represent that its use would not infringe privately owned rights. Reference herein to any specific commercial product, process, or service by trade name, trademark, manufacturer, or otherwise, does not necessarily constitute or imply its endorsement, recommendation, or favoring by the United States Government, any agency thereof, or any of their contractors or subcontractors. The views and opinions expressed herein do not necessarily state or reflect those of the United States Government, any agency thereof, or any of their contractors.

Printed in the United States of America. This report has been reproduced directly from the best available copy.

Available to DOE and DOE contractors from
U.S. Department of Energy
Office of Scientific and Technical Information
P.O. Box 62
Oak Ridge, TN 37831

Telephone: (865)576-8401
Facsimile: (865)576-5728
E-Mail: reports@adonis.osti.gov
Online ordering: http://www.osti.gov/bridge

Available to the public from
U.S. Department of Commerce
National Technical Information Service
5285 Port Royal Rd
Springfield, VA 22161

Telephone: (800)553-6847
Facsimile: (703)605-6900
E-Mail: orders@ntis.fedworld.gov
Online order: http://www.ntis.gov/help/ordermethods.asp?loc=7-4-0#online

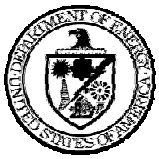

SAND2005-6838
Unlimited Release
Printed November 2005

Micro Mass Spectrometer on a Chip

Matthew G. Blain and Dolores Cruz
MicroAnalytical Systems

James G. Fleming
MEMS Technologies S&T

Sandia National Laboratories
P.O. Box 5800
Albuquerque, NM 87185-0603

ABSTRACT

The design, simulation, fabrication, packaging, electrical characterization and testing analysis of a microfabricated a cylindrical ion trap (μCIT) array is presented. Several versions of microfabricated cylindrical ion traps were designed and fabricated. The final design of the individual trap array element consisted of two end cap electrodes, one ring electrode, and a detector plate, fabricated in seven tungsten metal layers by molding tungsten around silicon dioxide (SiO_2) features. Each layer of tungsten is then polished back in damascene fashion. The SiO_2 was removed using a standard release processes to realize a free-hung structure. Five different sized traps were fabricated with inner radii of 1, 1.5, 2, 5 and 10 μm and heights ranging from 3-24 μm. Simulations examined the effects of ion and neutral temperature, the pressure and nature of cooling gas, ion mass, trap voltage and frequency, space-charge, fabrication defects, and other parameters on the ability of micrometer-sized traps to store ions. The electrical characteristics of the ion trap arrays were determined. The capacitance was 2-500 pF for the various sized traps and arrays. The resistance was in the order of 1-2 Ω. The inductance of the arrays was calculated to be 10–1500 pH, depending on the trap and array sizes. The ion traps' field emission characteristics were assessed. It was determined that the traps could be operated up to 125 V while maintaining field emission currents below 1×10^{-15} A. The testing focused on using the 5-μm CITs to trap toluene (C_7H_8). Ion ejection from the traps was induced by termination of the RF voltage applied to the ring electrode and current measured on the collector electrode suggested trapping of ions in 1-10% of the traps. Improvements to the to the design of the traps were defined to minimize voltage drop to the substrate, thereby increasing trapping voltage applied to the ring electrode, and to allow for electron injection into, ion ejection from, and optical access to the trapping region.

This page intentionally left blank

TABLE OF CONTENTS

LIST OF FIGURES

LIST OF TABLES

PUBLICATIONS

Cruz, D., Chang, J.P. and Blain, M.G. (2005) “Field emission from a tungsten MEMs device,” Applied Physics Letters 86, 153502.

Blain, M.G., Cruz, D., Austin, D.E., Riter, L.S., Wu, G., Cooks, R.G. (2004) “Towards a Handheld Mass Spectrometer,” Int. J. of Mass Spect. 236 91-104.

1.0 INTRODUCTION

To elucidate the motivation for developing a micro mass analyzer, a brief introduction is offered on the increased efforts in the development and deployment of hand-portable chemical analysis systems. Miniaturization efforts of various mass analyzers and detectors are discussed, and a detailed discussion of the fundamental operation of various mass analyzers (i.e., magnetic sector, time of flight, linear quadrupole and the quadrupole ion trap) is given. A concise introduction is presented to the theory and application of the ion trap. The presentation of the theoretical treatment is based on the force derived from the Mathieu equation and a demonstration of the equivalence of the force action on an ion in a RF quadrupole field.

1.1 Microfabricated Sensors

The research described herein focuses on the design, simulation, fabrication and analysis of a micro mass analyzer based detector for gas phase chemical analysis. Detectors identify unknown chemical substances or verify chemical identities and have the ability to quantitatively identify quantities which have concentration levels on the order of ppm and ppb (Grob 1995). However, detectors are usually laboratory-scale in size restricting their portability and accessibility. Miniature and field portable instruments are desirable for a variety of *in situ* analysis applications that include environmental analysis and remediation, process monitoring, emissions monitoring and control, emergency response applications, forensics and chemical and biological weapons detection. Due to recent events, there is urgent need for revolutionary changes in detection technologies for homeland security, and accelerating the prototyping and deployment of new technologies that reduce homeland vulnerabilities is critical. Consequently, there is a need for miniaturization of instruments which have the ability to detect threat agents and subsequently prevent acts of terrorism.

Detection technologies that enable such changes are possible by the employment of micro-electro mechanical systems (MEMS). MEMS devices have revolutionized technology by the miniaturization of large scale components. Their small size (usually in the order of micrometers - microns) yields portability, low power consumption and the possibility of integration with complimentary metal oxide semiconductor (CMOS) technology on the same wafer. MEMS devices also realize low costs due to batch process fabrication. Micro-sensors represent an important fraction of MEMS applications. They are microfabricated and integrated with CMOS devices to provide a complete chip-based sensing system; however, unlike MEMS based actuators, they usually contain no moving parts.

Detectors are a critical component of sensor based technology, serving as the transducer in any analytical system. Although the application of micro-fabricated devices to gas-phase analysis was first demonstrated 26 years ago (Terry, Jerman et al. 1979), further applications of these devices have not been prolific due to their poor performance because of mass-transfer issues. In recent years, sensors have evolved from discrete devices (requiring separate electronics) to integrated devices, where sensors and operating electronics are located on the same chip or substrate. For example, Sandia National Laboratories (SNL) has developed a micro-ChemLab^{TM} (Casalnuovo, Frye-Mason et al. 1999; Frye-Mason, Manginell et al. 1999; Mowry, Kottenstette et al. 2002; Manginell, Lewis et al. 2004) for chemical sensing. The system

uses three microfabricated analysis stages. Stage one collects and concentrates the sample. This stage includes a micro-hot plate preconcentrator for sample collection and preparation. By applying a selectively-adsorbent coating to the surface of a micromachined micro-hotplate, selective preconcentration of target analytes, followed by rapid thermal desorption, is achieved. The preconcentrator is typically a resistive metal thin film on a silicon nitride membrane. Stage two is a micro-gas chromatograph (GC) for separation of the analytes, which are injected into it by the preconcentrator. The silicon based GCs are made using a Bosch deep reactive ion etch to produced a rectangular column typically 400 μm deep and 100 μm wide. The 25 μm separations between adjacent sections of the spiral column allow for a ~1 m total length to be achieved in a 1.5 cm^2 area. Stage three consists of a surface acoustic wave detector array for detection. A four-element array of surface acoustic wave detectors is used for analysis of the GC effluent: there are three active coated sensors and one uncoated reference. Chemical selectivity is built into each of the coatings. The three stages are shown schematically in Figure 1.1. The micro-ChemLab™ is a good example of a system based on micro-fabricated components. The system has been packaged in a hand-held unit and been demonstrated to successfully separate and detect organic gases, as well as low-boiling point chemicals. The initial system application was the selective detection of chemical warfare agents; however, the range of analytes has been expanded to include pharmaceutical solvents, petrochemicals, toxic industrial chemicals and tri-halo-methanes. Sensitivity in the ppm range has been recorded.

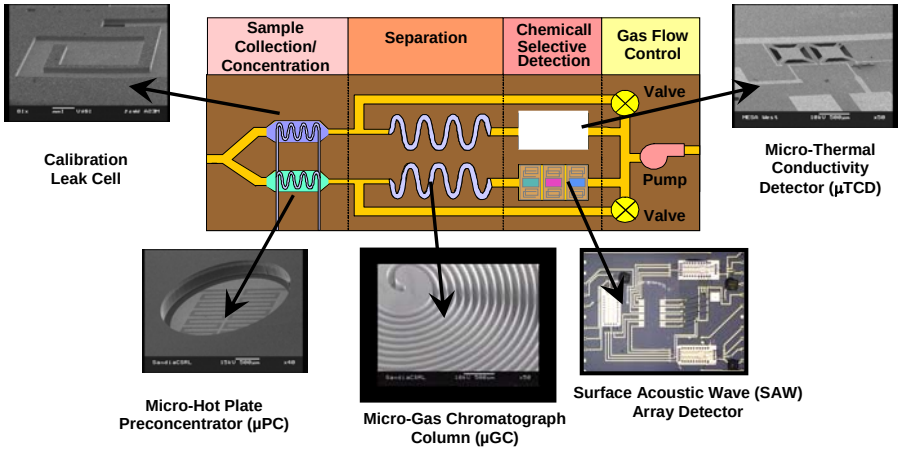

Figure 1.1. A schematic diagram of the phases of the micro-ChemLab™ from SNL. There are three main stages; a micro-hot plate preconcentrator is used to prepare the sample, a micro-gas chromatograph column is used for sample separation and a surface acoustic wave array detector is used for sample detection. A micro-thermal conductivity detector has been added to supplement the detection and a calibration leak cell has been added to maintain an internal standard.

In addition to the surface acoustic wave detector (Martin, Frye-Mason et al. 1996) which is implemented in the micro-ChemLab^{TM} system, there are currently a number of micro-detectors being investigated. These include a flame ionization detector (FID) (Moorman, Manginell et al. 2003), ion mobility spectrometers (Peterson, Rhode et al. 2003) and a flexural plate wave (FPW) detector (Martin, Butler et al. 1998; Martin, Butler et al. 1998). Although these detectors offer good sensitivity (ppm) and selectivity (the ability of a sensor to respond primarily to only one species in the presence of others) they do not offer the versatility that a mass-spectrometer offers (Grob 1995; Abian 1999; March 2000). Mass spectrometers offer mass-selective analysis and often ppb sensitivity.

1.2 Mass Analyzers

Several approaches to mass analysis serve as the basis of mass spectrometers; these are magnetic sector, time of flight, and the quadrupole technique. Table 1-1 shows the different mass spectrometry techniques and their corresponding governing equations. Here m/z is the mass to charge ratio of the ion being analyzed, B is the magnetic field, V is the applied voltage to the instrument, V_{rf} is the time varying potential, f is the frequency, and Ω is the angular frequency ($2\pi f$), q_z is a stability parameter, z_0 is the half-height of the ion trap, L, r and r_0 are the characteristic length scales of the analyzers and t is time. The table also summarizes how the free variable is affected when the characteristic dimensions is reduced to 10 μm.

Table 1-1. Comparison of mass spectrometry techniques when geometry and operating voltage are scaled down by several orders of magnitude. Examples are shown for m/z 300 amu, V= 10 V and the length scale (r or L) is 10 μm.

Technique	Governing Equation	Result for Free Variable*
Magnetic deflection	$m/z = \frac{B^2 r^2}{2V}$	B= 788 T
Time of flight	$m/z = \frac{2Vt^2}{L^2}$	T=4±0.02 ns
Linear Quadrupole	$m/z = \frac{7e6V_{rf}}{f^2 r_0^2}$	f=47 MHz, length of rod is mm
Quadrupole ion trap	$m/z = \frac{8V_{rf}}{q_z(r_0^2 + 2z_0^2)\Omega^2}$	f=59 MHz, z_0= 7 μm

There has been much effort and research in the field of mass spectrometry and developing miniature analyzers which are more portable and have less stringent vacuum requirements (Brewer, DeVoe et al. 1992; Taylor, Tunstall et al. 1998; Tunstall, Taylor et al. 1998; Henry 1999; Syage, Nies et al. 2001). Ferran (Ferran and Boumsellek 1996) has developed a miniature quadrupole mass analyzer and commercialized a micropole array. Chutjian has attempted to miniaturize the quadrupole mass filter as well as the ion trap (Orient, Chutjian et al. 1997; Orient and Chutjian 2002). Cotter (Berkout, Cotter et al. 2001) developed a miniaturized orthogonal time-of-flight mass spectrometer. Ramsey has developed a trap with radius of 0.5 mm (Yang,

Whitten et al. 1995; Kornienko, Reilly et al. 1999; Kornienko, Reilly et al. 1999). Cooks (Reyna and Sobehart 1994; Badman, Johnson et al. 1998; Badman and Cooks 2000; Badman and Cooks 2000; Badman and Cooks 2000; Badman and Cooks 2000; Riter, Laughlin et al. 2002) has developed a miniature cylindrical ion trap, with the smallest ion trap having a 350 μm radius; however the majority of his work is reported for millimeter sized analyzers and his smallest working trap is 2.5 mm. Diaz (Diaz, Giese et al. 2001; Diaz, Giese et al. 2001; Diaz, Giese et al. 2002) has developed a miniaturized magnetic sector analyzer with a radius of curvature in the order of 20 mm. Table 1-2 summarizes the miniaturization efforts in the mass spectrometry field.

Table 1-2. Summary of different miniaturization efforts

Research Group	Mass Analyzer	Length Scale
Cooks, Purdue University	Cylindrical ion trap	2.5 mm
Ramsey, Oak Ridge National Laboratories	Cylindrical ion trap	0.5 mm
Chutjian, Jet Propulsion Laboratory	Linear quadrupole	25.0 mm
Ferran, Ferran Scientific	Linear quadrupole	10.0 mm
Cotter, Johns Hopkins University	Time of flight	0.4 m
Diaz, Universidad de Costa Rica	Magnetic Deflection	20.0 mm

Because there are many differences in the physical basis of mass separation and in their implementation as mass spectrometers, it is important to recognize their strengths and weaknesses when they are miniaturized. The mode of operation and some of the advantages and disadvantages of the different techniques are described in the following sections.

1.2.1 Magnetic Sector Mass Analyzers

Magnetic sectors determine mass via the balance between the centrifugal force and the force exerted on the ions by the magnetic field (centripetal force). Ions are accelerated to a kinetic energy given by:

$$\frac{1}{2}m\upsilon^2 = eV \qquad (1.1)$$

where m is the mass of the ion, υ is the ion velocity, e is the charge of an electron and V is the applied voltage. The ions enter a flight tube between the poles of a magnet and are deflected by the magnetic field, B. Only ions of mass-to-charge ratio that have equal centrifugal and centripetal forces pass through the flight tube of radius r:

$$\frac{m\upsilon^2}{r} = Be\upsilon \qquad (1.2)$$

where r is the radius of curvature of the ion path. Rearranging Equation (1.2) and solving for υ in Equation (1.1) yields:

$$r = \frac{m\upsilon}{eB} = \frac{1}{B}\sqrt{\frac{2Vm}{e}} \qquad (1.3)$$

which leads to the mass analysis equation in magnetic sectors:

$$\frac{m}{e} = \frac{B^2 r^2}{2V} \qquad (1.4)$$

Figure 1.2 shows a schematic diagram of the magnetic sector operation.

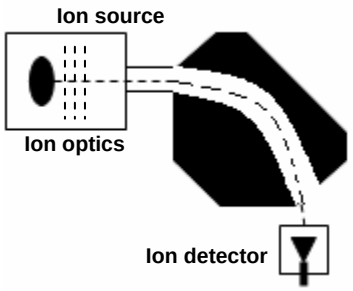

Figure 1.2. A schematic diagram of a magnetic sector, E × B, mass analyzer. Ions are accelerated into the sector and only ions whose centripetal force equals the centrifugal force pass through a curved flight tube.

Magnetic sectors are attractive because they do not require an RF field. RF fields typically require more power than the variable-amplitude fields necessary for the operation of sector instruments. Moreover, static fields are easily generated without complicated electronics. However, as the radius of curvature of the ion path is decreased the mass range decreases and extremely high magnetic fields are required. For example, 788 T required for the magnetic sector instrument in Table 1-1 would require approximately 1182 MJ of energy to be powered for about 2 seconds.

1.2.2 Time of Flight Mass Analyzers

Mass analysis in a time of flight (TOF) mass spectrometer is based on the measurement of the flight time (t) of ions accelerated by a voltage (V). Thus, Equation (1.1) applies. The magnitude of the ion velocity is given as:

$$\upsilon = \frac{L}{t} \qquad (1.5)$$

where L is the length of the flight tube and t is the time of flight. Substituting (1.5) into (1.1) the mass analysis equation can be obtained for time of flight:

$$\frac{m}{e} = \frac{2Vt^2}{L^2} \qquad (1.6)$$

The energy and mass resolution are dependent on the instrument and the calibration of the time scale can be determined by the position of known peaks in the mass spectrum taken at two different energies. The peak width Δt in the time spectrum is translated into the energy or mass scale by:

$$\Delta E = \frac{dE}{dt}\Delta t = -\frac{mL^2}{t^3}\Delta t \qquad (1.7)$$

$$\Delta m = \frac{dm}{dt}\Delta t = \frac{4eVt}{L^2}\Delta t \qquad (1.8)$$

TOF mass spectrometry provides a high mass to charge range ratio and is the standard for the detection of high molecular weight biological species. However, TOF flight requires low operating pressures, 1×10^{-9} Torr. Moreover, TOF is highly dependent upon the initial kinetic energy, position and time of ionization since wide variations will cause discrepancies on the flight time of the ions and affect the resolution. These initial conditions impose constraints on the resolution achieved at certain kinetic energies. Figure 1.3 shows a schematic diagram of a time of flight mass spectrometer. Like magnetic sectors, they do not require an RF potential, simplifying their operation and driving electronics. The detectable mass range of the mass analyzer is increased as the length of the path tube is decreased. However, mass resolution is sacrificed. For example, in the case outlined in Table 1-1, for ΔE = 0.016 eV the mass resolution m/Δm is about 100. For a typical time-of-flight ionization method ΔE is in the order of unity (Muhle, Dobeli et al. 1999).

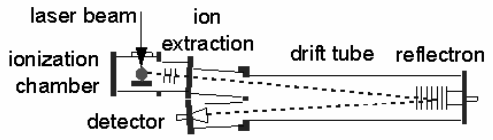

Figure 1.3. A schematic diagram of a time of flight mass spectrometer. Ions are accelerated with energy, eV, into the drift tube and are detected based on their time of flight through the tube.

1.2.3 Linear Quadrupole Mass Analyzers

Linear quadrupoles are one of the most widely used techniques in mass spectrometry. They consist of four rods, ideally hyperbolic in shape. An RF (V) and DC (U) voltage are applied to the rods. Using the appropriate amplitude and sign of the applied voltages, the trajectories of ions of a range of mass-to-charge ratios can be made to be stable in both the x- and y-directions as they travel through the rod assembly. The quadrupole operates as a mass analyzer when conditions are selected such that only ions of a single mass-to-charge ratio have stable trajectories, all others being unstable in the x- and/or y-directions and hence being lost from the two-dimensional trapping field. By scanning the applied DC and RF voltages applied to the rods at a fixed U/V ratio (typically 0.17), a full mass spectrum can be obtained as the trajectories of ions corresponding to a single mass-to-charge ratio (or a small range of values) in turn become stable under the operating conditions and pass along the axis of the rods to the detector. Figure 1.4 shows the schematic of a linear quadrupole mass spectrometer.

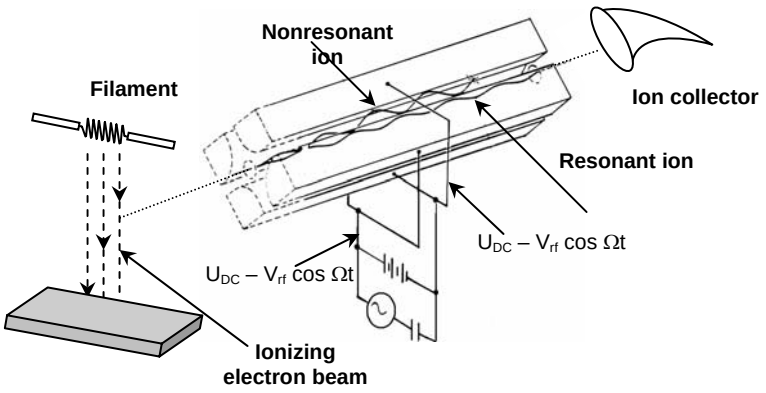

Figure 1.4. A schematic diagram of a linear quadrupole mass spectrometer. Ions are accelerated into an RF electric field (V) with a DC (U) component. Voltages are applied to the rods at a fixed U/V ratio and corresponding ions become stable and pass along the axis of the rods to an ion detector.

Mass range is increased in the linear quadrupole as the size of the mass analyzer is decreased; moreover, the analyzer can be operated at lower voltages with an increase in frequency to compensate for the decrease in size. Linear quadrupoles can also be operated at relatively higher pressures when compared with other mass analyzers because of the reduction of the ion path length and the subsequent reduction in the number of collisions. Although the linear quadrupole mass analyzers are good candidates for miniaturization, their fabrication in massive parallel arrays becomes difficult because the rod length must still be large compared to r_0 (inscribed circle of rods). For example, rod length would be several mm in the example in Table 1-1.

1.2.4 Quadrupole Ion Trap Mass Analyzers

The quadrupole ion trap (March, 1989), functions both as an ion storage device in which ions can be kept for a period of time and as a mass spectrometer of considerable mass range and variable mass resolution. Its versatility makes it a powerful instrument for mass detection. The components of the ion trap when serving as a mass spectrometer are shown in Figure 1.5. An electron source, such as a filament or field emitter, is used to generate ions via electron impact ionization of the target gas of neutrals. The electron beam is focused using electrostatic lenses and ions are created *in situ* or external to the trap. For external ionization, the ions are accelerated into the trap. The ion trap serves as both the mass filter and storage device. An electron multiplier or channeltron is used for ion detection. The trap is operated by applying an RF potential to the ring electrode and conventionally grounding the end caps.

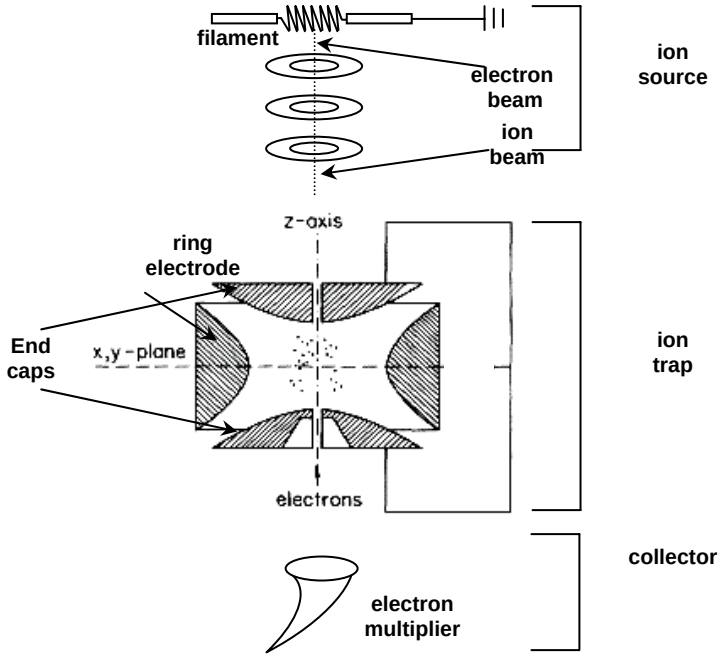

Figure 1.5. A schematic diagram of an ion trap serving as a mass analyzer. Ions created by electron impact are accelerated into the trap. An RF voltage is applied to the ring electrode and ions become trapped if their trajectories are stable. As RF voltage is scanned, ions become unstable in the trap, are ejected, and then detected at the collector.

The ion trap is attractive because its operation is simple. Ion trapping occurs because of the formation of a trapping potential well when the appropriate time varying potentials are applied to the electrodes of the device. The potential well is altered so that ions will become unstable in the well and will leave the trap and be detected in order of ascending mass to charge ratio.

The ion trap offers many advantages in its miniaturization. As the trap radius is decreased the mass range is increased. Like linear quadrupoles they require RF fields and an increased frequency with lower operating voltages. Ion traps have high sensitivity and can operate at relatively higher pressures than other mass analyzers. Moreover they have the ability to perform MS/MS experiments with no modification except for the applied voltages. The simplicity of electrodes makes the ion traps amenable to microfabrication and fabrication in massive parallel arrays. Consequently, the ion trap was chosen as the mass analyzer which would be miniaturized in the work reported here. A more detailed discussion of trapping physics and trap operation is given in the next section.

1.3 The Ion Trap

The ion trap is a widely used tool in several areas of physical science, including mass spectrometry (Paul 1990), atomic frequency standards (Fisk 1997), studies of fundamental quantum dynamics (Liebfried, Blatt et al. 2003), and quantum information science (Cirac and Zoller 1995; Steane 1997). In general traps support two fundamental areas of science atomic, optical, and molecular physics and analytical chemistry.

In 1989, the Nobel Prize in Physics was awarded to Wolfgang Paul, Hans G. Dehmelt and Norman Ramsey for the "invention of the ion trap technique." (Frangsmyr 1990) Since its inception, the use of the ion trap has widened. Ion traps permit the observation of isolated particles, even the confinement of a single ion, over a long period of time. Thus, according to the Heisenberg uncertainty principle, particle properties can be measured with extremely high accuracy. Before the confinement of a single particle, all property measurements were performed on an ensemble of particles and thus, measured values were an average over many particles. Observing a single trapped particle allows the determination of its own discrete behavior (Paul 1990).

Moreover, the wide use of ion traps in mass spectrometry applications has lead to a large number of analytical mass spectrometers using ion traps as the mass filter. Although there are numerous applications presented by the ion trap, the research described herein focuses on the applications of the ion trap to mass spectrometry and as a detector of samples in the gas phase. Although many of the applications would benefit from miniaturized ion trap dimensions several orders of magnitude below the current centimeter and millimeter scale, the work here focuses on the application of ion traps to mass spectrometry.

1.3.1 Ion Traps for Mass Spectrometry

Paul and Steinwedel introduced the quadrupole ion trap in 1953 (Paul and Steinwedel 1953). They proposed a device consisting of three electrodes with surfaces of hyperbolic rotation, Figure 1.6 (a). This geometry allows the defining of a quadrupolar electric field in the trap. The trapping efficiency and resolution are dependent upon the trap size (r_0) and trap depth (D_z) (Dziuban, Mroz et al. 2004), and the operating voltage and frequency. Since its introduction by Paul to the early 1960s the quadrupole ion trap (QIT) was widely used as an ion storage device for mass spectrometric applications and radio frequency spectroscopy. The original ion trap had hyperbolic electrodes, but Langmuir introduced the much simpler cylindrical ion trap (CIT) and was granted the patent for the cylindrical ion trap in 1962 (Langmuir, Langmuir et al. 1962) (Langmuir 1957). A schematic of the cylindrical ion trap is shown in Figure 1.6 (b), with comparable detection efficiency to the quadrupole ion trap (QIT). The corresponding potential fields inside a QIT and a CIT are shown in Figure 1.6 (c) and (d) for comparison. The contour fields were simulated using SIMION software. Ion trap simulations will be discussed in detail in Chapter 5. Although the fields differ, the potential fields in the CIT are a good approximation to those in the QIT.

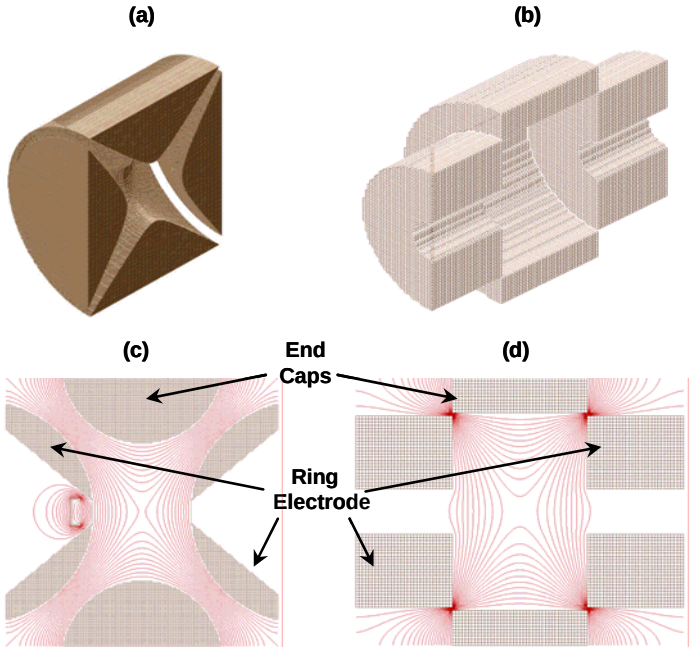

Figure 1.6. A comparison of quadrupole and cylindrical ion traps with r_0 = 1 mm. (a) Schematic of an ion trap with hyperbolic electrodes. (b) Schematic of an ion trap with cylindrical electrodes. (c) The potential fields in a hyperbolic ion trap, simulated by SIMION when 5 V are applied to the ring electrode. (d) The Potential fields in cylindrical ion trap, simulated by SIMION when 5 V are applied to the ring electrode.

1.3.2 Ion Trap Operation

Ion traps work by the application of an RF potential to the middle of three electrodes and adjusting the voltage and frequency of the potential to trap different masses. Figure 1.7 shows the mechanical analogue model for an ion trap with a steel ball as the particle. Earnshaw's Theorem states that no single charged particle can be in stable static equilibrium under the influence of electric forces alone (Jones 1980). Thus ion traps would not work without their varying potential, since particles can not be trapped in a stable static equilibrium. Ions are trapped radially during half of the RF cycle and axially during the other half.

1.3.3 Motion of Ions

Understanding the motion of ions trapped in the electric fields is of great importance in predicting mechanisms of ion injection and chemical reaction and dissociation. McLahlan (McLahlan 1947) has treated the mathematics governing ion motion in detail. Dawson (Dawson 1976) has developed equations of motion as they are applied in the quadrupole ion trap. March has edited several good monographs concerning ion trap physics and instrumentation (March 1989; March and Todd 1995; March 1997).

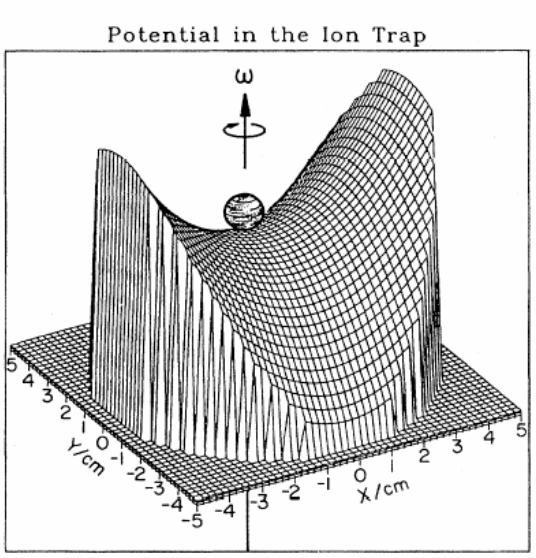

Figure 1.7. A mechanical analogue model for ion trap with a steel ball as the particle.

For the cylindrical ion trap, simple solutions for the potential distribution do not exist. Where as the fields and equations of motion for the quadrupole ion trap are uncoupled, this is not the case for the cylindrical ion trap (March 1989). Benilan and Audoin concluded that ionic motion could be described by the Mathieu equations (March 1989) in cylindrical ion traps.

Ion motion in the trap is governed by the applied electrical potential. The applied potential produces a quadrupolar electric field (ϕ) and the field may be expressed at any point by:

$$\phi = \frac{\phi_o}{r_o^2}\left(\lambda x^2 + \sigma y^2 + \gamma z^2\right) \qquad (1.9)$$

where:

$$\lambda + \sigma + \gamma = 0 \qquad (1.10)$$

Solving Laplace's equation for the cylindrical ion trap, it is found that:

$$\lambda = \sigma = 1, \gamma = -2$$

Ion motion in a quadrupole field can be described by the solutions to the second order differential equations described originally by Mathieu. The solutions to the equations describe regions of stability and instability in terms of the RF and DC voltages. These ideas can be applied to the trajectories of ions confined in the trap and help define the limits of trajectory stability.

The canonical form of the Mathieu equation is:

$$\frac{d^2u}{d\xi^2} + (a_u - 2q_u \cos 2\xi)u = 0 \qquad (1.11)$$

where u represents the coordinate axis x, y and z, and ξ is a dimensionless parameter equal to $\Omega t/2$ such that Ω is the radial frequency ($2\pi f$) and t is time. Note that a and q are known as trapping parameters and relate to the DC and RF voltage, respectively.

Substituting for ξ into Equation (1.11):

$$\frac{d^2u}{dt^2} = \frac{\Omega^2}{4}\frac{d^2u}{d\xi^2} \qquad (1.12)$$

Multiplying (1.12) by m and rearranging terms:

$$m\frac{d^2u}{dt^2} = \frac{-m\Omega^2}{4}(a_u - 2q_u \cos\Omega t)u \qquad (1.13)$$

The right hand side of the equation represents the force on an ion; i.e., mass times acceleration in each of the x, y and z-directions.

The force on the ion in the x-direction can be given by:

$$F_x = ma = m\frac{d^2x}{dt^2} = -e\frac{\partial\phi}{\partial x} \qquad (1.14)$$

Substituting the constants in the expression for ϕ, leads to:

$$\phi_{x,y,z} = \frac{\phi_o}{r_o^2}\left(x^2 + y^2 - 2z^2\right) \qquad (1.15)$$

Changing (1.15) to cylindrical coordinates:

$$\phi_{r,z,\theta} = \frac{\phi_o}{r_o^2}(r^2\cos^2\theta + r^2\sin^2\theta - 2z^2) \qquad (1.16)$$

which simplifies to:

$$\phi_{r,z} = \frac{\phi_o}{r_o^2}\left(r^2 - 2z^2\right) \qquad (1.17)$$

The initial potential is given by:

$$\phi_o = U + V\cos\Omega t \qquad (1.18)$$

where U is the DC component and V is the RF component. Ω is defined as the angular frequency ($\Omega = 2\pi f$), where f is the operating frequency.

Differentiating Equation (1.17) with respect to x and substituting Equation (1.18) for ϕ_0, leads to:

$$\frac{\partial\phi}{\partial x} = \frac{2x}{r_o^2}(U + V\cos\Omega t) \qquad (1.19)$$

Substituting (1.19) into (1.14):

$$m\frac{d^2x}{dt^2} = \frac{-2e}{r_o^2}(U + V\cos\Omega t)x \qquad (1.20)$$

The trapping parameters in Equation (1.11) can be solved and leading to:

$$a_x = \frac{8eU}{mr_o^2\Omega^2} \qquad (1.21)$$

$$a_z = \frac{-16eU}{mr_o^2\Omega^2} \qquad (1.22)$$

$$q_x = \frac{-4eV}{mr_o^2\Omega^2} \qquad (1.23)$$

$$q_z = \frac{8eV}{mr_o^2\Omega^2} \qquad (1.24)$$

1.3.4 Ion Stability

Cylindrical ion trap operation is governed by the stability of the trajectory of an ion within the time varying electrical field. Two types of solutions to Mathieu's equations are (i) periodic but unstable and (ii) periodic and stable. Solutions of type (i) form the boundaries of unstable regions in the stability diagram. These boundaries correspond to a new trapping integral parameter β_z, which is a complex function of a_z and q_z. Solutions of type (ii) determine the motion of ions in the trap. Figure 1.8 shows the stability lines with iso-β lines in a_z-q_z space. Thus regions of stability are bounded by constant lines of β_z=0, β_z=1, β_r=0 and β_r=1. If ions are outside this region, they will not be stable and therefore not trapped. The boundaries represent the point at which the trajectory of an ion becomes unstable. β_u is defined precisely by a recursive fraction expression in terms of a_u and q_u:

$$\beta_u^2 = a_u + \cfrac{q_u^2}{(\beta_u+2)^2 - a_u - \cfrac{q_u^2}{(\beta_u+4)^4 - a_u - \cfrac{q_u^2}{(\beta_u+6)^6 - a_u \ldots}}} + \cfrac{q_u^2}{(\beta_u-2)^2 - a_u - \cfrac{q_u^2}{(\beta_u-4)^4 - a_u - \cfrac{q_u^2}{(\beta_u-6)^6 - a_u \ldots}}} \quad (1.25)$$

Lines of constant β in Figure 1.8 were determined using a program written in C to within ± 1×10^{-5}. The program is presented in Appendix A. The ion motion has the general appearance of a Lissajous curve, or figure-of-eight, composed of two fundamental frequency components, $\omega_{r,0}$ and $\omega_{z,0}$ of the secular motion. These secular frequencies are given by:

$$\omega_{u,n} = (n + \tfrac{1}{2}\beta_u)\Omega \qquad 0 \le n \le \infty \quad (1.26)$$

$$\omega_{u,n} = -(n + \tfrac{1}{2}\beta_u)\Omega \qquad -\infty \le n \le 0 \quad (1.27)$$

β_u can be estimated by the Dehmelt approximation for $q_r < 0.2$ and $q_z < 0.4$ to be:

$$\beta_u \approx \sqrt{\left(a_u + \frac{q_u^2}{2}\right)} \quad (1.28)$$

Ion trap operation can be considered at a constant a_z, i.e., a constant DC voltage. In this case only a certain range of q_z values will yield stability. For example, if $a_z = -0.2$ then only q_z values in the range of 0.7 to 1.1 will yield stability. Correspondingly, ion trap operation with a constant q_z will yield a certain range of a_z values which yield stability.

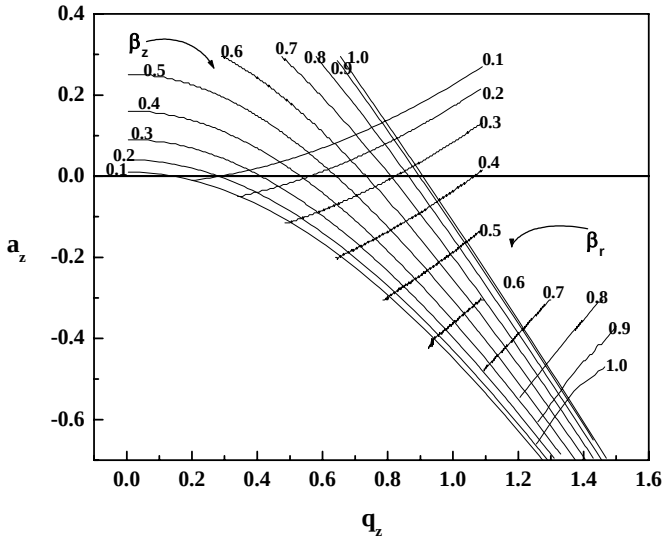

Figure 1.8. Stability diagram showing iso-β lines in a_z-q_z space. The regions of stability are bounded by β_z=0, β_z=1, β_r=0 and β_r=1.

Stafford et al. (March 1989) envisioned that the traps could be operated in a "mass-selective instability mode." In this case operation is made so that there is no DC component to the field, i.e., $a_z = 0$. Therefore from Figure 1.8 it is seen that stability in an ideal hyperbolic trap will only be achieved with q_z values in the range of 0.2 to 0.908. As the RF voltage is increased the q_z value of the ion increases as well. Therefore, by linearly increasing the magnitude of the RF voltage, the ion can "move" along the $a_z = 0$ line towards a q_z value of 0.908. Values greater than 0.908 yield instability, at that point ions are ejected from the trap. The mass-to-charge limit of the ion trap may be determined by the solution of q_z (Equation (1.24)). This assumes ion stability along the z-direction and operation of the trap with no DC component:

$$\left(m/z\right)_{\max} = \frac{8V_{0-P}}{q_{z-eject}(r_o^2 + 2z_o^2)\Omega^2} \qquad (1.29)$$

Equation (1.29) is the governing equation in determining the mass range and operating parameters of the trap. $V_{0\text{-}P}$ is the RF voltage from zero to peak. q_{eject} is the value of q_z in the Mathieu stability diagram when the ion is ejected from the trap, if $a_z = 0$. If the trap is operated in the mass-selective instability mode ($q_{eject} = 0.908$), then for a given r_0 and corresponding z_0, the voltage and RF frequency can be set for a range of m/z. Ideally, a microfabricated CIT would operate in the mass-selective instability mode. The work here explores the design of a micrometer-scaled cylindrical ion trap with high mass range, good resolution, high sensitivity, and low operating voltage.

2.0 OVERVIEW OF CYLINDRICAL ION TRAPS: DESIGN, MICROFABRICATION, TESTING AND SIMULATION

An overview of the results for the design, microfabrication, testing, and simulation of cylindrical ion trap devices is given in this chapter. More detailed descriptions and discussions of each of these activities is provided in the subsequent chapters.

2.1 Cylindrical Ion Traps: Design

The confinement of ions in three dimensions requires a three-dimensional potential energy. From Coulomb's law and Earnshaw's theorem (Jones 1980) it is realized that such a potential energy minimum cannot be achieved through the sole use of electrostatic fields. However, trapping can be accomplished through time-dependent electric fields. A sinusoidal time-varying electric dipole field does not trap ions, since the effects of the electric field on the ion motion cancel each other out over one cycle of the field, and the ion retains a zero net movement and its initial thermal velocity. Therefore fields which are dependent on position, i.e., linear fields or fields of higher order are needed. Thus, as the ion moves it will experience fields of different strengths during one cycle of the electric field, resulting in a non-zero net effect. While the field is focusing in one direction, it is defocusing in the orthogonal direction. The time variation of the sign of the field reverses the focusing and defocusing periodically. The net effect can be a focusing or defocusing of the ion, depending on the operating conditions, i.e., on the strength of the alternating electric field, its frequency, and the mass of the ion. If the net effect is focusing, the ion will be trapped. This method of trapping ions was discovered and subsequently exploited by Wolfgang Paul and colleagues at the University of Bonn (Paul and Steinwedel 1953). The design of a micro-cylindrical ion trap array is presented here, while its fabrication is detailed in section 2.2.

Numerous reviews have described the theory of RF ion traps used for ion storage and for ion trap mass spectrometry (Wuerker, Shelton et al. 1959; Dehmelt 1967; Dehmelt 1969; Horvath, Thompson et al. 1997; March 1997; Hao and March 2001). RF trap mass spectrometers feature near-linear fields and are thus quadrupole traps. Quadrupole with higher order components suppressed fields are formed via hyperbolic electrodes. Hyperbolic electrodes are difficult to fabricate, and as a result the cylindrical ion trap which provides linear fields with higher order components was invented.

Although hyperbolic electrodes provide a field with minimal higher order components, leading to more effective ion trapping, they are nearly impossible to machine using microfabrication techniques. Thus the advantage gained by having hyperbolic electrodes is lost by the difficulty in their realization in the micrometer scale. Cylindrical ion traps offer a quite satisfactory approximation to the quadrupole field attained by the hyperbolic electrodes, as previously depicted in Chapter 1. Therefore the design pursued here focused on miniaturizing cylindrical ion traps. For applications to mass analysis, multiple traps in large arrays were configured to increase signal. Ideally the driving and sensing electronics would be incorporated on the same chip as the mass-analyzer, to realize a system on a chip.

Equation (2.1) shows the relationship between the mass to charge ratio of the trapped ion and the voltage, size and operating frequency.

$$m/z = \frac{8V_{0-P}}{q_z\left(r_0^2 + 2z_0^2\right)\Omega^2} \qquad (2.1)$$

As seen from this relation, as the size of the trap is decreased the mass of the trapped ion is increased. This is in contrast to the other physical approaches to mass analysis, where ion mass decreases with device dimension. Moreover, miniaturization of an ion trap mass analyzer should allow the operation of the ion trap at much lower voltages; currently ion traps in the mm-cm scale require thousands of volts. Micro-sized traps could potentially be operated with tens of volts at higher frequencies. Figure 2.1 shows the theoretically calculated mass of a trapped ion as a function of the operating voltage at 500 MHz and 1 GHz for a r_0=1 μm trap.

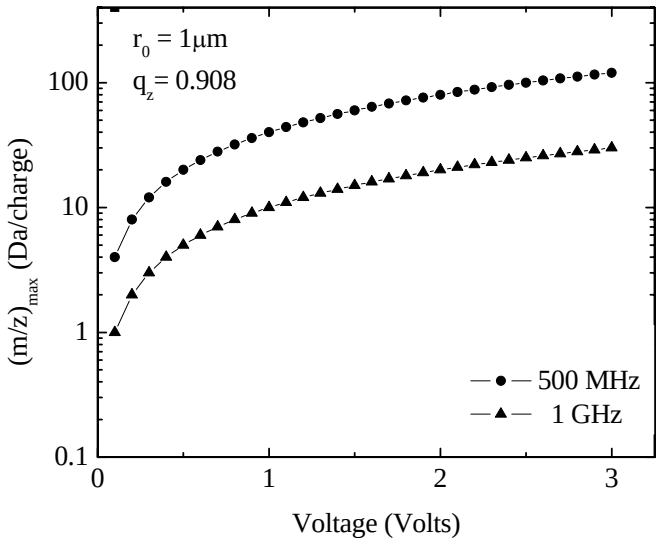

Figure 2.1. Mass to charge ratio of trapped ions as a function of voltage for an r_0=1μm trap at f=500 MHz and f=1GHz.

The cylindrical ion trap was chosen for miniaturization because of its simple electrode design and its demonstrated low power consumption. (Beaty 1987; Badman, Johnson et al. 1998; Wells, Badman et al. 1998) As with other mass analyzers, miniaturization of the ion trap brings losses in performance, in this case an inherit loss of sensitivity due to the reduced ion trapping volume. To address this problem, arrays of CITs can be constructed to regain the sensitivity lost in miniaturization (Badman and Cooks 2000). This use of arrays follows their introduction for this purpose in quadrupole mass filters (Boumsellek and Ferran 2001) and their subsequent use in sets of CITs (Zheng, Badman et al. 1999; Badman and Cooks 2000; Tabert, Griep-Raming et al. 2003).

The simplified geometry of the CIT facilitates its microfabrication. Thus, for the work here structures were designed to maintain a cylindrical geometry while reducing overlap capacitance and maintaining ease of fabrication. Electrode features were maintained at widths of 1.2 μm or less due to the tungsten stress. Trap half heights were determined by the ratio, $r_0^2=2z_0^2$, and the spacing between electrodes was maintained at approximately 0.5 μm. Figure 2.2 shows a Solid Works drawing of the proposed microfabricated cylindrical ion trap array unit cell. The design includes a top end cap, a ring electrode, a bottom end cap and a collector, all positioned on a dielectric atop the silicon substrate.

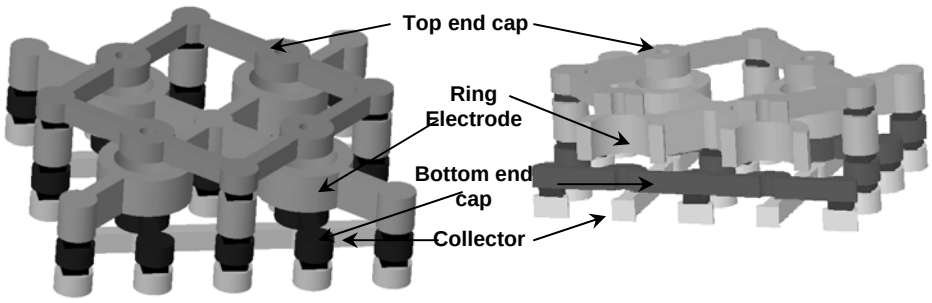

Figure 2.2. SolidWorks™ three dimensional representation of proposed design for microfabricated cylindrical ion trap arrays: (a) the unit cell and (b) the array in cross-section.

2.2 Cylindrical Ion Traps: Microfabrication

The trap microfabrication approach employed a molded tungsten fabrication sequence, involving eight masks and consisting of a series of processing steps of photolithography, thin film deposition, plasma etching, and chemical mechanical polishing (CMP). Processing for these parts was performed at the Microelectronics Development Laboratory (MDL) at SNL. A 6" 2-20 Ω-cm p-Si wafer with dielectric layers of silicon dioxide and low-stress silicon nitride was the starting material. Figure 2.3 (a) shows the pad layout for the ion trap arrays and (b) shows the detailed features for the ion trap arrays.

Silicon dioxide was used as the mold for the features and was deposited using a TEOS precursor in a PECVD reactor and then patterned and etched using a CHF_3 plasma. After the oxide patterning, tungsten was over deposited via CVD with a WF_6 precursor to fill the feature and then planarized to the oxide thickness by CMP. All electrode layers were anchored to the substrate. At total of seven levels, including electrodes and vias were fabricated. An 8000 Å Al thin film was deposited on contact pads to facilitate electrical connections. After fabrication, the structure was released in a buffered HF acid solution to minimize the etching of aluminum. Figure 2.4 shows a scanning electron microscopy micrograph of a fabricated ion trap array with r_0 =1 μm.

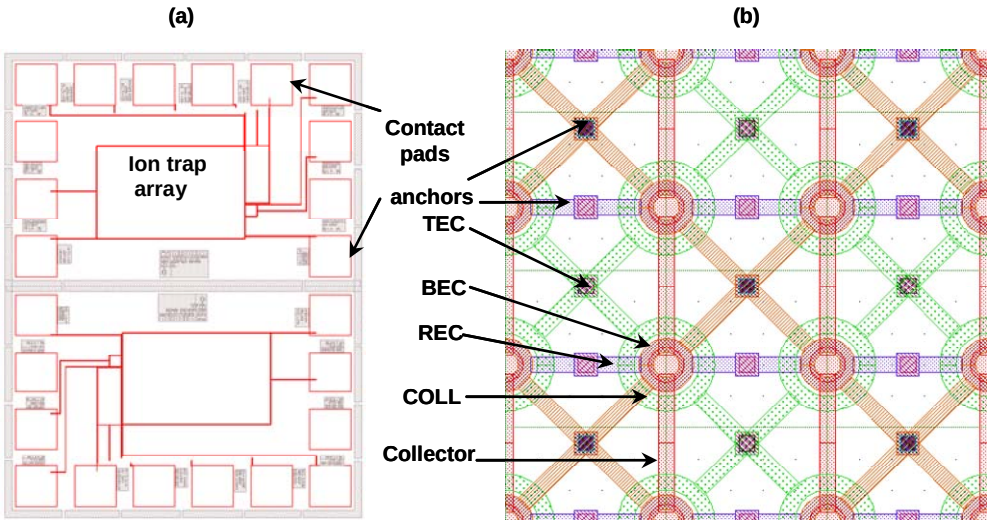

Figure 2.3. (a) The pad layout for ion trap arrays. Two array sizes were fabricated, r_0=1 μm and r_0 = 1.5 μm. (b) Detail of the mask layout for molded tungsten fabrication layout for a r_0=1 μm ion trap array.

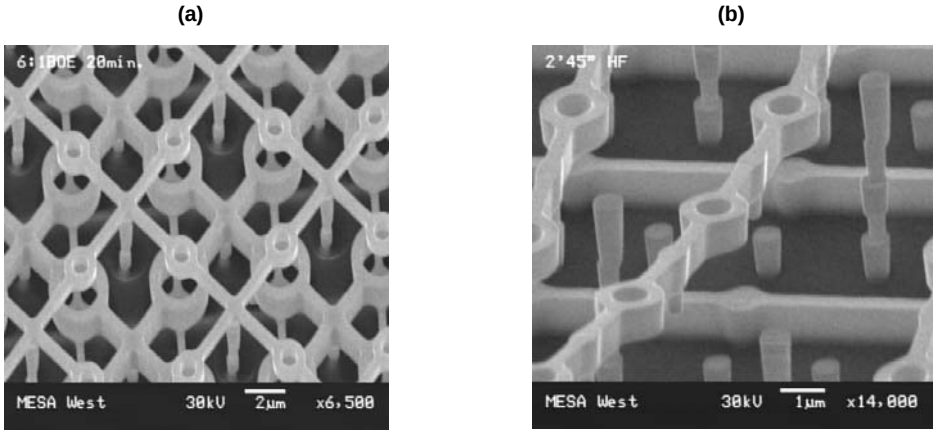

Figure 2.4. SEM images of microfabricated ion trap arrays (r_0=1μm) using a molded tungsten fabrication sequence (a) Electrodes were able to stay in place because the structure was not fully released and oxide was holding the top end cap in place. (b) SEM image showing lifting of end cap after a complete release due to insufficient anchor area.

As seen in Figure 2.4 (b), the anchor area was insufficient to hold the top end cap in place. When the structure was released to the bottom electrode, W layers began to lift off due to the W stress. Figure 2.4 (a) shows all electrodes in place because the structure was slowly released in a BOE 6:1 solution and the oxide was not fully removed. Thus the top end cap was held in place by the remaining oxide. To circumvent this problem, the anchor area was significantly increased, as shown in Figure 2.5. Figure 2.5 (a) also shows a redesign of the pad layout. A ground signal ground input was implemented for the signal inputs in order to ensure better propagation of the

wave at the operating frequencies of 100 MHz – 1 GHz. Figure 2.5 (b) shows the increase in anchor area. Appendix E details the mask layout.

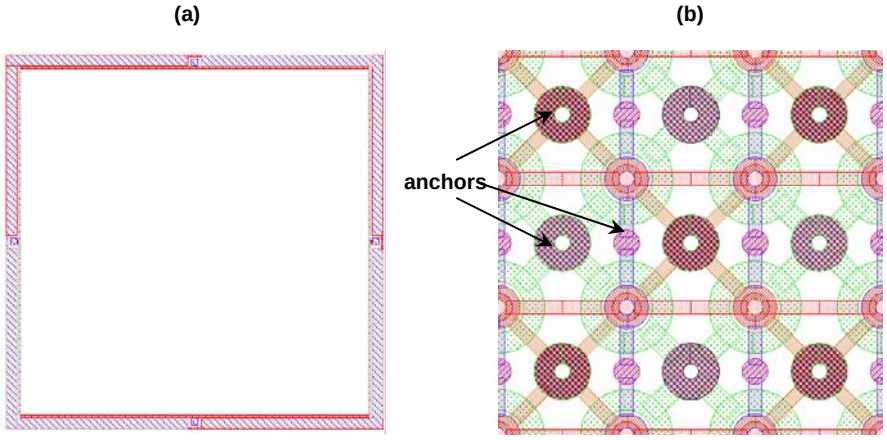

Figure 2.5. (a) Ground signal ground pad layout.
(b) Detail of ion trap array showing increased anchor areas.

In this re-design, more trap sizes were implemented as well. Traps with radii of 1, 2, 5 and 10 μm were fabricated. As the height of the trap increases more ring electrode layers were implemented to supplement the trap height. The layers are created via the oxide mold and limitations in the height of this mold, c.a. 2.5 μm, create the need for additional layers. The fabrication sequence was repeated until all layers were completed and thus, four fabrication runs were necessary for the four trap sizes. All four trap sizes as well as electrical characterization structures were incorporated in one die layout. Figure 2.6 shows a SEM micrograph of a r_0 = 2 μm fabricated structure.

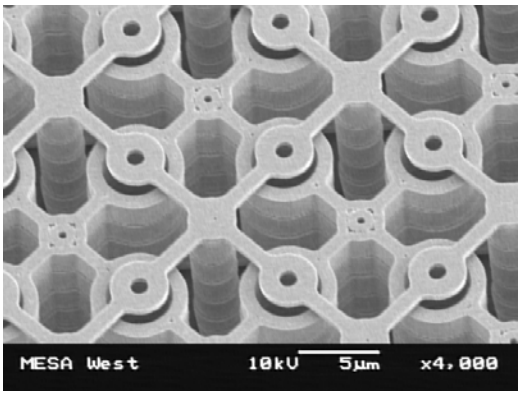

Figure 2.6. SEM image of microfabricated ion trap array with r_0=2 μm.

It is apparent from Figure 2.6 that the anchor area was sufficient in this design. The overall structure height for the r_0 = 5 μm trap was on the order of 12 μm, and the anchor area was sufficient to anchor a structure four times in height as the structure in the initial W design. The r_0=10 μm traps were on the order of 24 μm in height, or eight times the height of the original design.

2.3 Microfabricated Cylindrical Ion Trap Arrays: Testing Setup

The test set up for the microfabricated cylindrical ion trap array is depicted in Figure 2.7. Ion current measurements were attempted, after applying RF trapping pulses to the ring electrode. The trap could not be operated in the mass instability scan mode as the trapping characteristics of the ion trap could not be discerned. Analytes were ionized by electron impact ionization with two rhenium filaments operated in parallel at 70 eV. These were gated using the marker on a Tektronix AWG710 arbitrary waveform generator. The AWG710 was also used to simultaneously drive the ring electrode. The AWG710 can provide sine waves with amplitudes of 0.5 $V_{0\text{-}P}$. An Amplifier Research (AR) amplifier was incorporated for voltage amplification and 2 Thruline Bird power meters were used to monitor the forward and reflected powers during steady state operation. The top and bottom end caps were typically grounded. The collector electrodes were utilized as Faraday cups for ion detection. Since the collector and ring electrodes were capacitively coupled, a low-pass filter was included to separate the wave signal picked up by the collector from the ion signal. As the ion current was expected to be on the order of 1-50 nA, based on the number of trapped ions, a Keithley 428 current to voltage amplifier was used to increase the output signal and a Tektronix TDS540 oscilloscope was utilized for data acquisition. The chamber was pumped down with a Pfeiffer TMH-071 turbo pump backed with a mechanical pump. The base pressures ranged from 8×10^{-6} to 1×10^{-5} Torr. The analyte was introduced into the chamber through a leak valve increasing the pressures to the range of 1×10^{-4} to 5×10^{-4} Torr, as monitored by a Granville-Phillips microion gauge.

Figure 2.8 depicts a sample sequence, and typical ion signal response from a 5-μm cylindrical ion trap array of 1×10^{5} traps. A decrease in the signal was observed when toluene ions were introduced into the trap and as well as the RF turn off which was not filtered.

2.4 Cylindrical Ion Trap Array: Simulation

Simulations of ion trapping micro-scaled cylindrical ion traps were performed using SIMION 7.0 (Dahl 2000). Contour lines and potential gradients were determined with SIMION and Poisson Superfish (Cooper, Menzel et al. 1987). Ion Trap Simulation Program (ITSIM) (Bui and Cooks 1998) was utilized in the early stages of this research to generate mass spectra.

SIMION makes use of potential arrays which define geometries and potentials of electrodes and magnetic poles. The potentials of points outside electrodes and poles are determined by solving the Laplace equation (Equation (2.2)) by finite difference methods.

$$\nabla^2\phi = 0 \qquad (2.2)$$

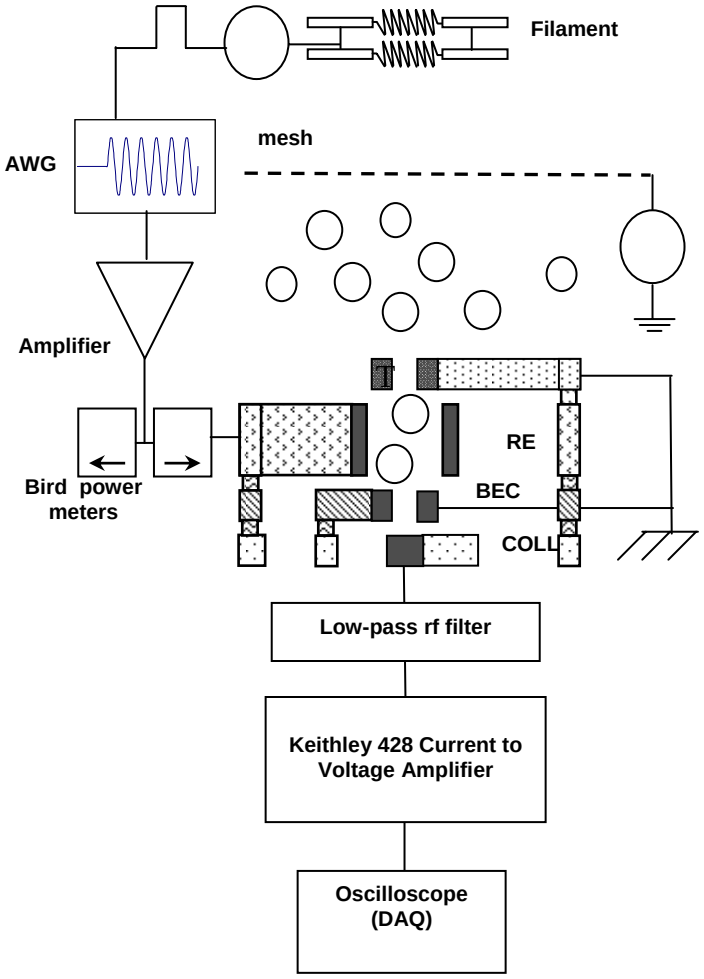

Figure 2.7. Test set-up for testing the microfabricated cylindrical ion trap arrays. RF voltage was applied to the ring electrode using an arbitrary waveform generator and signal was measured at the collector electrode. A gated dual rhenium filament provided electrons. Electrons were guided to the traps via a biased mesh. A low pass filter removed RF signal from the collector and a current to voltage amplifier was implemented for signal amplification. Data acquisition was made by an oscilloscope.

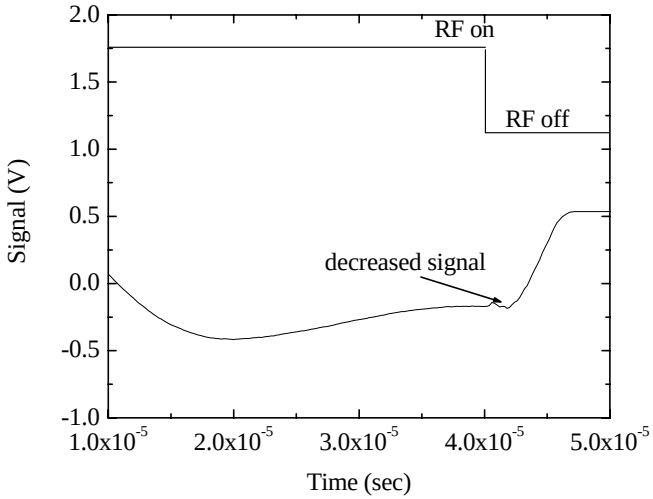

Figure 2.8. Signal response for the 5 μm ion trap array; toluene ions were introduced at P_{Tol}=1×10^{-4} Torr.

The specific method used in SIMION is a finite difference technique using over-relaxation. This technique is applied to two or three dimensional potential arrays of point potentials representing electrode and non-electrode regions. Relaxation methods use iteration, a technique of successive approximation. Thus numerical computation errors are minimized, solutions are stable and computer memory storage requirements are minimized. The relaxation method uses nearest neighbor points to obtain new estimates for each point, four points in two dimensions and six points in three dimensions. For the simulations the potential arrays were refined to a convergence limit of 10^{-7}, the smallest limit possible in SIMION. Moreover, the micrometer sized cylindrical ion traps were defined using a 3-dimensional non-symmetric array utilizing the actual photomasks dimensions. Ion trajectory computations are a result of three interdependent calculations. First, electrostatic, magnetic and charge repulsion (if applicable) forces are calculated based on the current position and velocity of the ions. These forces are used to compute the current ion acceleration by a fourth order Runge-Kutta method to predict the position and velocity of the ion at the next time step. The time step itself is then continuously adjusted to maximize trajectory accuracy while minimizing the number of integration steps per trajectory.

2.4.1 Cylindrical ion trap array potential definitions

In order to be able to simulate the ion behavior in the traps, the geometry of the electrodes of the ion trap must first be defined. Potential arrays were defined in three dimensions to capture any asymmetries. First, the potential array for a conventional cylindrical ion trap was considered. Figure 2.9 shows the drawn potential arrays and dimensions. The top and bottom end caps are identical and have an end cap aperture, r_a, of 0.85 μm and an outer radius of 2 μm. The spacing between the end cap electrodes and the ring electrode is 0.2 μm. The ring electrode inner radius is 1 μm and outer radius is 1.4 μm.

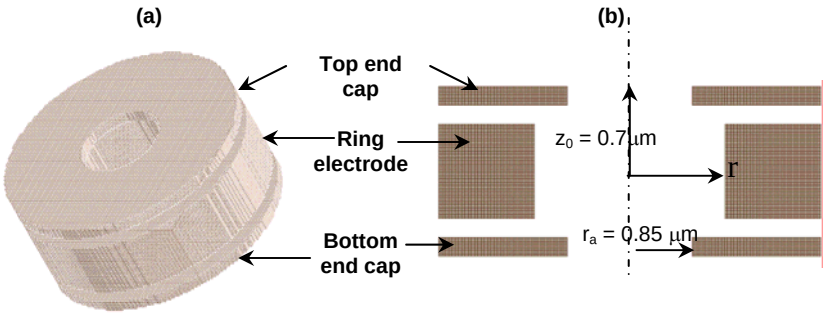

Figure 2.9. Potential arrays drawn in SIMION of an r_0=1 μm cylindrical ion trap. This is a conventional trap where the electrodes have the same outer radii and the trap half-height is defined by $z_0^2=r_0^2/2$. The end cap apertures, r_a, are 85% of r_0. (a) A three dimensional view and (b) the z-r cross sectional view.

Figure 2.10 shows the geometry configuration of the Al electrode CIT where r_a is equal to r_0, with the addition of a collector. The half-height to radius ratio was kept the same as in the conventional trap, $1/\sqrt{2}$. Electrode spacing was also kept also at 0.2 μm.

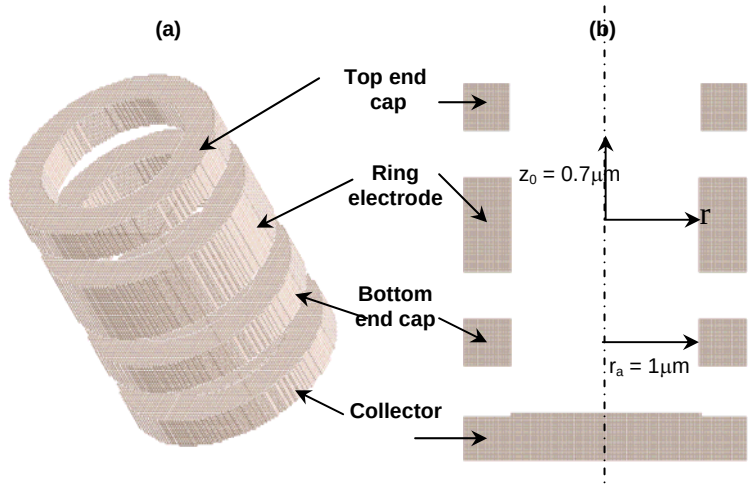

Figure 2.10. Potential arrays drawn in SIMION of an r_0=1 μm CIT. The trap has electrodes with the same inner radii, i.e., the end cap apertures, r_a, are equal to r_0, and the trap half-height is defined by $z_0^2=r_0^2/2$. (a) A three-dimensional view and (b) the z-r cross sectional view.

Figure 2.11 shows the potential array of the W-electrode ion trap structure, where the end cap outer radius is equal to the ring electrode inner radius, 1 μm. End cap apertures were 35% of r_0 and the half-height was kept at 0.7 μm. In this case electrode wall thicknesses were kept at 0.5 μm for the ring electrode and 0.65 μm for the end caps. This is an asymmetric structure.

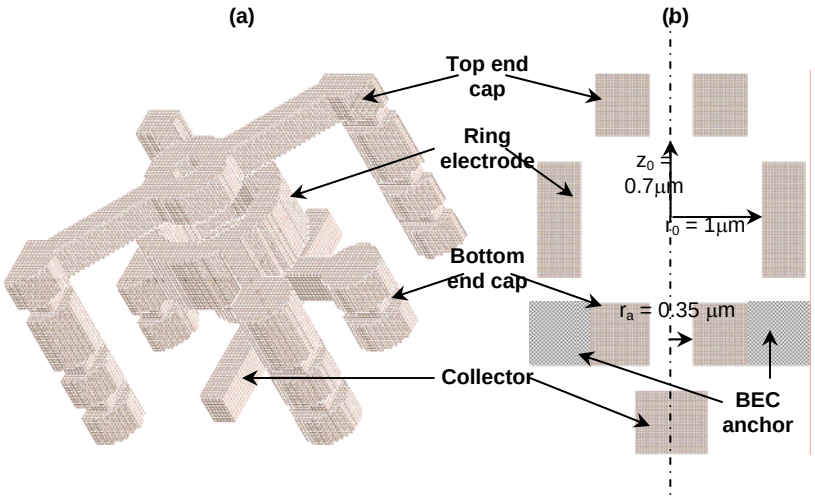

Figure 2.11. Potential arrays drawn in SIMION of a r_0=1μm cylindrical ion trap. This trap design has the end cap electrodes with outer radii equal to the ring electrode inner radius. The structure is suspended via straps anchored to the substrate. (a) A three-dimensional view, and (b) the z-r view with the bottom end cap showing part of its anchoring strap.

2.4.2 Simulation Conditions

A user program was written utilizing the SIMION programming language in order to apply a time varying potential to the ring electrode, randomize ion's initial starting conditions and simulate ion-neutral collisions. The end caps were conventionally grounded and simulations were run at 1 GHz. The collector was also grounded, however, a negative bias was applied to determine if this would interfere with the ion trapping potential field. The ion of interest was toluene at m/z = 93. Through the user-program the ring electrode voltage was defined as:

$$V_{0-P} = V_0 \cos \Omega t \qquad (2.3)$$

Table 2-1 shows the parameters defined in this work using SIMION. These variables were utilized in the user program to simulate the ion trajectories and ion trapping in micrometer scaled cylindrical ion traps. The ion starting conditions were also programmed. The initial ion energies were randomized to a Maxwellian distribution with kT, where k is Boltzmann's constant, as the mean energy. The ion positions were randomized to a cylindrical volume with a radius equal to the end cap aperture and the height equal to the height of the trap. The program is discussed in detail in Appendix F.

Table 2-1. Parameters defined in SIMION simulations.

Parameter	Starting Value
Top end cap voltage	0 V
Bottom end cap voltage	0 V
Collector voltage	0 V
Ring electrode voltage	5 V
Total number of cycles	2000
Frequency	1 GHz
mm/grid unit	0.001
PE update/ μs	1×10^{-5}
Pulse out voltage	10 V
Mass of the ion	93
Ion's kinetic energy	0.02 eV

2.4.3 The Effect of Simulation Parameters

Ion trapping efficiency, defined as the percentage of ions remaining with respect to the number of starting ions, was determined as a function of frequency, voltage and the stability parameter, q_z. Changes in the ion kinetic energy were briefly investigated, but not thoroughly quantified. Ions were considered to be trapped if they remained in the trap for 2000 cycles. At 1 GHz this is equivalent to 2 μs. As seen in Figure 2.12 (lines were included to guide the eyes), there exists a q_z value where the ions show maximum trapping efficiency and this theoretically and experimentally agrees with results for macroscopic traps. For a given voltage, a q_z value of ~0.4 was found to be optimum.

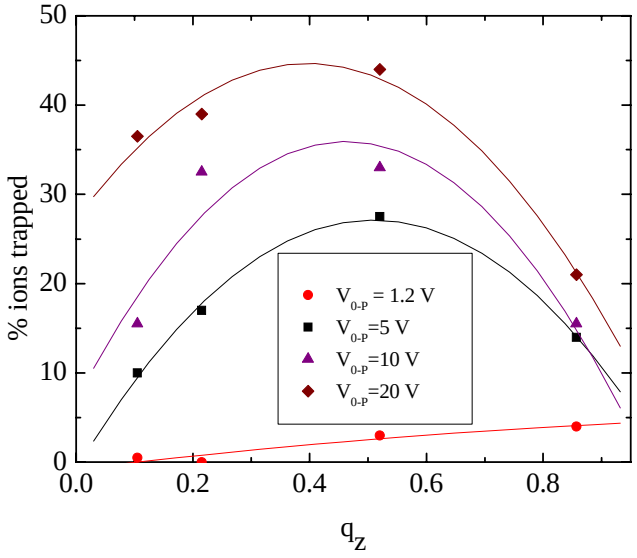

Figure 2.12. Ion trapping efficiency versus q_z. Simulation was performed for design 3, r_0=1μm. q_z values of ~0.4 were found to be optimum.

The relationship of ion trapping efficiency versus the applied ring electrode peak voltage was also examined. For a given q_z value the trapping efficiency saturates as the voltage is increased, thus increasing the voltage arbitrarily does not increase the trapping efficiency. Efficiencies became saturated in the range of 5- 20 V as seen in Figure 2.13. (Once again lines were added to guide the eyes).

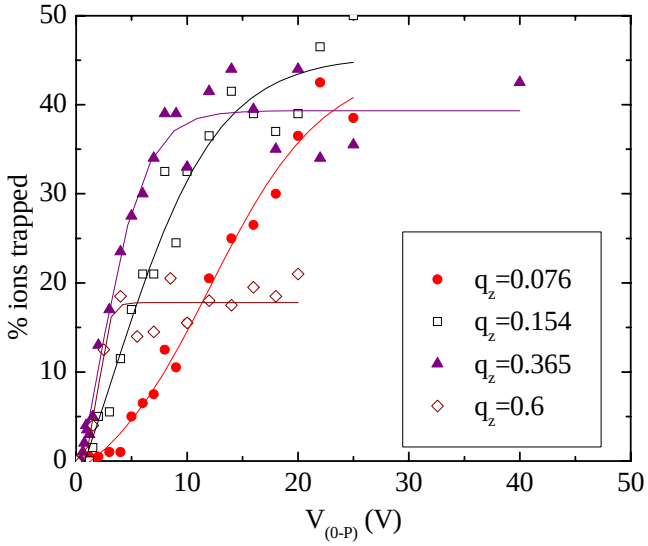

Figure 2.13. Ion trapping efficiency as a function of voltage for the r_0=1μm sized ion trap. The frequency was 1 GHz. The trapping efficiency saturates as the voltage is increased allowing trap operation to be in the range of 5-20 V.

2.4.4 Potential Gradient Simulation

Poisson Superfish is a code provided by the Los Alamos Accelerator Code Group (LAACG) (Cooper, Menzel et al. 1987). It is a two-dimensional code package of more than 30 programs for the design of RF cavities, magnet components, electrostatic elements, and waveguide devices. An over-relaxation method is used to solve the generalized Poisson's equation in two dimensions. Eigenfrequencies and fields for arbitrarily shaped two-dimensional waveguides in Cartesian coordinates and three-dimensional axially symmetric RF cavities in cylindrical coordinates can be determined. The program is used as input to ITSIM. Figure 2.15 shows the simulated potential field from the program. Although the fields were calculated with great accuracy, the program does not handle the asymmetries present in the trap design.

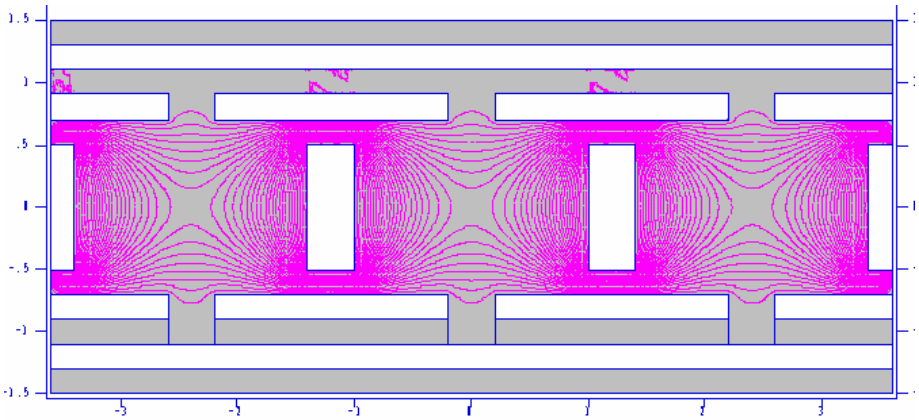

Figure 2.14. Potential fields in a micrometer sized cylindrical ion trap arrays simulated by Poisson Superfish.

2.4.5 Mass Spectra Simulation with Ion Trap Simulation

The Ion Trap SIMulation (ITSIM) software program was utilized to generate mass spectra. This program was developed at Purdue University in Prof. Cooks' group. The program uses the simulated field gradients from the Poisson Superfish program to determine ion trajectories and simulate mass spectra. Figure 2.15 shows a simulated ion trajectory for a m/z = 600 ion in an r_0=1 μm ion trap. Figure 2.16 shows the corresponding simulated mass spectrum.

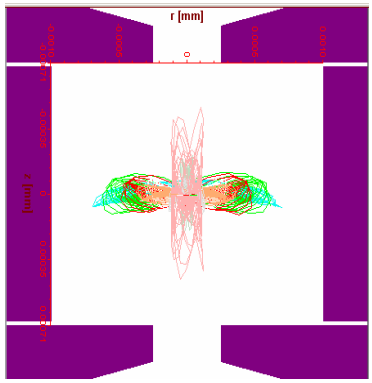

Figure 2.15. Simulated ion trajectory by ITSIM.
The ion of interest has a m/z = 600 amu and the trap a radius of 1 μm.

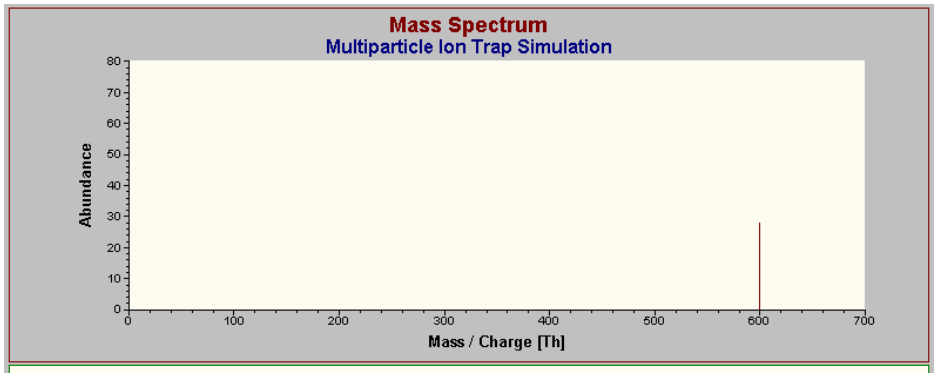

Figure 2.16. Simulated mass spectrum for a m/z of 600 ion from ITSIM program.
The trap has a radius of 1 μm.

3.0 ION TRAP DESIGN

A detailed discussion of the design considerations of microfabricated cylindrical ion traps is presented. The ion trap design is critical in achieving optimal performance while maintaining minimal power consumption. Materials and fabrication methods for the creation of microfabricated ion traps are considered. Aluminum and tungsten were determined to be good materials for the micro-fabrication of cylindrical ion traps. Moreover, the ion trap array electrical characteristics were considered when determining the electrode layout and power consumption was expected to be on the order of 10 W. The electric field calculations revealed minimal field deviation from ideality. The simulations of trapping as a function of the ion's kinetic energy determined that trapping could occur in the order of tens of volts.

3.1 Introduction

Although ion traps have application in the fields of atomic, optical, and molecular physics and chemistry, the research in this dissertation deals with the microfabrication of cylindrical ion traps to mass spectrometry. Miniaturized mass spectrometers have become an important and expanding field in physical science and many groups have considered and attempted the miniaturization of different mass spectrometers, as mentioned in the introduction of this dissertation.

The simplified geometry of the CIT has facilitated construction of a low power-consumption miniaturized instrument, as recently described in the literature (Patterson, Guymon et al. 2002; Riter, Laughlin et al. 2002; Riter, Peng et al. 2002). This mass spectrometer utilizes a CIT mass analyzer (r_0=2.5 mm, z_0=2.88 mm) one quarter the size of a conventional r_0=1 cm device and is operated with an RF drive frequency of 2 MHz and a maximum voltage of 1000 $V_{0\text{-}P}$. These incremental improvements in the mass, volume, and power requirements are being realized by straightforward scaling-down of current CIT instruments via the downsizing and re-engineering of standard spectrometer subsystem components. To enter the hand-held domain, the size, weight, and complexity of the mass spectrometer must be reduced by orders of magnitude. A promising route to this goal involves the microfabrication of a micron-sized CIT and its use in a massively parallel array of traps. The theoretical analyses have shown that the micro-sized trap could be operated with tens of volts at higher frequencies. Figure 3.1 shows a plot of the mass of the ion versus operating voltage at f=500 MHz and f=1GHz for an r_0=1μm trap.

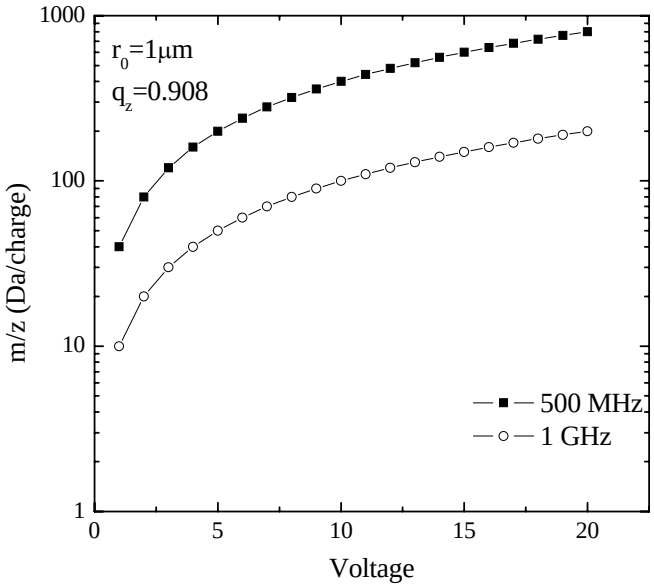

Figure 3.1. Mass to charge ratio as a function of voltage for an r_0=1μm trap at f=500 MHz and f=1GHz.

In this chapter the design considerations of microfabricating ion traps as much as four orders of magnitude smaller than conventional ion traps are discussed.

3.2 Design Considerations for Micro-scaled Ion Traps

3.2.1 Electrode Materials

The materials used to make the ion traps determine the method of microfabrication and the constraints on the size of the traps. Similarly, the desired size and electrode shape dictate the microfabrication method.

If conventional thin film deposition techniques are utilized, such as electron-beam evaporation or sputtering, the films are restrained to a few microns in thickness (Madou 1997). This method of depositing and subsequently etching the films would enable the fabrication of ion traps which have nominally a one micrometer radius. Electroplating or lithographie galvanoforming abformung (LIGA) would facilitate microfabrication of larger sized traps in the 100 micron range; however, making interconnects for a three or four electrode structure would become difficult (Madou 1997). Another fabrication method where trap electrodes are molded in oxide and deposited by chemical vapor deposition (CVD) can also be used for the fabrication. This method utilizes the damascene processes for back end metallization used in the semiconductor industry (Andricacos, Uzoh et al. 1998). This method provides the ability to create taller structures by stacking films atop each other, constrains the height of trap to the total oxide thickness in which the features are molded, and relaxes the limitations in the interconnect design compared with those in electroplating.

The method of fabrication also determines the materials used for the trap electrodes. For example, a good RF conductor is desired for this application. Table 3-1. summarizes different metals and their thermal and physical properties, as well as methods for deposition. The skin depth is defined as the distance to which incident electromagnetic radiation penetrates; or the depth below the surface of the conductor at which the current is 1/e (about 0.37) of the current at the surface. At low frequencies the skin effect is negligible and the current distribution is uniform. At high frequencies the depth to which the current flow can penetrate is reduced. Skin effect causes the apparent resistance to increase above its DC value, lowering the Q-factor (Q=ΩL/R) in resonant circuits and reducing efficiency. If the skin depth is greater than the wire radius then the apparent resistance should be the conductor's DC resistance. The skin depth was calculated using the following relation (Benenson, Harris et al. 2002);

$$\delta = \sqrt{\frac{2\rho}{\Omega \mu_r \mu_0}} \qquad (3.1)$$

where ρ is the density of the conductor, Ω is the angular frequency ($2\pi f$), μ_r is the relative magnetic permeability of the conductor and μ_0 is the magnetic constant, the permeability of the vacuum, where $\mu_0 = 4\pi \times 10^{-7}$ N A^{-2}.

The loss tangent is defined as the ratio of the magnitude of the conduction current density $\sigma \overrightarrow{E_x}$ to the magnitude of the displacement current density $j\varpi\varepsilon \overrightarrow{E_x}$ in the material medium. The loss tangent can be determined through (Rao 1994):

$$\tan \ell = \frac{\sigma}{\Omega \varepsilon} = \frac{1}{\Omega \rho_r \varepsilon} \qquad (3.2)$$

where σ is the conductivity of the material, Ω is the angular frequency, ε is the dielectric constant of the material and ρ_r is the resistivity of the material. In practice, the loss tangenet is, however, not simply inversely proportional to Ω since both σ and ε are generally functions of frequency. Not enough information on the dielectric of metals was obtained, and thus the loss tangent was not calculated. However, it remains an important property to be considered and is thus noted.

Table 3-1. Potential materials used for the microfabrication of the cylindrical ion traps and their relevant properties. (Lide 2004)

Property	Aluminum (Al)	Copper (Cu)	Gold (Au)	Intrinsic Silicon (Si)	Tungsten (W)
Density at 25^{o}C (gm/cc)	2.7	8.96	19.3	2.3	19.3
Resistivity (μΩ cm)	2.709	1.712	2.255	2.3×10^{11}	5.39
Skin depth (μm) at 100 MHz	8.0	6.58	7.55	220	11.68
Skin depth (μm) at 1 GHz	2.6	2.08	2.4	71	3.6
Thermal Conductivity (W/cm·K)	2.37	4.01	3.17	1.48	1.74
Young's Modulus	70	120	78	160	410
Coefficient of linear expansion $\times 10^{6}$ (K^{-1})	23.1	16.5	14.2	3	4.5
Specific heat (J/g·K)	0.904	0.384	0.129	0.71	0.132
Melting Temperature (^{o}C)	660.32	1084.62	1064.18	1410	3414
Deposition Technique	Sputter, e-beam evaporation	e-beam, electroplating	Sputter, e-beam, electroplating	CVD, e-beam	CVD, sputter

As shown in Table 3-1. copper has the smallest resistivity and at 1 GHz the skin depth is about 2.08 μm. Copper is thus the best candidate for making ion traps. High resistivity materials, such as silicon, are not good candidates, since the resistivity will cause the electrodes to heat and affect the ion trapping by creating hot spots in the electric field (Yu-Rong, Mang et al. 2001; DeVoe and Kurtsiefer 2002).

Copper was considered as the electrode material. However, it was determined that a lift-off patterning process would not yield a smooth side wall, altering the pseudopotential and creating enhancement in the field. Figure 3.2 shows a SEM image of a lift-off profile of a 2-μm tall patterned copper cylinder. Note that, the sidewall is not smooth, the jagged edges potentially lead to problems in the formation of a linear and radially uniform electric field.

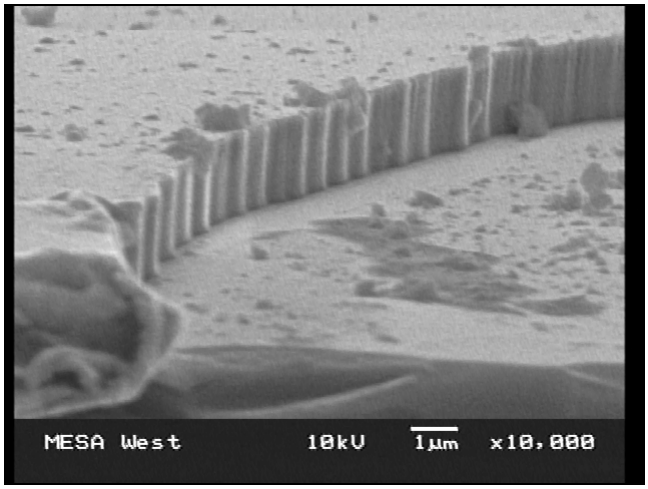

Figure 3.2. Lift-off profile of patterned copper cylinder.
The edges were jagged, leading to higher order fields inside the trap.

Thus, the materials listed in Table 3-1. having low resistivity and able to be patterned by means other than lift-off are potential candidates for the microfabrication of ion trap electrodes. For designs considered here, electrode materials of aluminum and tungsten were investigated.

3.2.2 Electrode Design

The first consideration in the realization of the micro-ion trap is the electrode design and fabrication. It was determined that hyperbolic electrodes would be too difficult to micromachine because of the fundamental 2-D nature of microfabrication. Microfabrication utilizes photomasks to define features in the x-y plane. The third dimension is created by deposition or etching of thin films, creating a hyperbolic structure in the z-x plane is nearly impossible. While cylindrical electrodes are a simplification of hyperbolic electrodes, their design and microfabrication are not trivial. The electrodes must be able to provide a sufficient trap potential depth, as well as minimize higher order fields (Wang and Franzen 1994; Lee, Oh et al. 2003). Consider the ion trap depicted in Figure 3.3 (a). This ion trap consists of two end cap electrodes, and a ring electrode. An ion collector is shown integrated with the device. The electrodes are separated by dielectric spacers and a time varying field is applied to the ring electrode. In a hyperbolic trap of similar nature, the number of trapped ions based on space charge considerations is estimated by Equation (3.3), based on Hans Dehmelt space charge limit (Dehmelt 1967)

$$N_{\max} = \frac{3}{16\pi} \frac{V^2}{m z_0^4 \omega^2} \qquad (3.3)$$

Equation (3.3) to can be used to approximate the maximum number of ions trapped. Table 3-2 shows the number of ions that are trapped based on space charge considerations for different radii and trap potential depth.

A single trap of radius of 1 μm is able to trap at most about 100 ions. However, if 10^6 traps are arrayed in parallel, about 1×10^8 ions could be trapped. Thus, a massively parallel array of

traps would have a trapping capacity comparable to that of a single r_0=1 cm-sized trap. The micro-sized trap would have the advantage of operating at much lower voltages and theoretically lead to less power consumption. Figure 3.3 (b) shows a three-dimensional perspective of the traps in a parallel array, packed in a hexagonal close packed configuration. The electrodes are separated by layers of silicon dioxide (SiO_2) or comparable dielectric. Although a massive parallel array of millions of traps would be difficult and tedious to machine, this is not the case if the traps are made through microfabrication techniques. The entire array of traps is included on a single photomask and is exposed simultaneously. Thus, either one or one million features can be exposed with equal facility. The number of traps arrayed in a given area is determined by the ion trap inner radius and spacing.

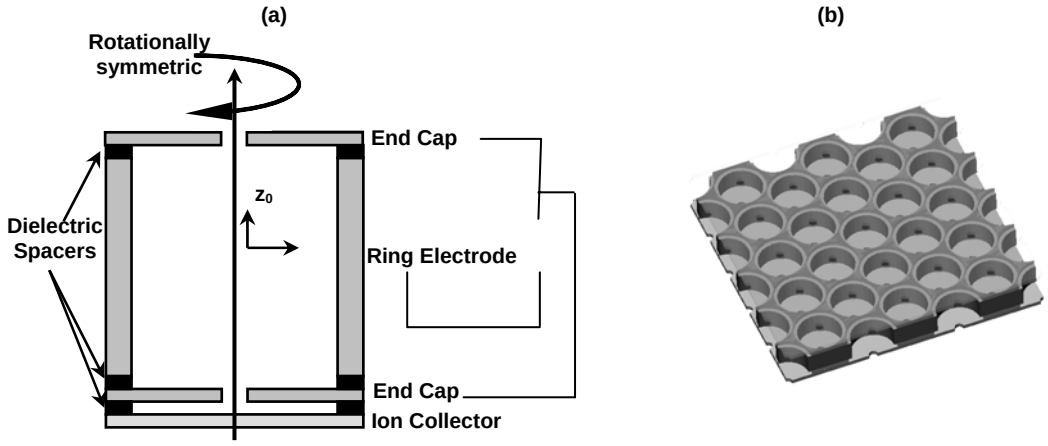

Figure 3.3. (a) A schematic diagram of a single cylindrical ion trap. The trap consists of two end cap electrodes and a ring electrode separated by dielectric spacers. An ion collector has been added in the schematic. (b) A Solidworks three-dimensional depiction of an array of cylindrical ion traps arranged in a hexagonal closest packed configuration.

Table 3-2. Maximum number of ions that can be trapped for a given radius and trap potential depth based on Dehmelt's pseudopotential approximation.

r_0	D_z (V)	N_{max} (Ions/Trap)
1 cm	500	1×10^9
1 mm	10	1×10^7
1 μm	0.5	1×10^2

The design depicted in Figure 3.3 can be made with thin film deposition and etching techniques, along with a release process. However, the alignment of the electrodes could be problematic. A structure can be made through a self-aligned etch which would ensure alignment of the electrodes. To further the simplicity of the fabrication, the end cap apertures can be made equal to the ring electrode radius. This trap is depicted in a schematic shown in Figure 3.4 (a). This trap provides a sufficient trap potential; however, due to the relatively large end cap apertures, higher order fields are not minimized. Figure 3.4 (b) shows a top view of how the

traps are laid out in an hcp fashion and Figure 3.4 (c) shows a three-dimensional perspective view of the array.

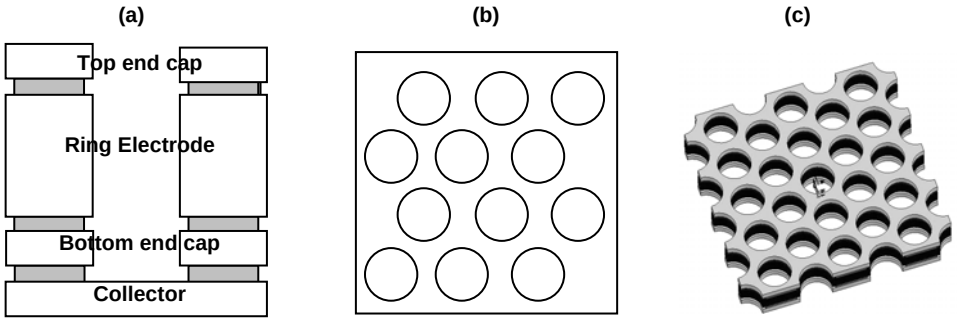

Figure 3.4. Self-aligned trap where the end cap apertures are equal to the ring electrode radius: (a) a single trap. (b) a hexagonally closest packed array of traps, and (c) a Solidworks three-dimensional perspective view of the hcp array.

The details of the fabrication of this trap are discussed in Chapter 6. This trap arrangement offers simplicity in fabrication and can be made with thin film depositions and etch processes. However, this electrode design, as well as the conventional ion trap design depicted in Figure 3.3 (a), constrains the height, and therefore the radius, of the trap due to stress caused by increasing thin film thicknesses. In these designs the electrode shape is determined after the deposition of the film by subtractive processing.

In order to reduce overlap capacitance, a second design using overhung structures was pursued. In this design layers are independently anchored to the substrate by dedicated vias. The outer radius of the end caps is less than or equal to that of the ring electrode. Overlap between electrodes only occurs where their support struts overlap with the previous electrodes. Although this design greatly reduces the overlap between the electrodes, vias must be patterned. This increases the number of photomasks required for building the structure since it is not a blanket dielectric film that is deposited in between electrodes as in the aforementioned designs, and each electrode is dependent on the previous layers for anchoring and support. Figure 3.5 (a) shows a cross-sectional perspective of the electrode design, which is an overhung structure. Figure 3.5 (b) shows the unit cell of an array consisting of four traps.

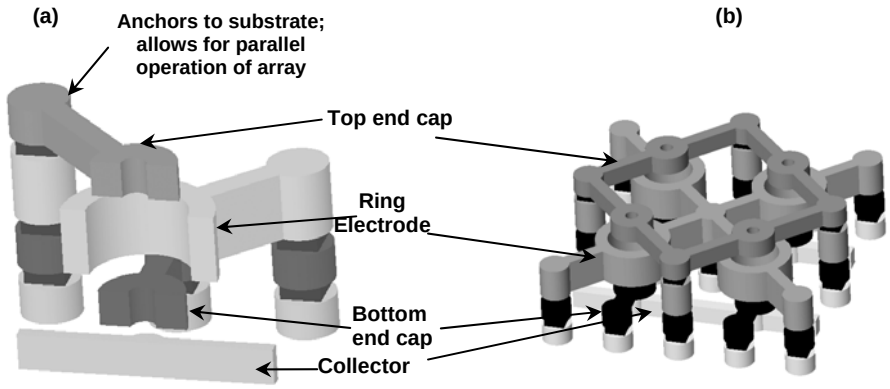

Figure 3.5. (a) A cross-sectional perspective view of an over-hung ion trap design. The ion trap consists of two end cap electrodes, a ring electrode, and an ion collector. All electrodes are anchored to the substrate by vias. (b) A unit cell of the hcp array of the overhung ion traps.

3.2.3 Electrical Characteristics

Although the shape of the trap electrodes is predetermined, i.e., a cylinder, the arrangement of the electrodes yield a wide variety of electrical characteristics. The capacitance, inductance and resistance of the structure will determine the resonant frequency and power delivered to the structure, and are therefore important characteristics to be considered. If the power consumption of the structure is too high, then the benefits achieved by the miniaturization of the trap are lost.

First, consider two parallel plates separated by a dielectric of permittivity ε, where ε is the product of the permittivity of free space (ε_0) and the relative permittivity (ε_r). When a voltage is applied to one of the plates and the other is grounded, a parallel plate capacitor is formed, as depicted in Figure 3.6.

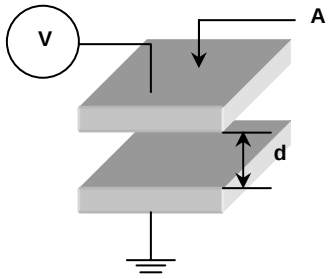

Figure 3.6. The schematic diagram of a parallel plate capacitor. Two parallel plates overlapping in area A are separated by a dielectric medium of height d. A voltage is applied to one of the plates and the other one is grounded.

The overlap capacitance is given by:

$$C = \frac{\varepsilon A}{d} \qquad (3.4)$$

where C is the overlap capacitance, ε is the permittivity of the medium separating the plates, d is the vertical distance separating the plates and A is the overlap area of the plates.

The ion trap structure in nature is a parallel plate capacitor as it consists of overlapping metal electrodes. The overlap capacitance, calculated from Equation (3.5), for a 1 cm^2 area (the area needed to array 10^6 traps) separated by a 0.5 μm gap (where the dielectric is silicon dioxide, SiO_2) is approximately 8 nF. If vacuum or free space is used as the dielectric, the capacitance is decreased by a factor of four. Moreover if the overlap area of the electrodes is decreased, the capacitance is further decreased.

The capacitance was calculated for several ion trap electrode configurations. The first calculation was for the design depicted in cross-section in Figure 3.7. Cylinders are created in metal thin films and the overlap occurs between electrodes. Figure 3.8 shows the unit cell for the ring electrode film in a parallel array of ion traps. The traps are arrayed in a hexagonal close packed (hcp) configuration. In this top view, the shaded gray area depicts the overlapping area of the ring and the end cap electrodes and s denotes the spacing between ring electrodes. The rhombic structure depicts the area of the unit cell.

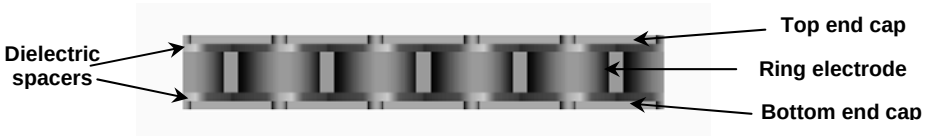

Figure 3.7. A cross-sectional view of a cylindrical ion trap array
Top end cap, ring electrode and bottom end cap are shown, separated by dielectric spacers.

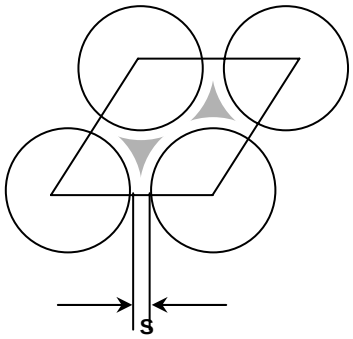

Figure 3.8. The unit cell of an hcp cylindrical ion trap array.
The ring electrodes have spacing s in the array. The overlap area between the ring electrode and end caps is determined by the space between ring electrodes. In this design, this area is made of air and dielectric material. The dielectric material is denoted by the shaded gray area.

The area of the unit cell is given by:

$$A_{Total} = \frac{a^2\sqrt{3}}{2} \qquad (3.5)$$
$$a = 2r_0^2 + s$$

The area of the ring electrode is given by:

$$A_{ring} = \pi r_0^2 \qquad (3.6)$$

In this design, the electrodes are separated by air and a dielectric, silicon dioxide (SiO_2). The SiO_2 is assumed to be undercut during its release and thus does not fill all of the overlapping area. The area of the air overlap is given by:

$$A_{air} = \pi\left(r_0 s + \tfrac{1}{4}s^2\right) \qquad (3.7)$$

while the area of the oxide can be determined by:

$$A_{oxide} = A_{Total} - A_{ring} - A_{air} \qquad (3.8)$$

The capacitance of the air and oxide is given by:

$$C_{Total} = \frac{C_{air}C_{SiO_2}}{C_{air} + C_{SiO_2}} \qquad (3.9)$$

Hence, for traps with r_0=1 μm, a distance s of 0.4 μm and end cap to ring electrode (vertical) distance of 2000 Å, the capacitances for an array of 2×10^6 traps are C_{air} = 0.122 nF and C_{SiO2} = 0.164 nF. From Equation (3.9) the total capacitance C_{Total} is estimated to be ~70 pF.

From this the power can be estimated from the reactive capacitance, X_c, of the structure.

$$X_C = \frac{1}{\omega C} \qquad (3.10)$$
$$P = \frac{V^2}{X_C} \qquad (3.11)$$

Therefore, if the traps are operated at a frequency of 1 GHz and a zero-to-peak voltage of 10 $V_{0\text{-}P}$, the estimated power consumption is c.a. 10 W based on the capacitance consideration alone.

Another important characteristic is the inductance of the structure. The inductance however is likely to be dictated by the length of the interconnects. For a single layer coil, the inductance is determined by:

$$L = \frac{(N \times R)^2}{(9R) + (10B)} \qquad (3.12)$$

where L is the inductance in microhenries, N is the number of turns, B is the length of the coil in inches and R is the mean radius in inches. Figure 3.9 shows a typical air core coil inductor and the dimensions.

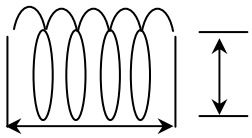

Figure 3.9. Coil dimensions used in the inductance formula. The wire diameter does not enter into the formula.

For the microfabricated cylindrical ion traps, the inductances originate from the length of interconnects. A typical set of interconnects and dimensions are depicted in Figure 3.10 and Figure 3.11, for two different array sizes.

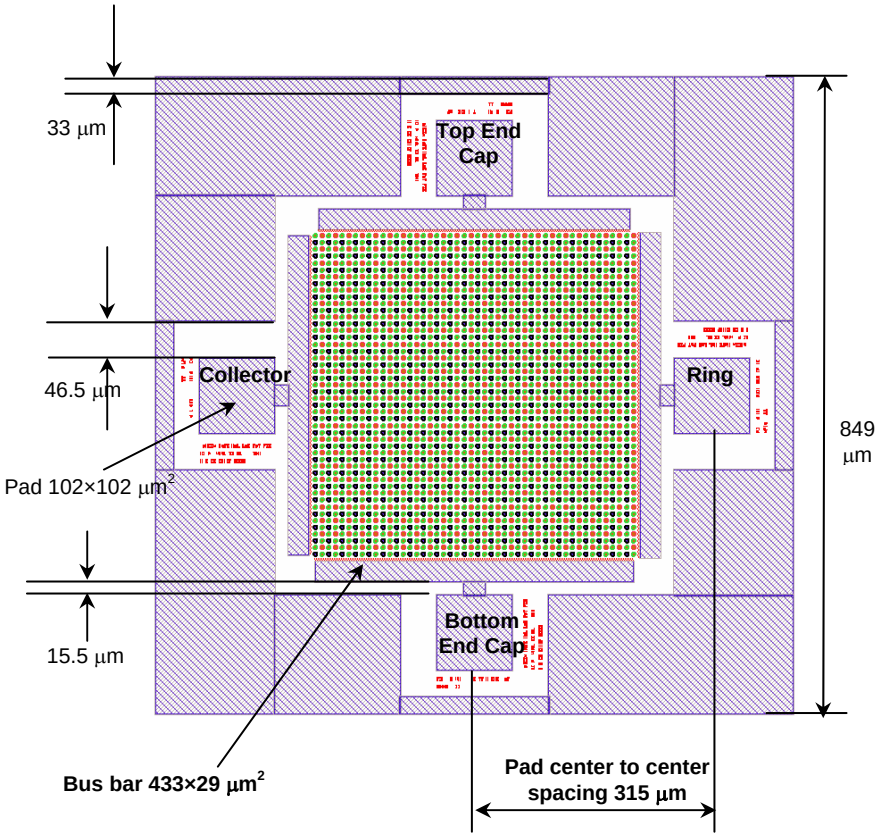

Figure 3.10. Interconnect layout for microfabricated cylindrical ion traps in a 10^3 sized array.

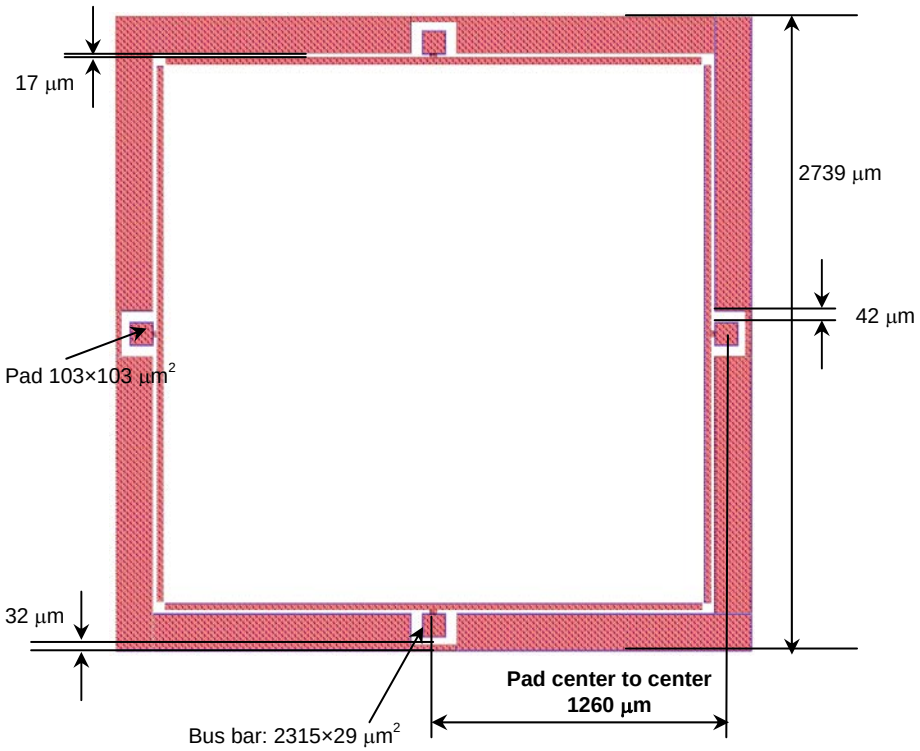

Figure 3.11. Interconnect layout for microfabricated cylindrical ion trap medium sized array (approximately 10^4 traps).

The resistance of the structure can be determined by

$$R = \frac{\rho_r L}{A} \qquad (3.13)$$

where R is the resistance, ρ_r is the resistivity of the conductor, L is the length of the film and A is the cross-sectional area.

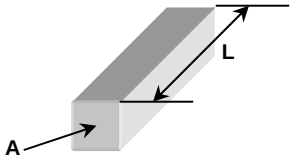

Figure 3.12. The schematic of a thin film resistor and its dimensions.

The resistance of the structure was calculated to be approximately 2 Ω for a length of 1 cm with W as the conductor. In this case, the resistance can be incorporated into the power calculation. A more general from of Equation (3.11) is given by Equation (3.14). In this case the average power into a general AC circuit is given by P_{av}:

$$P_{av} = \tfrac{1}{2} VI \cos\phi \qquad (3.14)$$

The factor, cos ϕ, is called the power factor of the circuit. For a pure resistance, ϕ = 0 and cos ϕ =1. For a pure capacitance or inductance, ϕ = ±90^o, cos ϕ = 0 and P_{av} = 0. For an L-R-C, circuit the power factor is equal to R/Z, where Z is the impedance and for a series L-R-C circuit the magnitude of Z is given by:

$$Z = \sqrt{R^2 + \left(X_L - X_C\right)^2} \qquad (3.15)$$

Thus the average power into the trap at a frequency of 1 GHz operated at 10 V is on the order of 16 W. The power estimated could be more accurate if the inductance could be estimated from first principles; however, this presents a challenge because only the single coil model was available for the inductance calculation.

The capacitance, resistance and inductance of the structure are of importance since they will determine the kind of matching circuit to be built. Ideally, one would design the structure to have a 50-Ω impedance. However, one is constrained by the geometry of the trap, the materials to be utilized, and the methods of fabrication, making a first principle calculation of the impedance problematic. Numerical simulation of the impedance from a geometric model of the electrode structure using, e.g., HFSS, would be possible, but was not done for the design discussed here. High Frequency Structure Simulator (HFSS) is a software for S-parameter and full-wave SPICE extraction and for the electromagnetic simulation of high-frequency and high-speed components. HFSS is widely used for the design of on-chip embedded passives, PCB interconnects, antennas, RF/microwave components, and high-frequency IC packages. This software was not available during the course of this work and could not be used as a result.

3.2.4 Trapping Fields in Cylindrical Ion Traps

The exact nature of the trapping fields in an ion trap is a crucial factor since the ion behavior depends directly on the potential distribution and thus the field strength. For the ideal quadrupole ion trap, the electrical field in the axial (*z*) direction increases linearly with displacement from the center. However, the existence of end cap apertures (necessary for ion/electron injection and ion ejection) introduces negative higher order field components. Such non-linear fields degrade the ideal field linearity and cause RF heating and de-stabilization of trapped ions, consequently affecting the trapping efficiency and storage time.

Among the higher order fields, of most interest are the octopole and dodecapole fields since the weights of other higher order fields are normally very small. The deliberate introduction of a positive higher order field (in most cases octopole field) to some extent compensates for the unavoidable negative higher order field (in most cases dodecapole field) and reduces the time

over which ion ejection occurs. For the commercial quadrupole ion trap, positive octopole fields are introduced intentionally by either stretching the end cap separation in the axial (z) direction or by modifying the hyperbolic angle of the end caps. The geometry for the 1-μm CIT has an inner ring electrode radius r_0=1 μm and the two end caps each have apertures with radius of approximately 0.4 μm (Figure 3.13 (a)). The potential distributions inside this μCIT, calculated using Poisson/Superfish software, are shown in Figure 3.13 (b) where the applied voltage was 5 $V_{0\text{-}P}$ at 1 GHz.

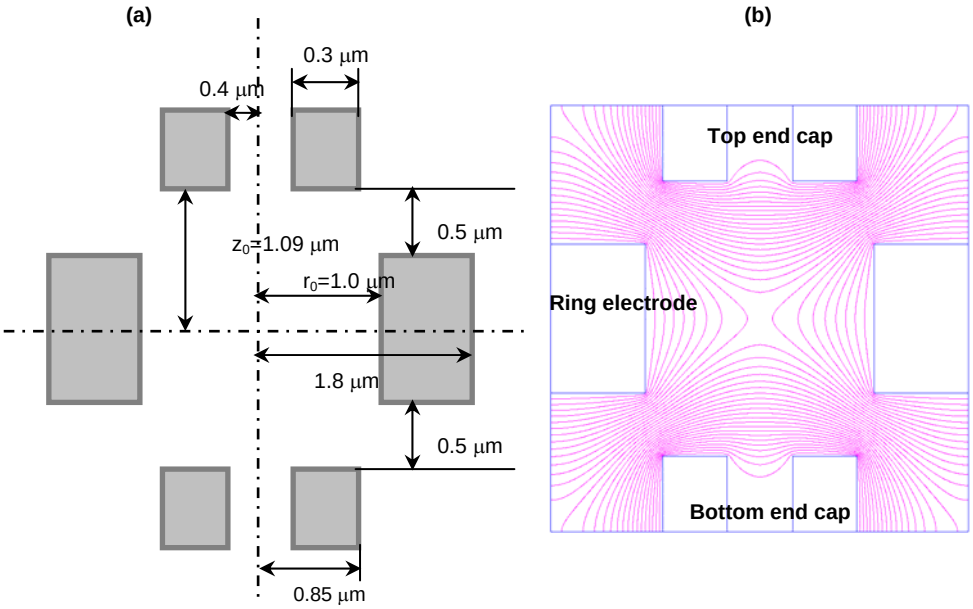

Figure 3.13. (a) A cross-sectional schematic of CIT of dimension r_0=1 μm, with end cap holes and spacing between end caps and ring electrode. This is an overhung structure. (b) The calculated potential distributions inside the 1-μm CIT with V=5V and f=1GHz.

The higher-order fields for this geometry, represented by multipole expansion coefficients, were also calculated as described by (Todd, Waldren et al. 1980). For the r_0 = 1 μm CIT, the values for the field coefficients were $A2$ = 0.628, $A4$ = 0.050 and $A6$ = −0.101. The normalization radius used was 1 μm. The positive non-linear octopole field partially compensates for the negative dodecapole field, and therefore should allow rapid ejection of ions from the trap and maximum mass spectral resolution. By comparison, for a r_0 = 2.5 mm with r_a = 1 mm the field coefficients are $A2$ = 0.634, $A4$ = 0.061, and $A6$ = −0.134, while for the commercial r_0 = 10.0 mm QIT with an r_a = 4 mm with $A2$ = 0.894, $A4$ = 0.015, and $A6$ = 0.006. These results are summarized in Table 3-3.

Table 3-3. Comparison of the multipole expansion coefficients for quadrupolar (A_2), octopolar (A_4), and dodecapolar (A_6) field components for traps of different sizes.

r_0	A_2 Quadrupole	A_4 Octopole	A_6 Dodecapole
1 cm	0.894	0.015	0.006
2.5 mm	0.634	0.061	-0.134
1 μm	0.628	0.050	-0.101

Note: trap geometry is hyperbolic for the 1 cm trap and cylindrical for the 2.5 mm and 1 μm traps.

The resulting total axial electric field (on axis) is plotted as a function of the normalized axial (z) position (z/z_0) in Figure 3.14. Ideally, this plot would show a linear field region throughout the entire trap until $z/z_0 = 1$, at which point the field should drop abruptly to zero (a vertical line at this value). As Figure 3.14 shows, both the 1-μm size and the 2.5-mm size traps have a large region where the field is linear, however both deviate from linearity at about $z/z_0 = \pm 0.6$. The commercial ion trap has a steep but non-instantaneous drop from the field region to the field free region with the non-linear field region beginning at $z/z_0 = \pm 0.95$. The non-linear regions close to the edges of the field region can cause ejection delays as ions oscillate in the lower field region, as they become sequentially stable and instable as the z/z_0 position changes (March and Todd 1995; Plass, Li et al. 2003).

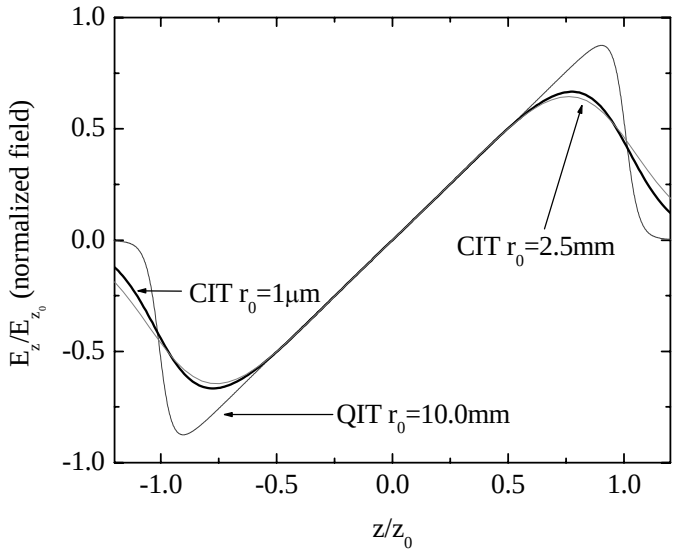

Figure 3.14. Calculated total axial electric field on-axis as a function of the normalized axial (z) position (z/z_0) for 1-cm QIT commercial hyperbolic trap and 2.5 mm and 1 μm CITs.

This causes shifts in mass peak positions and loss of mass resolution. The commercial QIT trap has been stretched to introduce positive higher-order fields to correct for the ejection delay.

3.3 Operating Parameters

Trap operating parameters must also be taken into account when trap performance is considered. Equation (1.29) shows that as the size of the trap decreases the mass range increases, thus it is feasible to assume that ions may be trapped with much lower voltages and higher frequencies. However, the ion's kinetic energy and the trapping potential needed to trap the ions must be considered. If the ion's kinetic energy exceeds the trap strength, it will not be trapped; therefore the operating voltages can not be chosen arbitrarily small. The potential in the z direction can be estimated according to Dehmelt (Dehmelt 1967) by:

$$D_z = \frac{q_z V_{eff}}{8} \; ; \; V_{eff} = 0.55 \; V_{0\text{-}P} \qquad (3.16)$$

In the r-direction the pseudopotential is half of (3.16).

The pseudopotential configuration is given by:

$$\Phi = D_z \frac{r^2 + 4z^2}{r_0^2 + 2z_0^2} \qquad (3.17)$$

If ions have thermal energy with a Maxwell distribution then the minimum pseudopotential well depth for trapping ions must be $D_z = 3kT_i/e$, where k is Boltzmann's constant, T_i is the temperature of the ions, and e is the charge of an electron. For room temperature ions, one can calculate the minimum voltage that must be applied to the ring electrode, $V_{ring,}$ as a function of q_z for trapping to occur. The function is plotted in Figure 3.15. For a given q_z value ($q_z \leq 0.4$), the pseudopotential well depth depends only on the RF amplitude. A reduction in the RF amplitude will decrease the pseudopotential well depth and subsequently the trapping efficiency and mass resolution. This approach provides a very rough estimate since Equation (3.16) is valid only for $q_z \leq 0.4$, while trapping experiments are often performed at higher q_z values.

Thus, the RF amplitude can not be made arbitrarily small. One may also view this in terms of the spatial spread of the ions. The spatial spread of the ions is determined by the ratio of the ion kinetic energy to the pseudo-potential well depth. Therefore, a reduction in the pseudo-potential leads to an increased spatial spread of the ions. One consequence of this for mass analysis with macro-scale traps is that during mass-selective instability scans an increased spatial spread causes an increased spread in the ejection time, leading to decreased mass resolution of the trap. This suggests that mass analysis with a 1-μm ion trap may require a trap-detect protocol other than mass-selective instability.

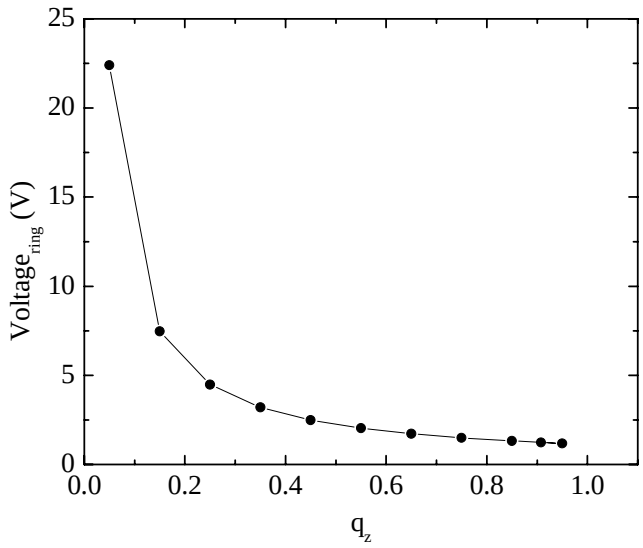

Figure 3.15. Minimum ring voltage ($V_{0\text{-}P}$) estimated using Dehmelt's approximation as a function of q_z for the trapping of ions having initial energies equal to $eD_z = 3kT_i$ at 300 K. For $q_z \leq 0.4$, Dehmelt's approximation holds; for $q_z > 0.4$ the values are less certain.

3.4 Ion Generation

Because of small trapping potentials at 10s of volts, ions can not be accelerated into the trap and must be formed *in situ.* Consequently, another important consideration for trapping in micro traps is ion generation and ion losses inside the trap. If the ion loss rate exceeds the ion formation rate then no ions will be trapped. Electron impact ionization provides a suitable ionization method. The number of ions formed can be determined from the total ion current, $I_i(T)$ produced by the electron beam (Mark and Dunn 1985).

$$I_i(T) = I_e(T)\rho L\sigma_T(T) \qquad (3.18)$$

Equation (3.18) shows the relationship between the ion current formed, I_i, and the current of a beam of electrons, $I_e(T)$, having an incident temperature of T, the number density ρ of atoms or molecules in the gas, and the collision path-length L over which the ions are collected. σ_T is the total ionization cross section at a temperature of T. The number density ρ is given by:

$$\rho(cm^{-3}) = \frac{2.7x10^{-19}\, p(Torr)}{760} \qquad (3.19)$$

The path-length can be estimated to be the height of the trap, ~ 2×10^{-4} cm for the r_0=1 μm trap. The total cross-section is available for different molecules at different energies from the National Institute of Standards and Technology (NIST) (Kim, Irikura et al. 2005). Argon has a cross-section of 2.8×10^{-16} cm^2 at 100 eV. From simulations, an ion loss rate of ~1×10^9 ions/sec was determined, for the r_0=1 μm trap operated at 8 V and 1 GHz. This corresponded to a requirement of approximately 1 μA of electron current, a current that is achievable with a

filament. Therefore, electron impact ionization was concluded to be a suitable method for the *in situ* ionization of ions.

3.5 Electrical Characterization Structures

In order to electrically characterize the arrays of ion traps, electrical test structures were designed in order to determine the ion trap's electrical characteristics (Rao 1994). These structures included scattering parameter structures. In a microwave circuit the amplitude and phase of the incoming wave on a transmission line have certain characteristics. This incoming wave is "scattered" by the circuit and its energy is partitioned between all the possible outgoing waves on all the other transmission lines connected to the circuit. The scattering parameters (s-parameters) are fixed properties of the (linear) circuit which describe how the energy couples between each pair of ports or transmission lines connected to the circuit. The s-parameters can be defined for any collection of linear electronic components, whether or not the wave view of the power flow in the circuit is necessary. They are algebraically related to the impedance parameters (z-parameters), also to the admittance parameters (y-parameters) and to a notional characteristic impedance of the transmission lines. To facilitate the electrical characterization of the trap arrays, S_{11} and S_{12} structures were designed.

An n-port microwave network has n arms into which power can be fed and from which power can be taken. In general, power can get from any arm (as input) to any other arm (as output). There are thus n incoming waves and n outgoing waves. The power can be reflected by a port, so the input power to a single port can partition between all the ports of the network to form outgoing waves.

Associated with each port is the notion of a "reference plane" at which the wave amplitude and phase is defined. Usually the reference plane associated with a certain port is at the same place with respect to the incoming and outgoing waves.

The n incoming wave complex amplitudes are usually designated by the n complex quantities, a_n, and the n outgoing wave complex quantities are designated by the n complex quantities, b_n. The incoming wave quantities are assembled into an n-vector $\vec{A}$ and the outgoing wave quantities into an n-vector $\vec{B}$. The outgoing waves are expressed in terms of the incoming waves by the matrix equation $\vec{B} = S\vec{A}$ where S is an n by n square matrix of complex numbers called the "scattering matrix". It completely determines the behavior of the network. In general, the elements of this matrix, which are termed "s-parameters", are all frequency-dependent.

In a particular case where a microwave network has only two ports, an input and an output, the s-matrix has four s-parameters, designated as

$$\begin{bmatrix} b_1 \\ b_2 \end{bmatrix} = \begin{bmatrix} S_{11} & S_{12} \\ S_{21} & S_{22} \end{bmatrix} \begin{bmatrix} a_1 \\ a_2 \end{bmatrix} \qquad (3.20)$$

These four complex quantities actually contain eight separate numbers; the real and imaginary parts, or the modulus and the phase angle, of each of the four complex scattering parameters.

Let us consider the physical meaning of these s-parameters. If the output port 2 is terminated, that is, the transmission line is connected to a matched load impedance giving rise to no reflections, then there is no input wave on port 2. The input wave on port 1 (a_1) gives rise to a reflected wave at port 1 ($S_{11}a_1$) and a transmitted wave at port 2 which is absorbed in the termination on port 2. The transmitted wave size is ($S_{21}a_1$). If the network has no loss and no gain, the output power must equal the input power and so in this case $|S_{11}|^2 + |S_{21}|^2$ must equal unity.

It is clear that the magnitude of S_{11} and S_{21} determine how the input power splits between the possible output paths (Smith 2000). Therefore, these s-parameters help determine a match to the input wave. In addition, shorted and open structures were included in the trap array test structures to characterize the electrical contributions of the bus bars. These results are discussed in Chapter 7.

4.0 SIMULATIONS OF ION TRAPPING IN MICROMETER-SIZED CYLINDRICAL ION TRAPS

A detailed discussion regarding SIMION (Dahl 2000) simulations of ion behavior in micrometer-sized cylindrical ion traps is presented in this chapter. Simulations examined the effects of ion and neutral temperatures, the pressure and nature of cooling gas, ion mass, trap voltage and frequency, space-charge, fabrication defects, and other parameters on the ability of micrometer-sized traps to store ions. Due to voltage limitations at this size scale, the pseudo-potential well depth of traps is shallow and thermal energies contribute significantly to ion losses. Trapping efficiency falls off gradually as q_z approaches 0.908, possibly complicating mass-selective ion trapping or ejection. Anharmonic field effects due to space-charge result in a trapping limit of a single ion per trap. If multiple ions are produced in a trap, all but one ion are ejected within a few microseconds, and the remaining ion tends to have favorable trapping parameters and a much longer trapped lifetime. Typical microfabrication defects affect ion trapping only minimally. The relationship of the simulations to the expected performance of the microfabricated array is also discussed.

4.1 Introduction

Elucidation of the ion trapping properties of the miniaturized cylindrical ion traps is of great importance. Ion traps in the size regime of micrometers have several limitations not present in larger sized ion traps. For example, the voltage difference between electrodes must remain below the field emission limit, but must be large enough to create a suitable potential well depth which will trap ions (Cruz, Chang et al. 2005). The field emission properties of these ion traps are discussed in Chapter 7 along with the trap's electrical characteristics. The operating frequencies needed to trap ions may be on the order of GHz or several hundred MHz for traps with r_0 = 1, 2, 5 or 10 μm. Fabrication induced defects such as misalignment between layers, tapering, and surface roughness must also be considered. Thus it is important to gain an understanding of these effects before the actual fabrication. The simulations summarized here were mainly geared towards the understanding of the overhung structure, since this design was more time and monetarily consuming as far as microfabrication.

Numerous studies have examined ion trapping behavior in macroscopic traps of various geometries, including cylindrical ion traps (Baril, Le et al. 1990; March, Londry et al. 1992; Reiser, Julian et al. 1992; Londry, Alfred et al. 1993; Nappi, Weil et al. 1997; Perrier, Nguema et al. 1997; Yoshinari 2000; Ding, Sudakov et al. 2002; Sheretov, Philippov et al. 2002; Lee, Min et al. 2003; Lee, Oh et al. 2003). However, ion traps with dimensions in the micrometer scale have not previously been constructed, and ion behavior in this range has not been studied. In order to understand the ion trapping limitations resulting from the much reduced trap size, decreased operating voltage and increased operating frequencies, detailed ion simulations, which focus on the effects of temperature, pressure, voltage, and frequency, have been performed, using SIMION v. 7 a commercial software.

4.2 Computational Method

As discussed in section 2.5.2.1 the specific method used in SIMION is a finite difference technique called over-relaxation. The relaxation method uses nearest neighbor points to obtain new estimates for each point, four points in two dimensions and six points in three dimensions. The trap dimensions and an image of the potential array defined in SIMION for an $r_0 = 1$ μm CIT are shown in Figure 4.1.

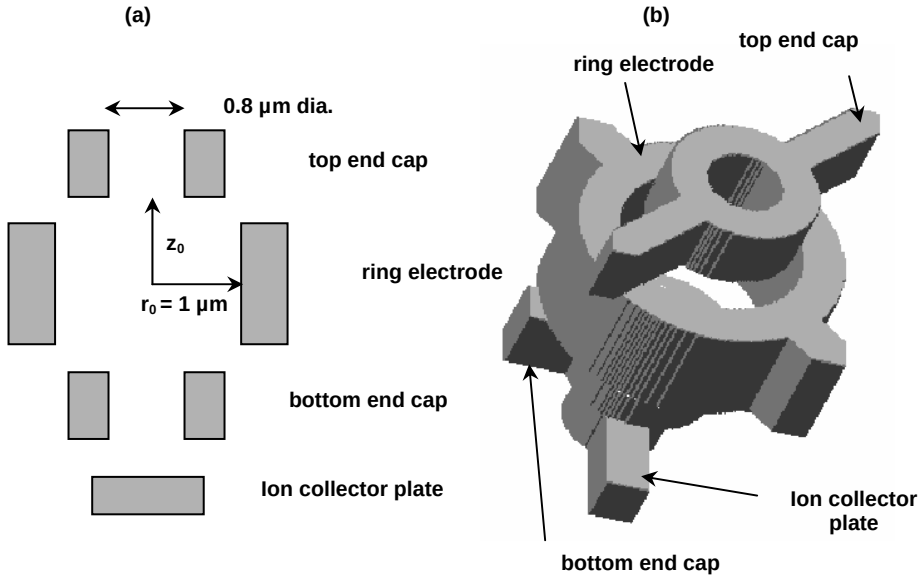

Figure 4.1. Potential arrays with the exact geometry for an $r_0 = 1$ μm CIT. (a) A cross-sectional view with dimensions, and (b) a three-dimensional perspective of the potential array, showing asymmetries due to connecting straps.

Ion trajectory computations are a result of three interdependent calculations, including the calculation of electrostatic, magnetic and charge repulsion forces (if applicable) based on the current position and velocity of the ions. These forces are used for the computation of the ion acceleration by a fourth order Runge-Kutta method to predict the position and velocity of the ion at the next time step, followed by a continuous adjustment of the time step to maximize trajectory accuracy while minimizing the number of integration steps per trajectory. The fourth order Runge-Kutta formula is outlined below:

$$k_1 = hf(x_n, y_n) \tag{4.1}$$

$$k_2 = hf(x_n + \frac{1}{2}h, y_n + \frac{1}{2}k_1) \tag{4.2}$$

$$k_3 = hf(x_n + \frac{1}{2}h, y_n + \frac{1}{2}k_2) \tag{4.3}$$

$$k_4 = hf(x_n + h, y_n + k_3) \tag{4.4}$$

$$y_{n+1} = y_n + \frac{1}{6}k_1 + \frac{1}{3}k_2 + \frac{1}{3}k_3 + \frac{1}{6}k_4 + O(h^5) \tag{4.5}$$

where k_1 is the slope at the beginning of the interval, k_2 is the slope at the mid-point of the interval using k_1 to determine the value of y at the point of $x_n+h/2$ with Euler's method, k_3 is the slope at the midpoint using k_2 to determine the y-value, and k_4 is the slope at the end of the interval using k_3 to determine the y-value. The next y-value is a weighted average of the slopes, with more weight given to the slopes determined at the mid-points.

A user-written code establishes the time-varying electric fields, initialized ion parameters, collisions and control functions. An overview of the code, including algorithms, is included in Appendix F. Although SIMION itself does not handle the actual ionization event, ion formation can be randomized accordingly utilizing the user-written code.

Ionization is assumed to take place *in situ*. The initial positions of ions were randomized within a cylindrical volume, with radius equal to that of the aperture of the top end cap electrode, and with length equal to the distance between the inner surfaces of the end cap electrodes. This corresponds to the volume within the trap that is accessible to electron impact ionization and therefore initial positions are not randomized to the entire trap volume. Trapping efficiencies would be significantly different if the entire trap volume were used, as the trapping efficiency decreases with increased distance from the trap center. Initial ion velocities and temperatures were randomized to a Maxwell distribution and ion creation was randomized with respect to the phase of the applied RF.

In simulations involving collisions with a neutral gas, the neutrals were defined to have random velocities following a Maxwell distribution at the moment of impact with the ion. The temperature of the collision gas was independently varied from the initial ion temperature; however, the ions and neutrals started at the same temperature as expected from nondissociative *in situ* ionization (Mark and Dunn 1985). Ions created via a dissociative process are likely to have a significantly greater kinetic energy and would likely be lost due to the insufficient potential well depth. Ions and neutrals were assumed to have diameters of 8 and 3 Å respectively; approximately the Langevin diameters of toluene and nitrogen.

The collisions can be defined as elastic or inelastic. The fundamental quantity which characterizes a collision is its cross section $\sigma(\upsilon_r)$ were υ_r is the relative velocity between the particles before colliding (Lieberman and Lichtenberg 1994). The flux of particles can be given by:

$$d\Gamma = -\sigma(\upsilon_r)\Gamma n_g dx \qquad (4.6)$$

where Γ is the flux, n_g is the neutral density and dx is the distance in which the collision happens. Equation (4.6) can be re-written as:

$$\frac{d\Gamma}{\Gamma} = -\sigma(\upsilon_r) n_g dx \qquad (4.7)$$

Upon integrating Equation (4.7),

$$\Gamma(x) = \Gamma_0 e^{-n_g \sigma(\upsilon_r) x} \equiv \Gamma_0 e^{-x/\lambda} \qquad (4.8)$$

The mean free path, λ, is defined as the distance over which the uncollided flux decreases by 1/e from its initial value of Γ_0 at x=0. If the relative velocity of the particles is υ_r, then the mean time between interactions is:

$$\tau = \frac{\lambda}{\upsilon_r} \tag{4.9}$$

Its inverse is the collision frequency:

$$\nu \equiv \tau^{-1} = n_g \sigma \upsilon_r \tag{4.10}$$

This is the number of interactions or collisions per second that an incident particle has with the target population. In the case of two hard spheres of radii a_1 and a_2 colliding, the cross section can be identified as the area of a circle with a radius of a_{12}, where $a_{12}=a_1 + a_2$. Then $\sigma = \pi a_{12}^2$, and the collision frequency is given by:

$$\nu = n_g \upsilon_r \pi a_{12}^{\ 2} \tag{4.11}$$

The probability that a collision between an ion and a neutral occurred during a given time step dt is determined by:

$$P = 1 - e^{-n_g \sigma \upsilon_r dt} \tag{4.12}$$

Ion-neutral collisions were assumed to be elastic. Scattering angles and velocities resulting from collisions were calculated using three dimensional momentum and energy conservation calculations. The momentum and energy equations yielded four out of six unknowns. The remaining two unknowns were randomized values of orthogonal scattering angles. The probability distributions of these randomized angles were derived from the two-dimensional projected impact parameter space, assuming hard spheres. Further details about the collision calculations are given in Appendix G.

In most of the simulations performed for this work, space charge effects were not considered. This effectively simulates a large array of traps with a single ion created randomly in each trap. If ions are lost more quickly than they are formed then the ion-ion interactions can be ignored. However, simulations were also performed where space charge effects were taken into account. Such is the case where ions are formed more quickly than they are lost and a given trap will have more than one ion at a time. SIMION estimates coulombic repulsion via either line charge or point charge assumptions and hence each ion is assumed to represent a point charge. There are three methods of Coulomb repulsion used by SIMION, namely “Beam” repulsion, “Coulombic” repulsion and “Factor” repulsion. Beam repulsion is estimated via line charge assumptions. Each ion is assumed to represent a line charge, and the line charge density is determined by apportioning the beam current between the ions according to their charge, adjusted by their charge weighting factor and divided by the ion’s velocity. Coulombic repulsion apportions the total coulombs of charge between the ions according to their charge adjusted by their charge weighting factor. Factor repulsion determines the ion’s effective charge by multiplying its

charge by the charge multiplication factor, adjusted by its charge weighting factor. Factor repulsion with the factor set to 1 was used, so that each ion had a total charge of *e*.

SIMION allows the user to set the computation level, ranging from -500 to +500, and a value of zero is the least accurate. Positive values invoke algorithms for field curvature detection, boundary checking, and velocity reversal detection, with +500 having the smallest computation (time) increment. Negative values do not include velocity reversal detection, but computational increments are the same, with -500 being the most accurate. Computational quality levels were studied in order to find an appropriate level to minimize computation time while maintaining accuracy. Simulations run at higher computational qualities, for example +150 and +500, showed approximately 5% fewer ions trapped than simulations run at low levels of computational quality (e.g., 0, -3, -5). The observed discrepancies occurred in the first 100 RF cycles, the loss rates between the different computational qualities being the same past this point. To minimize the computation time, the majority of simulations were performed at a computation level of -5. The duration of a simulation performed at a computational quality of +500 was more than five hours. In contrast, the time for completion of a simulation performed at a computational quality of -5 took about 2 hours.

Unless otherwise noted simulations were run for 2000 RF cycles to calculate the trapping efficiency. Ions were considered trapped if they remained in the trap for this length of time, and the trapping efficiency was defined as the ratio of ions trapped and ions created. It should be mentioned that for GHz drive frequencies, 2000 cycles represents trapping times of microseconds. To determine the ability of the micro-ion traps to confine ions on the order of milliseconds, times typical of mass instability detection techniques, simulations were also run for 10^6 to 10^7 RF cycles. Trapping trends were similar in both time scales, although the absolute values of trapping efficiencies were different, as expected.

Ion trapping simulations were mainly performed assuming a vacuum environment. Table 2-1 summarized the input parameters used and their starting values. These user define variables could be altered throughout the program. Simulations of the trapping of toluene at one of its main peaks, m/z=93, were performed. The ions were given a mean energy of kT. The energy was distributed using a Maxwell distribution via the user-written program. Figure 4.2 shows the potential field distribution for the baseline conditions outlined in Table 2-1.

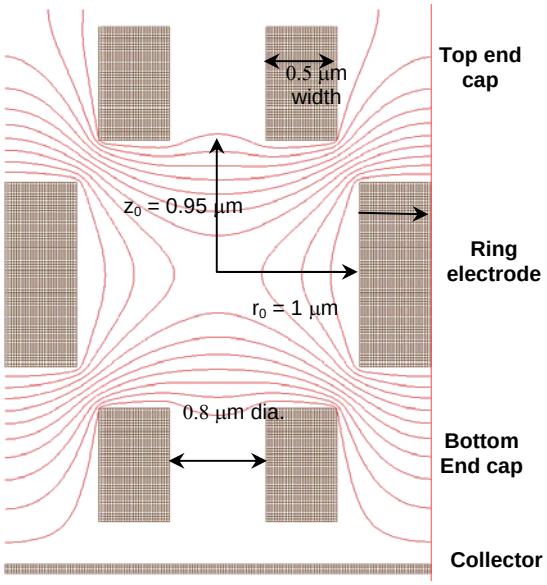

Figure 4.2. Potential field distribution in micron-sized cylindrical ion trap array. 5 V were applied to the ring electrode, and the end caps and the collector were grounded. The trap has r_0=1 μm and z_0=0.95 μm. The end cap apertures are 0.8 μm in diameter and electrode wall thickness were 0.5 μm.

4.3 Simulation Results

First the behavior of isolated ions in a collisionless trapping environment was examined, and the effects of pressure and Coulombic repulsion were later determined. Finally the effects of trap electrode geometry defects are presented. Each point in the following figures is the result of creating and attempting to trap 500 independent ions unless otherwise indicated. Error bars in the following plots represent ±1% standard deviation calculated using Poisson statistics. Trap voltages are reported as zero to peak ($V_{0\text{-}P}$), and RF frequencies are given in GHz.

4.3.1 Ion Trapping in Vacuum

Figure 4.3 shows the initial position of successfully trapped ions in a trap operated at 8V and 1.2 GHz. Note that ions shown in this figure originated in the whole trap volume, rather than the electron ionization cylinder used for subsequent simulations. Figure 4.3 (a) shows the simple radial function (R), while Figure 4.3 (b) shows the radial distribution function (Rr^2), which included the r^2 volume element term in the randomization of the initial ion positions. This plot illustrates and confirms that ions near the center of the trap are more likely to be trapped than ions originating farther from the center. Although this result would appear obvious, it is important to note that in situ ionization is limited to this region, that injected ions would need to be thermalized within this region, and that the ratio of the trapping volume to the cylindrical ionization volume defines an upper limit to the simulated ion trapping efficiencies.

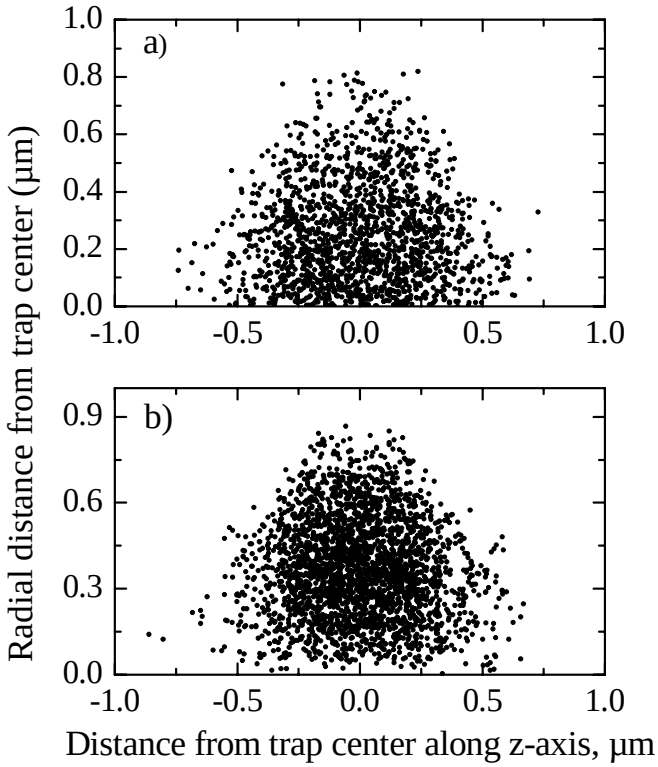

Figure 4.3. Initial positions (r, z) of successfully trapped ions. Ions with m/z of 93 originate with thermal kinetic energies (300 K), and the trap is operated at 8V and 1.2 GHz. (a) The simple radial function (R), and (b) the radial distribution function (Rr^2). Although the probability is high that an ion created at the trap center will be trapped, the probability is low that an ion will be created exactly at the center.

Figure 4.4 shows regions of collisionless ion trapping as a function of trap voltage (RF amplitude) and frequency. Ions were defined with m/z=93 and initial kinetic energies corresponding to 300K. Also shown are curves defined by $q_z = 0.908$ (the Mathieu instability limit) and $q_z = 0.1$. Shaded regions indicate combinations of voltage and frequency for which the trapping efficiency exceeds the indicated level. For electrical reasons it is desirable to operate the array of micrometer-sized ion traps at the lowest possible frequency and voltage, while keeping ion trapping at an acceptable level. When RF amplitude drops too low, the pseudopotential well is too shallow to trap ions, and as the RF amplitude and well depth increase, the probability that a given ion will be trapped increases.

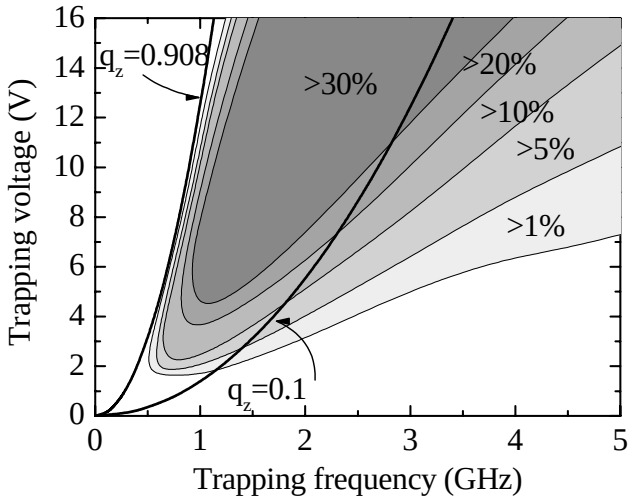

Figure 4.4. Calculated collisionless ion trapping efficiency as a function of RF amplitude (voltage) and operating frequency of a microfabricated cylindrical ion trap. Shaded regions indicate combinations of voltage and frequency for which trapping efficiency exceeds the indicated values. Parabolae of constant q_z are shown for q_z = 0.908 (the Mathieu instability boundary) and 0.1 (for reference).

Figure 4.5 shows the collisionless ion trapping efficiency as a function of the stability parameter, q_z, in the absence of any DC offset ($a_z = 0$). Trap voltage and frequency were held constant, and the m/z of ions was varied (38–1500) to produce the indicated q_z values. Varying trap parameters while ion mass was held constant produced a similar result. Ion trapping showed a strong dependence on q_z, with a maximum at intermediate q_z values and minima for both high and low values. This result corresponds qualitatively with the escape velocity curves derived by Abraham for ions in macroscopic traps (Abraham, Chatterjee et al. 2004). At intermediate q_z values the barrier for escape is higher, while for other values the initial kinetic energy of ions, coupled with their phase and position, make escape more likely. Thus for a given set of conditions in a micrometer-sized trap, trapping efficiency is somewhat mass selective. Note that values presented for the stability parameter, q_z, were calculated using the formula:

$$q_z = \frac{8eV}{m\left(r_0^2 + 2z_0^2\right)\Omega^2} \qquad (4.13)$$

which is only strictly true for an ideal hyperbolic trap. Thus, these q_z values are only approximate.

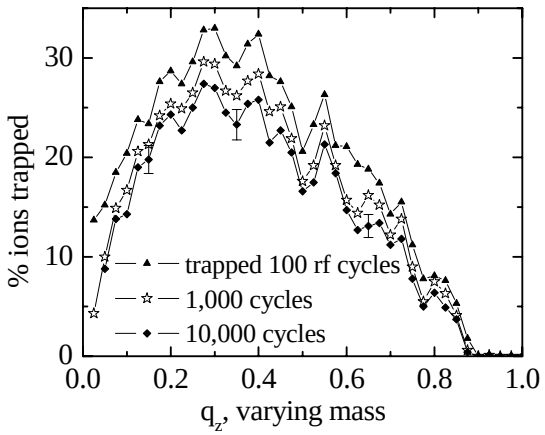

Figure 4.5. Calculated collisionless ion trapping efficiency as a function of the stability parameter, q_z. The ion mass is varied, while trap voltage and frequency are held constant at 8 V and 1.2 GHz, respectively. The same ions are followed through 10^2, 10^3, and 10^4 RF cycles.

Figure 4.6 shows ion trapping over a much longer time scale than previous figures. In this case, simulations continued for 1-2 million RF cycles. Ions continue to be lost for the entire trapping time, but loss rates steadily decline, such that ions can remain trapped for longer than 1 ms in a collisionless vacuum. Simulations of a few ions for 100 million RF cycles show some ions trapped for 100 ms. Long-term ion trapping may not have application to portable mass spectrometry, where pressure effects limit the ion trapping time, but may have application to experiments in quantum computing and spectroscopy, where operating pressures are much lower (Steane 1997).

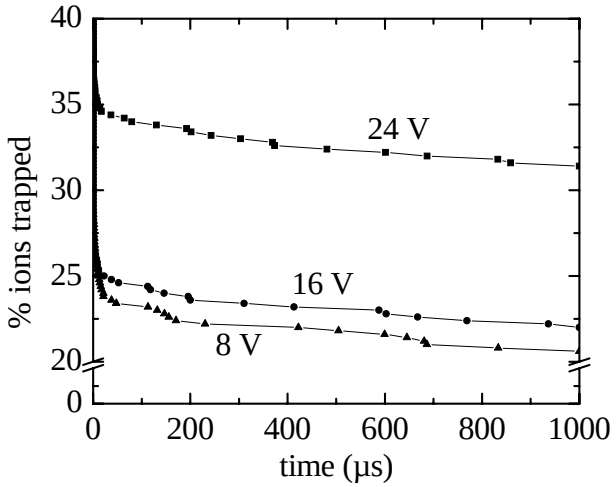

Figure 4.6. Simulations results for the percent of ions remaining trapped as a function of time. In the absence of collisions ions can remain trapped for milliseconds. Trapping voltages of 8, 16, and 24 V are shown.

It is interesting to note that simulations show ion trajectories precessing about the z-axis with a non-constant rate. The magnitude of precession varies sinusoidally with a period of several hundred to a few thousand RF cycles, depending on the ion. This oscillation is not possible in a perfectly cylindrically-symmetric system. The non-cylindrically-symmetric force acting on the ion motion appears to be the result of the mechanical and electrical support struts leading up to the ring electrodes, similar to the observation of oriented Wigner-type crystals in cold trapped ions (Liebfried, Blatt et al. 2003). It is not expected that this oscillation will have a significant effect on the ability of microfabricated traps to store, analyze, or detect ions.

4.3.2 Ion Trapping with Collision Gas

To understand the effect of ion-neutral collisions in a micrometer-sized ion trap, simulations examined ion trapping in the presence of helium, air, and other gases at pressures ranging from 1 mTorr to 10 Torr. Because of the small length scale of ion motion, collisions in micrometer-sized traps are extremely infrequent at pressures of a few mTorr, and many ions survive 2000 cycles having had no collisions. Figure 4.7 shows ion trapping efficiency as a function of pressure for several trap voltage and gas temperature conditions, with air as the collision gas. The data for trapping efficiency as a function of pressure are fit well by limited growth curves of the form

$$\%\quad ions\quad trapped = a\exp\left(-\left(P/P_0\right)^k\right) \qquad (4.14)$$

where a is the trapping efficiency at zero pressure, P_0 is the pressure at which trapping is reduced by $1/e$, and k is a fit parameter. These best-fit curves are included in the figure.

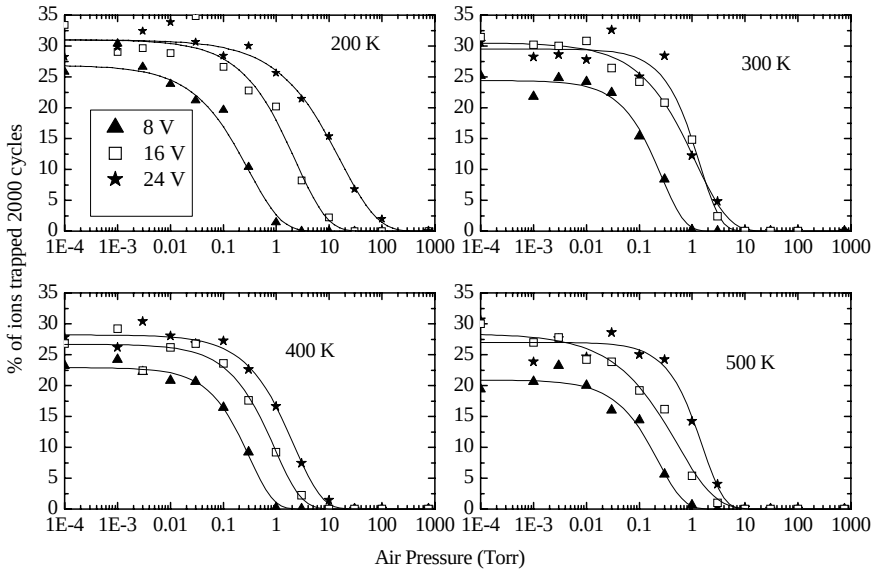

Figure 4.7. Calculated ion trapping efficiency as a function of pressure for several trap voltages and gas temperature conditions. Ions have m/z = 93, and the neutral gas is air.

In each case, trapping efficiency is reduced as pressure increases, and the collisionless environment represents the longest trapping time. Similarly, trapping efficiency is reduced as the mass of the neutral species (collision gas) increases, as shown in Figure 4.8. In this figure, the fraction of ions remaining is shown as a function of time for several different collision gases with pressure 0f 0.1 Torr. While a small pressure of cooling gas improves performance in larger ion trap systems where ions are injected into the trap, collisions reduce trapping efficiency and trapped ion lifetime for ions generated *in situ* in a micrometer-sized trap. In a macroscopic ion trap, collisions effectively cool trapped ions, and ions become concentrated at the center of the trap where anharmonicities and RF heating are minimized. In contrast, ions generated *in situ* in a microscopic ion trap are not cooled by the collisions they experienced, and their trajectories remain farther from the center than they would be if cooled. Nevertheless, depending on the length of time needed for ion storage and mass analysis, operation at pressures up to 0.1 Torr may be possible in the micrometer-scaled trap.

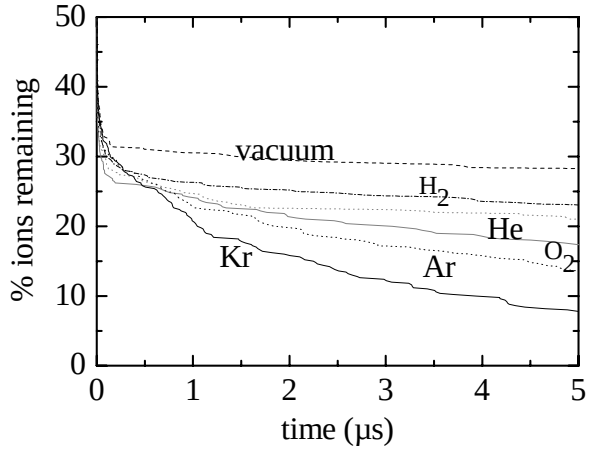

Figure 4.8. Simulation results for the fraction of ions remaining trapped as a function of time with several different collision gases, H_2, He, O_2, Ar, and Kr, with pressure 0.1 Torr. Vacuum is shown as a reference. The simulated trap was operated at 16 V, 300 K, and ions have m/z=93.

Although some losses are a result of collisions, the time required for an ion to be lost due to collisions is not a simple function of the number of collisions the ion experiences. Figure 4.9 shows the mean number of collisions needed to eject trapped ions as a function of the pressure and mass of the collision gas. The mass of neutrals was varied such that the ratio of ion to neutral masses, m_i/m_n, was 10, 5, 2, and 1. At very low pressures collisionless loss mechanisms dominate (losses due to field anharmonicities and RF heating), and ions are ejected having had few or no collisions. At higher pressures, the mean number of collisions an ion experiences before ejection varies slightly as a function of pressure. That is, ion ejection is not solely dependent on the number of collisions, but also on the rate at which those collisions occur. As expected, as the neutral mass increases, the number of collisions needed to eject ions decreases.

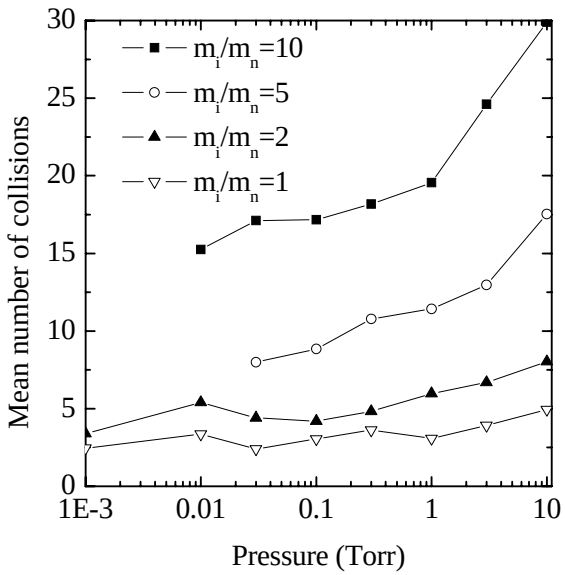

Figure 4.9. Mean number of collisions needed to eject trapped ions as a function of pressure and neural mass. Ions had m/z = 100, and neutrals had masses of 100, 50, 20, and 10, corresponding to mass ratios, m_i/m_n, of 10, 5, 2, and 1. Only ions with otherwise favorable trapping parameters were considered in the average.

The shallow pseudopotential well (typically 0.3 V) in a micrometer-sized trap operated at 10-20 volts suggests that the thermal energies of ions may have a significant effect on ion trapping. Figure 4.10 shows simulations of ion trapping in which both the initial ion energies and collision gas temperature (1 Torr helium) vary together from 200 K to 500 K. Different series of data show also the effect of operating the ion trap at 8, 12, 16, and 20 V. The value of q_z for each of these simulations was 0.4. As the initial kinetic energy of ions increases, trapping efficiency decreases. Additionally, an increased trap voltage results in improved ion trapping. Temperature may be an important consideration since any RF heating of the trap electrodes would increase the neutral (and hence the ion) temperature. The effect of gas temperature on ion trapping illustrates the importance that energetic ions resulting from dissociative ionization processes are likely not to be trapped under the conditions considered here.

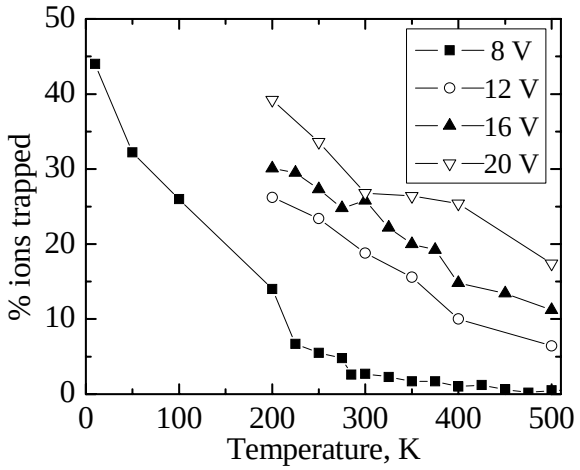

Figure 4.10. Trapping as a function of temperature. Ions and neutrals all originate with a kinetic energy distribution corresponding to the indicated temperature. The collision gas, helium, has a constant density, equivalent to 1 Torr at 300 K.

4.3.3 Space-Charge Effects

The maximum density of singly-charged particles that can occupy an ideal hyperbolic ion trap is estimated by the relation:

$$N_{\max} = \frac{3\varepsilon_0 V_0^2}{4m\Omega^2 z_0^4} \qquad (4.15)$$

Whereas a macroscopic trap at modest trapping voltages can typically store 10^3-10^6 ions, an ideal micrometer-sized trap has a calculated storage capacity of 10^2 ions. Simulations show, however, that only a single ion can be trapped for a useful length of time in a micrometer-sized cylindrical ion trap operated in the range of 5-20 V. Regardless of the number of ions created, after about 1 μs, only one ion remains trapped. For multiple ions in a given trap, each ion experiences an anharmonic field which eventually leads to an unstable trajectory and loss of all but one ion. The remaining ion no longer experiences any space-charge force or effect. Simulations with ideal hyperbolic trap geometries, as well as traps with larger sizes (2-, 5-, and 10-μm) show that this effect is general, but that the time scale of ion loss due to this mechanism increases rapidly as the trap size, RF amplitude, and field ideality increase. For instance, the average time required to lose all but one ion is ~10 μs for an ideal hyperbolic trap with r_0 = 1 μm, and on the order of 1 ms for a 10 μm cylindrical trap. Thus the estimated charge density relation, N_{max}, is true only for a relatively short time scale. For macroscopic traps this loss process also occurs, but is slow compared to a typical mass analysis experiment.

Ejection of all but one ion due to space charge has an interesting result: the single ion remaining in a trap tends to have a favorable combination of kinetic energy and trajectory such that it will likely be trapped for a long period of time in a collisionless environment. In addition, the remaining ion is no longer affected by space-charge from neighboring ions. To explore this

phenomenon 100 ions were introduced into a trap during the first RF cycle, and Coulombic repulsion was calculated between each ion. Due to charge repulsion the trapped ion population was quickly reduced to a single, cooler ion. This simulation was repeated 100 times. After 10^4 RF cycles (8.3 μs), in 97 of the 100 cases the trap still had a single trapped ion. Of those ions that remained after 10^4 cycles, 96% continued to be trapped for an additional 10^5 cycles. Although this simulation demonstrates the charge-induced ion loss process, it represents a physically improbable situation since ions cannot be formed within a trap at this rate.

A more realistic situation was simulated in which 25 argon ions were created at random times over defined periods ranging from 250 ns to 2.5 ms, corresponding to average ionization rates of 100 to 0.1 ions per μs. The trap was simulated with 5 mTorr argon at 8 V and 1.2 GHz. For each simulation space-charge eliminated all but one ion, and the lifetime of the remaining ion was recorded. The simulation was repeated 50 times for each ionization rate. These results are shown in Figure 4.11. The median lifetime is equivalent to the time at which the trap has a 50% probability of being empty, and a 50% probability of having a single ion.

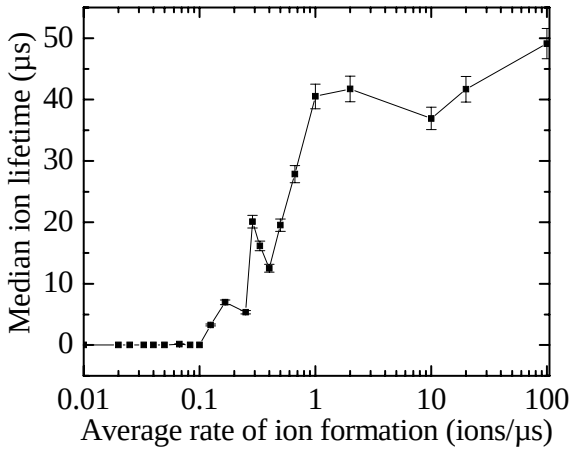

Figure 4.11. Median ion lifetime as a function of the average ion formation rate. Argon ions in 5 mTorr argon, with the trap operated at 16 V. Ion lifetime begins at the end of the ionization event, rather than at the moment the last ion is formed. Thus, for low ionization rates (<0.1 ion/μs), the median ion is already lost before the end of the ionization event, resulting in a value of zero in this figure.

In no case did a trap have more than one ion at this point in time. When ionization rates are sufficiently fast, Coulombic repulsion selects the more favorably trapped ion, and rejects the others, similar to the effect illustrated above. However, when the rate of ion formation is lower than the rate of ion loss, no net accumulation or selection of ions occurs in the traps. Consequently, successful operation of micrometer-sized traps will require ion formation rates exceeding ion loss rates. Of course, even one ion per microsecond per trap is a difficult level for *in situ* ionization to achieve. Because temperature, pressure, q_z, voltage, and other parameters affect ion lifetimes, they are also relevant in determining the necessary ion formation rate. For instance, a trapping voltage of 50 V may allow for a smaller ion generation rate.

Importantly, space-charge does not cool the (eventual) remaining ion, it simply allows the selection of one favorably-trapped ion and rejection of all the other ions. For one randomly

generated ion per trap, an array of traps will have a small number of traps with one trapped ion, while most traps will be empty. The remaining ions will have favorable trapping parameters (kinetic energy, position, etc.). On the other hand, if the same traps are each populated with several ions, after some time a majority of the traps will contain one trapped ion. Another result of charge-induced selection is that loss rates are more rapid immediately following the ionization event, and fewer stray ions will interfere with mass analysis and detection.

4.3.4 Trap Electrode Geometry Effects

Fabrication of micrometer-sized traps using plasma etching produces an 85-87 degree sidewall taper on all trap electrodes. The direction of tapering is such that an electrode is wider at the top and narrower near the substrate. Although the taper results in an additional nonlinearity of the electric field in such a trap, simulations indicated that trapping efficiency is only minimally affected. For example, traps with a taper of 85 degrees were simulated under conditions of various voltage, frequency, and pressure conditions. The trajectories of ions showed visible distortion in tapered traps. However, the percent of ions trapped using tapered electrodes was generally only 1-3% lower than that for non-tapered electrodes under identical conditions, well within the error limits for each simulation. These results imply that the tapering of the electrode surfaces has a negligible effect on ion trapping.

In cylindrical ion traps, unlike hyperbolic traps, the ratio of z_0 to r_0 can be varied over some range without significantly modifying the ion trapping and mass analysis properties. Figure 4.12 shows a similar result for the micrometer-sized cylindrical ion traps operated at 8V and 1.2 GHz. The value of r_0 was held constant at 1 μm, and z_0 was varied from 0.6 to 1.3 μm. Under identical starting conditions ions were trapped for 25000 RF cycles with no collision gas. Ion trapping shows a broad maximum for values of z_0 in the range 0.7 to 1.0 μm, and drops off gradually for values outside this range. Of course, ion traps can be fabricated in a range of sizes, from r_0 = 1 μm up to several micrometers, with z_0 scaling accordingly. It is suggested that ion trapping in larger traps will increasingly resemble trapping in macroscopic traps. However, factors such as sustainable voltage, structural mechanics, and operating pressure range each vary differently and must be considered in designing larger microfabricated traps.

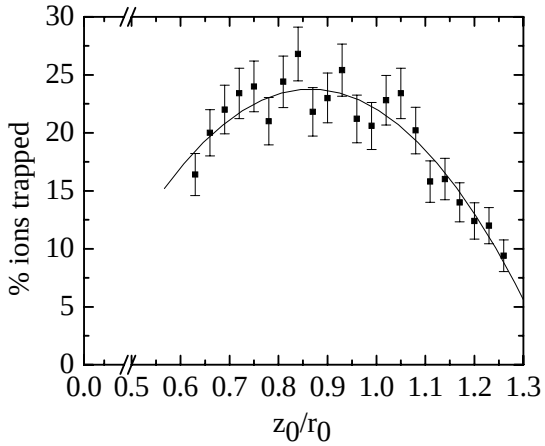

Figure 4.12. Collisionless trapping efficiency as a function of z_0, with r_0 held constant at 1 μm, with the trap operated at 8 V and 1.2 GHz, and ions with m/z = 93 trapped for 20 μs. The trend-line shows best-fit parabolic curve.

The misalignment of end cap electrodes with respect to the ring electrode is dictated by the alignment tolerance of the photolithography tool that defines the patterns. For the exposure tool used in this work (a GCA XLS stepper), the alignment tolerance is 150 nm (3σ) layer to layer, therefore the maximum ring electrode to end cap misalignment would be 300 nm (as there is a via layer between the ring electrode and end cap). The results from the first microfabrication indicated that the actual misalignment (end cap to ring) is much smaller—on the order of 50 nm. Table 4-1 shows simulated normalized ion trapping efficiencies for geometries involving layer misalignment. Normalized trapping efficiencies were expressed as a fraction of the trapping in a perfectly-aligned trap. Data are shown for different misalignments with offsets of 50, 100, and 150 nm. Ion trapping was not noticeably reduced for 50 nm distortions, but begins to deteriorate for larger misalignments. These results imply that expected and actual process-induced misalignment of the end caps has a relatively minor effect on trapping efficiency for micrometer-scaled ion traps. Preliminary simulations of the effects of misalignment on ion ejection efficiencies also indicate a minor effect.

Table 4-1. Normalized trapping efficiencies for electrode misalignments, expressed as a fraction of the trapping efficiency when no misalignment is present. (The trapping efficiency is 25.4% with no misalignment under these simulation conditions.) Error for each value is ±5%.

	Electrode Displacement			
Nature of Misalignment	**0 nm**	**50 nm**	**100 nm**	**150 nm**
Top end cap offset	1.0	0.98	0.84	0.87
Ring electrode offset	1.0	0.98	0.75	0.61
Bottom end cap offset	1.0	0.98	0.88	0.74
Top and bottom offset in opposite directions	1.0	0.96	0.94	0.90
Top and bottom offset in orthogonal directions	1.0	1.00	0.89	0.83

4.4 Conclusions from Simulations of Micro-Ion Traps

These simulations demonstrated that ion trapping is possible for micrometer-sized cylindrical ion traps. However, several aspects of micrometer-sized traps make them less effective than large traps for trapping ions. Shallow pseudopotential wells, necessitated by the desire for low voltage and power requirements, limit ionization to *in situ* methods. The shallow well coupled with space-charge also limits ion storage capacity to essentially a single ion per trap on the time scale needed for mass analysis and detection (Blain, Riter et al. 2004). Although a single trap is capable of trapping only one ion on a useful timescale, sensitivity is achieved by creating a large parallel array of traps. An array of 10^6 traps with $r_0 = 1$ μm has the same total trap volume as, but greater ion capacity, than a single trap with $r_0 = 0.1$ mm. The standard mass-selective-instability scanning mode may be unable to achieve high mass resolution due to the absence of a sharp instability boundary at q_z=0.908, as is typical in larger traps. This gradual instability boundary also results in some mass selectivity in ion trapping and storage. As a consequence, good performance may require alternative mass analysis modes, such as mass-selective trapping followed by a pulse-out of the ions. Additionally, the difficulty of creating ions inside the small trap volume may require novel ionization methods.

Simulations show evidence of kinetic energy coupling between r and z directions, consistent with nonlinear resonances observed in larger traps (March and Todd 1995). Although nonlinear fields are present in all traps, particularly cylindrical traps, the magnitude of the nonlinear contribution is zero at the trap center. Thus ions that are cooled to the center of the trap experience minimal nonlinear effects. In micrometer-sized traps, however, thermal energies of ions result in a large ion excursion relative to the total trap volume. Ions spend significant time far from the trap center, and nonlinear effects may be significant. Collisional cooling does not benefit trapping of ions generated *in situ*, however, operating pressures may be higher, due to the short path length and timescales involved, than in conventional ion trap instruments, and pumping requirements may be reduced. Additionally, the issues of ionization rate, mass analysis mode, and signal detection sensitivity must be investigated to attain a working instrument.

5.0 MICROFABRICATION AND PACKAGING OF CYLINDRICAL ION TRAP ARRAYS

A detailed description of the microfabrication and packaging of the different designs of cylindrical ion traps and their arraying is offered in this chapter. Details concerning the microfabrication of a self-aligned aluminum/silicon dioxide trap are presented. The fabrication approach is based on the utilization of a chromium hard mask and the etching of alternating thin film layers of silicon dioxide and aluminum. Additionally, specifics pertaining to the microfabrication of a suspended free-standing air gap cylindrical ion trap utilizing a molded tungsten fabrication sequence are given. The approach utilized the iterative patterning and etching of silicon dioxide layers and the deposition and planarization of tungsten layers. Release of the resulting W electrodes in an HF solution completed the realization of the suspended, free-standing, air gap cylindrical ion traps.

5.1 Overview

In this chapter the microfabrication of cylindrical ion traps in large arrays to be used as mass analyzers for mass spectrometry is discussed. The devices described were microfabricated in either a class 1 or a class 1000 clean room, and sometimes processing occurred in both. To fabricate the two versions of the microfabricated ion traps, three basic steps in the microfabrication were used: patterning features using photomasks, depositing films – either metals or dielectrics, and etching and/or planarization of these films. The techniques used in accomplishing these basic steps were previously detailed in Chapter 2.

The version 1 cylindrical ion trap was fabricated using a process sequence which consisted of seven alternating aluminum (Al) and silicon dioxide (SiO_2) layers. Cr was selected as the hardmask for etching the 7-layer stack. The etching of chromium (Sewell 1978; Naguib, Bond et al. 1983; Walker and Tarn 1991), aluminum, and silicon dioxide has been previously studied and detailed in section 6.2. Aluminum and silicon dioxide have been widely used in combination as an interconnect for microelectronic integrated circuits (Jaeger 1993), and these materials provided a well-understood foundation for the microfabrication of miniaturized sensors.

The version 2 cylindrical ion traps were fabricated using a tungsten molding process. This process is similar to the damascene process described by Andricacos, Uzoh, and et. al. (Andricacos, Uzoh et al. 1998). Damascene plating involves deposition of the seed layer over a patterned material, in this case an insulator. Damascene electroplating is ideally suited for the fabrication of interconnect structures, since it allows inlaying of metal simultaneously in via holes and trenches by a process called dual damascene. In a similar fashion, tungsten is molded around features etch in silicon dioxide simultaneously creating the trap electrodes and vias for the next level.

Figure 5.1 shows the scanning electron microscopy (SEM) images of the different microfabricated cylindrical ion traps, while their detailed fabrication processes are discussed later in this chapter.

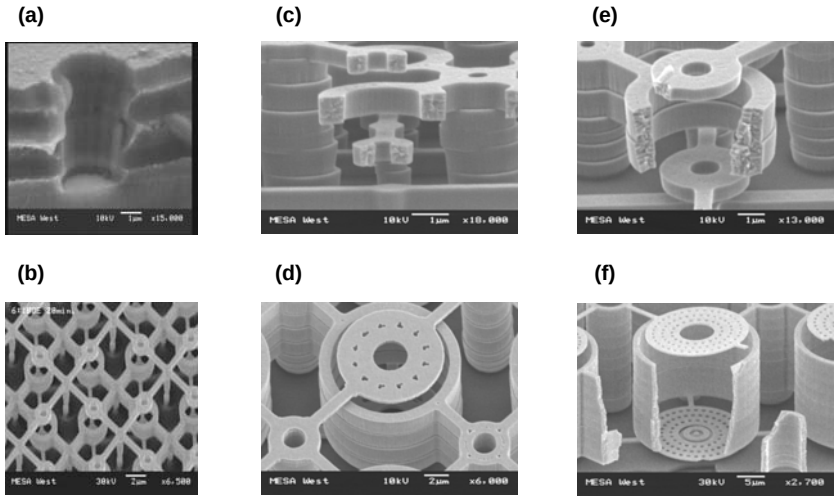

Figure 5.1. SEM micrographs of the different fabricated cylindrical ion traps. (a) self-aligned structure with alternating layers of aluminum as the metal electrodes and silicon dioxide as the dielectric, r_0 = 1 μm; (b-f) an overhung structure fabricated by molded tungsten with (b) r_0 = 1 μm; (c) r_0 = 1 μm; (d) r_0 = 5 μm; (e) r_0 = 2 μm; (f) r_0 = 10 μm.

5.2 Microfabrication of a Self-Aligned Aluminum Ion Trap

The micro-cylindrical ion trap with Al electrodes was created by depositing alternating layers of Al metal and SiO_2 dielectric and finally etching the structure to the bottom metal layer. Aluminum was chosen as the metal because of its properties as a good RF conductor and its ease of deposition. The deposition of alternating metal and dielectric films created a stacked structure with four metal layers, including a collector, the bottom end cap electrode, the ring electrode, and the top end cap electrode, as shown in Figure 3.4. Three dielectric layers separate the metal electrodes. Once the films stack is formed, a through-etch to the bottom layer creates self-aligned apertures.

Before the depositions, wafers were cleaned with a piranha solution (H_2SO_4:H_2O_2 4:1) to remove any organics and HF to remove any native oxide. Thermal oxide was then grown to act as an insulating layer between the silicon wafer and the device. A steam oxidation was performed in a 6" furnace, and the thermal oxide thickness was approximately 1 μm.

After the oxidation, the wafers underwent a piranha clean and DI water rinse. They were then dried with nitrogen and patterned with photoresist. The lithography for each of the metal layers defined large pads (1 mm × 1 mm) for electrical contacts. The wafer was first patterned for the collector layer, and the pads and array area were defined with a liftoff process. After the liftoff, the wafers were cleaned and silicon dioxide was deposited using plasma enhanced chemical vapor deposition (PECVD). This process was repeated until all metal electrodes were deposited. Another insulating layer was deposited to prevent Al contact with the Cr hard mask. In order to pattern the Cr, a silicon dioxide hard mask was used and this was patterned using a thin resist, AZ4110. The minimum dimension was 2 μm. Figure 5.2 summarizes the process flow for the self-aligned alternating aluminum and silicon dioxide based cylindrical ion trap. Two hard masks (SiO_2 and Cr) were used to pattern the features and alternating etches in an ICP reactor were used to pattern SiO_2 and Al.

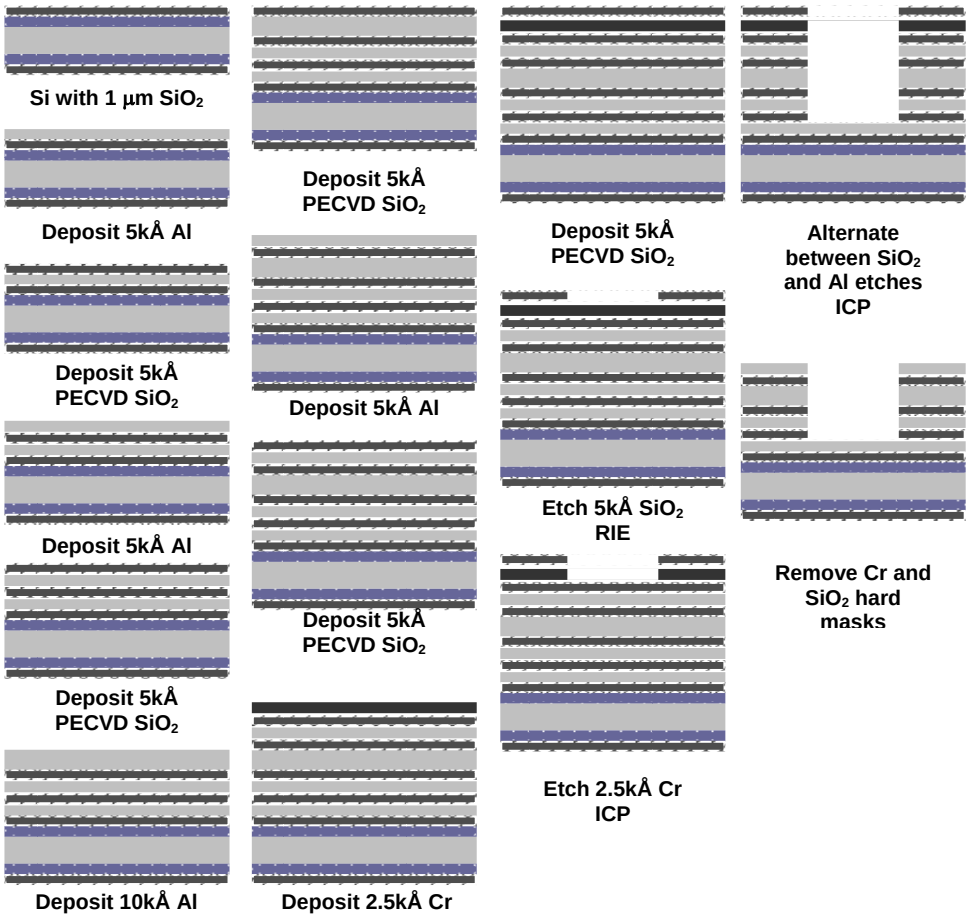

Figure 5.2. A process flow schematic for microfabrication of self-aligned aluminum cylindrical ion trap. Alternating depositions between aluminum and silicon dioxide were performed, along with deposition of the hard masks. The hard masks were then patterned and etched. Alternating etches for silicon dioxide and aluminum were performed in an ICP reactor and finally the Cr and SiO_2 hard masks were removed.

Chromium, tungsten and nickel were considered as hard masks for the stack etch. However, it was found that the selectivity of chromium was 6 times that of tungsten in the aluminum etch chemistry. Although nickel demonstrated good selectivity to the Al etch chemistry, a wet etch had to be used to pattern the nickel. This created an undesired undercut and affected the Al profile evolution during the etch. Since Al profile control is of importance in defining the electrode shape, Cr was selected as the hard mask.

The Cr hard mask and stack structure were etched in an inductively couple plasma (ICP) reactor. Etch times were determined based on measured etch-rates. All the reported deposition rates were determined by a linear regression of the thickens measured as a function of time with at least three data points, and the regression coefficient is > 0.99 unless otherwise stated. When etching the ring electrode, bottom end cap and dielectric layers, 50-100 % over etch was used to

compensate for the small feature size and the high aspect ratio. An aspect ratio of 4:1 was achieved in the structures.

Plasma etching of the silicon dioxide hard mask was performed in a reactive ion etch (RIE) reactor. The photoresist exhibited infinite selectivity in the etch chemistry, a CHF_3/O_2 plasma. The SiO_2 etch rate was measured to be approximately 400 Å/min. The photoresist thicknesses were monitored using the Nanospec™. Ho, et. al. present a detailed mechanism for the reaction. (Ho, Johannes et al. 2001)

The silicon dioxide provided very high etch selectivity, approximately 1:140, in the ICP Cr etch, using a Cl_2/O_2 chemistry. The photoresist was not removed prior to the Cr etch and was etched away by the Cl_2 plasma.

5.2.1 Chromium Deposition

Chromium was thermally evaporated in a CVC evaporator as a mask, on top of the stack structure and the final insulating layer. The typical evaporator pressures were 5×10^{-7} Torr, which was lowered to 1×10^{-7} Torr once the Cr deposition started, and the deposition rate was approximately 7-10 Å/min. Because of film stress, the greatest film thickness which could be evaporated was 3000 Å. Thicker Cr films caused the other metal layers to delaminate due to the stress. Final Cr thicknesses were targeted to be about 2500 Å.

5.2.2 Plasma Etching of Chromium

The reactor for etching Cr is a dual chamber PlasmaTherm ECR/ICP reactor with a load lock and a wafer handling chamber. Chlorine-oxygen plasma (Sewell 1978) with 16% of argon was used. Table 5-1 shows the etch parameters used to etch the Cr in the ICP reactor. The chromium etch in the ICP reactor was very aggressive, the photoresist etch-rates being approximately 1 μm/min. In order to resolve the small feature size (diameter of 2 μm), a thin AZ 4110 photoresist of about 1 μm in thickness has to be used. Therefore, Cr hard mask could not be patterned using a photoresist, and a hard mask of silicon dioxide was used to pattern the chromium. The SiO_2 hard mask was deposited in the same fashion as the other dielectric layers, as described later.

Table 5-1. Etch parameters used in Cl_2/O_2 plasma used to etch Cr in the ICP reactor.

Etch Parameters	
Cl_2	30 sccm
Ar	20 sccm
O_2	20 sccm
He	50 sccm
Power	800 W
Pressure	10 mTorr

Oxygen was added to increase the chlorine radical density (Naguib, Bond et al. 1983) and the chlorine radicals reacted with chromium to form a volatile etch product, chromium trichloride. The main etch mechanism can be described as follows:

$$3Cl^{\cdot} + Cr \rightarrow CrCl_3 \qquad (5.1)$$

No grassing or sputtering was observed on the sample, indicating that there was no redeposition of the volatile metal etch product. Helium was also added to the etch chemistry to increase the ion density. The 2.2 MHz source power used was 800 W, the highest available in the tool. A DC time averaged bias of 250 V was applied to the substrate holder at a frequency of 13.56 MHz. The substrate holder was elevated in the chamber during the etches, allowing the substrate to be immersed where the ion density was greater in the plasma, and increasing the etch rate. The etch rate was found to be approximately 1480 Å/min. Wet etching the chromium with Cr-7 (Walker and Tarn 1991) was considered. However, the plasma etch is three times faster than the wet etch and creates a smooth sidewall and no undercut, which is important for the feature profile evolution. Figure 5.3 shows the measurement results of the etch depth of Cr as a function of time made with a profilometer. Figure 5.4 shows a SEM image of an etched Cr feature with a SiO_2 hard mask.

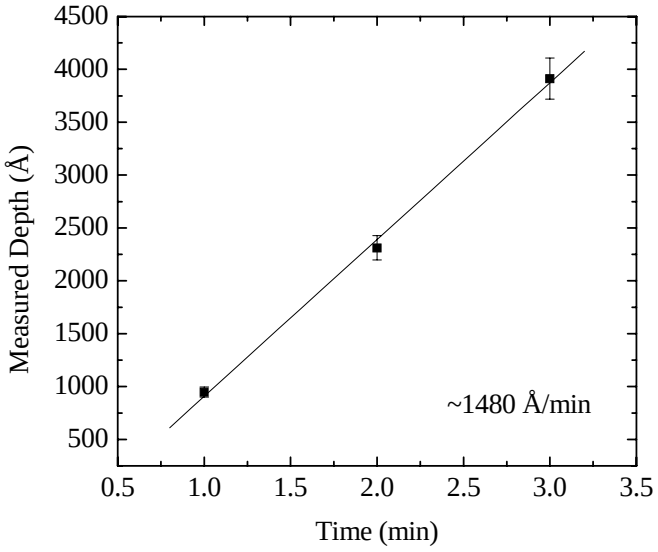

Figure 5.3. Measured etch depth of Cr as a function of time. Depth was measured with a profilometer. Cr was etched using a chlorine plasma in an ICP reactor. The etch rate based on a linear regression was approximately 1480 Å/min.

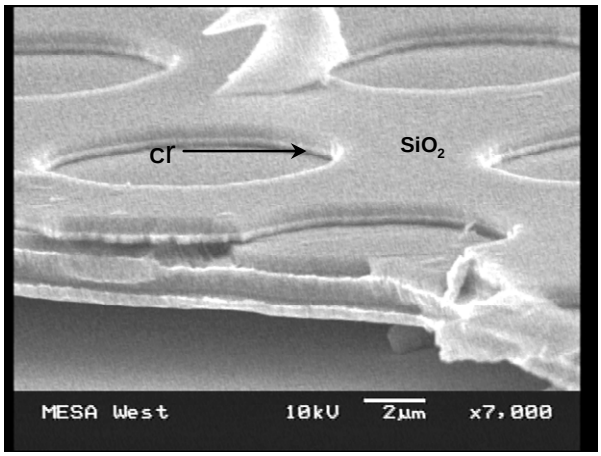

Figure 5.4. A SEM micrograph of Cr etched in an ICP reactor with a Cl_2 plasma. A SiO_2 hard mask was used to pattern the Cr.

In order to characterize the plasma, the ICP process conditions were reproduced in an ECR plasma reactor (Sha and Chang 2004) which was equipped with an *in situ* optical emission spectrometer (OES). Helium was not used in this recipe, possibly decreasing the Cl ion density. To achieve plasma stability in the reactor, the pressure was lowered to 6 mTorr, while the power and the substrate bias were reduced to 600 W and 150 V, respectively. The flow rates were halved to maintain the same pressure.

Figure 5.5 shows the time evolution of optical emission from Cl (837.6 nm) and Cr (520.8 nm). The OES results showed that the reaction of Cl with Cr reduced the Cl optical emission intensity when the bias was turned on, and a corresponding increase in the Cr optical emission intensity. The Cl optical emission intensity increased once again when the bias was turned off, indicating that it was no longer reacting with Cr. The Cr signal correspondingly drops, as it is no longer being etched. The Cr etch rate was calculated to be about 102 Å/min in the ECR reactor, significantly lower than the etch rate measured in the ICP reactor as a result of the reduced flow rates, power and bias.

5.2.3 Silicon Dioxide Deposition

Silicon dioxide was deposited using a plasma enhanced chemical vapor deposition (PECVD) process with a SiH_4/NO_2 plasma at 250^{o}C and 400 mTorr. Table 5-2 shows the deposition parameters used to deposit the films in the PECVD VacuTek reactor. Film thicknesses were determined with the Nanospec™ and ellipsometer. The refractive index was measured to be ~1.45. A Si monitor sample was placed in the chamber to determine the final thickness and the deposition rate, since the silicon dioxide could not be measured atop the aluminum due to the reflection from the aluminum. The uniformity of the film was found to be approximately 1.4% when measured across a 4" silicon wafer. All depositions were preceded with a CF_4/O_2 chamber clean and a seven-minute conditioning run with the SiH_4/NO_2 plasma to condition the reactor. The deposition rate was on the order of 220 Å/min.

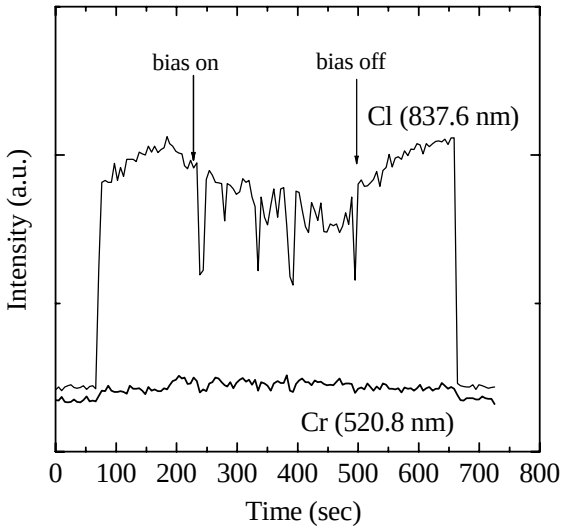

Figure 5.5. The time evolution of optical emission from Cr and Cl. A Cl_2 plasma was used to etch Cr in an ECR reactor. The time evolution shows a decrease in the intensity of the Cl intensity and an increase in the Cr intensity, as Cl etched Cr.

Table 5-2. Deposition parameters used for the PECVD of SiO_2.

Deposition Parameters	
SiH_4	70 sccm
N_2O	32 sccm
Temperature	250 ^oC
RF power	25 W
Pressure	400 mTorr

5.2.4 Silicon Dioxide Etching

After the chromium hard mask was etched, silicon dioxide was etched in the same ICP chamber. The chamber was not opened between etches. The silicon dioxide was etched using a SF_6 plasma. Table 5-3 shows the etching parameters used to etch SiO_2 in the ICP reactor. Ar, O_2 and N_2 were also added. The source power was 800 W with a 250 V DC substrate bias and the pressure was 15 mTorr. Figure 5.6 shows SiO_2 removed as a function of time in the SF_6 plasma. The achieved etch rate was approximate 1740 Å/min. The SiO_2 retained a smooth sidewall throughout the stack etch.

Table 5-3. Etch parameters used in the SF_6 plasma to etch SiO_2 in the ICP reactor.

Etch Parameters	
SF_6	10 sccm
Ar	20 sccm
O_2	3 sccm
N_2	10 sccm
Source power	800 W
DC substrate bias	25 V
Pressure	15 mTorr

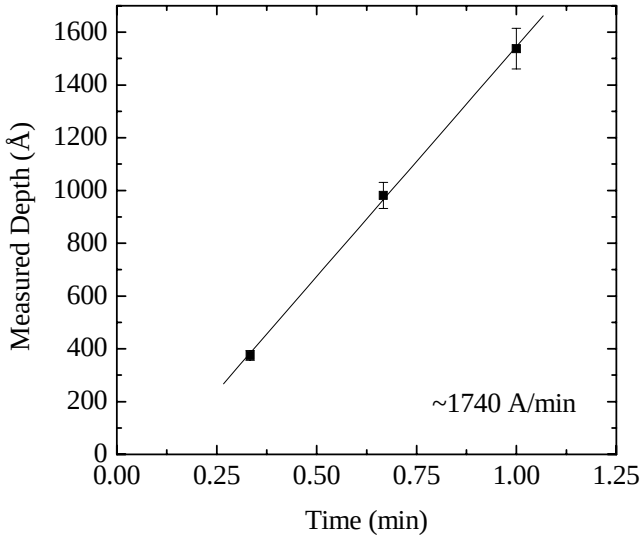

Figure 5.6. Etch characteristics of SiO_2 in a SF_6 plasma in an ICP reactor. Measured etch depth of silicon dioxide is shown as a function of time. The etch rate as determined by linear regression was ~1740 Å/min.

Chromium showed excellent selectivity in the SiO_2 etch. The selectivity of SiO_2:Cr in the SiO_2 etch process was ~50:1. Figure 5.7 shows the thickness change as a function of time for Cr in the SiO_2 etch process. The Cr etch rate was ~37 Å/min. The regression coefficient was $R^2 = 0.89$. The etch depth did not linearly increase as expected after six minutes of etching. This is possibly due to re-deposition on the Cr preventing further etching of the material. Different samples were utilized during the etches to determine the etch rate and contamination of one of the samples could induce differences in the etch characteristics of the Cr.

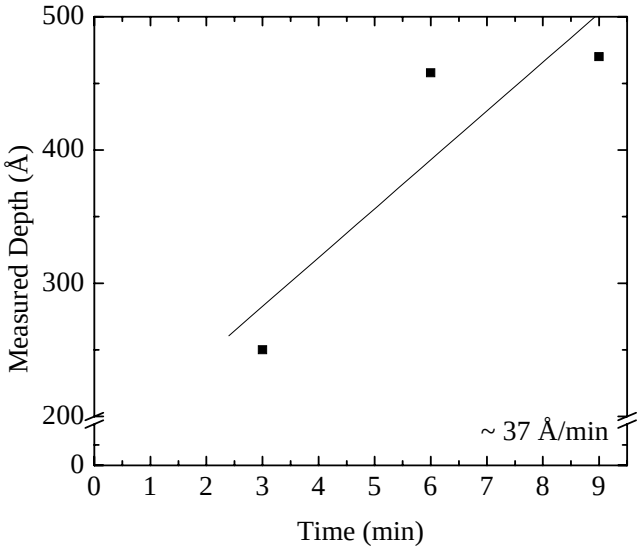

Figure 5.7. Etch characteristics of Cr in the ICP SiO_2 etch process. Measured etch depth of Cr is shown as a function of time. The etch rate of Cr was calculated to be ~37 Å/min. The selectivity of SiO_2:Cr in the SiO_2 etch process was ~50:1.

5.2.5 Aluminum Deposition

The aluminum was thermally evaporated in a CVC evaporator. A 100 Å titanium (Ti) layer was evaporated to aid Al adhesion to the silicon dioxide layer. The aluminum was lined with a 500 Å titanium nitride (TiN) layer to prevent hillock formation (Herman, Schuster et al. 1971; Cadien and Losee 1984; Singh 1985; Rocke and Schneegans 1988; Puttlitz, Ryan et al. 1989; Martin, Tracy et al. 1995; Kim, Heiland et al. 2000; Zaborowski and Dumania 2000). High purity (99.99%) nitrogen gas was introduced into the reactor as titanium was evaporated, at a chamber pressure of 5×10^{-5} Torr. Upon nitrogen reaction with the titanium, the chamber pressure was reduced to 2×10^{-5} Torr. The Al source was 99.999% pure and it was evaporated for several minutes before opening the shutter to expose the substrate. The base chamber pressure was about 5×10^{-7} Torr before deposition. Aluminum thicknesses were measured using a profilometer. Thicknesses for each film in the entire stack are summarized in Table 5-4. After deposition, the wafers were soaked in acetone for a couple of hours and then sprayed with an acetone gun for liftoff. After liftoff, wafers were cleaned using a standard solvent clean sequence of with acetone, methanol, and isopropanol and high resistivity D. I. water.

Table 5-4. Layers and their thickness for the self-aligned aluminum/silicon dioxide ion trap. Bottom layer is listed first.

Layer Number	Layer	Thickness (Å)
1	Collector – Al	5000
2	Dielectric Spacer – SiO_2	5000
3	Bottom End Cap – Al	5000
4	Dielectric Spacer – SiO_2	5000
5	Ring Electrode – Al	10000
6	Dielectric Spacer – SiO_2	5000
7	Top End Cap – Al	5000
8	SiO_2 Layer	5000
9	Hard Mask – Cr	2500
10	Hard Mask – SiO_2	5000

5.2.6 Aluminum Etching

After the chromium and silicon dioxide etches, aluminum was etched in the same ICP reactor without breaking vacuum. A breakthrough etch was performed since the surface chemistry of Al is different than the bulk film chemistry, due to surface oxidation and formation of Al_2O_3. The aluminum was etched using a Cl_2 /BCl_3 plasma (Hebner, Blain et al. 1999; Hebner, Blain et al. 1999; Malyshev, Donnelly et al. 2000; Cooperberg, Vahedi et al. 2002) with nitrogen to help passivate the sidewall, since the etching is isotropic. The breakthrough occurred at five seconds. Figure 5.8 shows the measured depth of Al as functions of time for the breakthrough etch. Figure 5.9 shows the measured depth of Al as functions of time for the main Al etch. A ten-second breakthrough etch was performed to ensure breakthrough over the entire substrate surface. The added nitrogen flow was not enough to prevent undercutting, as seen in Figure 5.10 (a) and Figure 5.10 (b). Figure 5.10 (a) depicts a SEM micrograph of the stack etched through the chromium hard mask, oxide layer and the top end cap. Figure 5.10 (b) shows a SEM micrograph of the stack structure etched through the bottom end cap layer. Figure 5.10 (c) shows a SEM micrograph of the arrayed etched stack structure. Although the hard mask provided a smooth straight sidewall, the lack of sidewall passivation during the aluminum etch created an unwanted undercut, which will alter the electric field in the device.

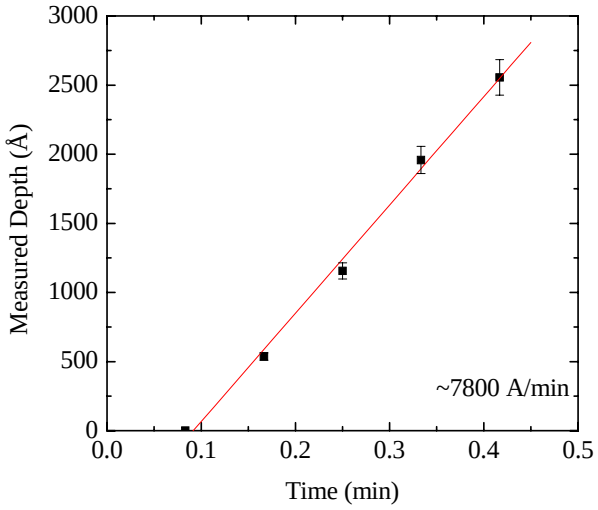

Figure 5.8. Etch characteristics of Al in the Al breakthrough etch process in a Cl_2/BCl_3 plasma. Measured etch depth of Al is shown as a function of time. The break through happened at 5 seconds.

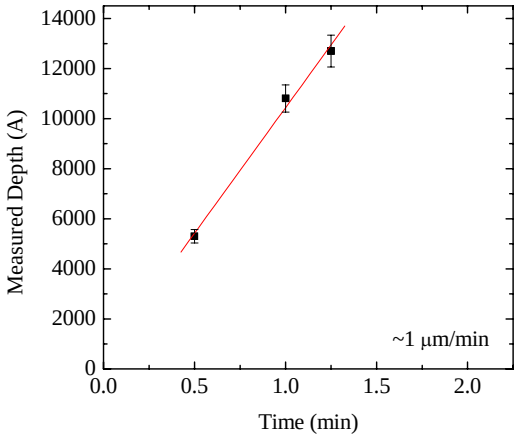

Figure 5.9. Etch characteristics of Al in the main Al etch process in a Cl_2/BCl_3 plasma. Measured etch depth of Al is shown as a function of time preceded with a 10 second breakthrough etch. The calculated etch rate was ~1 μm/min.

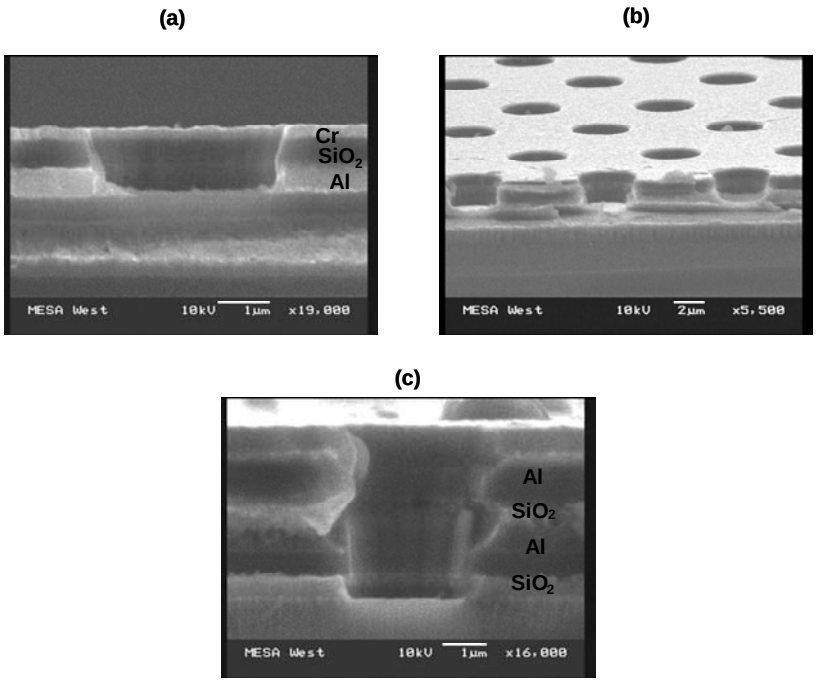

Figure 5.10. SEM images of the aluminum/SiO_2 stack when (a) the stack was etched through the top end cap, (b) the stack was etched through the ring electrode, and (c) the stack was etched through the bottom end cap. Cr was used as the hard mask and alternating etches of SF_6 and Cl_2/BCl_3 plasmas in an ICP were performed.

Figure 5.11 shows the etch characteristics of Cr in the Al etch process. The Cr etch rate was ~140 Å/min. Chromium showed excellent selectivity in the Al etch. The selectivity of Al:Cr in the Al etch process was ~75:1.

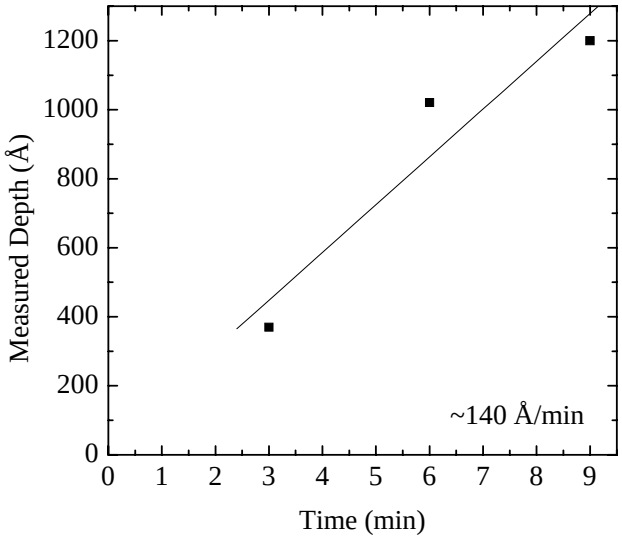

Figure 5.11. Etch characteristics of Cr in the Al etch process. Measured etch depth of Cr is shown as a function of time. The etch rate of Cr was calculated to be ~140 Å/min. The selectivity of Al:Cr in the Al etch process was ~75:1.

The aluminum etch was very aggressive, achieving an etch rate of 1 μm/min. It is interesting to note that the photoresist etch rate in the aluminum etch chemistry was considerably lower than in the SiO_2 and Cr etches. However, because of the alternating etches and the length of the etches a hard mask had to be used. Although the hard mask achieved the desired stack etch, its lack of producing organic species for sidewall caused undercut rather than anisotropic etch profiles in the Al layers and passivation led to a new design of the cylindrical ion trap based on tungsten electrode material and is described later in this chapter.

To further elucidate the mechanisms and behavior of the stack etch process, the same process conditions were again used in the ECR reactor in order to characterize the etch products. The Al and B optical emission could not be identified in the OES spectra because of their low intensities. Figure 5.12 shows the time evolution of optical emission from Cl (837.6 nm) and Cr (520.8 nm) during the etching process. The Cl intensity showed a sharp decrease in intensity when the bias was turned on. The Cr peak did not show a significant increase in intensity, confirming that it was not greatly etched under these conditions. The Al etch rate was about five times lower in the ECR reactor than in the ICP reactor, 2000 Å/min. The Cr etch rate was significantly lower as well, 125 Å/min. The selectivity between Al and Cr in a Cl_2/BCl_3 based chemistry was about 3 times higher in the commercial ICP reactor.

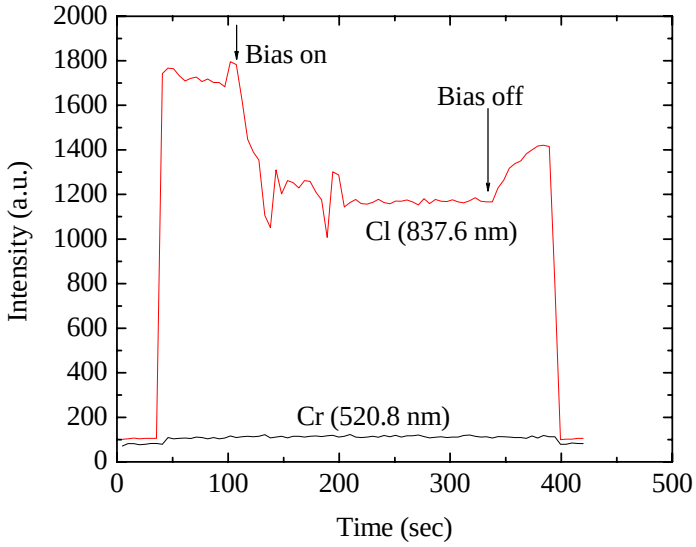

Figure 5.12. The time evolution of optical emission from Cr and Cl. A Cl_2/BCl_3 plasma was used to etch Al in an ECR reactor. The time evolution showed a sharp decrease in the intensity of the Cl peak and no significant change in intensity in the Cr peak as Cl etched Al.

5.3 Microfabrication of a Suspended Free-Standing Tungsten Ion Trap Array

The suspended free-standing air gap cylindrical ion trap was microfabricated in the Microelectronics Development Laboratory (MDL) at SNL. This is a class one clean room facility utilized for the fabrication of radiation hardened CMOS devices and MEMS devices fabricated using the SUMMiT V^{TM} fabrication sequence. Well established processes were utilized in the fabrication of the traps, and therefore no additional verification of the processes such as thin film analysis or plasma characterization were performed. The fabrication process methodology has also been used for the fabrication of the photonic crystal lattice (Fleming, Lin et al. 2002). The ion traps were microfabricated using a molded tungsten fabrication sequence. The general description of the method is as follows. Silicon dioxide was deposited, patterned and etched. Next tungsten was deposited, filling the features previously etched in the silicon dioxide mold. The tungsten was then planarized to the oxide thickness by chemical mechanical polishing (CMP). The process was then repeated until all levels have been made. Figure 5.13 depicts the process flow for the fabrication.

This molded tungsten process was used to fabricate two design revisions of cylindrical ion traps. In total 5 different ion trap sizes were fabricated. In the first molded W design revision r_0=1 μm and r_0=1.5 μm sized traps were fabricated. For these traps the anchor area was not sufficient and the W electrodes delaminated as the structure was released. The second design revision encompassed four different sizes, r_0 = 1, 2, 5 and 10 μm. Since only one die was used for all modules of the different sizes, flattened and stretched traps were also constructed. Figure 5.14 (a) shows a flattened 10-μm trap fabricated during the r_0=1 μm fabrication sequence and Figure 5.14 (b) shows a stretched 1-μm trap fabricated in the r_0 = 10 μm sequence. These flattened and stretched traps were not tested nor packaged.

5.3.1 Photolithography

Alignment and photolithography of the levels for the microfabrication of W electrodes for the cylindrical ion traps was performed using a GCA XLS stepper. A positive photoresist was used to pattern the features. Six inch (~150 mm) wafers were used and the die size was 1.7×1.7 cm^2. Figure 5.15 shows a layout of the die and a close-up view of a module for a small sized array of 10^3 traps. There were 40 different modules included in the die, with modules for r_0 = 1, 2, 5 and 10 μm traps and three different sized arrays of ~10^3, 10^5, 10^6 traps for each of these traps. The die also included RF characterization structures, as previously described in Chapter 2. The die was stepped and repeated throughout the 6" wafer using the GCA XLS stepper. Approximately 52 dice were made in each wafer.

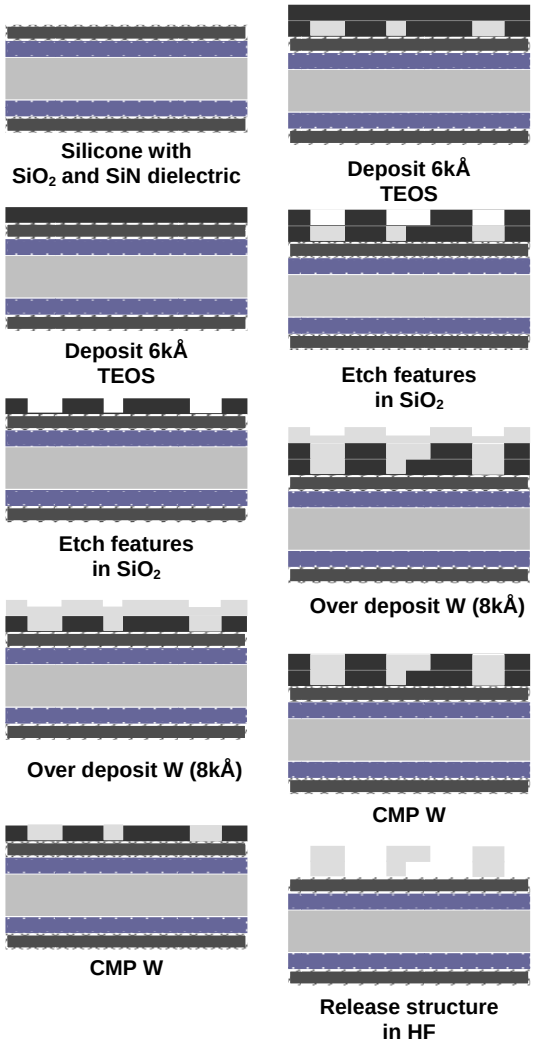

Figure 5.13. A schematic diagram of process flow for a suspended free-standing cylindrical ion trap array with a two layered SiO_2/W stack. Silicon dioxide was deposited and features were etched in the oxide. Tungsten was over deposited and then planarized via CMP. The process was repeated until all layers were formed. The structure was released in an HF solution to realize a free-standing air gap structure.

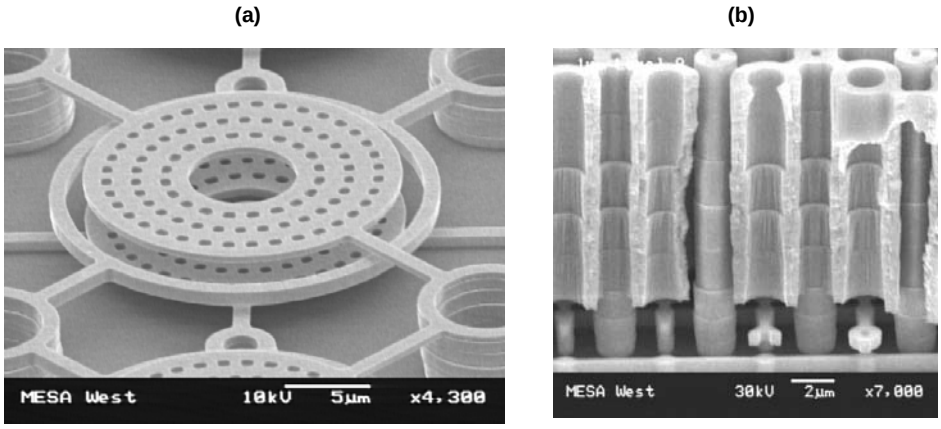

Figure 5.14. (a) SEM image of a flattened r_0=10 μm trap made in the r_0=1 μm fabrication process. (b) SEM image of a stretched r_0=1 μm trap made in the r_0=10 μm fabrication process.

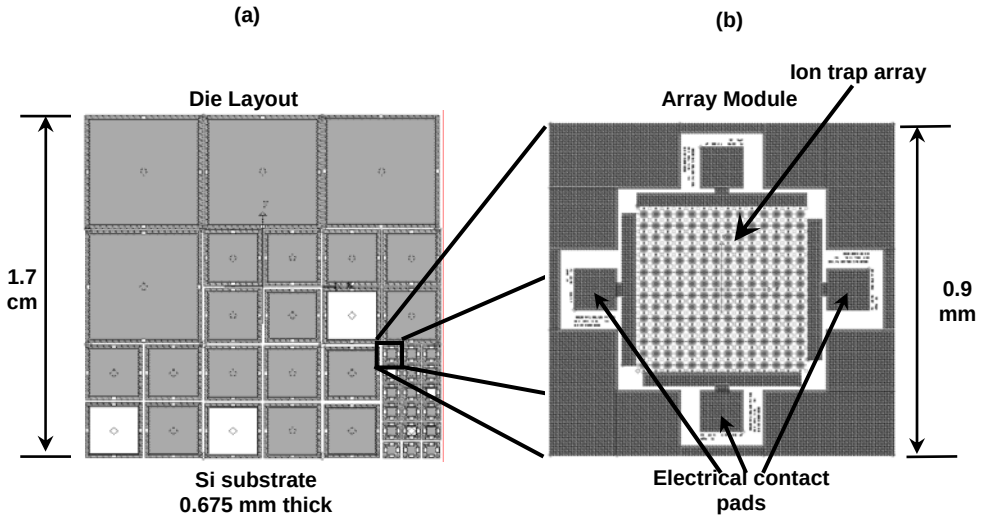

Figure 5.15. (a) A die layout for the cylindrical ion trap array. This layout contains a total of 40 modules. Modules include r_0 = 1, 2, 5, and 10 μm sized traps, along with different array sizes. The die also includes RF electrical S_{11}, S_{12}, shorted and opened structures for the different sized traps and arrays. (b) An amplified view of a r_0 = 1 μm small sized array, showing electrical contact pads, along with the ion trap array.

Features with a critical dimension of 0.35 µm were patterned in this fabrication process sequence. The resolution of the stepper is given by:

$$R = \sigma \frac{\lambda}{NA} \qquad (5.2)$$

where σ is the partial coherence, λ is the wavelength of operation and NA is the numerical aperture of the stepper. The GCA XLS exposure wavelength was 248 nm and the NA was 0.53. The partial coherence is ~0.315, for a resolution of 0.15 μm, thus enabling the patterning of very fine features.

5.3.2 Silicon Dioxide Deposition with Tetraethylorthosilicate (TEOS)

For the molded W process sequence, the first step is silicon dioxide deposition using a tetra-ethyl-ortho-silicate (TEOS) precursor in a plasma enhanced chemical vapor deposition (PECVD) reactor (Applied Materials P5000). While the SiO_2 deposited by PE-TEOS contained more surface defects than LPCVD TEOS, the defects in the SiO2 did not affect the device, as the SiO2 was eventually etched away in an HF solution. The plasma reaction of TEOS to SiO_2 can be summarized as follows:

$$Si(OC_2H_5)_4 \longrightarrow SiO_2(s) + 4C_2H_4 + 2H_2O \qquad (5.3)$$

PE-TEOS depositions varied in thickness depending on the size of the ion trap being fabricated. For the 1-μm traps, all SiO_2 layers were approximately 0.5 μm. The 2-μm traps had ring electrodes of 2.2 μm in thickness and required two SiO_2 layers of 1.1 μm to form the ring electrode. Table 5-5 shows the corresponding ring electrode heights and the number of layers that were used to fabricate the ring electrodes of these traps. The end cap and collector electrodes, as well as the via levels, utilized the same film thicknesses, ~0.5 μm, for all fabrication processes. The thickest PE-TEOS film deposited was on the order of 2.5 μm.

Table 5-5. Ring electrode heights for the corresponding ion traps, with number of layers required to micro-fabricated trap and layer thicknesses.

r_0 (μm)	Ring Electrode Height (μm)	Layer Thickness (μm)	Number of Layers
1	0.5	0.5	1
2	2.2	1.1	2
5	8.8	2.2	4
10	20.0	2.5	8

5.3.3 TEOS Etch

The SiO_2 was patterned and then etched using a CHF_3 plasma. The etch was an important step in the fabrication since it defines the feature. A smooth and straight oxide sidewall was essential in controlling the W profile evolution through the fabrication process. The r_0=1 μm trap showed that the etch profile yielded a >85^o taper along the inner side wall of the electrodes. Simulations showed that this would not affect the trapping efficiency of the ion traps, as previously discussed in Chapter 5.

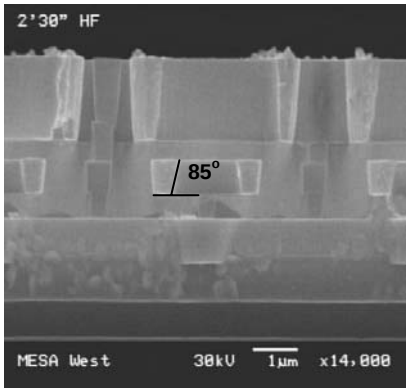

Figure 5.16. SEM micrograph of microfabricated r_0 = 1 μm cylindrical ion trap. An 85^o taper on the electrode sidewall caused by the silicon dioxide etch in a CHF_3 plasma is shown.

5.3.4 Tungsten Deposition

The use of tungsten, as an interlevel interconnect in ULSI microelectronics, has been integrated into mainstream technology for several years. (S.White, Blumenthal et al. 1990; Schmitz 1992) Resistance to electromigration, high deposition rate, and ease of planarization by chemical-mechanical polish (CMP), makes chemically-deposited tungsten desirable (Lujan, Fleming et al. 1994). Tungsten was deposited via chemical vapor deposition (CVD) in a cold wall reactor, (Smith, Fleming et al. 1993; Fleming, Roherty-Osmun et al. 1995), using tungsten hexafluoride (WF_6) as the precursor. The wafers were held at approximately 400^{o}C, during deposition and the system pressure was maintained at a fixed level in the range of 200 to 260 mTorr. An AMAT Centura 5200 system was used to deposit tungsten onto a liner consisting of 200Å Ti capped by a 500Å TiN, and liner deposition was preceded by a 75Å sputter etch.

The films were deposited into features which were 1.1 µm in width. Thus for electrodes of span greater than 1.1 µm, holes were placed in the electrodes, as shown in Figure 5.17 , to accommodate the tensile stress of W.

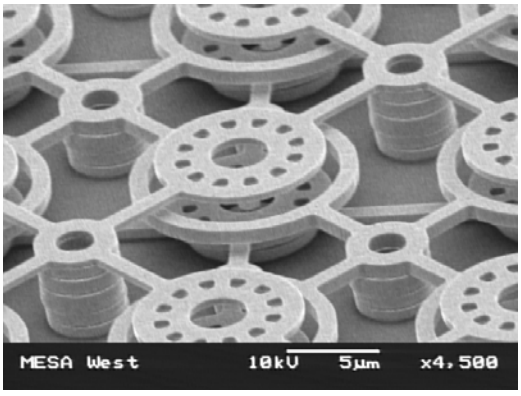

Figure 5.17. SEM micrograph of the cylindrical ion trap array. Electrodes with a wall thickness greater than 1.1 μm have perforations added, so that the W can be grown without bending deformation.

5.3.5 Tungsten Chemical Mechanical Polishing

Chemical mechanical polishing (CMP) of tungsten (Nasby, Sniegowski et al. 1996; Stein, Guilinger et al. 1996; Merkle and Myers 1998; Stein and Her 2000) involves placing the wafer against a polyurethane pad, flowing acidic slurry containing an oxidizer and colloidal alumina over the pad, applying pressure to the backside of the wafer and rotating both the pad and the wafer to achieve polishing. In this work Tungsten CMP (WCMP) was performed using an IPEC Avanti 472 polisher. Material removal occurred on the primary platen, which was covered by a K-grooved IC-1400 polyurethane pad (Rodel Corporation, Newark, DE). The slurry used was a Babot D7300 fumed silica at 270 cc/min. The tungsten was planarized down to the oxide. The wafers were decontaminated with a 15 second dip in 49% HF diluted with 100 parts of DI water.

5.3.6 Structure Release in Hydrofluoric (HF) Acid Solution

Complete W trap electrode structures were released in a hydrofluoric (HF) acid solution. Preliminary releases were performed in solutions containing a 49% HF solution diluted with 1 part water ($HF:H_2O$ 1:1). (The HF solution was further buffered to prevent attack to the Al defining the electrical pads.) This allowed the determination of successful release of the structures. It was determined that not enough anchor area was allotted in the first revision of the ion trap, as the top end cap layer delaminated upon release. From SEM images it was determined that this occurred as the structure was released past the bottom end cap electrode level. If the structure was not completely released, the top end cap could stay anchored via the oxide. To verify this, these structures were released in a BOE buffered oxide etch solution (BOE) $NH_4F:HF$ 6:1 solution. BOE has a slower etch rate than the $HF:H_2O$ 1:1 solution, enabling better control of the amount of oxide etched. Figure 5.18 (a) shows an SEM image of such a trap, where the structure is not fully released to the bottom most electrode. The oxide was able to keep the structures in place. Figure 5.18 (b) shows a greater magnification image of the released structure.

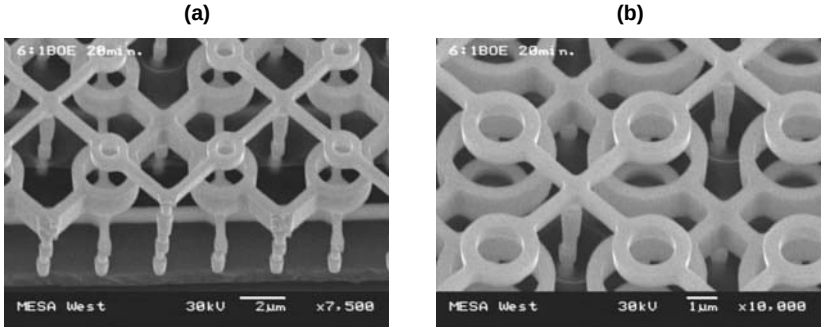

Figure 5.18. SEM images of released ion trap arrays using a 6:1 BOE solution. The anchors were not strong enough to hold the top end cap in place, instead the structure was held together by the unreleased oxide. (a) Image of the array at 7500x magnification, and (b) higher magnification (10000x) image of the array.

Since HF isotropically etches SiO_2, SiO_2 was etched in the vertical and horizontal direction at the same rate. The r_0=10 μm traps were on the order of 24 μm total thickness (vertical direction). Bus bars were about 30 μm in width (horizontal direction), thus the width of the bus

bars was comparable to the height of the r_0 = 10 μm traps. Since the oxide holding the aluminum to the tungsten was etched by the release solution, Al on the bus bars was lifted during the SiO_2 release.

5.4 Packaging of Ion Trap Arrays

The dice were packaged in RF quad-flat-pack packages (G3333M-1) from StratEdge (Stratedge 2005). These packages have a cavity well and straight leads protruding from all four sides. The packages were made of glass with 20% Al and the leads were made of an F-15 alloy. The dice were attached to the bottom of the packages using a non-conductive epoxy and electrical connections were made to the leads from bond pads on the dice through low inductance gold ribbon bonds. The dice were wired so that they retained a ground signal ground. The package leads were soldered onto Duroid® having 50-ohm microstrip lines tapered into 50-ohm coplanar wave guides (CPWs) and SMA connectors. Figure 5.19 shows the Duroid® board with SMA connectors, microstrip lines and CPWs, along with the packaged ion trap array.

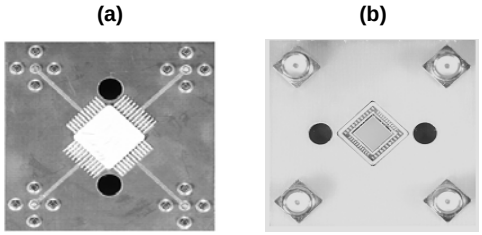

Figure 5.19. Packaged cylindrical ion trap arrays. Packaged parts were placed in a Duroid® board with 50-Ω microstrip lines tapering into a 50-Ω GSG configuration. SMA connectors were used to make electrical connections to the equipment. The images show (a) the back side of board and (b) the front side with ion trap array.

5.5 Summary of Cylindrical Ion Trap Microfabrication

Two different ion trap designs were microfabricated. The first design involved the development of a self-aligned aluminum etch using chromium as a hard mask. A chromium etch chemistry was developed and chromium showed high selectivity in the aluminum and silicon dioxide etch processes. Characterization of the different plasmas chemistries was performed utilizing OES analysis. This ion-trap design was not tested for ion trapping due to poor Al profile control. Two revisions of the second design utilizing a tungsten molding process were fabricated in the MDL, a class 1 clean room facility, at SNL. The first revision was unsuccessful due to the under-sizing of anchors. The final revision realized traps which had radii of 1, 2, 5 and 10 μm. Ion traps were packaged using a StratEdge glass wall RF flat-pack package.

6.0 ELECTRICAL CHARACTERIZATION OF MICRO ION TRAP ARRAYS

A detail presentation regarding the electrical characteristics and field emission properties of microfabricated ion traps is given in this chapter. A concise summary of electrical circuits and how they can be applied to the microfabricated ion trap structure is presented. The presentation of the electrical characterization and field emission properties was based on resistance, capacitance, and vector network analyzer measurements, along with the application of DC voltages under vacuum and atmospheric pressure conditions.

6.1 Introduction

The electrical characterization of the ion trap array and, importantly, ion trap arrays is essential in shaping how power is delivered to the ion trap array. Before application of the ion trap array for species identification, the physical electrical characteristics of all elements must be considered since electrodes in the ion trap act as electrical circuit components such as capacitors, resistors and/or inductors. The notional description of the ion trap array is as a circuit having an RF wave originating from the source, traveling through a line and being terminated at an arbitrary load, as shown in Figure 6.1. It is necessary to determine the impedance of the arbitrary load, in order to form a matching circuit. The computated values of the circuit elements can aid the design development of ion trap structures and target component values. *In-situ* RF lab measurements need to be considered to determine the actual values during operation.

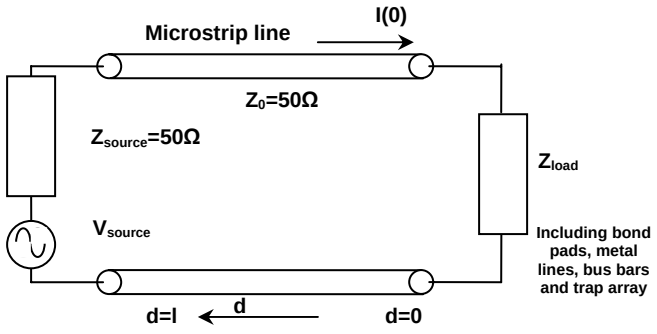

Figure 6.1. A schematic diagram of a circuit of a wave traveling through a line, of length l, and being terminated at an arbitrary load impedance. Typically the line and source impedance are 50 Ω.

Ideally, to maximize the voltage transfer during operation, i.e., minimizing zero reflected power, the line input impedance should be the complex conjugate of the generator internal impedance. This may be impossible if the impedance of the load is vastly different than the impedance of the generator, and illustrate the importance of making detailed electrical measurements.

6.2 Electrical Circuits – an Overview

The impedance of the ion trap array can be determined by fitting an equivalent circuit to the measured S_{11} parameters, and is discussed in this chapter. As an overview to the electrical circuits involved in this work, the three main circuit elements associated with the ion trap array, a capacitor, a resistor and an inductor, are discussed. The capacitance of the trap arises from three main sources – the fringing field, the overlap capacitance between trap electrodes, and the capacitive coupling of the electrodes through the substrate. The overlap capacitance was minimized in the design (layout) phase by creating a free-suspended structure (as shown in Figure 6.2) which overlapped only at certain parts of the supports holding the electrodes. The capacitive coupling between electrodes via the substrate, discussed later in this chapter, was deconvolved from the overlap and fringe field components.

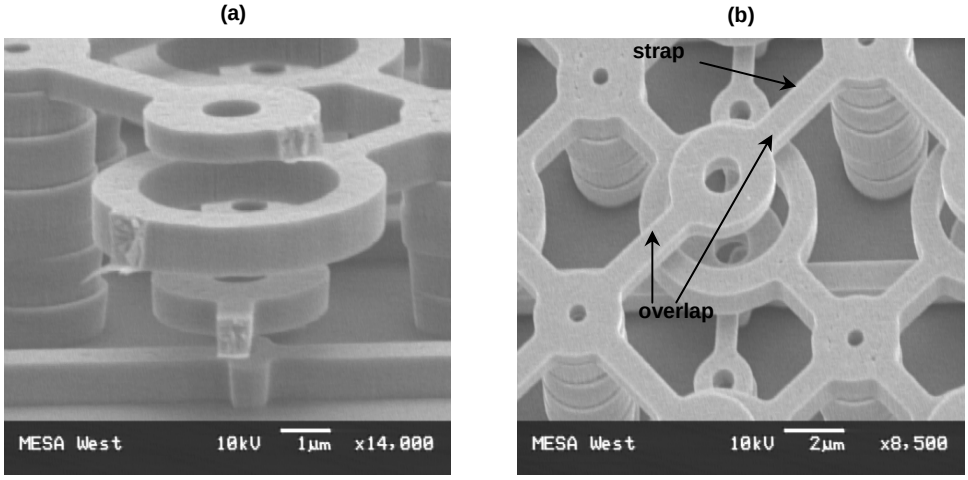

Figure 6.2. SEM images of the microfabricated overhung structures. As shown in (a) or (b) overlap occurs between the straps holding the end caps and part of the ring electrode structure.

The resistive component comes from electrical connections to the ion trap array and the resistance of the metals used in forming the ion traps, i.e., the tungsten. This resistance is determined by the metal properties and can only be altered through the geometry. The inductance is created through any length of metal used, i.e., the bus bar, the ground ring, and the connections to the package. The inter-relationship of these three elements determines the impedance of the overall ion trap structure. Figure 6.3 depicts the series and parallel equivalent RLC circuits. The elements can be all in parallel or all in series or a combination of the two.

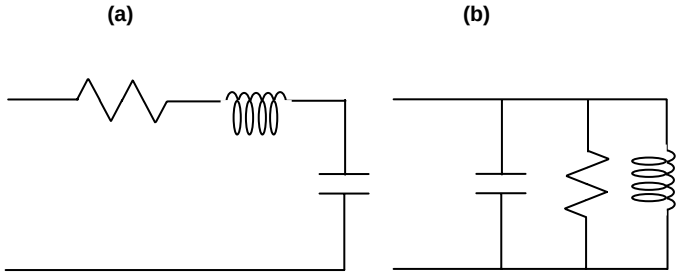

Figure 6.3. (a) A circuit schematic of a series R-L-C circuit. (b) A circuit schematic of parallel C-R-L circuit.

Note that the main goal in obtaining a match for this circuit is to deliver as much voltage to the ring electrode as possible in order to increase the ion trapping capacity in the ion traps. Thus, the objective is not to build a specific circuit with a specified impedance as is often the case in microwave circuits.

The impedance of a circuit is given by:

$$\overline{Z}_{load} = \overline{R}_{load} + j\overline{X}_{load} \tag{6.1}$$

where R_{load} is the real resistive part of the impedance and X_{load} is the imaginary portion of the impedance given by the inductive and capacitive reactance.

The amplitude and phase angle are given by:

$$\left|\overline{Z}_{load}\right| = \sqrt{R_{load}^2 + X_{load}^2} \tag{6.2}$$

$$\varphi_Z = \arctan\left(\frac{X_{load}}{R_{load}}\right) \tag{6.3}$$

The inductive reactance is proportional to the inductance and the capacitive reactance is inversely proportional to the capacitance. The reactance of the load, when the capacitance and inductance are in series, is given by:

$$X_{LOAD} = \left(\omega L - \frac{1}{\omega C}\right) \tag{6.4}$$

where ω is the angular frequency equal to $2\pi f$. The reactance is thus dependent on the frequency, $f = \omega/(2\pi)$. At the resonant frequency the capacitive and inductive reactance cancel each other and the total resistance is then real and equals the ohmic resistance. At this condition, the current (I) takes a maximum value for a given applied voltage. The resonant frequency is given by:

$$f_{res} = \frac{1}{2\pi\sqrt{LC}} \tag{6.5}$$

The time varying voltage is:

$$V(t) = RI(t) + L\frac{dI}{dt} + \frac{1}{C}\int_{-\infty}^{\infty} I(\tau)d\tau \tag{6.6}$$

its derivative is then:

$$\frac{1}{L}\frac{dV}{dt} = \frac{d^2I}{dt^2} + \frac{R}{L}\frac{dI}{dt} + \frac{1}{LC}I(t) \tag{6.7}$$

Equation (6.7) determines the voltage minima and maxima with respect to time or frequency. The traps should be operated at a voltage maximum in order to capitalize on getting the most voltage input to the ring electrode with the least amount of amplification.

6.3 Test Structures

Basic electrical characterization structures were designed and fabricated to gain a better understanding of the electrical characteristics of the ion trap array and to facilitate the formation of a matching network. Table 6-1 summarizes the different structures that were fabricated.

Table 6-1. Electrical characterization structures fabricated in each die. The S_{11} structures were fabricated for all die and array sizes. The S_{12} collector, S_{12} ring electrode, shorted and null structures were fabricated for certain die or array sizes as summarized in the table.

r_0 (μm)	Array Size (# of Traps)	S_{11}	S_{12} Collector	S_{12} Ring Electrode	Shorted	Null
1	Large (10^6)	✓				
	Medium (10^5)	✓	✓	✓	✓	✓
	Small (10^3)	✓	✓	✓	✓	✓
2	Large (10^5)	✓				
	Medium (10^4)	✓	✓	✓		
	Small (10^3)	✓	✓	✓	✓	✓
5	Large (10^5)	✓				
	Medium (10^4)	✓	✓	✓	✓	✓
	Small (10^2)	✓	✓	✓		
10	Large (10^4)	✓				
	Medium (10^3)	✓	✓	✓	✓	✓
	Small (10^2)	✓	✓	✓	✓	✓

The S_{11} structures were defined by a one port input without an output into the four different electrodes (two end caps, ring electrode, and collector); i.e., there was only one pad where an electrical input or an output was made. These were the structures used for the ion trapping experiments since each of the four electrodes can then be accessed individually. For example, the S_{12} collector structure had an input port to the collector structure as well as an output port, while the rest of the electrodes were shorted together within the array. Likewise, the S_{12} ring electrode structure had an input port to the ring electrode as well as an output port, and the rest of the electrodes were shorted together within the array. The shorted structure had four inputs into an array where all electrodes were shorted together. The null structure had inputs into a completely open structure, as there were no electrodes inside the array area, i.e., it was all free space. All inputs were made in a ground signal ground (GSG) configuration, as depicted in Figure 6.4.

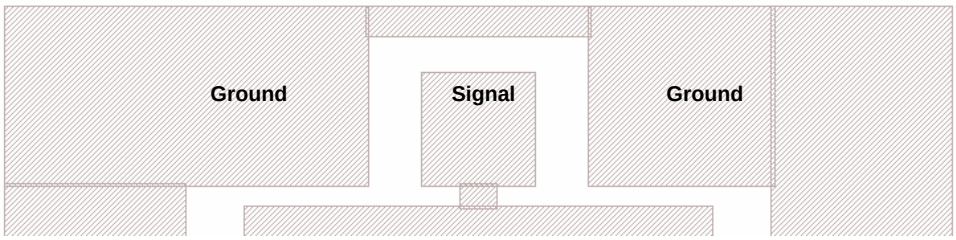

Figure 6.4. The mask layout of an electrical pad structure. A ground ring surrounds the electrical pad, where the signal is inputted, creating a ground signal ground input into the array.

The ground signal ground configuration acts as a waveguide which permits the wave to travel at a certain impedance. Although the GSG pads ideally would have a 50-Ω impedance for the frequency of interest, this was not the case for the trap arrays designed here.

6.4 Resistance Measurements

After the ion trap structures were released, they were tested for shorts and opens between electrodes. An HP3478A digital multimeter was used in conjunction with a Cascade Microtech probe station to make the measurements. The multimeter indicates an open at resistance values greater than 30 MΩ. However, measured opens for the trap arrays were approximately 7 GΩ to 1 TΩ, based on the measured leakage currents from 0 to 10 V. Shorts between electrodes varied from 100 Ω to 30 MΩ, however, the majority (>90%) occurred between the ring electrode and the top end cap, with various causes. For example, particulates represent a cause of shorted structures, as shown in the microscope image in Figure 6.5. Appendix H summarizes some of the measurements.

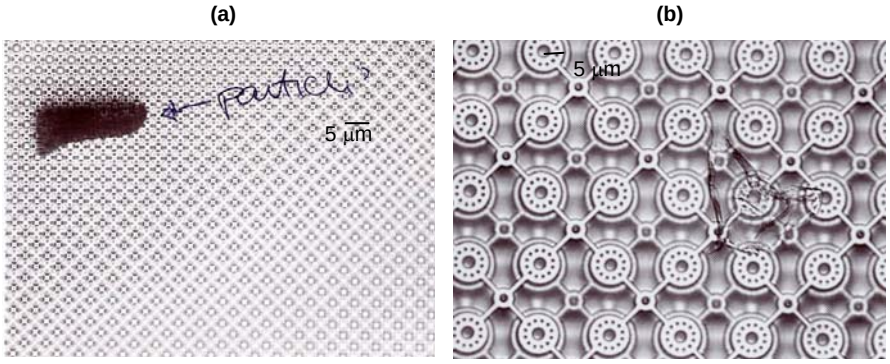

Figure 6.5. Micrsoscope images showing the top views of microfabricated cylindrical ion trap arrays with particles which presumably were the main cause of shorts between layers. The images were taken at 100× magnification for (a) r_0=1 μm. (b) r_0=5 μm.

6.5 Capacitance and Conductance Measurements

The capacitance and conductance of the cylindrical ion trap arrays were measured using an HP4284 LCR meter in the C_p-G_p mode at a 100 mV level. Figure 6.6 shows the circuit schematic for the measurement. Samples were placed on a 1/8" thick Teflon stage for the measurement. It is important to note that when the samples were placed on a gold (conductive) stage, significantly different conductance values were measured. For example for a r_0=1μm large sized ion trap array, the conductance at 100 KHz was 9 micro-Siemens (μS) when measured on the Au stage, but only 2 μS when measured on the Teflon stage. This indicates that although silicon has a relatively high resistance compared to tungsten, it still acted as a conductor and the electrodes were capacitively coupled through the substrate, even though the traps resided on a dielectric stack (SiN and SiO_2). Some of the measurements are summarized in Appendix I. The capacitance and conductance at 10 KHz and 100 KHz between either the top or bottom end cap and the ring electrode were measured from the S_{11} structure. The capacitance between all electrodes, top end cap, bottom end cap, the collector, and the ring electrode was measured using the S_{12} structure.

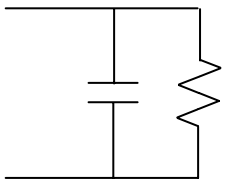

Figure 6.6. An equivalent circuit for capacitance measurement using the C_p-G_p mode. Te capacitance and resistance were assumed to be in parallel.

Table 6-2 summarizes the capacitance and conductance of the S_{12} structures as measured by the LCR meter. The 10-μm sized ion traps were not tested because they were not successfully released, as mentioned in Chapter 6.

Table 6-2. Measured capacitance and conductance values for different sized ion trap arrays for each given radius. The conductance was measured at 10 and 100 KHz, using an HP 4284 LCR meter.

r_0 (μm)	Array Size (# of Traps)	Capacitance (pF)	Conductance – 10 KHz (μS)	Conductance – 100 KHz (μS)
	1073290	587.00	0.050	3.500
1	217156	122.00	0.007	0.300
	7396	4.40	0.000	0.002
	331776	400.00	1.060	2.000
2	66564	72.00	0.005	0.130
	2304	3.02	0.000	0.005
	104976	250.00	0.150	2.000
5	20736	50.00	0.002	0.150
	784	2.60	0.000	0.001

6.6 Decoupling of Capacitance Values

The three main contributors to the capacitance (the overlap capacitance, the fringing field capacitance, and the capacitance coupled through the substrate) in the ion trap array structures were assessed, using three different sized ion trap arrays for a given r_0 with either air or silicon dioxide as the dielectric. Table 6-3 summarizes the capacitance measurements for the r_0=1μm ion traps.

Table 6-3. Capacitance measurements for released (air as dielectric) and unreleased (SiO_2 as dielectric) r_0=1 μm arrays.

# of Traps	C (pF) (Released)	C (pF) (Unreleased)	C (pF)/Trap (Released)	C (pF)/Trap (Unreleased)
1073290	587.0	1682.0	0.000547	0.001567
217156	122.0	356.0	0.000562	0.001639
7396	4.4	12.5	0.000595	0.001690

The capacitance coupled through the substrate was determined as the unaccounted capacitance when comparing the capacitance from the released and unreleased structures. If all capacitance was due to the overlap capacitance and the fringing field capacitance, the capacitance from the unreleased structure would be approximately 4 times that the released structure, signifying the difference in the dielectric constants of SiO_2 and air. However, if this was not true, the difference can be accounted for by the capacitance coupled through the substrate. From Table 6-3, the average capacitance per trap of the released structures was calculated to be $5.68\times10^{-4} \pm 0.24\times10^{-8}$ pF and the average capacitance per trap of the unreleased structures to be $1.63\times10^{-3} \pm 0.62\times10^{-8}$ pF. If the capacitance per trap coupled through the substrate (in pF) is *x*, it can be calculated by equating $4\cdot(0.000568 - x)$ and $1\cdot(0.001632 - x)$ to

be 2.13×10^{-4} pF. Thus, the capacitance coupled through the substrate accounts for approximately 37.5% of the total capacitance from the unreleased structure. Table 6-4 and Table 6-5 summarize the measured capacitance from the r_0=2 μm and r_0=5 μm arrays. By using the method outlined above it was determined that 33% of the capacitance in the unreleased r_0=2 μm arrays is due to capacitive coupling of electrodes through the substrate. Similarly, 30% of the capacitance in the r_0=5 μm unreleased arrays is due to capacitive coupling of electrodes through the substrate.

Table 6-4. Capacitance measurements for released (air as dielectric) and unreleased (SiO_2 as dielectric) r_0 = 2 μm arrays.

# of Traps	C (pF) (Released)	C (pF) (Unreleased)	C (pF)/Trap (Released)	C (pF)/Trap (Unreleased)
331776	400.00	1259.0	0.001206	0.003795
66564	72.00	225.0	0.001082	0.003380
2304	3.02	8.4	0.001311	0.003646

Table 6-5. Capacitance measurements for released (air as dielectric) and unreleased (SiO_2 as dielectric) r_0=5 μm arrays.

# of Traps	C (pF) (Released)	C (pF) (Unreleased)	C (pF)/Trap (Released)	C (pF)/Trap (Unreleased)
20736	51.47	161.00	0.002482	0.007764
784	2.60	6.93	0.003316	0.008839

To further confirm if these measurements and calculations yielded accurate results, capacitance measurements of the r_0=1 μm arrays fabricated in the 2 μm array lot were made. Again, these are taller structures as previously discussed in Chapter 6 but with the same anchor and bus bar areas as the regular r_0=1 μm arrays. These measurements are summarized in Table 6-6. Similarly, measurements of the r_0=2 μm array fabricated in the 1μm array lot were made, i.e., shorter structures but with the same anchor and bus bar areas as the regular r_0=2 μm arrays. The substrate coupling capacitance values per trap for the 1 μm arrays fabricated in the 2 μm lot to be ~ 0.000169 pF and for the 2 μm arrays fabricated in the 1 μm lot to be ~ 0.000449 pF. These measurements are consistent with the substrate coupling capacitance per trap of 0.000213 pF and 0.000398 pF for the real 1 μm and 2 μm ion traps, respectively. These results are summarized in Table 6-7.

Table 6-6. Capacitance measurements for released (air as dielectric) and unreleased (SiO_2 as dielectric) r_0=1 μm arrays fabricated in the r_0 = 2μm array lot. These are taller structures than those made in the 1 μm array lot, but with the same anchor area.

# of Traps	C (pF) (Released)	C (pF) (Unreleased)	C (pF)/Trap R(eleased)	C (pF)/Trap (Unreleased)
1073290	650.00	2330.00	0.000606	0.002171
217156	136.56	421.00	0.000629	0.001939
7396	4.52	14.86	0.000611	0.002009

Table 6-7. Capacitance measurements for released (air as dielectric) and unreleased (SiO_2 as dielectric) r_0=2 μm arrays fabricated in the r_0 = 1μm array lot. These are shorter structures than those made in the 2 μm array lot, but with the same anchor area.

# of Traps	C (pF) (Released)	C (pF) (Unreleased)	C (pF)/Trap (Released)	C (pF)/Trap (Unreleased)
331776	420.03	1153.00	0.001266	0.003475
66564	66.17	195.00	0.000994	0.002930
2304	2.77	7.28	0.001202	0.003160

6.7 Vector Network Analyzer (VNA) Inductance Measurements

The real and the imaginary parts of the S_{11} parameters were measured using an HP 8510C and a Wiltron 360b vector network analyzer (VNA), from 45 MHz to 5.045 GHz. The analyzers were first warmed up for approximately 30 minutes and then calibrated with open, shorted and 50-Ω load structures. Figure 6.7 shows the real and imaginary S_{11} parameters from the three test structures.

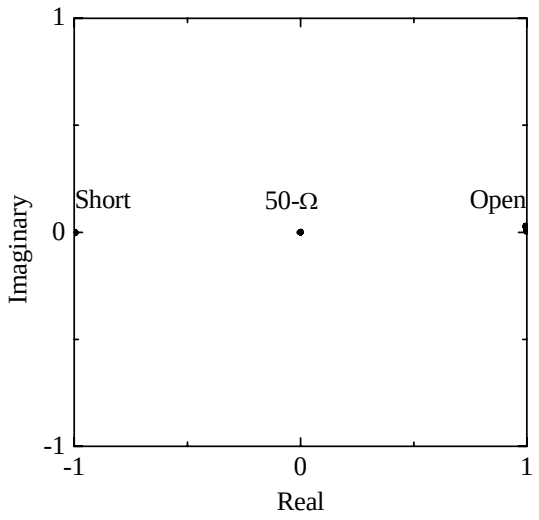

Figure 6.7. The S_{11} imaginary and real parameters measured from an open, a shorted and a 50-Ω load structure for calibrating the vector network analyzers.

The S_{11} parameter is given by:

$$S_{11} = \frac{Z_{in} - Z_{VNA}}{Z_{in} + Z_{VNA}} \tag{6.8}$$

where Z_{in} is the input impedance (R+jX), and Z_{VNA} is the impedance of the network analyzer, typically 50 Ω. Open structures had infinite resistance and the real portion of the S_{11} parameter was 1, as the imaginary portion vanishes with no reactive components. With a short, the resistance approached 0 and therefore the real part of the S_{11} parameter became -1. The 50-Ω load equaled the impedance of the analyzer and therefore the real part of the S_{11} parameter vanished. Thus the S_{11} parameters are very useful in providing an adequate circuit model of the microfabricated ion trap arrays. Equation (6.8) can be rearranged to solve for the real and imaginary parts of the input impedance.

$$Z_{in} = Z_{VNA}\left(\frac{1+S_{11}}{1-S_{11}}\right) \tag{6.9}$$

$$Z_{in} = Z_{VNA}\left(\frac{1+R+jX}{1-R-jX}\right) \tag{6.10}$$

$$Z_{in} = Z_{VNA}\left(\frac{1+R+jX}{1-R-jX}\right)\left(\frac{1-R+jX}{1-R+jX}\right) \tag{6.11}$$

$$Z_{in} = Z_{VNA}\left(\frac{1-R^2-X^2+2jX}{(1-R)^2+X^2}\right) \tag{6.12}$$

$$Z_{in}(\mathrm{Re}) = Z_{VNA}\left(\frac{1-R^2-X^2}{(1-R)^2+X^2}\right) \tag{6.13}$$

$$Z_{in}(\mathrm{Im}) = Z_{VNA}\left(\frac{2X}{(1-R)^2+X^2}\right) \tag{6.14}$$

Thus Equation (6.13) and (6.14) can be used to solve for the resistance and reactance of the ion trap structures. If a series resistance, inductance and capacitance (R-L-C) circuit is assumed for the ion trap arrays, as depicted in Figure 6.3 (a), its reactance, X, is given by:

$$X = X_L - X_C = \omega L - \frac{1}{\omega C} \tag{6.15}$$

The series R-L-C model was assumed to fit the ohmic resistance and reactance to the measured values. The fitted parameters were matched using the sum of the difference of squares method to within 0.001 in the range of 45-545 MHz. If 0.001 could not be reached, 0.01 was used instead. The solver program in Microsoft Excel was used in order to solve these three parameters simultaneously. The tolerance was thus given by:

$$Tolerance = \sum_{f=45MHz}^{545MHz} \left(\begin{array}{l} (S_{11}(real)_{fit} - S_{11}(real)_{measured})^2 + \\ (S_{11}(imaginary)_{fit} - S_{11}(imaginary)_{measured})^2 \end{array} \right) \tag{6.16}$$

Figure 6.8 shows the fitted and measured S_{11} parameters for an r_0=1 μm medium sized array (217156 traps). The fit was good up to 545 MHz and then began to deviate. The deviation was likely due to the capacitively coupling of electrodes through the substrate. At higher frequencies, the capacitor began to behave like a short and the resistance of the substrate must be taken into account. However, the R-L-C model was adequate up to 545 MHz.

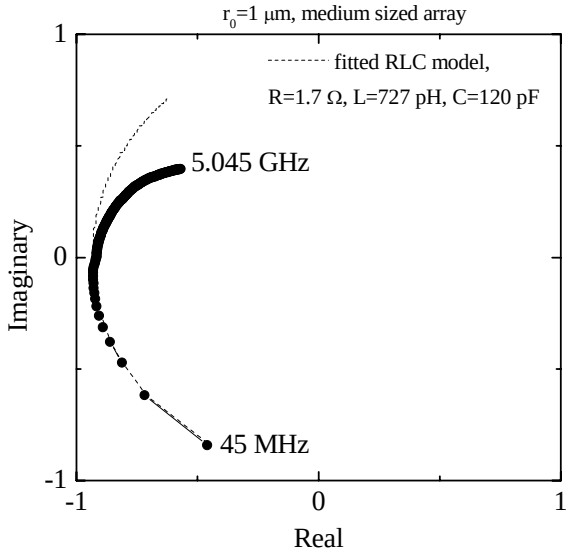

Figure 6.8. The measured S_{11} parameters (symbol) and fitted series R-L-C model for an r_0=1 μm medium sized array. Measurements were taken using an HP 8510C VNA. The fit was good from 45 MHz to 545 MHz and then began to deviate. The fitted parameters were: R=1.7 Ω, L=727 pH and C=120 pF.

Measurements of the r_0 = 1μm large sized array (1073290 traps) were made and the measured and fitted data are depicted in Figure 6.9. The capacitance and inductance were a little over twice as high, when compared to the medium sized array. The effect of the high capacitance was clear, since the capacitor behaved more like a short at lower frequencies, i.e., the imaginary portion of the S_{11} parameters approached 0.

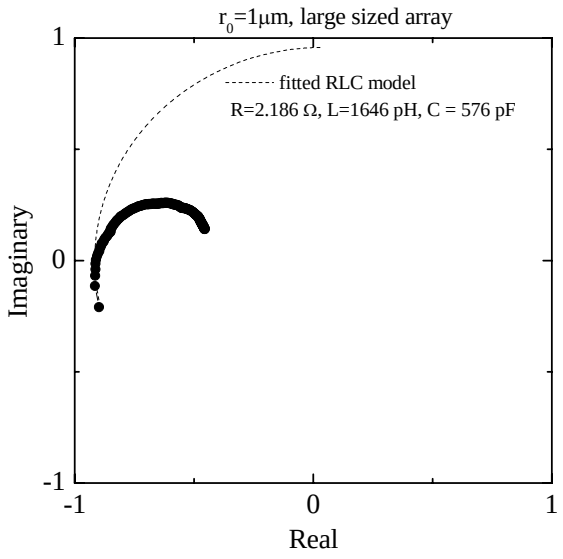

Figure 6.9. The measured S_{11} parameters (symbol) and fitted series R-L-C model for an r_0=1 μm large sized array. Measurements were taken using an HP 8510C VNA. The fit was good from 45 MHz to 545 MHz and then began to deviate. The fitted parameters were: R = 2.186 Ω, L=1646 pH, and C=576 pF.

Table 6-8 summarizes the fitted parameters for the various r_0 values and different array sizes. The tolerance value is also noted to demonstrate the adequacy of the fit.

Table 6-8. The fitted series R-L-C parameters from vector network analyzer data.

r_0 (μm)	Array Size	R (Ω)	L (pH)	C (pF)	Tolerance
1	1073290	2.18	1646.00	576.00	3.17×10^{-2}
	217156	1.74	712.22	120.87	1.29×10^{-3}
	7396	8.99	9.99	4.92	3.00×10^{-3}
2	331776	1.57	1190.00	399.98	1.39×10^{-2}
	66564	1.48	596.8.00	73.76	5.52×10^{-4}
	2304	33.70	9.97	3.44	2.98×10^{-2}
5	20 736	7.06	554.00	51.60	2.80×10^{-3}
	784	16.50	99.99	2.83	3.00×10^{-3}

The inductive effects of the bus bar were measured through one of the medium sized shorted structures. The measured and fitted parameters are shown in Figure 6.10. It is clear that the structure behaved like a short at lower frequencies. Since the structures were shorted, the capacitance had a zero value and the reactance was positive, as seen from Equation (6.8). The bus bars contributed about 500 pH.

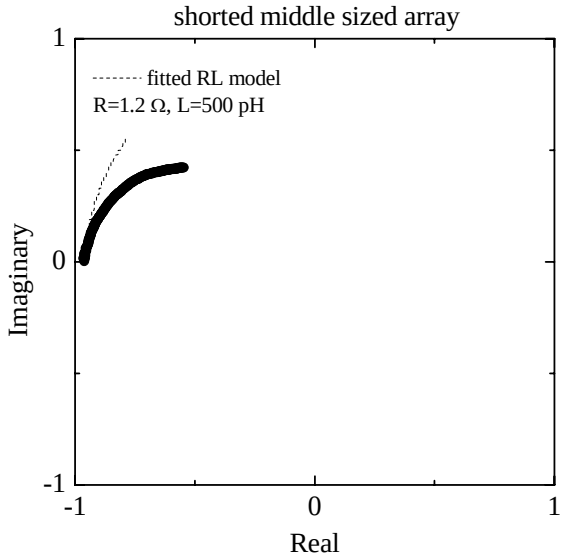

Figure 6.10. S_{11} real and imaginary parameters for a r_0=2μm shorted medium sized array. In this case there was no capacitance, and the fitted RL model yielded values of R=1.2 Ω, L=500 pH.

The contribution to the inductance of the bus bars were further assessed by taking measurements of the r_0=2 μm medium sized S_{11} and S_{12} arrays. In the measurement of the S_{11} structure, all electrodes were shorted to ground through wirebonds, except for the ring electrode. In the measurements of the S_{12} structures two tests were performed, one in which the electrodes were shorted through one pad (the top end cap (TEC) pad) and in the other the structure was shorted through two pads, the TEC and bottom end cap (BEC) pads. Figure 6.11 depicts the real and imaginary parts of the S_{11} parameters measured from the r_0=2 μm medium sized array. Small differences were observed when the TEC and BEC were shorted to ground versus when all of the electrodes were shorted to ground. The S_{12} structure in which only the TEC structure was shorted to ground showed a significant difference in the response. This is reflected in the fitted parameters, where there was not a noticeable difference in the resistance and capacitance, but a substantial difference in the inductance. Table 6-9 summarizes the fitted R-L-C parameters. Based on these measurements it was determined that the best method to decrease the inductance is to short the TEC and BEC to the ground ring at die level. Otherwise the inductive path for the reflection of the RF increases.

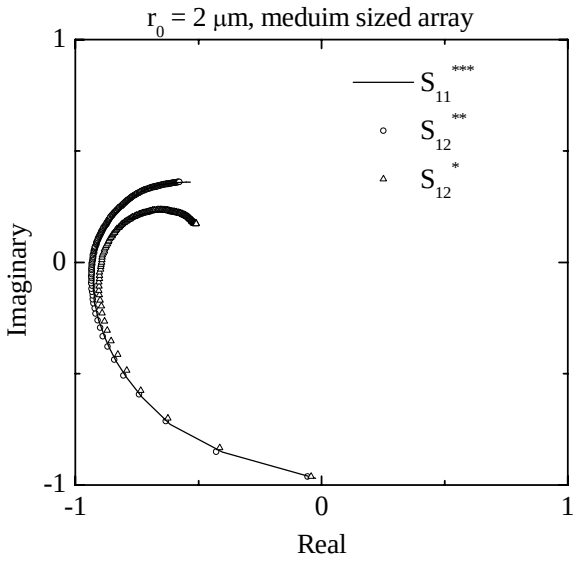

Figure 6.11. The measured S_{11} real and imaginary parameters for the r_0=2 μm, medium sized array (66564 traps). The structures measured were bonded differently to assess the inductive contributions from the electrodes shorting to ground. (Note: S_{11}^{***} represents 3 wirebonds shorting to ground, S_{12}^{**} represents 2 shorting to ground - all structures but ring shorted to each other, while the S_{12} structure* involves 1 wirebond shorting to ground - all structures but ring shorted to each other.)

Table 6-9. Fitted R-L-C parameters for r_0=2μm medium sized array structures. The structures were bonded differently in order to determine the inductance of bus bars in the arrays. Fits were made from 45-545 MHz.

Structure	R (Ω)	L (pH)	C (pF)	Tolerance
S_{11}^{***}, all levels grounded through wire bonds	1.62	616.3	71.72	9.99×10^{-4}
S_{12}^{**}, levels grounded through two pads via wire bonds	1.48	596.8	73.76	5.52×10^{-4}
S_{12}^{*}, levels grounded through 1 pad via a wire bond	2.28	1024.6	73.08	1.69×10^{-3}

The r_0=5μm sized traps and the packaged traps were measured using a Wiltron 360B vector network analyzer. Measurements were taken from 40 MHz to 4.040 GHz and the values were fitted using the sum of the difference of squares method. Figure 6.12 shows the measured and fitted values for the r_0=5 μm medium sized array. The capacitance and inductance fit well to the model, however, the resistance was relatively high. The higher resistance was attributed to either the oxidation on the surface of the aluminum pads or not having good electrical contacts between the pads and probes.

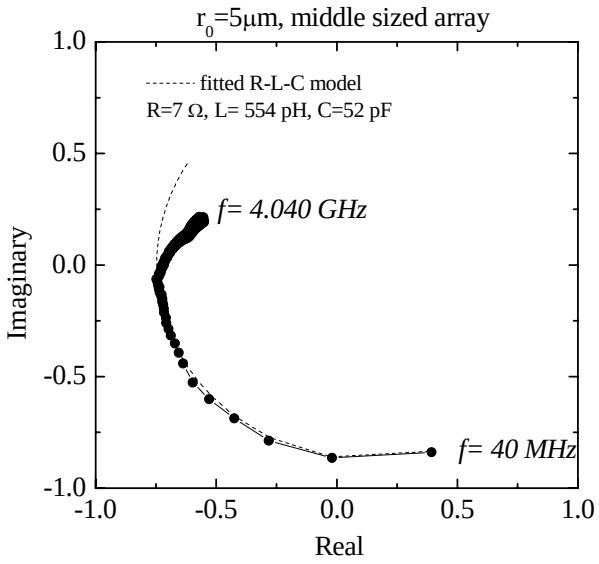

Figure 6.12. The measured S11 parameters and fitted series R-L-C model for an r_0 = 5 μm medium sized array, using a Wiltron 360B VNA. The fit was good from 40 MHz to 540 MHz and then began to deviate. The fitted parameters were: R = 7 Ω, L= 554 pH, and C = 52 pF.

VNA measurements were also performed on packaged parts in order to assess the wirebond and package lead inductances. A Stratedge glass package (G3333M-1) was used for the packaging of the trap arrays. Figure 6.13 shows the differences in the measured S_{11} parameters between the die level tests and the packaged level tests. The first set of data shows the packaged part, where the TEC, BEC and collector (COLL) were shorted to ground through the package leads. The second set of data shows the packaged part where the TEC, BEC, and COLL were shorted to ground through their respective pads to the ground ring. The third set of data shows the unpackaged part, the die level test, where the TEC, BEC and COLL are shorted to ground through their respective pads to the ground ring.

Differences in the inductance between all measurements and differences in the resistance between the unpackaged and packaged parts were observed. The capacitance remained the same, as shown by the first data points at 40 MHz. Table 6-10 summarizes the fitted parameters to the series R-L-C model for the r_0=2 μm and r_0=5 μm medium sized array packaged parts. For this data, the TEC, BEC and COLL were shorted to ground through the package leads. The 5-μm tall parts were also measured, and a slight decrease in the overall capacitance of the structures, ~5 pF, was seen. The resistance and inductance remained nearly the same.

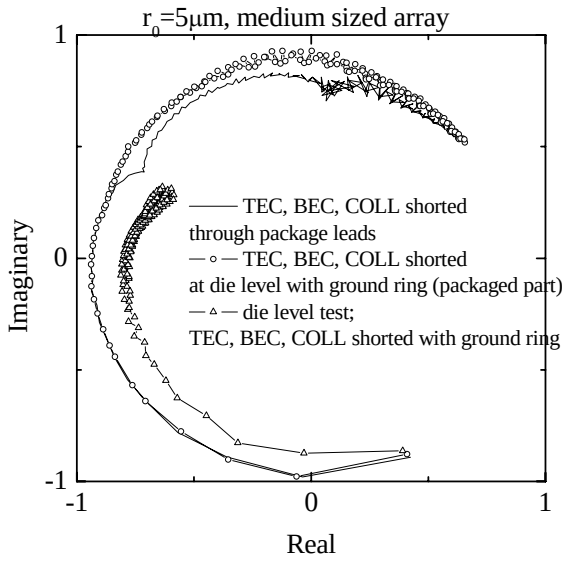

Figure 6.13. The measured S_{11} parameters of the r_0=5 μm medium sized array. The measurements were made using a Wiltron 360B VNA. The first set of data shows the packaged part, where the TEC, BEC and COLL were shorted to ground through the package leads. The second set of data shows the packaged part where the TEC, BEC, and COLL were shorted to ground through their respective pads to the ground ring. The third set of data shows the unpackaged part, the die level test, where the TEC, BEC and COLL were shorted to ground through their respective pads to the ground ring.

Table 6-10. Fitted series R-L-C parameters for the r_0 = 2 μm and 5 μm packaged parts. Measurements were made with a Wiltron 360B VNA and the S_{11} parameters were measured with an input into the ring electrode; the TEC, BEC, and COLL were shorted to ground via the package leads.

r_0 (μm)	Array Size	R (Ω)	L (pH)	C (pF)	Tolerance
2	66 564	6.76	3303	70.0	1.750
5	20 736	1.77	4386	49.6	0.006
5 (tall)	20 736	2.18	4779	44.0	0.009

Table 6-11 shows the fitted parameters for the series R-L-C model for the r_0=2 μm and r_0=5 μm medium sized array as packaged parts. In this case, however, the TEC, BEC and COLL were shorted to ground via their respective pads to the ground ring at the die level. Comparing this set of results to the previous measurements, the inductance was decreased by about 1000-2000 pH, due to the inductive contribution of the package leads.

Table 6-11. Fitted series R-L-C parameters for the r_0 = 2 μm and 5 μm packaged parts. Measurements were made with a Wiltron 360B VNA and the S_{11} parameters were measured with an input into the ring electrode; the TEC, BEC, and COLL were shorted to ground via their respective pads to the ground ring at the die level.

r_0 (μm)	Array Size	R (Ω)	L (pH)	C (pF)	Tolerance
2	66564	5.16	2251	70	1.90×10^{0}
5	20736	2.21	2096	50	3.77×10^{-1}
5 (tall)	20736	1.60	3707	45	6.60×10^{-3}

As shown by the fitted inductance values, the wirebonds added approximately 3000 pH of inductance to the circuit. In order to assess the inductance of the wirebond, VNA measurements were performed on packages with different wire bond lengths connecting to ground. In this fashion, the inductance per unit wirebond length could be determined. Table 6-12 summarizes the fitted RL parameters. The wirebonds added approximately 3300 pH of inductance per millimeter of length.

Table 6-12. Fitted R-L parameters for different lengths of wirebond. Measurements were made using a Wiltron 360B VNA.

Wire Bond Length (mm)	R (Ω)	L (pH)	L/Length (pH/mm)	Tolerance
1.00	0.7	3362	3362	1.70×10^{-3}
1.25	0.8	4132	3305	1.99×10^{-3}
1.50	0.9	4699	3132	2.00×10^{-3}

6.8 Matching Circuit

To maximize the voltage delivered to the ion trap array, where to set up the matching circuit must be determined. As previous analyses showed, inductance was added to the overall circuits from the leads of the RF-package housing the ion-trap array and the ribbon bonds used to make connections to the ion-trap array from the package. If the matching circuit was set up outside of the package, it is likely that not enough voltage could be delivered into the ion trap array.

A matching circuit was not used to try to match the impedance of the structure. Instead, it was attempted to operate the traps at a resonant frequency where a voltage maximum was obtained. In this case Q values were about 8. The Q value is a representation of the amplification of the power delivered to the trap structure. High Q values represent a small band frequency matching, $\Delta f = f/Q$, and smaller Q values are more adequate for a broadband frequency matching, i.e., a larger range of frequencies can be matched. The Q value can be simply calculated by:

$$Q = \frac{X_C}{R_s} \qquad (6.17)$$

where X_C is the capacitive reactance and R_S is the series resistance. The capacitance values are summarized in Table 6-8 for a given r_0 value and an ion trap array size.

Although this method of matching is not ideal, especially since the line impedance and load impedance are so mismatched, it provided the most input voltage that could be acquired.

6.9 Electrical Characteristics Improvements

It is clear that the electrical characteristics of the ion trap arrays must be improved. Ideally the capacitance and the inductance of the arrays would be much lower than their current values; however a simple solution in the fabrication process which does not require new photomasks is to utilize high resistivity silicon substrates. The current silicon substrates have a resistivity of 2-20 Ω·cm, corresponding to a resistance of 30-300 Ω for the medium sized array. Because the resistance is so low the substrate acts as a voltage divider and must be considered part of the series R-L-C circuit. In this case, the series resistance is no longer 2 Ω, but 30-300 Ω.
In Figure 6.3 (a) the current is the same across all circuit components at any given time; however the voltage leads the current by a 90^o phase angle in the inductor and lags the current by 90^o in the capacitor. At any given moment the voltage differs in phase between these two components by 180^o, meaning that at each instant the voltage is opposite in sign. The voltage drop across each of the components can be determined if the root mean square current (I_{rms}) is calculated. The I_{rms} can be calculated from the following relationship:

$$I_{rms} = V_{source} \big/ Z \qquad (6.18)$$

The voltage across a circuit component is given by its reactance multiplied by the rms current. Equations (6.19) to (6.21) outline the voltage equations for the circuit components.

$$V_{resistor} = R \times I_{rms} \qquad (6.19)$$

$$V_{inductor} = X_L \times I_{rms} \qquad (6.20)$$

$$V_{capacitor} = X_C \times I_{rms} \qquad (6.21)$$

If high resistivity silicon (6-17kΩ·cm) is used, it will act as an insulator having a resistance of about 250 MΩ and there will no longer be a conductive path to ground through the silicon (Durr, Erben et al. 1998; Milanovic, Ozgur et al. 1998; Warns, Menzel et al. 1998). This will reduce the series resistance to be about 2 Ω. Figure 6.14 shows the rms current as a function of frequency for two different resistances, at 2 and 30 Ω, corresponding to a high and low resistivity silicon substrates.

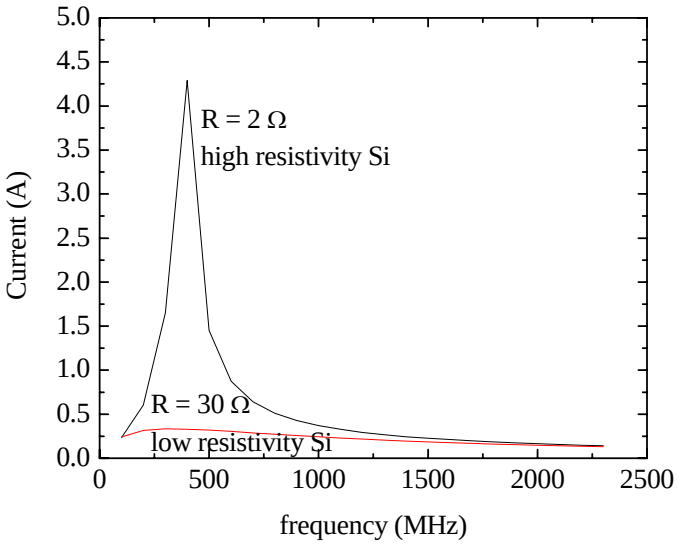

Figure 6.14. The calculated rms current as a function of frequency for an R-L-C circuit with a voltage source of 10V, L=4000 pH and C=50pF. The resistances were varied at 2 and 30 Ω, corresponding to the series resistances when high and low resistivity silicon is used as the substrate of the ion trap arrays.

From the rms current, it is apparent that the use of high resistivity silicon will provide a higher voltage drop to each of the trap components. More importantly is the RF voltage applied to the ring electrode. Figure 6.15 shows the voltage across the capacitor component of the circuit for high and low resisitivity silicon substrates. In this case, when operation is at the resonant frequency, RF peak voltages of 45 V can be obtained for a voltage source of 10 V.

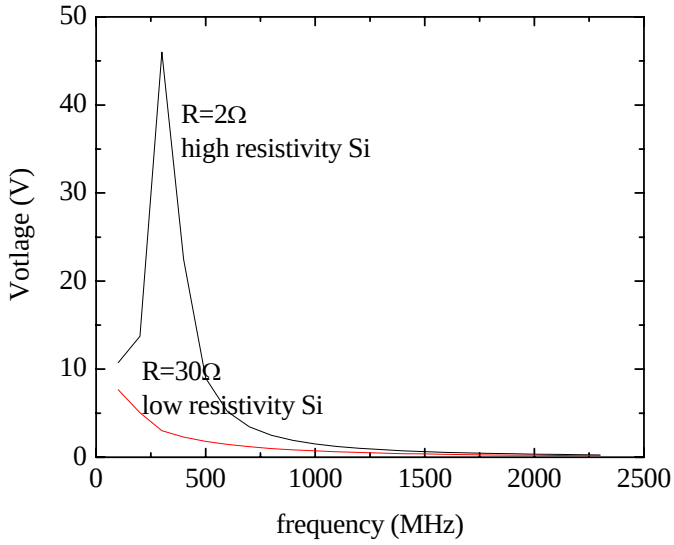

Figure 6.15. The calculated voltage across the ring electrode (capacitive component of the circuit) as a function of frequency for a series R-L-C- circuit with a voltage source of 10V, L=4000pH and C=50pF. The resistances were varied at 2 and 30 Ω, corresponding to the series resistances when high and low resistivity silicon substrates are used for the fabrication of the ion trap arrays.

6.10 Field Emission Properties

Examining the different properties of the microfabricated ion trap arrays is of great importance in order to understand and elucidate their mode of operation. In this section the field emission characteristics (FE) of microfabricated cylindrical-ion-trap arrays are discussed. Field emission refers to an induced current emission under reduced pressure conditions from low work function metals such as tungsten (work function ~ 4.5 eV) (Gomer 1961; Tondare, Pradeep et al. 2001) due to a high electrostatic field of 30-60 MV/cm. A field of this order can be attained with small voltages for very small gaps between metal electrodes, thus miniaturization of field emission devices has been a progressing field since microfabrication techniques have become more enabling. Conventional microfabricated FE devices consist of metal Spindt tips (Spindt, Brodie et al. 1976) (named after their inventor) or silicon tips. Figure 6.16 shows a schematic of a field emission device, in this case a conventional Spindt tip is made out of silicon with a work function 4.85 eV (Gomer 1961). There are three main components: the anode, the gate and the emitter. The gate defines the strength of the electric field based on the voltage applied to the gate and the spacing between the gate and the emitter, which is grounded. The gate is defined by deposition of a thin metal film. The emitter tip is self aligned with the gate so that the tip experiences the same field everywhere. This is important because if the field is not uniform field emission is not likely to be as efficient. The anode directs the path of the electrons by having a positive biased applied to it. The anode is also defined by a thin metal film.

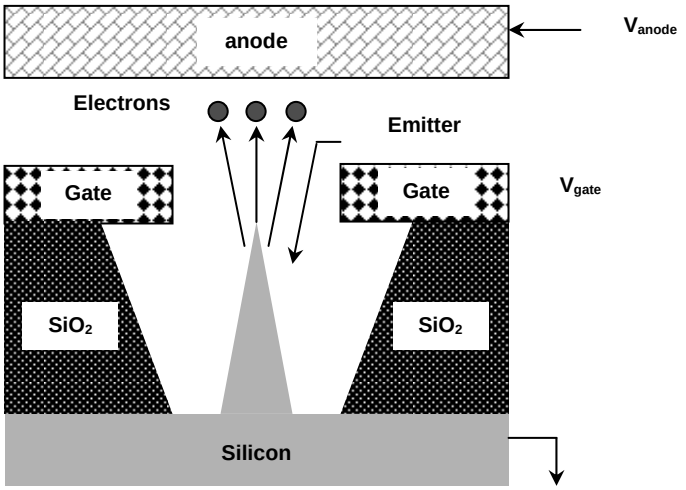

Figure 6.16. A schematic diagram of a silicon Spindt tip. The gate voltage forms the field to cause the tunneling of electrons from the tip and the anode voltage is used to guide the electrons from the emitters.

More recently carbon nanotubes (Fursey, Novikov et al. 2003) have been investigated for their field emission properties. However, most of these FE devices still require high anode voltages (~kV) and a high vacuum ambient (< 10^{-6} Torr). Lateral field emission devices (Milanovic, Doherty et al. 2001), as well comb shaped field emitters (Itoh, Tsuburaya et al. 1992), utilize small gaps, about 0.5 μm, to achieve very high electric fields. There is also work on FE structures which operate at atmospheric pressures (Driskill-Smith, Hasko et al. 1997).

These devices use the basic concepts of the Spindt tip to try and achieve smaller anode voltages and operation at higher pressures.

Figure 6.17 (a) shows a schematic of a single ion trap. The electrode gap for these structures is in the order of 0.5 μm. Because of the small gaps between tungsten layers and their sharp edges created by the microfabrication process, it was a concern that this structure would field emit electrons at common trap operating voltages, interfering with the normal operation of the ion trap. In the case of the ion trap, it is possible to envision that the ring electrode would act as the gate, creating the field between the ring electrode and either the bottom or top end cap. The end caps would then act as emitters. The opposite could also be envisioned, the case where the end caps act as gates and the ring electrode as a field emitter. Since the intended purpose of the structure is not as an emission device but as an ion trap, elucidation of its characteristics and operational mode as a field emission device can determine the limits of trap operating voltage. A secondary goal for this work is to understand if this electrode design might indeed have application as a field emission device since it is necessary to ionize neutrals inside the trapping volume. Figure 6.17 (b) shows the array structure and common anchor points which permit the operation of the ion traps in parallel. Further shown in Figure 6.17 (c) is a perspective cross-section view of the ion trap with inner radius of 1 μm. Figure 6.17 (d) shows the expected electron path for field emitted electrons, electron emission is from the bottom end cap to the ring electrode or vice versa.

6.10.1 Preparation of Devices

Good electrical contact between the pads and the electrical probes is necessary to ensure that the devices received the appropriate voltages and were grounded properly. Some of the devices tested in this work did not go through the entire fabrication process. For example, the device depicted in Figure 6.17 (d) was not completely formed, since the top end cap is missing. However, the ring electrode and bottom end cap are enough to test for field emission between those two electrodes. For those devices, a Ti/Au layer was evaporated on the tungsten metal pads prior to release to provide good electrical contact between the device and the testing probes. The metal layers were patterned via a liftoff process. These devices were released in an $HF:H_2O$ 1:1 solution without the Au pads lifting. Devices which were fully processed having a layer of TiN/Al as the electrical contact were also tested and are briefly discussed. These devices were released in a special HF buffered formula which does not attack the aluminum. Two different ion trap sizes (inner ring electrode radius, r_0 = 1 μm and 1.5 μm) and three different array sizes (10^4, 10^5 and 10^6) were fabricated and tested. Before testing the devices with applied voltages, the resistance between the various electrodes was measured to ensure that there were no electrical shorts. The surface leakage current was also monitored at 0.1 V; the corresponding resistances were approximately 10 TΩ in vacuum and 0.2 TΩ in atmosphere pressure.

After release, a standard solvent clean was performed. However, no special cleaning of the surfaces or bakes of the devices was performed. This is important to note, since the work function of tungsten is altered as gas species are absorbed onto the tungsten surface.

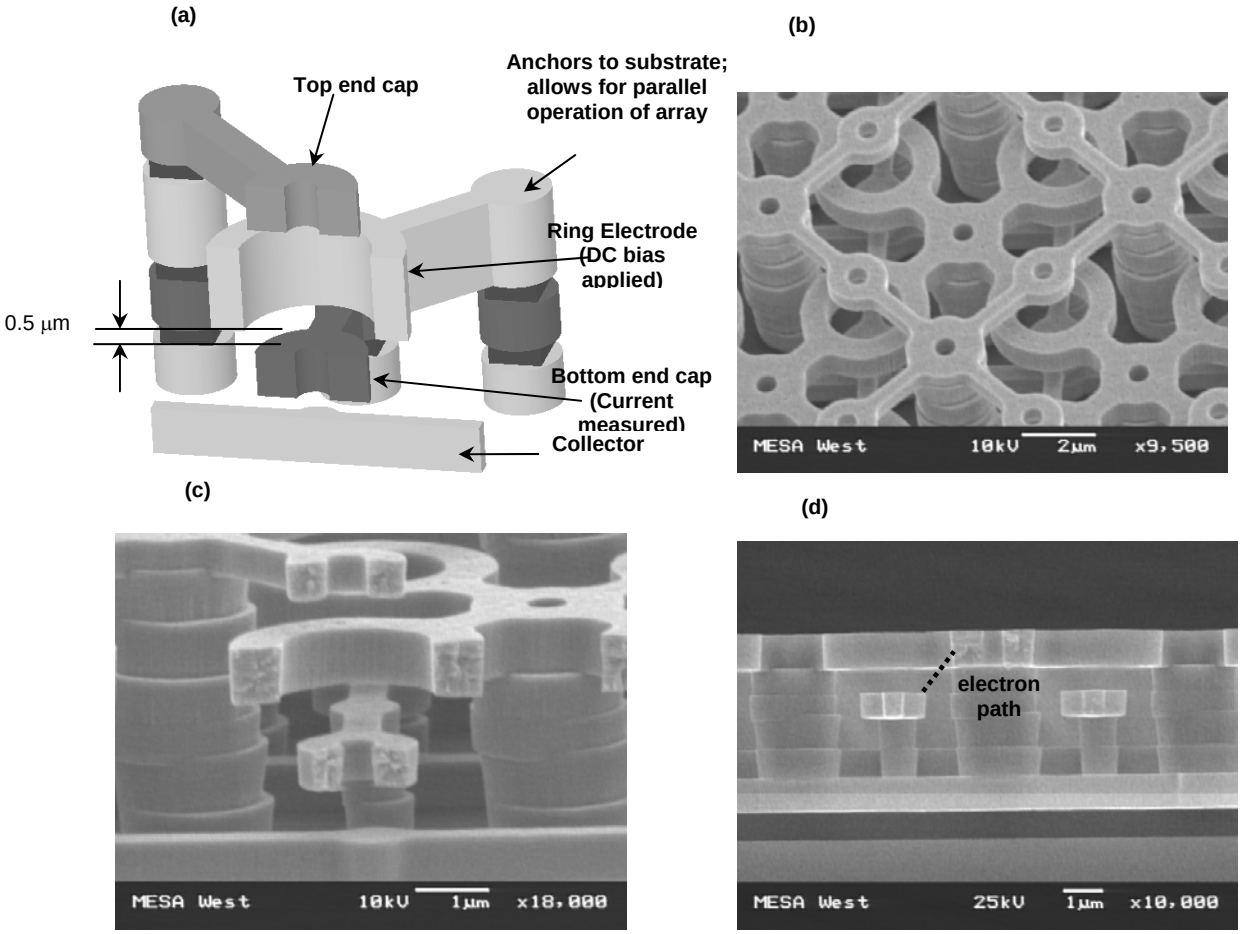

Figure 6.17. (a) A schematic illustration of a cylindrical ion trap with indications of the electrodes and anchors. The SEM micrographs of the cylindrical ion trap array: (b) top-down view of a two-dimensional array, (c) a cross-sectional perspective, and (d) a side view indicating the electron tunneling path from the bottom end cap to the ring electrode.

6.10.2 Application of Voltage

Voltage sweeps were applied to the ring electrode (RE) and the current was measured at the bottom end cap (BEC) using a Keithley 6487 picoammeter voltage source. The picoammeter was controlled using a Labview program from National Instruments. A schematic of the test set up is shown in Figure 6.18.

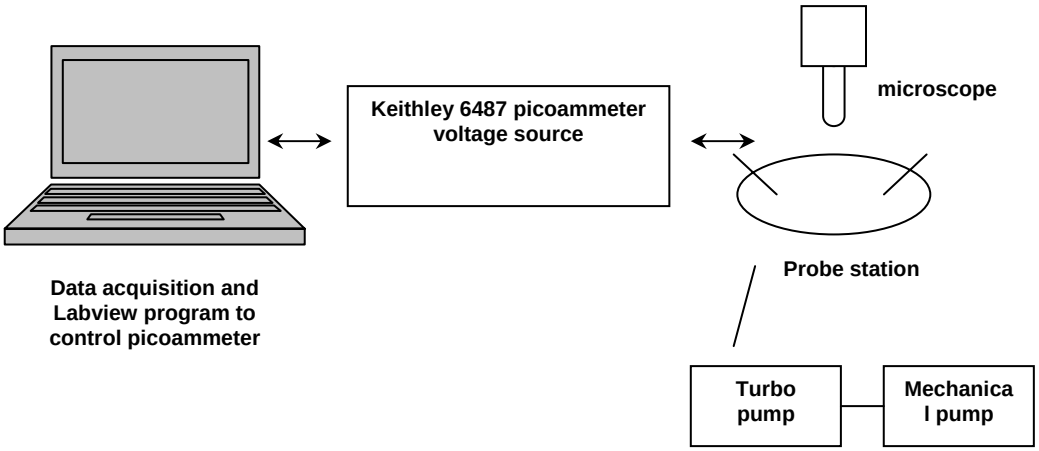

Figure 6.18. The test setup for the field emission measurements. A probe station was used to make the electrical contacts to the device. Vacuum tests were performed in a vacuum chamber. The vacuum was achieved with a mechanical pump and a turbomolecular pump.

A voltage sweep consisted of a voltage ramp from 0 to –500 V, then –500 V to 500 V, and finally from 500 V to –500 V at a ramp rate of 1V/step. Note that 500V corresponds to the highest attainable field, 10 MV/cm, which is the maximum voltage attained by the Keithley 6487. The voltage-ramp from 0 to –500 V prevented shock to the device and assured that the measured current was due to field emission, while the reverse sweep revealed any hysterisis or asymmetries. Approximately 12 such sweeps were performed on each device to confirm repeatability of the emission characteristic. These tests were performed in vacuum (10^{-5} Torr) and at atmospheric pressure (625 Torr). The vacuum tests were performed on a low temperature vacuum probe station from MMR Technologies, Inc and the atmospheric tests were performed on a Cascade Microtech DC probe station. Figure 6.19 shows the first three voltage sweeps performed on a device. Anomalies were observed in the first couple of sweeps, possibly due to adsorbed surface species or roughness of the tungsten. However, after sweep 3, sweeps were consistent and no increases or decreases of current are seen in Figure 6.19.

6.10.3 FE Results

The ion traps, $r_0 = 1.5$ μm in an array of 10^5, were tested as field emitters at atmospheric pressure. Voltage sweeps performed in atmosphere showed FE at an electrostatic field of ~ 3 MV/cm, corresponding to a turn-on voltage of 150 V for both the forward and reverse biases. The resulting I-V characteristic is shown in Figure 6.20 and an emission current of 60 nA was measured at 6 MV/cm. Almost identical I-V curves were observed in both forward and reverse biases, as expected for an edge field emitter, except for a slight asymmetry (as amplified in the Fowler-Nordheim graph in Figure 6.21) due to the differences in edge sharpness between the BEC edge and RE edge. The top edge of the BEC was polished using CMP while the bottom of the RE was created by molding tungsten in the bottom of an etched SiO_2 trench. Figure 6.21 shows the Fowler-Nordheim plot in the applied voltage range of 150-300 V.

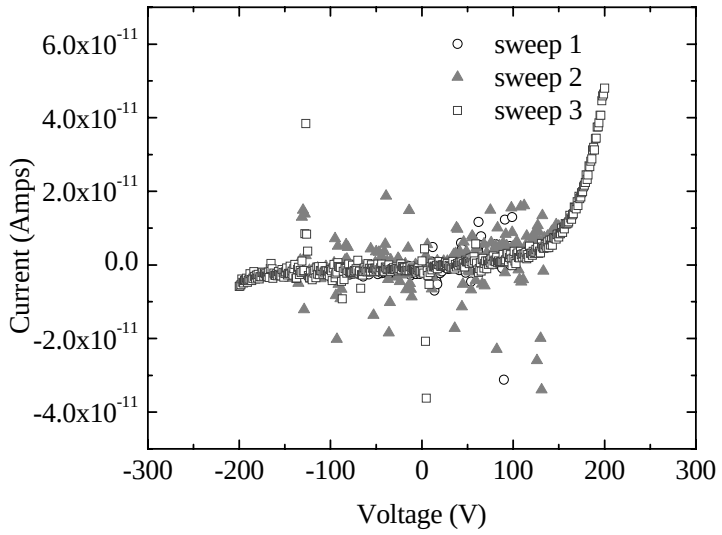

Figure 6.19. A series of three voltage sweeps for an r_0=1 μm ion trap in an array of 10^4. The first two sweeps showed some anomalies in the current measurements, but they decreased as the number of sweeps increased, as seen from the sweep number 3.

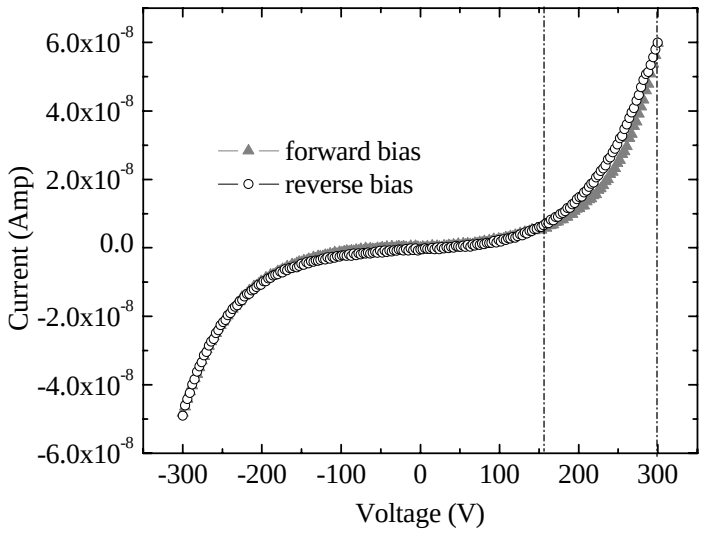

Figure 6.20. Current-voltage characteristics of ion traps of r_0=1.5 μm in a 10^5 array at atmospheric pressure. The forward and reverse bias sweeps are shown.

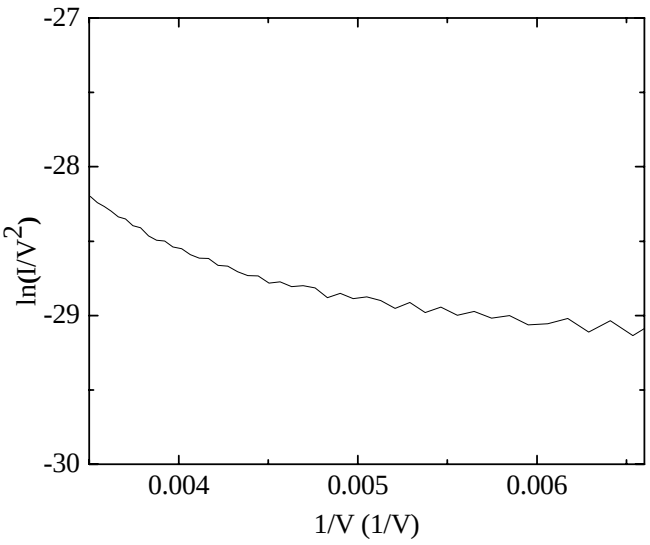

Figure 6.21. The Fowler-Nordheim plot for ion traps of r_0 = 1.5 μm in a 10^5 array at atmospheric pressure from 150-300 V.

The I-V response for the Fowler-Nordheim emission is (Spindt, Brodie et al. 1976; Yuasa, Shimoi et al. 2002):

$$\frac{I}{V^2} = a \cdot \exp\left(\frac{-b}{V}\right) \qquad (6.22)$$

Where

$$a = \frac{\alpha A \beta^2}{1.1\phi} \exp\left(\frac{B\left(1.44\times10^{-7}\right)}{\phi^{1/2}}\right),$$

$$b = 0.95B\phi^{3/2}/\beta,$$

α is the emitting area (m^2) and β is the local field conversion factor at the emitting surface, which can be expressed as the ratio of field enhancement to the cathode-anode distance, $A = 1.54\times10^{-6}$ and $B = 6.87\times10^{7}$ are dimensionless constants (Gomer 1961), and ϕ is the work function (eV). The F-N plot shows non-linear and linear characteristics in the range of 150-300V. The non-linear characteristics are due to a gas ionization contribution, initiating at 200V. The linear characteristics in the semi-log Fowler-Nordheim plot confirmed the FE process, and the intercept, ln a, and slope –b were determined to be –21.4 and –2951.8, respectively. This corresponds to an emitting area of 3.55×10^{-12} cm^2 and a β value of 21120, for an assumed work function of 4.5 eV, leading to a field enhancement value of about 0.11. Both the area and field enhancement value are lower than expected.

Figure 6.22 summarizes the field emission measurement at atmosphere under various conditions. The currents are shown as a function of field strengths and array sizes for the r_0 = 1μm device. A non-linear increase is observed in current as a function of the field strength, as expected from the F-N equation. A linear increase in current is expected with the addition of parallel portions of geometrically similar arrays. However, super-linear functions are seen at applied fields of 2 and 6 MV/cm as array sized is increased. This non-linearity at atmosphere suggests the presence of a gas ionization process.

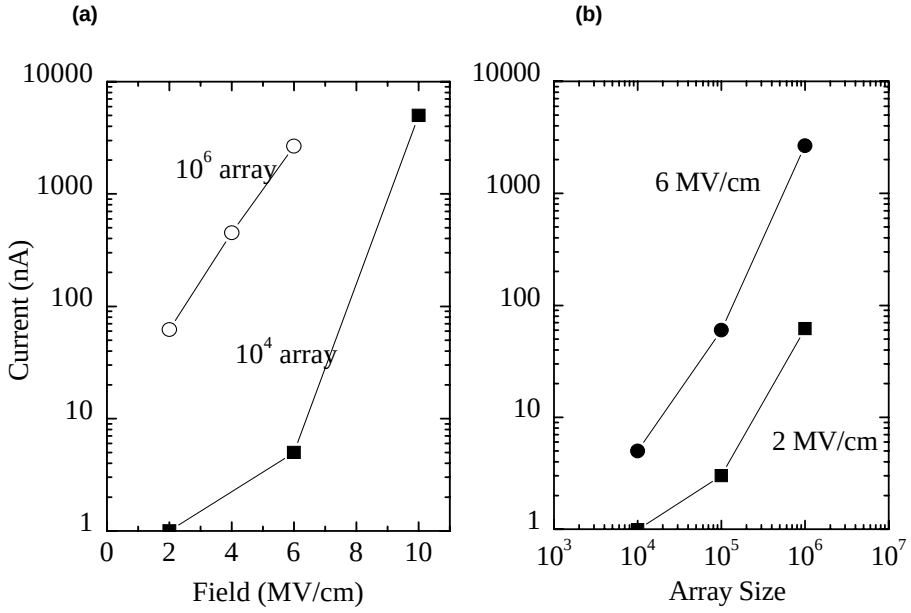

Figure 6.22. The dependence of emission current, at atmosphere, on (a) the field strengths and (b) the array sizes for the r_0=1.0 μm device.

To verify the presence of a gas ionization process at atmospheric pressure, devices of r0=1 μm in a 104 array were also tested in vacuum (10^{-5} Torr). Figure 6.23 shows the linear I-V characteristics, while Figure 6.24 shows the F-N plot in the applied voltage range of 175-250 V. The intercept, ln a, and slope –b were determined to be –23.84 and –2409, respectively. This corresponds to an emitting area of 0.2×10^{-12} cm^2 and a field enhancement value of 0.13. Vacuum testing confirms field emission characteristics; however, the results yield an emitting area which is an order of magnitude smaller than that in atmospheric pressure. Moreover, the attained currents of 0.3 nA were much smaller than those obtained in atmosphere. The turn-on voltages in forward and reverse biases were larger than those at atmospheric pressure by about 17%.

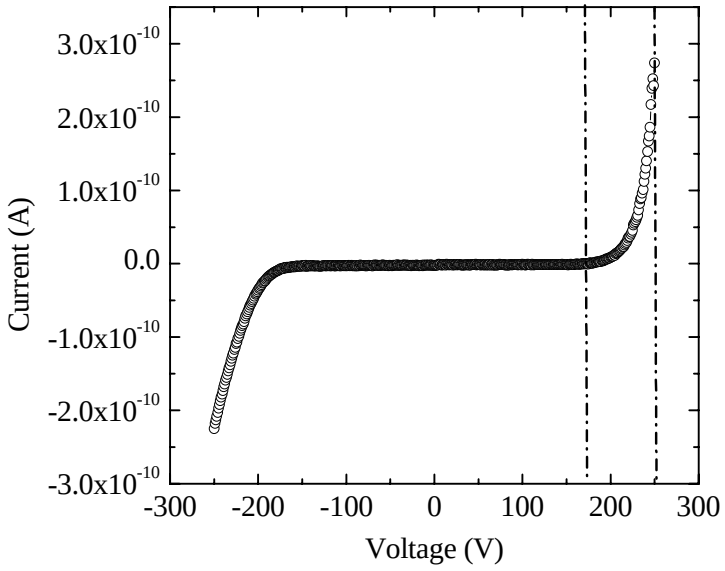

Figure 6.23. Current-voltage characteristics of ion traps of r_0 = 1 μm in a 10^4 array at a vacuum pressure of 10^{-5} Torr.

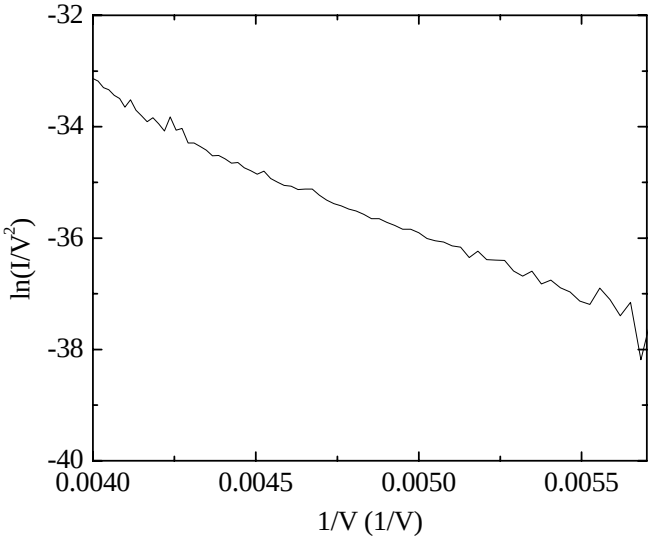

Figure 6.24. The Fowler-Nordheim plot for ion traps of r_0 = 1 μm in a 10^4 array at a vacuum pressure of 10^{-5} Torr in the range of 175-250 V.

The observed difference in emitting area, currents and turn-on voltages between atmospheric and vacuum conditions suggests a gas ionization contribution at atmospheric pressure. The observed emitting area is smaller than expected in both atmospheric and vacuum pressure tests. If the edge of the electrode was consistently sharp and the gap value (nominally 0.5 μm) was uniform along the edge length distance, the emission along all of the electrode edge is expected to be equal. However, because the electrodes are planarized using CMP, the edges are not uniformly sharp. Moreover, misalignment induced variance in gap distance will cause non-

uniform edge emission. These inconsistencies from electrode to electrode are possibly the main cause for the smaller emitting area. In order to increase emitting efficiency, the edge sharpness should be made more uniformly and alignment should be precise. Another contribution to the emitting area could also be due to an increased work function. As no special cleaning of the surfaces was performed, contributions of adsorbed gases on the W surface could lead to an increased work function.

In order to further confirm field emission, field emission stability measurements were made. For these measurements, ion traps of $r_0 = 1$ μm in a 10^4 array at 10 MV/cm were used. Five-hundred volts were applied to the RE without ramping the voltage. As shown in Figure 6.25, the current was measured at 40 nA initially due to the shock to the device at 500 V, and then decayed to a stable emission current of ~ 2 nA for eleven minutes. Sharp increases in the current were seen at 3.5 and 6 minutes, and the overall emission current was averaged to be 2.03 nA. Similar results were obtained for the 1.5-μm traps in various array sizes. One would expect the attained FE current to scale linearly with respect to RE size (i.e., edge length) and array size. However, field emission can occur additionally between the RE and the mechanical strut holding the BEC in place. The spacing between these is not the same for the 1 and 1.5 μm traps, causing a non-linear effect in the rise of the emission current. The effect could also be due to inconsistencies in edge sharpness and gap distances as mentioned previously.

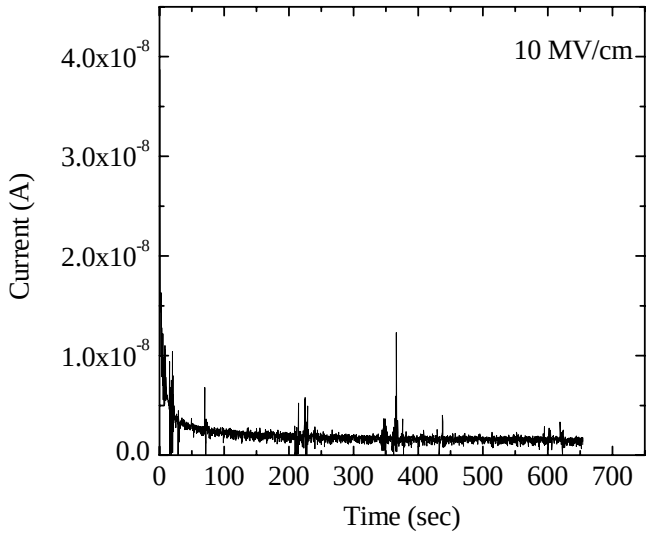

Figure 6.25. Emission current stability measurements for the r_0 =1 μm device in a 10^4 array at 10^{-5} Torr and 500 V.

In summary, the field emission characteristics of micro-cylindrical ion trap arrays were determined. Field emission was observed with currents of 2 nA at 10 MV/cm in vacuum, whereas currents of up to 60 nA were attained at 6 MV/cm in atmospheric pressure presumably due to gas discharge. Currents of up to 3 μA were achieved for the largest array at 6 MV/cm and smaller trap size at atmosphere, largely due to a gas ionization contribution. The measured current-voltage responses in vacuum fitted well the Fowler-Nordheim characteristics confirming

the increase in current was the result of field emission. Calculated emitting areas showed inconsistencies in edge sharpness and/or gap value asserting the need for an improved fabrication method if the device were to be operated as a field emitter. However, the maximum operating voltages were determined for trap operation such that the field emission was below 10^{-9}, 10^{-12} and 10^{-15} A at the voltage values of 300, 175 and 125 V, respectively. The emission current stability of 2.03 nA was achieved for eleven minutes at 10 MV/cm.

6.11 Electrical Characterization Conclusions

The electrical characteristics of the ion trap arrays, including their series resistive, capacitive, inductive and field emission properties were determined. A further assessment must be made as to the fabrication and features of the device, as their electrical properties present an obstacle in attaining high voltages (> 5V) to the ring electrode. The use of high resistivity silicon was suggested as an alternative to the current fabrication process. However, despite the electrical characteristics the devices were tested and their trapping characteristics are discussed in Chapter 8.

7.0 TESTING OF MICRO CYLINDRICAL ION TRAPS

In this chapter ion trapping experiments with an array of 5-μm internal radius (r_0) sized cylindrical ion traps (CIT) are described. Of the four different sized ion traps fabricated, the experiments were focused on the trapping of toluene (C_7H_8) and methane (CH_4), masses of 92 and 16 amu, respectively, using arrays of 5-μm sized traps. *In situ* ionization of the neutral gas occurred using an external, electron emitting filament. Ion ejection from the traps occurred due to the termination of the RF voltage applied to the ring electrode. A current signal was noted afterwards on the collector electrode. It was clear that the observed was not entirely due to trapped ions as a large RF turn-off noise spike was consistently present, and attempts were made to reduce this noise. Favorable trapping conditions were attained, however, such as a significant pseudopotential well and an ionization rate twice the ion loss rate as determined by simulation, and evidence was obtained suggesting trapping of ions in 1-10% of the traps in the array.

7.1 Introduction

Miniaturizing ion traps by several orders of magnitude yields new challenges not encountered in the macro-scale. Although the trapping mechanism remains the same, as elucidated by simulations, the mechanical and electrical characteristics of the structures become an important factor when applying RF voltage to the traps. Array inductances and capacitances for the devices fabricated and tested here proved to be an impediment to attaining suitable drive voltages and frequencies, as discussed in Chapter 7. In order to axially confine the ions, the potential well depth must be, $D_z >> kT$. Changes in $V_{0\text{-}P}$ must be compensated by changes in the frequency, *f*. The down-selection to one ion occurs in the 5-μm traps, on a timescale greater than in the 1-μm traps (on the order of tens of microseconds), and ions can last several milliseconds in the traps, as elucidated by simulation. In these experiments, the trapping time was 20 to 100 μsec, on the same order as the time for down selection to one ion.

The confinement of a single ion represents an elementary quantum system, which is well isolated from the environment. In the arrays used for testing there are approximately 20000 traps operating in parallel as mass analyzers and therefore the ion motion across the traps is expected to be coupled. Ideally for mass spectrometry applications, all ions would achieve a coherence which would allow them to be ejected at the same time, thus yielding a greater instantaneous ion current and therefore a higher signal to noise ratio. The microfabricated ion traps consist of four electrodes: two end cap electrodes, a ring electrode and a Faraday cup detector for signal collection. Since a Faraday cup is used to detect the signal, there is no signal amplification as in macro-scale ion traps where electron multipliers and channeltrons are used to detect ions.

7.2 Experimental

Since testing was focused on r_0=5μm devices, their scanning electron microscopy micrographs are shown in Figure 7.1. Each trap consists of two end cap electrodes (a top end cap designated TEC and a bottom end cap designated BEC), one ring electrode (designated RE), and a detector/collector plate (designated COLL), which are arranged in a large two-dimensional array. The electrodes and supporting anchors are made of tungsten; the electrodes are vertically separated by a 0.5 μm gap and horizontally separated by 4.5 μm. Common anchor points of adjacent elements allow for the entire array of traps to be operated in parallel, as seen in Figure

7.1 (c). Anchor points of differing electrodes are separated by 8 μm or more and all anchors are landed on a dielectric stack of 800 nm of silicon nitride on 630 nm of silicon dioxide on the silicon substrate.

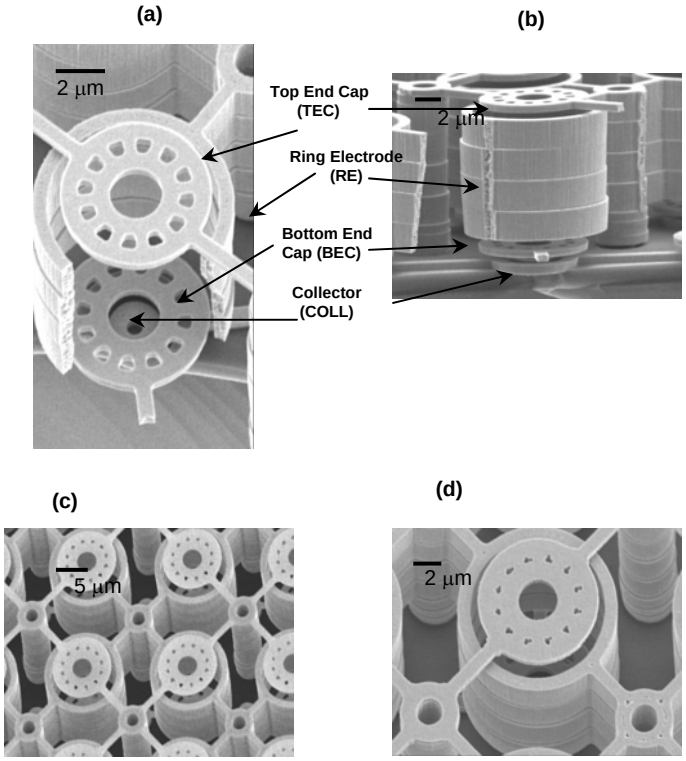

Figure 7.1. Scanning electron microscopy micrographs of the microfabricated r_0 = 5 μm CIT array. (a) The cross-sectional perspective view showing electrodes, (b) a side view showing electrodes, (c) a top view of the array, and (d) a top view of the trap.

7.2.1 Packaging Design

After the arrays were released, they were packaged in an alumina filled glass RF package from StratEdge©. The packages have a small cavity and straight leads extruding from the medium of the cavity for electrical connections. The ion-trap chips were attached with a non-conductive epoxy and gold ribbon bonds were used to make connections from the package leads to bond pads on the chip. The packages maintained a 50-ohm line when driven with a ground signal ground input. The packages were soldered onto a Duroid® board which had a microstrip 50-ohm line input to a 50-ohm coplanar wave guide and connections to the microstrip line were made with SMA connectors. This board fit on the flange of the vacuum chamber.

Achieving an adequate RF voltage on the ring electrode is one of the major challenges in attaining a trapping equilibrium with the micro-sized ion traps, since the magnitude of the RF voltage determines the pseudopotential. However, due to the electrical characteristics of the ion trap arrays, as summarized in Table 7-1, forming a matching circuit outside the package is not probable. The combined inductance and capacitance of the packaged traps give a resonant

frequency too low for the ions tested. Thus, the traps can not be operated at a voltage maximum. Figure 7.2 (a) shows a schematic of the equivalent series LRC circuit for the packaged traps.

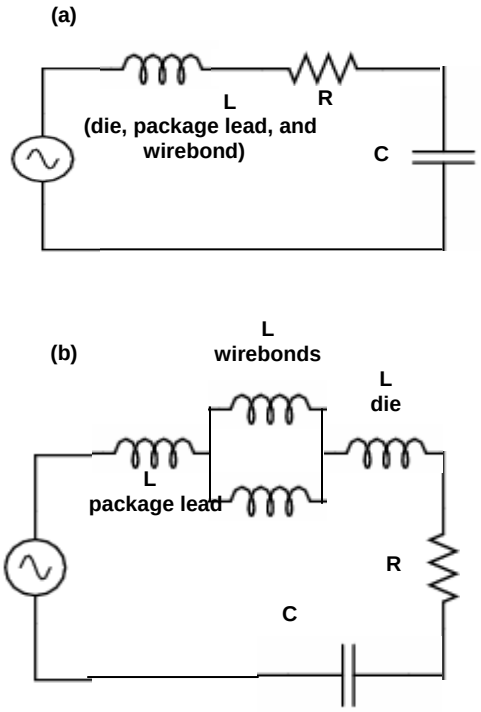

Figure 7.2. (a) An equivalent R-L-C circuit of microfabricated packaged cylindrical ion trap arrays. The inductance is mainly due to the wirebonds used for making electrical connections to packages, the bus bars of the fabricated die, and the package leads. (b) An equivalent R-L-C circuit with the parallel inductance by the addition of wirebonds.

As detailed in Chapter 7, the inductance, L, was largely due to the package leads, wire bonds and bus bars in the array. Approximately 550 pH of the inductance was due to the actual array. The package leads and wirebonds together increased the inductance to 4000 pH, as each contributed approximately 2000 pH. Consequently it was not possible to externally match the circuit outside the package. To reduce the inductance of the packaged trap arrays, parallel inductance was added to the arrays through wirebonds. The new equivalent circuit is shown in Figure 7.2 (b). Adding parallel wirebonds which have equal amounts of inductances reduces the inductance of the wirebonds by half. This overall reduction in inductance leads to a reduction in the reflected power and an increase in the resonant frequency at which the traps can be operated, and thereby increases the required voltage needed to trap ions of a specific mass. The difference in impedance between the packaged array and the 50-ohm transmission line creates a reflection in the wave propagation into the device. Ideally, the device would have a nominal impedance of 50-ohm and be matched with the transmission line, enabling no power loss in the input and no standing waves. However, due to the mismatch reflected powers from the load were in the range of 50-66% of the forward power. The standing wave ratio (SWR) was calculated to be approximately 4, using the following relationship:

$$SWR = 1 + \frac{\sqrt{\frac{P_{ref}}{P_{fwd}}}}{1 - \sqrt{\frac{P_{ref}}{P_{fwd}}}} \qquad (7.1)$$

where P_{ref} is the reflected power at the load and P_{fwd} is the forward power. If P_{ref} is close to 0 then the SWR approaches 1, the desired value. If P_{ref} approaches P_{fwd} then the SWR approaches infinity, a highly undesirable condition. A SWR of four indicates a substantial power reflection at the load due to the mismatch between the wave impedance and the load impedance. Because the SWR is so high creating a matching circuit is problematic.

Table 7-1. Electrical characteristics of ion trap arrays.

r_0 (μm)	Array Size	R (Ω)	L (pH)	C (pF)	Tolerance
1	1073290	2.18	1646.00	576.00	3.17×10^{-2}
	217156	1.74	712.22	120.87	1.29×10^{-3}
	7396	8.99	9.99	4.92	3.00×10^{-3}
2	331776	1.57	1190.00	399.98	1.39×10^{-2}
	66564	1.48	596.80	73.76	5.52×10^{-4}
	2304	33.70	9.97	3.44	2.98×10^{-2}
5	20736	7.06	554.00	51.60	2.80×10^{-3}
	784	16.50	99.99	2.83	3.00×10^{-3}
2 (packaged)	66564	6.76	3303	70.00	1.75
5 (packaged)	20736	1.77	4386	49.60	6.00×10^{-3}
5 (tall) (packaged)	20736	2.18	4779	44.00	9.00×10^{-3}

7.2.2 Test Setup

Despite of the transmission line discontinuity, various trapping experiments were performed. Figure 2.7 depicts the main test setup used for the trapping and detection of ions. The analytes were ionized by electron impact ionization with two rhenium filaments operated in parallel at 70 eV. These were gated using the marker on a Tektronix AWG710 arbitrary waveform generator, which simultaneously drove the ring electrode. The top and bottom end caps were typically grounded. However, there exists the option to apply DC voltage or an AC current to either one. The analyte was introduced into the chamber through a leak valve; analyte pressures of 1×10^{-4} to 5×10^{-4} Torr were achieved, as monitored by an ion gauge.

Measurements were made to determine the voltage delivered to the ring electrode. The test setup is depicted in Figure 7.3 (a), where the ARB was utilized to directly input the wave, $V_{P\text{-}P}$ = 1 V, into the ring electrode. The output was directly measured by the oscilloscope. This creates a baseline for the magnitude of the RF voltages that can be expected when using the amplifier.

With the baseline established, the signal was amplified and the forward and reflected powers were monitored, as shown in Figure 7.3 (b). The RF signal was converted into a DC-signal using a diode (Cantenna), and the amplitude of the wave, from 0 to peak, was monitored with a voltmeter.

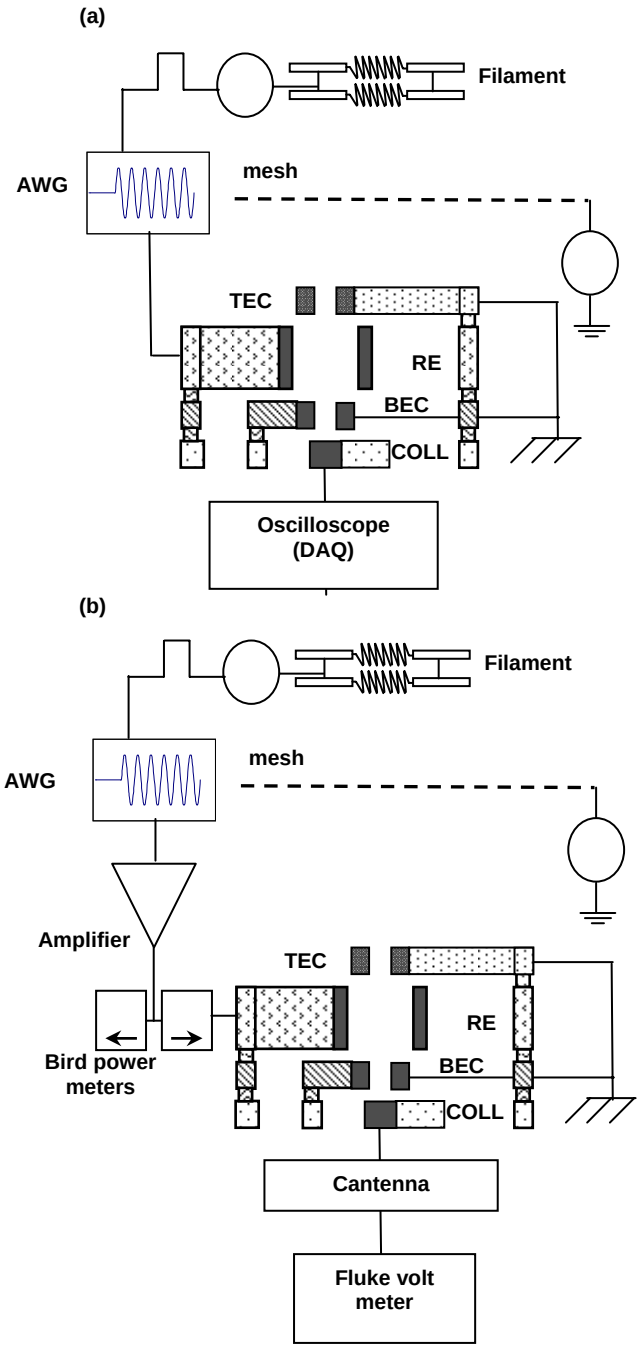

Figure 7.3. (a) Test set up used to determine the voltage on the ring electrode when wave is input from the ARB.The voltage is measured directly from the collector by the oscilloscope. (b) Test set up for measuring voltage on the ring electrode after RF amplification. The signal is converted with a rectifying diode (the Cantenna) and then measured with a fluke volt meter.

For clarity, the circuit schematic for the Cantenna is shown in Figure 7.4.

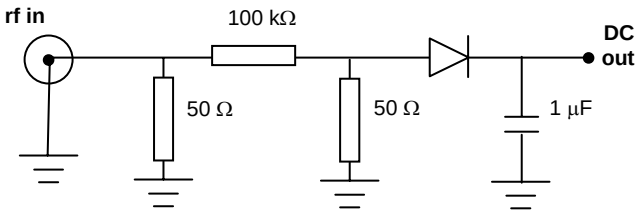

Figure 7.4. The circuit schematic for the Cantenna. A wave input to the circuit was rectified into a DC output proportional to $V_{0\text{-}P}$.

7.2.3 Ion Formation and Behavior under Non-Trapping Conditions

Ion trapping experiments were performed with toluene and methane. Table 7-2 summarizes the physical properties of the two analytes. Experiments were conducted with toluene (C_7H_8), mass 92 amu, which has parent ion peaks at m/z = 91, 92 and 93 (NIST 2005). Toluene was selected because it has a relatively high ionization cross-section, ~15×10^{-16} cm (Kim, Irikura et al. 2005), and a low ionization threshold energy, 8.8 eV (NIST 2005). Methane has a higher ionization threshold energy, 12.6 eV, but a smaller ionization cross-section, 3.5×10^{-16} cm (Kim, Irikura et al. 2005). An ion gauge determines pressure by detecting the amount of current generated from ionization of the gas within the chamber. Therefore, this technology is sensitive to the changes in analytes which have different ionization cross-sections. However, by performing the experiments with the gases yielding the same pressure readings via an ion gauge the number of neutral analyte particles within the chamber were expected to be the same. Additionally, the ion formation rate must exceed the trapping ion loss rate, in order to attain a suitable number of ions for detection purposes. Equation (7.2) (Mark and Dunn 1985) illustrates the estimated ion current due to the electron impact ionization:

$$I_i \big/ I_e = \rho\sigma(70eV)L \qquad (7.2)$$

where I_i is the ion current, I_e is the electron emission current, ρ is the neutral density, σ is the cross-section at 70 eV and L is the path length. The steady state experiments measuring ion formation determined that the ion formation rate exceeded the loss rate by a factor of two, as described below.

Table 7-2. Properties of toluene and methane.

Analyte	Mass (Kawamura)	Ion's Mass (Kawamura)	Ionization Cross Section (1×10^{16} cm^2)	Ionization Threshold (eV)
Toluene (C_7H_8)	92	91, 92, 93	15.0	8.8
Methane (CH_4)	16	14, 15, 16	3.5	12.6

The ion formation and loss behavior is important, since their combined effects determine the attainable trapping equilibrium. The electron emission from two rhenium filaments operated in parallel was studied, in conjunction with the measured electron currents on the trap electrodes and a mesh (previously used to gate the electrons), under the steady state condition. Figure 7.5 shows the emission current measured from the filaments as well as that arriving on the mesh (grounded). The filament emission initially decayed until it reached a steady state emission current of about 0.7 μA for a filament bias of -70 V. Approximately 30% of the filament emission current reached the mesh. It should be noted that filament emission can reach much higher currents, ~30 μA, at the beginning of the filament lifetime. While the filament steady state operation was reached more quickly as filament lifetime increased, overall emission current concurrently decreased.

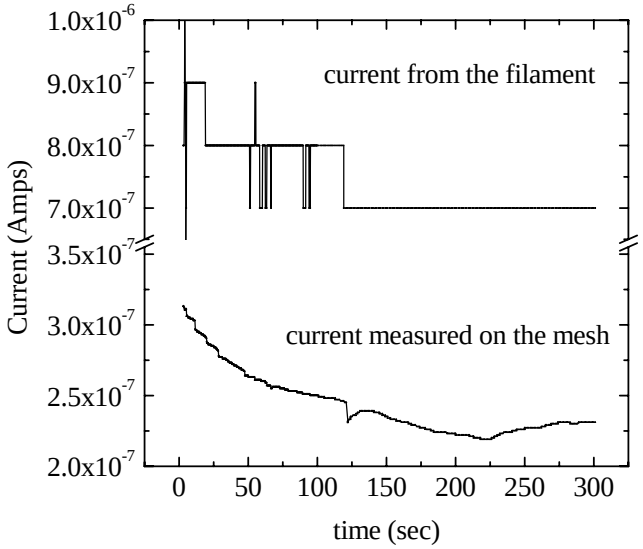

Figure 7.5. The emission current from two rhenium filaments operated in parallel and the corresponding current measured at the mesh. On the order of 1 μA was emitted from the filament and about 0.25 μA was measured on the mesh. The filament was biased at 70 eV and the mesh was grounded.

Figure 7.6 shows the effects on these currents upon introduction of neutral (methane, CH_4) addition into the system, the neutral pressure increasing from a starting base pressure of 8×10^{-6} Torr to 1×10^{-4} Torr, as monitored via an ion gauge. The electrodes shown in Figure 7.6 are the mesh, biased at -10 V and the ring electrode, biased at -15 V; the filament was biased at -70 V. As depicted, the measured negative electron current increased since ions were instantaneously accelerated to the biased electrodes. An increase in current could also be a result of fewer electrons reaching the electrodes; however, the experiment was performed with the electrodes grounded and no appreciable change in the electron current measured on the electrodes with the addition of methane was observed. Approximately 155 nA was measured on the mesh and this is attributed to ion formation between the filament and the mesh. Approximately 3 nA of ion current on the ring electrode, corresponding to 18750 ions/microsecond, was measured and this

value was about twice the ion loss rate as determined by simulation. In both cases about 0.7 μA of electron current was emitted from the filaments. Ion currents scaled with the filament current.

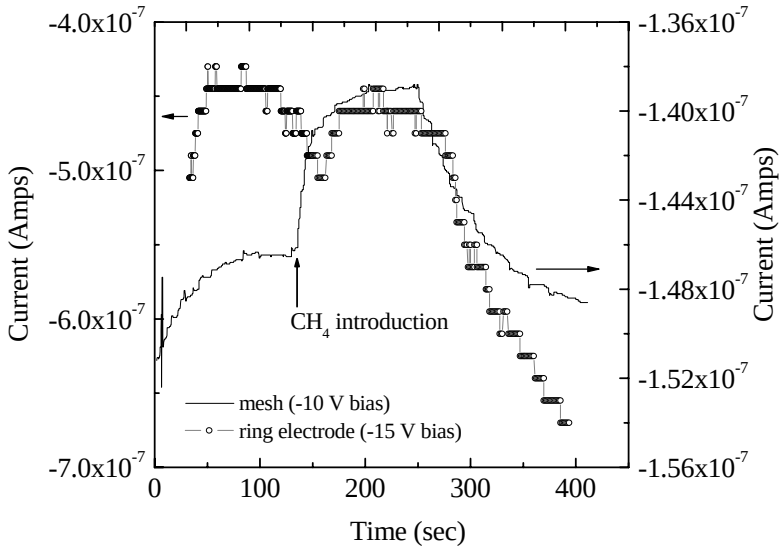

Figure 7.6. The measured current response when neutrals (CH_4) were added. A positive ion current was observed at both the mesh (biased at -10 V) 155 nA, and the ring electrode (biased at -15 V) 3 nA.

7.2.4 RF Voltage Characterization

Delivering sufficient RF voltage to the ring electrode is necessary for obtaining useful trapping potentials in micro-sized ion traps, since the RF voltage magnitude determines the pseudopotential. However, due to the large trap array capacitances and inductances, as summarized in Table 7-1, it was found to be problematic to form a sufficient matching circuit outside the package.

Various experiments were performed aimed at the characterization of the RF voltage input to the ring electrode. These experiments were carried out using the test setup depicted in Figure 7.3 (a) and (b). Figure 7.7 shows the voltage measured on the collector for various frequencies for the $r_0 = 2$ μm medium sized array. In this case, RF with $V_{P\text{-}P} = 1$ V was applied to the ring electrode and measurements were made directly with an oscilloscope. As expected, it was observed that the frequencies, at which the trap self-resonated, correspond to distinct peaks in the applied RF voltages. These results are consistent with the predicted resonance of 300 MHz for the 2-μm trap, based on its capacitance and inductance.

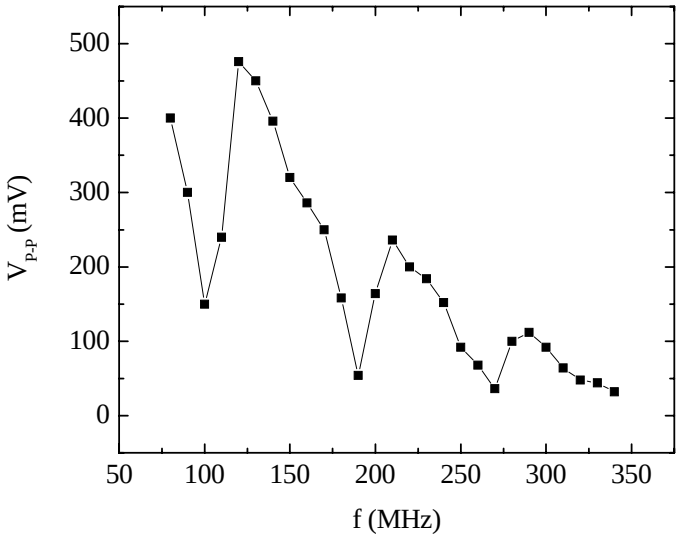

Figure 7.7. The voltage output measured on the collector when RF was applied with the arbitrary wave form generator with V_{P-P} = 1 V. The measurements were made with the r_0 = 2 μm medium sized array (66564 traps).

The input signal was amplified, utilizing the test setup in Figure 7.3 (b). In this case the RF amplitude was on the order of 7, 10 and 12 V_{0-P}. The measurements were made on the collector using the Cantenna to convert the signal to a DC output and the readings were made with a voltmeter. Figure 7.8 depicts the voltage characteristics of the r_0 = 2 μm medium sized array as a function of frequency. The behavior was consistent generally with measurements made without any amplification.

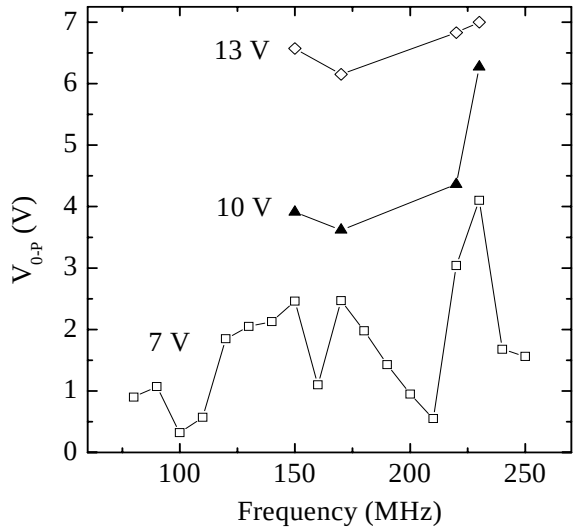

Figure 7.8. The voltage output characteristics of the r_0 = 2 μm medium sized array measured on the collector with the RF amplified and applied to the ring electrode with amplitudes of 7, 10 and 13 V_{0-P}.

Figure 7.9 depicts the voltage response after the parallel wirebond addition for a 5-μm medium sized trap array. The graph shows the response measured on the collector when the RF voltage was directly applied from the Tektronix AWG710 arbitrary waveform generator (ARB) (the mV scale on the left) and when the RF voltage was amplified with an AR amplifier (the V scale on the right). As the collector was capacitively coupled to the ring electrode, the actual voltage on the ring electrode was determined through the following relationship:

$$\frac{V_{cap}}{V_{source}} = 1 \Big/ \varpi RC \qquad (7.3)$$

where V_{cap} was the capacitively coupled voltage that is measured on the collector, V_{source} was the voltage on the ring electrode, ω was the angular frequency, R was the series resistance and C was the capacitance between the two electrodes.

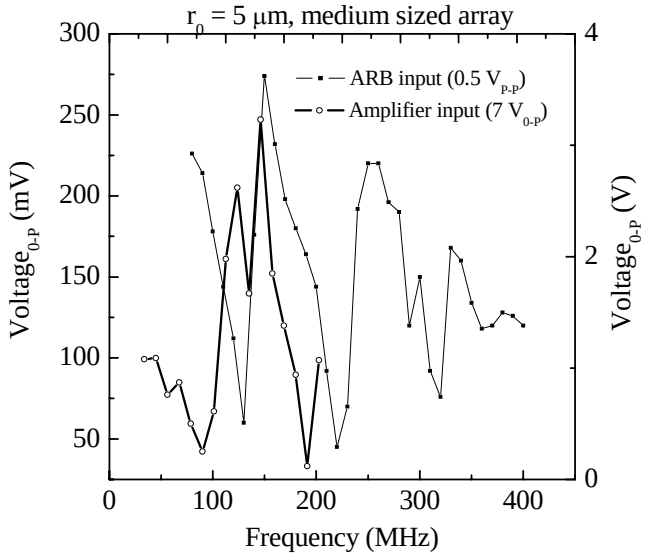

Figure 7.9. The voltage output measured on the collector when the RF was applied with the arbitrary waveform generator (mV scale on the left) and with the amplifier (V scale on the right) to the ring electrode. The ion trap array was an r_0 = 5 μm, medium sized array.

Using Equation (7.3) the voltage to the ring electrode from the capacitively coupled voltage measured on the collector was estimated. Table 7-3 summarizes the voltages on the ring electrode when the RF signal was amplified at various gains, attenuations and frequencies, and these measurements were performed on the r_0 = 5 μm, medium sized array.

Table 7-3. Calculated voltage characteristics from the ring electrode of a 5-μm medium sized array at various frequencies, attenuations and amplifier gains

Frequency (MHz)	Measured Voltage(0-P) on Collector	Calculated Voltage (0-P) on Ring Electrode	Gain Setting	Attenuation (dB)
80	1.08	0.60	0	1
90	1.09	0.68	0	1
100	0.76	0.53	0	1
110	0.87	0.67	0	1
120	0.50	0.42	0	1
130	0.25	0.23	0	1
140	0.61	0.60	0	1
150	1.98	2.09	0	1
160	2.62	2.95	0	1
170	1.67	2.00	0	1
180	3.23	4.10	0	1
190	1.85	2.48	0	1
200	1.38	1.95	0	1
210	0.94	1.40	0	1
220	0.12	0.19	0	1
230	1.07	1.75	0	1
200	1.48	2.09	0.5	1
200	1.86	2.63	0	1
200	3.27	4.62	1.5	8
200	4.27	6.42	1.5	6
200	5.10	7.21	1.5	5
200	6.00	8.48	1.5	4

Voltage maxima were recorded at several frequencies: 160, 180, 190, 200 and 230 MHz. Due to the amplifier's range of operational frequencies, 200 MHz was chosen as a good optimum. The voltage needed to trap a specific mass was increased with increased frequency, and at 200 MHz the roll-off of the RF amplifier was still manageable, enabling an adequate amount of voltage input. With an approximately 32V input from the amplifier, the measured voltages on the collector for various attenuations were between 3-6 $V_{0\text{-}P}$, corresponding to approximately 4-8.5 $V_{0\text{-}P}$ on the ring electrode. Therefore, the trapping conditions were f =200 MHz, $V_{0\text{-}P}$ = 4-8.5 V.

7.2.5 Trapping Experiments

The time sequence used to trap ions is shown in Figure 7.10. First, RF is applied to the ring electrode with the gate for electrons open for 30 microseconds. Presumably, ions formed *in situ* would be trapped during this period. This was followed by a trapping period, with the electron gate closed and no new ions formed, that varied from 20-100 microseconds and a 0 V DC for 1 ms was applied to the ring electrode to eject ions to the collector. A major source of noise was the RF signal capacitively coupled from the ring electrode to the collector. Although a low pass

filter was incorporated after the collector, as shown in Figure 2.7, the RF turn-on and turn-off was still observed in the signal. The RF amplifier also proved to be a source of noise. Although unsuccessful in eliminating this noise, it was reduced to approximately 50 mV in amplitude, corresponding to 5 nA at the 10^7 V/A current gain setting of the Keithley 428.

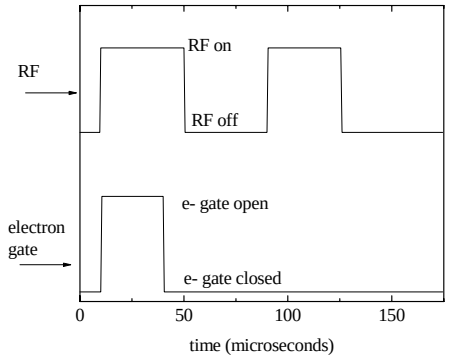

Figure 7.10. The timing diagram for trapping experiments. The gate for electrons is open, while the RF is on at the same time for a longer period. A second period of RF was applied in order to test the characteristics of the collector signal.

Experiments were performed at a constant frequency of 200 MHz, and used the standard 30 μs ionization period with $V_{0\text{-}P}$ = 4V, followed by 30 μs with just the RF trapping voltage, and 1 ms of 0 V DC. Figure 8.11 (a) shows the collector signal after the electron gate closed and there was only RF applied to the ring electrode. Table 7-4 summarizes the different trapping sequences used in the experiments.

Table 7-4. Sequences used in ion trapping experiments.

Waveform	Time
Rf trapping - 200 MHz sine wave (gate open; electrons ionizing neutrals)	30 μs
Rf trapping – 200 MHz sine wave (gate close; no ionization)	Varied 20-100 μs
DC (0 V)	Varied, 30, 60, 90 μs
Rf trapping – 200 MHz sine wave (gate close; no ionization)	40 μs
DC (0 V) – for ion pulse out to collector	1 ms

The timing sequence is depicted in Figure 7.11 (a) – (c) with the resulting current signal. Figure 7.11 (a) shows the collector signal when there was no analyte present and RF was applied along with electrons. The y-axis in Figure 7.11 shows the current collected. Due to the inverting output of the Keithley 428 amplifier, the electron current is positive and ion current is negative. In Figure 7.11 (a) during the 30 μs when the gate is on, more than 50 nA of electron current was measured on the collector. (The electron current was actually greater but can not be detected due to the saturation of the amplifier.) The current is seen to decrease once the gate is turned off and the signal was dominated by the RF signal. At RF turn-off, a large signal increase is observed. Figure 7.11 (b) depicts the collector signal when 3×10^{-4} Torr toluene was introduced. A slight

decrease in the measured electron current was observed, indicating that ions were indeed formed in the first 30 μs. The RF noise is also decreased and after the RF turn off a negative signal is observed, indicating a positive charge. Under these conditions, mass 91 would be trapped with an estimated q_z value of 0.43. The signal at the end of the RF turn-off seen in Figure 7.11 (b) suggests ions being pulsed out of the trap. Figure 7.11 (c) depicts the baseline subtracted collector signal (signal in (b) – signal in (a)). This is depicted in Figure 7.11 (c). During the ionization period a negative difference in the current is seen, showing that not as many electrons are reaching the collector due to ionization events. A large spike due to the RF noise is observed; however at the RF turn-off event an isolated ion signal is seen. This signal occurs when toluene is present.

To confirm whether the observed collector signal after baseline subtraction was due to trapped ions, methane (m/z=16) was substituted for toluene. Under identical trapping conditions (4 V and 200 MHz) methane is not expected to be trapped, as the estimated q_z value is 2.4, well beyond the stability region. For methane both the observed and the baseline subtracted signals were similar, however, the toluene signal was greater than the methane signal by about 5 nA, again suggesting that part of the signal is due to the trapped toluene ions. An alternative explanation for the larger signal amplitude in the case of toluene is that the RF coupling from R.E. to collector upon turn-off is larger due the larger dielectric constant of toluene relative to methane, as toluene is a polar molecule and methane is non-poplar.

The amplitude of the baseline subtracted toluene signal (Figure 7.11 (c)) was 0.1 V at a gain setting of 10^7 V/A, corresponding to 10 nA of current. The current preamplifier has a rise time of 10 μsec. If the entire signal was attributed to trapped ions and the rise time (10 μs for the current pre-amp) is equated to the ion pulse width, 625000 trapped ions are expected. If the 10 nA was all attributable to trapped ions this would lead to approximately 3000 ions for a 50 ns pulse width. With all traps in the array populated by 1 or 0 ions (as predicted by simulation), this indicates 15% of the traps being populated each with one ion. However, because the rise time was much longer than the estimated pulse width of about 50 ns, it is hard to deduce the expected number of trapped ions. Since one can not attribute all of the measured current to trapped ions, it is hard to discern the efficiency of the trap and validate the simulation results.

To further elucidate that the measured signal was due to trapped ions, after the initial RF trapping period periods of RF were applied for by adding periods of 0 V DC for 30, 60 or 90 μs and was followed by 4 V of 200 MHz RF lasting 40 μs, as shown in Figure 7.10 (b). During the second RF on period, no ion formation was expected as no electrons were introduced. Figure 7.12 depicts the baseline-subtracted signal on the collector electrode with the RF applied to the ring electrode as follows: ion formation for 30 μs, a trapping period of 10 μs, a 60 μs RF off period, and finally a 40 μs RF on period (with no ionization). Again, negative signal was observed at the collector at the first RF turn-off event, consistent with the previous experiments. At the second RF turn-on, another negative current change was seen as the RF turned on. A positive current change was observed at the second RF turn-off event, as indicated in Figure 7.12. This phenomenon is unexplained since neither ions nor electrons should be present at this time and therefore there shouldn't be any modulation of ions outside the traps by the RF. These tests showed that the observed signal is not solely due to trapped ions, however, the presence of the negative signal after the first RF turn-off event, but not after the second, strongly implies the presence of ions at the end of the trapping (first RF) period.

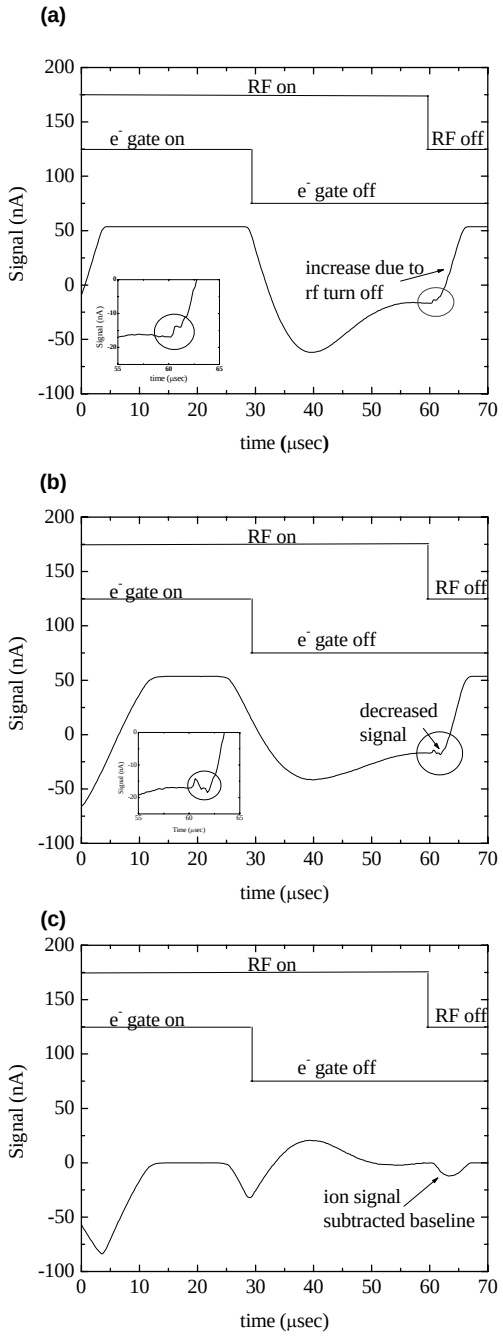

Figure 7.11. Signal from the collector electrode of the r_0 = 5 μm ion trap array: (a) the collector signal without ions, (b) the collector signal when toluene ions were introduced, and (c) the collector signal when toluene ions were introduced with baseline subtracted.

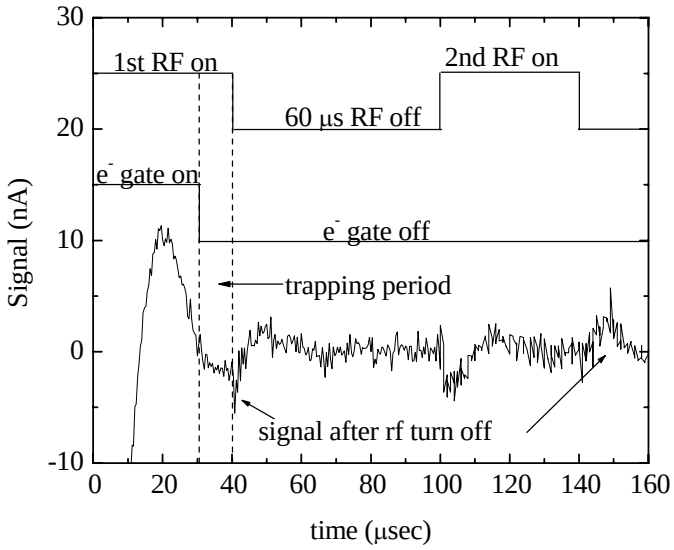

Figure 7.12. The collector signal of the r_0 = 5 μm CIT array. RF was applied to the ring electrode with toluene ions at a partial pressure of 3×10^{-4} Torr being formed via electron impact ionization for 30 μs. Next was an RF trapping period of 10 μs. There was a 0 V DC input to the ring electrode for 60 μs and an added RF sine wave for 40 μs with no ionization. Theoretically, no ions should remain trapped and the corresponding signal should not be due to trapped ions.

7.3 Discussion of Ion Motion/Ion Physics

The ion motion can be described by a slow secular harmonic oscillation at a frequency of $2\beta_i\Omega$, where β_i is a function of the stability parameters a_i and q_i and therefore mass dependent. The secular frequency is superimposed with a micromotion consisting of two fast harmonic oscillations at frequencies $(1\pm 2\beta_i)\Omega$, but of much smaller amplitude. In this study, the toluene (m/z=91) ion has q_z = 0.48, β_z is approximately 0.34 and the secular frequency of the ion is approximately 121 MHz, so that the micromotion frequencies should be about 321 and 79 MHz.

The pseudopotential well in these experiments ranged from 0.27 eV to 0.86 eV, about one to two orders of magnitude greater than kT if ions are assumed to be at room temperature (300 K). Previous simulations showed that approximately 25% of ions would be trapped under these conditions. Because of the traps uncharacterized stability parameters, the traps were not operated in the scan. The stability diagram is likely to be shifted and further experiments need to be performed to determine whether the trap can be operated in the scan instability mode.

Field anharmonicities are inevitable due to the variation of the trap geometry from ideality. Since the cylindrical geometry deviates from the ideal quadrupole and the end cap holes could create field imperfections, higher order fields could lead to ion heating and ion loss mechanisms. The ions were assumed to not be the products of dissociative ionization and therefore to be at room temperature (300 K), since they were ionized *in situ*. However, ions that gained substantial energy from the heating process are likely to be lost and not trapped. It is unlikely that ions

would be trapped outside the trap since anharmonicities are likely to be the highest there. Heating of the ions leads to losses, especially since the pseudopotential is only 10 - 100 times of kT. However, a potential well that is two orders of magnitude higher than kT does lead to favorable trapping conditions.

7.4 Conclusions

The ion trap array's electrical characteristics were determined and found to provide, at best, marginal trapping conditions necessary for toluene. Although the signal could not be fully attributed to ions, trapping of toluene ions in a massive array of 5-μm internal radius cylindrical ion traps is suggested by the observation of current signals about the noise floor upon RF turn–off after an ion trapping period. Future work should focus on reducing the intrinsic capacitance of the ion trap structures and changing the packaging scheme to eliminate wire bonds. The use of high resistivity silicon should reduce intrinsic capacitance by 30%. Furthermore, a thru hole through the silicon substrate should provide a further decrease in capacitance, allow electron injection to, ion ejection from, and optical access into trapping region, and enable detecting of ions via fluorescence.

APPENDIX A

In this section a computer program written in the computer language C is presented. This program was utilized to calculate the trapping parameter β, which is a recursive fraction of the stability parameters a and q.

```
// A program written by Dolores Cruz
// Sept. 17th, 2003
// This program will calculate beta(z) the stability parameter based on an infinite fraction

#include <stdio.h>
#include <math.h>
//#include <iostream.h>

int main(void)
{
    //defining variables
        double qz, az, ar, qr;
        double beta, oldbeta, betar;
        int n, k, j;
        double fraction[16], negfraction[16], qsqr;
        double fractionr[16], negfractionr[16], qrsqr;
        double tol, difference;

        //define output file
        FILE *stream;
        stream = fopen("beta4", "w");
        fprintf(stream, "Beta valuues for given az and qz\n");
        fprintf(stream, "\n");
        fprintf(stream, "qz\t az\t beta\t \n");

        // de90fine the tolerance
        // get first estimation of beta
        //cout << "Please enter a value for qz" ;
        qz=1.09; az=0; j=0; k=0;
        qr=0; ar=0;
        for(k=1;k<=83;k++){
            qz=qz+0.005;
            qr=-0.5*qz;
            az=-0.3;
            for(j=1;j<=83;j++){
                az=az-0.005;
                ar=-0.5*az;

                qsqr=pow(qz,2);
                beta = pow((az+qsqr/2),.5);
```

```
                                qrsqr=pow(qr,2);
                                betar = pow((ar+qrsqr/2),0.5);

                                tol=0.0000001;
                                oldbeta = 1;
                                do
                                {
                                        n=0;
                                        for(n=1;n<=16;n++){
                                                fraction[n-1]=pow((2*n+beta),2) -az;
                                                negfraction[n-1]=pow((beta-2*n),2) - az;

                                                fractionr[n-1]=pow((2*n+betar),2) -ar;
                                                negfractionr[n-1]=pow((betar-2*n),2) - ar;

                                        }

                                        beta = pow(az + qsqr/(fraction[0]-qsqr/(fraction[1]-
qsqr/(fraction[2]-qsqr/(fraction[3]-qsqr/(fraction[4]-qsqr/(fraction[5]-qsqr/(fraction[6]-
qsqr/(fraction[7]-qsqr/(fraction[8]-qsqr/(fraction[9]-qsqr/(fraction[10]-qsqr/(fraction[11]-
qsqr/(fraction[12]-qsqr/(fraction[13]-qsqr/(fraction[14]-qsqr/(fraction[15])))))))))))))))+
                                        qsqr/(negfraction[0]-qsqr/(negfraction[1]-
qsqr/(negfraction[2]-qsqr/(negfraction[3]-qsqr/(negfraction[4]-qsqr/(negfraction[5]-
qsqr/(negfraction[6]-qsqr/(negfraction[7]-qsqr/(negfraction[8]-qsqr/(negfraction[9]-
qsqr/(negfraction[10]-qsqr/(negfraction[11]-qsqr/(negfraction[12]-qsqr/(negfraction[13]-
qsqr/(negfraction[14]-qsqr/(negfraction[15])))))))))))))),.5);
                                        difference = fabs(oldbeta-beta);

                                        oldbeta=beta;

                                        betar = pow(ar + qrsqr/(fractionr[0]-qrsqr/(fractionr[1]-
qrsqr/(fractionr[2]-qrsqr/(fractionr[3]-qrsqr/(fractionr[4]-qrsqr/(fractionr[5]-qrsqr/(fractionr[6]-
qrsqr/(fractionr[7]-qrsqr/(fractionr[8]-qrsqr/(fractionr[9]-qrsqr/(fractionr[10]-qrsqr/(fraction[11]-
qsqr/(fraction[12]-qsqr/(fractionr[13]-qrsqr/(fractionr[14]-qrsqr/(fractionr[15])))))))))))))))+
                                        qrsqr/(negfractionr[0]-qrsqr/(negfractionr[1]-
qrsqr/(negfractionr[2]-qrsqr/(negfractionr[3]-qrsqr/(negfractionr[4]-qrsqr/(negfractionr[5]-
qrsqr/(negfractionr[6]-qrsqr/(negfractionr[7]-qrsqr/(negfractionr[8]-qrsqr/(negfraction[9]-
qsqr/(negfractionr[10]-qrsqr/(negfractionr[11]-qrsqr/(negfractionr[12]-qrsqr/(negfractionr[13]-
qrsqr/(negfractionr[14]-qrsqr/(negfractionr[15])))))))))))))),.5);
                                        }
                                while(difference>tol);
                                fprintf(stream, "%f\t %f\t %f\t %f\t %f\t %d\t %d\t %d \t\n", qz,
az, beta, betar,difference, n, k, j);
                                }
                        }
        }
```

APPENDIX B

This section details the masks used in the microfabrication of the Al/SiO_2 self-aligned cylindrical ion trap structure. The masks were drawn using the mask layout program DW2000.

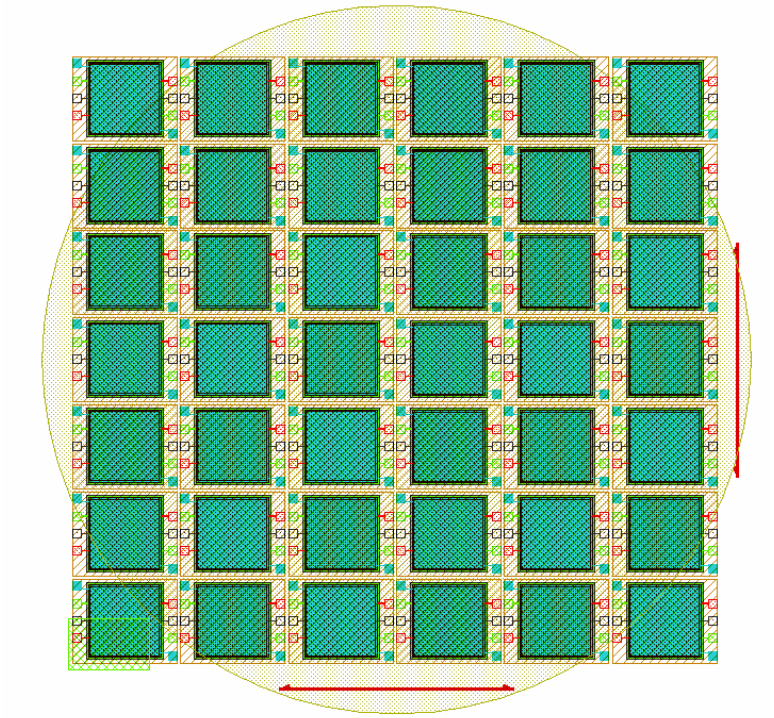

Figure B.1. An overall view of the mask layout, showing all dice and levels.

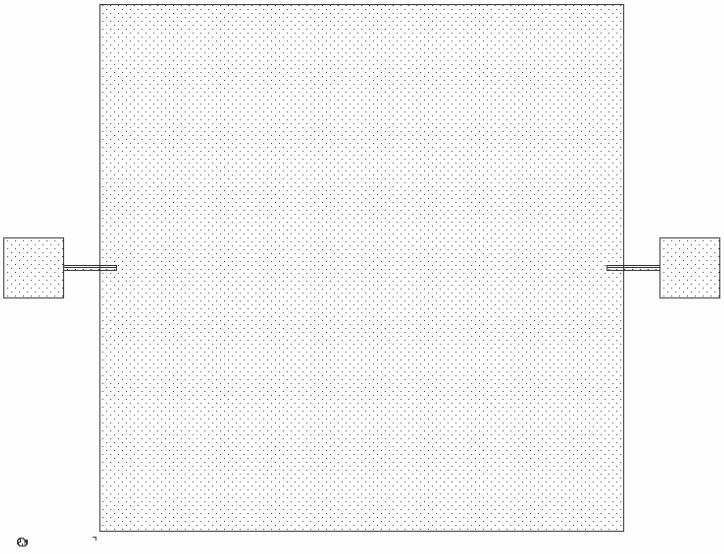

Figure B.2. A section of the mask detailing the pads and square region patterned using the collector mask level.

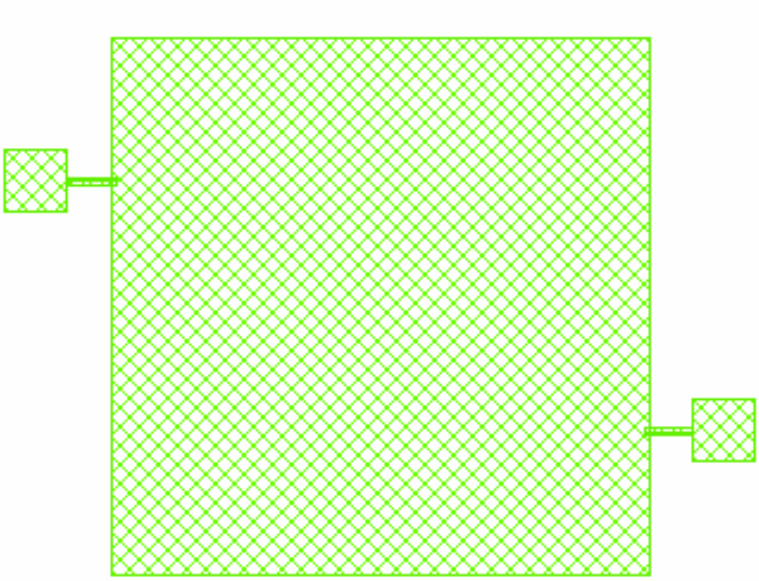

Figure B.3. A section of the mask detailing the pads and square region patterned using the bottom end cap mask level.

Figure B.4. A section of the mask detailing the pads and square region patterned using the bottom end cap mask level.

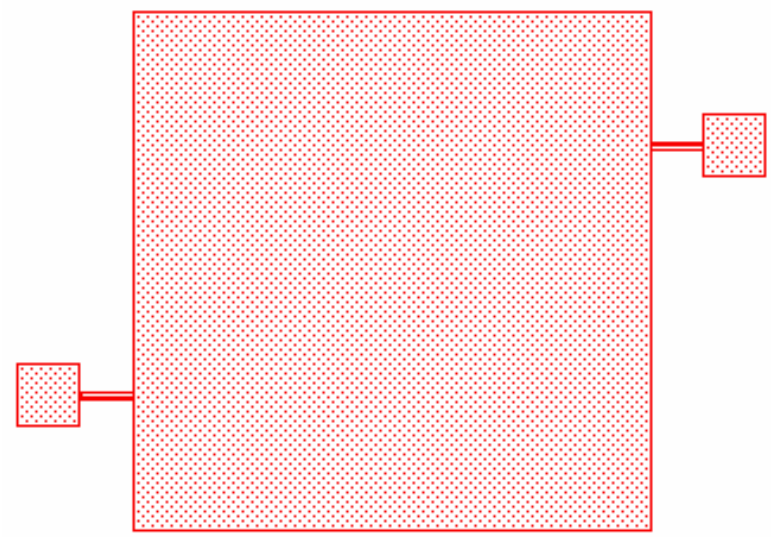

Figure B.5. A section of the mask detailing the pads and square region patterned using the top end cap mask level.

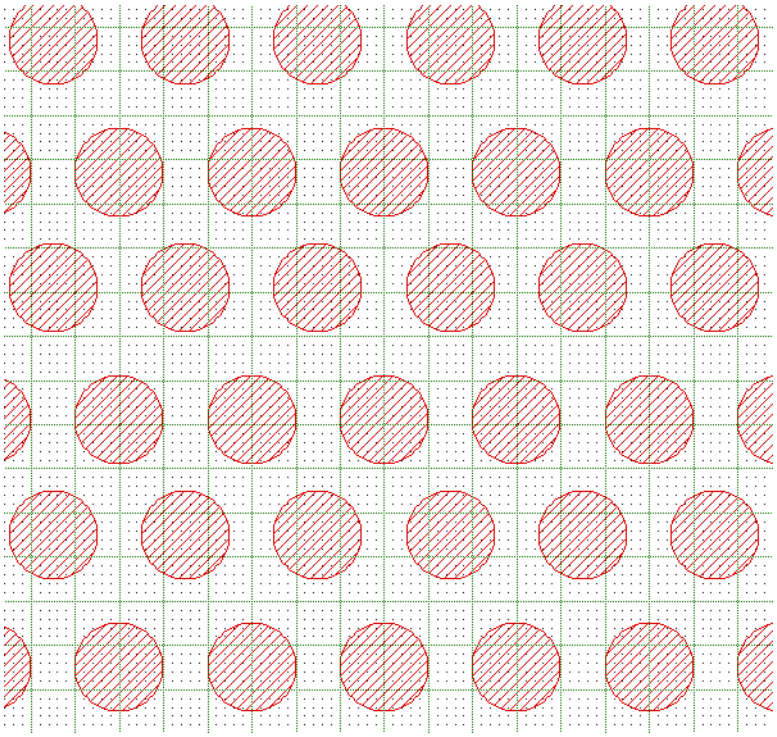

Figure B.6. A section of the mask detailing the etch holes arranged in an hexagonal close packed configuration.

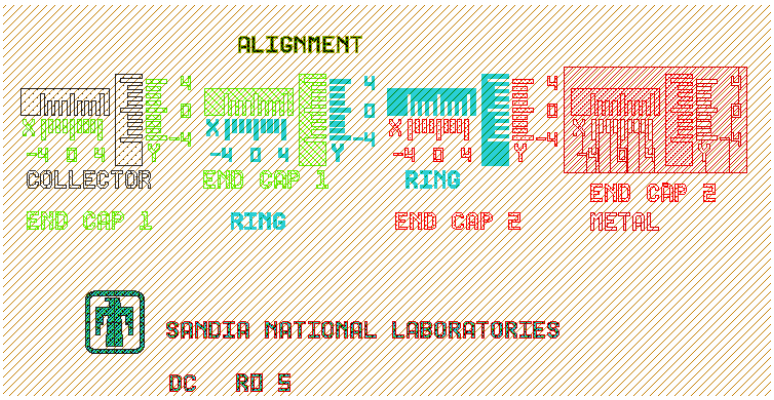

Figure B.7. A section of the mask detailing alignment marks used for aligning levels. Vernier alignment marks were used.

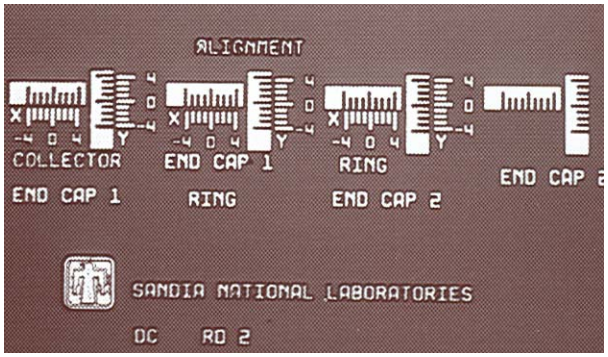

Figure B.8. A microscope picture of the patterned alignment marks used for aligning levels. Vernier alignment marks were used and the device has been patterned through to the end cap 2 (top end cap) level.

APPENDIX C

This section details the masks used in the microfabrication of the suspended free-standing tungsten ion trap array version 2. The masks were drawn using the mask layout program DW2000 from Design Workshop Technologies.

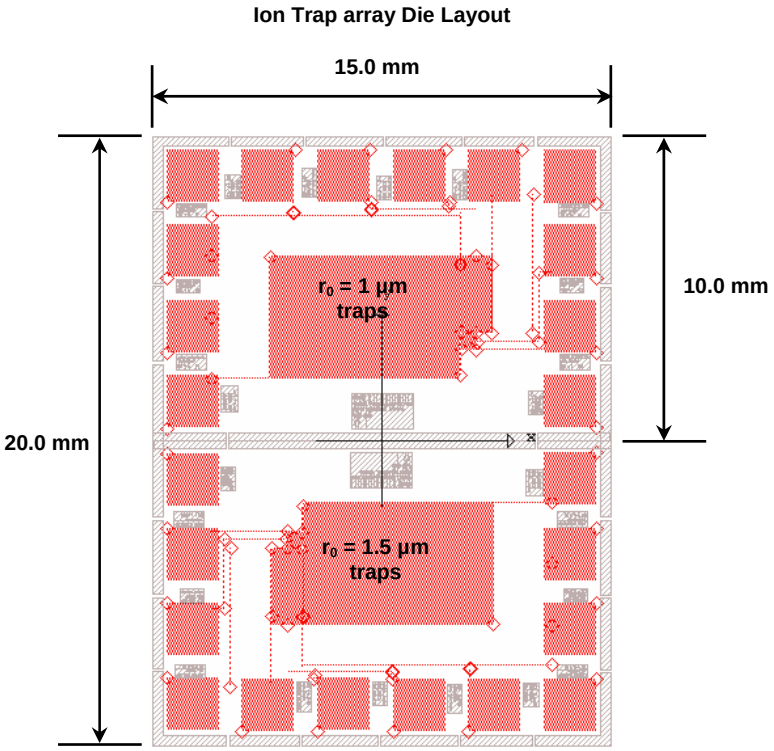

Figure C.1. Overall die layout used to microfabricate the suspended free-standing tungsten ion trap array version 2, with all levels showing. The die was step and repeated using a GCA XLS stepper.

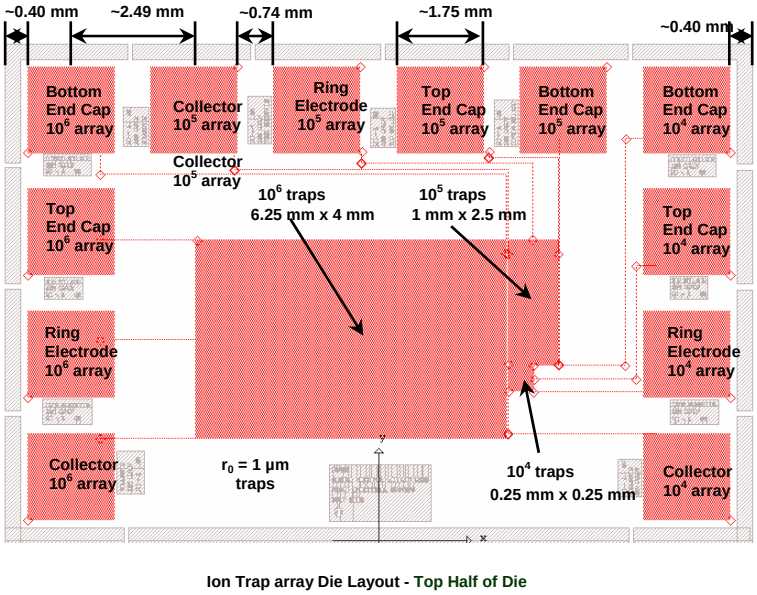

Figure C.2. Top half of die layout used to microfabricate the suspended free-standing tungsten ion trap array version 2, with all levels showing. The die was step and repeated using a GCA XLS stepper.

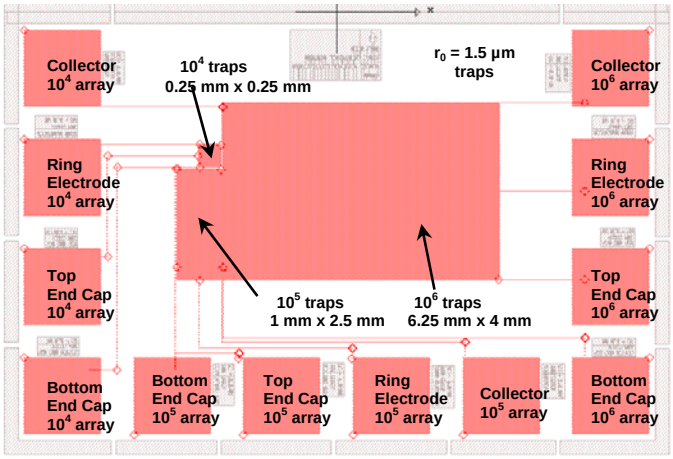

Figure C.3. Bottom half of the die layout used to microfabricate the suspended free-standing tungsten ion trap array version 2, with all levels showing.

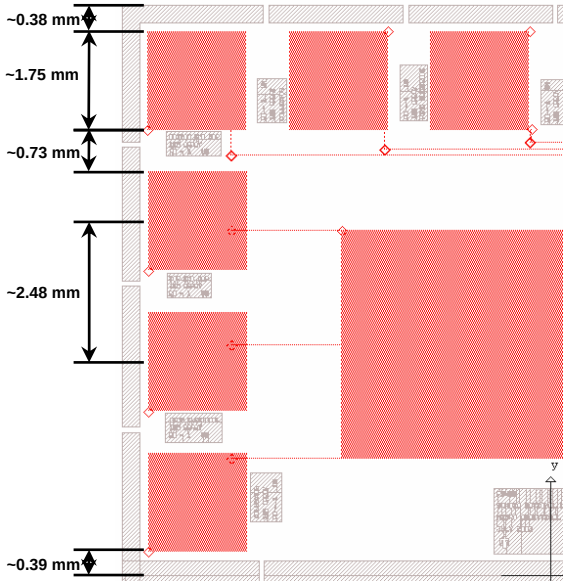

Top Left Quadrant of Die – Positions Mirrored about y-axis for Top Right Quadrant

Figure C.4. Top left quadrant of the die layout used to microfabricate the suspended free-standing tungsten ion trap array version 2, with all levels showing. The positions are mirrored about the y-axis for top right quadrant.

APPENDIX D

This section details the masks used in the microfabrication of the suspended free-standing tungsten ion trap array version 3. The masks were drawn using the mask layout program DW2000.

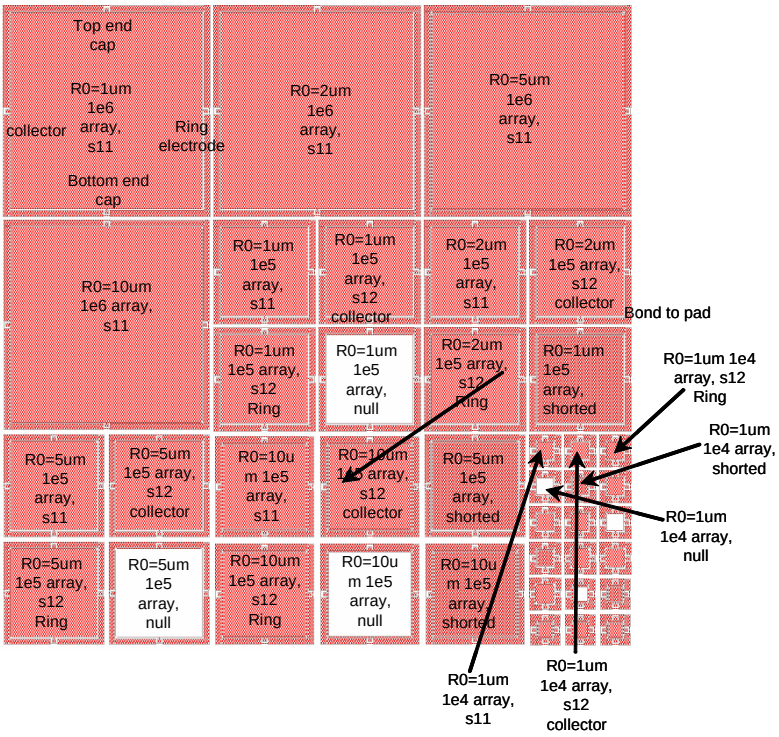

Figure D.1. Overall die layout used to microfabricate the suspended free-standing tungsten ion trap array version 3, with all levels showing. The die was step and repeated using a GCA XLS stepper.

Details of the mask layout are not included due to intellectual property rights.

The user program outlined below was written in the SIMION programming language, it was used to apply time varying potentials to the ring electrode.

```
; A simion program to apply time varying potentials to ring electrode.
; written by Dahl as sample for quadrupole ion trap
; adapted by Dolores Cruz - July 2003

; definitions of adjustable variables  ----------------------

    ; ---------- adjustable during flight -----------------

defa _Mean_Free_Path_mm       1E8     ; mean free path in mm
defa _Collision_Gas_Mass      4.0     ; assume helium
defa _gas_temp_K              295     ; temperature of collisional gas, Kelvin
defa _U_tune                  0.0     ; Qz tuning voltage, volts
defa _Detector_Voltage        0.0     ; voltage of detector target, electrode 4
defa _Right_Cap_Voltage       0.0     ; voltage on right cap, electrode 3
defa _v_init                  4.6     ; initial voltage on ring
defa _ion_colors              3       ; number of ion colors for collisions
defa _left_cap_frequency      0       ; frequency, Hz, of left cap rf
defa _left_cap_voltage        0.0     ; amplitude, 0-P. of left cap AC
defa _left_cap_offset_V       0.0     ; DC offset om left end cap


    ; ---------- adjustable at beginning of flight -----------------

defa PE_Update_each_usec      0.00001   ; pe surface update time step in usec
defa Percent_Energy_Variation 0.0       ; (+- 0%) random energy variation
defa Cone_Angle_Off_Vel_Axis  180.0     ; (+- 90 deg) cone angle
defa Random_z_Offset_mm       0.00095   ; del start position (z) in mm
defa Random_radial_offset_mm  0.0003    ; start position in radial direction
defa Random_TOB               1         ; random time of birth in cycles

defa Frequency_Hz             1.0E9     ; rf frequency of quad in (hz)
defa mm_per_Grid_Unit         0.00002   ; grid scaling mm/grid unit
defa v_ramp                   0         ; rf ramp slope in V/us
defa eject_after_n_cycles     2000      ; pulses out all ions after n cycles
defa pulse_out_amplitude_V    10        ; voltage and sign of push out pulse


; definition of static variables ----------------------------

defs first                    0.0   ; first pass flag
defs omega                    1.0   ; freq in radians / usec
defs wave                     0     ; wave property used in rf ramp
defs Next_PE_Update           0.0   ; next time to update pe surface
```

```
defs eject_flag                0    ; pass flag for pulse-ejecting ions


; program segments below ----------------------------------------




;-------------------------------------------------------------------------
seg initialize      ; randomize ion's position, ke, and direction
      1 sto Rerun_Flym               ; force rerun on
                                ; turns traj file saving off
      ;------------------- get ion's initial velocity components -------------
      rcl ion_vz_mm                  ; get ion's specified velocity components
      rcl ion_vy_mm
      rcl ion_vx_mm

      ;------------------- convert to 3d polar coords -------------
      >p3d                           ; convert to polar 3d

      ;------------------- save polar coord values ----------------
      sto speed rlup                 ; store ion's speed
      sto az_angle rlup              ; store ion's az angle
      sto el_angle                   ; store ion's el angle

      ;------------------- make sure Percent_Energy_Variation is legal ---------
                         ; force 0 <= Percent_Energy_Variation <= 100
      rcl Percent_Energy_Variation abs
      100 x>y rlup sto Percent_Energy_Variation

      ;------------------- make sure Cone_Angle_Off_Vel_Axis is legal ----------
                         ; force 0 <= Cone_Angle_Off_Vel_Axis <= 180
      rcl Cone_Angle_Off_Vel_Axis abs
      180 x>y rlup sto Cone_Angle_Off_Vel_Axis

      ; ---------------------- calculate ion's defined ke -------------
      rcl ion_mass                   ; get ion's mass
      rcl speed                      ; recall its total speed
      >ke                            ; convert speed to kinetic energy
      sto kinetic_energy             ; save ion's defined kinetic energy

      ; ---------------------- compute new randomized ke -------------
                                ; convert from percent to fraction
      rcl Percent_Energy_Variation 100 /
      sto del_energy 2 * rand *      ; fac = 2 * del_energy * rand
      rcl del_energy - 1 +           ; fac += 1 - del_energy
```

```
rcl kinetic_energy *          ; new ke = fac * ke

; ---------------------- convert new ke to new speed -----------
rcl ion_mass                  ; recall ion mass
x><y                          ; swap x any y
>spd                          ; convert to speed
sto speed                     ; save new speed

;-- compute randomized el angle change 90 +- Cone_Angle_Off_Vel_Axis -----
;-------- we assume elevation of 90 degrees for mean ----------
;-------- so cone can be generated via rotating az +- 90 -------
                              ; (2 * Cone_Angle_Off_Vel_Axis * rand)
2 rcl Cone_Angle_Off_Vel_Axis * rand *
                              ;  - Cone_Angle_Off_Vel_Axis + 90
rcl Cone_Angle_Off_Vel_Axis - 90 +

;-------------- compute randomized az angle change ------------
;--------- this gives 360 effective because of +- elevation angels ---
180 rand * 90 -               ;         +- 90 randomized az

;---------------------- recall new ion speed ------------------
rcl speed                     ; recall new speed

;--------- at this point x = speed, y = az, z = el --------------
;------------- convert to rectangular velocity components ---------
>r3d                          ; convert polar 3d to rect 3d

;------------- el rotate back to from 90 vertical -------------
-90 >elr

;------------- el rotate back to starting elevation -------------
rcl el_angle >elr

;------------- az rotate back to starting azimuth -------------
rcl az_angle >azr

;------------- update ion's velocity components with new values --------
sto ion_vx_mm                 ; return vx
rlup
sto ion_vy_mm                 ; return vy
rlup
sto ion_vz_mm                 ; return vz

;--------- randomize ion's position components to a cylinder--------
```

```
        rand
        sqrt
        rcl random_radial_offset_mm *
        sto radial_position
        rand 6.2832 *
        sto angle_el
        rcl angle_el
        sin
        rcl radial_position *
        sto x_offset
        rcl angle_el
        cos
        rcl radial_position *
        sto y_offset

        rcl ion_px_mm
        rcl x_offset +
        sto ion_px_mm               ; store random x start

        rcl ion_py_mm
        rcl y_offset +
        sto ion_py_mm               ; store random y start

        rand
        0.5 -
        2 *
        rcl random_z_offset_mm *
        rcl ion_pz_mm +
        sto ion_pz_mm               ; store random z start

        ;--------- randomize ion's time of birth --------
        rcl Random_TOB
        rand *                      ; create random time of birth
        1E6 *
        rcl frequency_Hz /
        sto Ion_Time_of_Birth       ; use it for ion
        ;---------------------- done ----------------------------------------



;-----------------------------------------------------------------------
seg Fast_Adjust                     ; generates trap rf with fast adjust
                                    ; has first pass initialization
    rcl first                   ; recall first pass flag
    x=0 gsb init                    ; if this is first reference  --> init
```

```
    rcl _Right_Cap_Voltage
    sto Adj_Elect03             ; electrode 3 voltage
    rcl _Detector_Voltage
    sto Adj_Elect04             ; electrode 4 voltage

    rcl Ion_Time_of_Flight              ; current tof in micro seconds
    rcl omega *                 ; omega * tof
    sin                         ; sin(omgga * tof)
    sto wave                    ; stores value of sin (tof*omega)
    rcl Ion_Time_of_Flight              ; tof in microsec
     rcl v_ramp *
     rcl _v_init +
     rcl wave *
    rcl _U_tune +
    sto Adj_Elect02             ; electrode 2 voltage

     rcl frequency_Hz
     rcl ion_time_of_flight *
     1E6 /                  ; number of cycles
     sto number_of_cycles
     rcl eject_after_n_cycles
     rcl number_of_cycles
     x>=y goto ejectall

     rcl _left_cap_Frequency        ; get AC ejection frequency
     6.28318E-6 *               ; to radians / microsecond
     rcl Ion_Time_of_Flight *       ; current tof in micro seconds
     sin                    ; sin(theta + (omega * tof))
     rcl _left_cap_Voltage *
     rcl _left_cap_offset_V +       ; add on DC offset to left endcap
     sto Adj_Elect01            ; left end cap

    exit                        ; exit program segment


lbl init                    ; parameter initialization subroutine

    1 sto first             ; turn off first pass flag
    rcl Frequency_Hz        ; rf frequency in hz
    6.28318E-6 *            ; to radians / microsecond
    sto omega               ; save frequency in radians / usec
    rtn                     ; return from subroutine


lbl ejectall                ; ejects all remaining ions by pulsing left endcap
```

```
      rcl eject_flag
      x=0 beep
      1 sto eject_flag
      rcl pulse_out_amplitude_V
      sto Adj_Elect01

      exit

;-------------------------------------------------------
seg tstep_adjust              ; keep time step <= 0.05 of trap frequency
   rcl frequency_Hz
   1000000 /                  ; cycles per microsecond
   1/x                     ; period of trap, microsec
   20 /
   sto min_time_step
   rcl ion_time_step
   rcl min_time_step
   x>y exit
   sto ion_time_step


;-----------------------------------------------------------------------
seg Other_Actions              ; control pe surface updates
   rcl ion_vz_mm               ; mean free path cooling using real collision parameters
   rcl ion_vy_mm               ; load velocity vectors
   rcl ion_vx_mm
   >p3d                     ; convert velocity to polar coords
      sto v                 ; save in temporary variables


   rcl v rcl ion_time_step *      ; compute distance from tstep * v
   rcl _mean_free_path_mm / chs e^x
   1 x<>y -                    ;(1-e(-d/fp))
   rand                     ;get random number from 0 - 1
   x>y goto next                ; no collision
                           ; collision follows

   rcl _gas_temp_k
   24943 *
   rcl ion_mass /
   sqrt                     ; this result is v=sqrt(3kT/m) in m/s
   0.001 *                    ; km/s or mm/us
   sto mean_velocity_neutral
   rand
   0.5 -
   8 /
```

```
1 +
rcl mean_velocity_neutral *
sto neutral_velocity
rand 0.5 -
360 *
sto el_neutral
rand 0.5 -
180 *
sto az_neutral
rcl el_neutral
rcl az_neutral
rcl neutral_velocity
>R3D
sto neutral_vx
rlup sto neutral_vy
rlup sto neutral_vz          ; defines properties of He atom prior to impact
rcl ion_vz_mm
rcl neutral_vz -
sto ion_vz                   ; ion velocity z in frame of ref of He
rcl ion_vy_mm
rcl neutral_vy -
sto ion_vy
rcl ion_vx_mm
rcl neutral_vx -
sto ion_vx                   ; ion velocities put in He frame of reference

rcl ion_vz
rcl ion_vy
rcl ion_vx
>p3d                        ; ion parameters in He frame in polar coordinates
sto ion_v_ref
rlup sto ion_az_ref
rlup sto ion_el_ref

1
rand
rand *
-
ASIN
sto omicron                  ; radial angle of impact
3.14
rand 0.5 -
*
sto psi                     ; modifies impact angle
rcl psi
SIN
```

```
rcl omicron *
57.3 *
sto beta_degrees
rcl psi
COS
rcl omicron *
57.3 *
sto phi_degrees
rcl ion_el_ref
rcl beta_degrees +
sto impulse_el
rcl ion_az_ref
rcl phi_degrees +
sto impulse_az                ; impulse direction specified in He frame
rcl impulse_el
rcl impulse_az
rcl ion_v_ref
>r3d
sto impulse_x
rlup sto impulse_y
rlup sto impulse_z
rcl impulse_y
rcl impulse_x /
sto T_impulse               ; T is v2y/v2x final velocities, direction of impulse
rcl impulse_z
rcl impulse_x /
sto U_impulse               ; U impulse direction, related to T

rcl _collision_gas_mass
rcl ion_mass /
sto M_impulse               ; ratio of masses, useful for future calculations

rcl ion_vz
rcl U_impulse *
rcl ion_vy
rcl T_impulse *
+
rcl ion_vx +
-2 *
sto b_quadratic
rcl U_impulse
rcl U_impulse *
rcl T_impulse
rcl T_impulse *
+
1 +
```

```
rcl M_impulse
1 +
*
sto a_quadratic
rcl b_quadratic
rcl a_quadratic /
sto Q_quadratic

rcl M_impulse
rcl Q_quadratic *
rcl ion_vx +
sto ion_final_vx

rcl M_impulse
rcl Q_quadratic *
rcl T_impulse *
rcl ion_vy +
sto ion_final_vy

rcl M_impulse
rcl Q_quadratic *
rcl U_impulse *
rcl ion_vz +
sto ion_final_vz          ; ion final velocities in He reference frame

rcl ion_final_vx
rcl neutral_vx +
sto ion_vx_mm

rcl ion_final_vy
rcl neutral_vy +
sto ion_vy_mm

rcl ion_final_vz
rcl neutral_vz +
sto ion_vz_mm             ; ions are now in lab reference frame after collision
15
rcl _ion_colors
x>y
15 sto _ion_colors
rcl _ion_colors           ; change ion color after collision
rcl ion_color
X>=Y gsb recycle
rcl ion_color
1 +
sto ion_color
```

```
   goto next

lbl recycle
   0 sto ion_color
   goto next

lbl next
   rcl Next_PE_Update            ; recall time for next pe surface update
   rcl ion_time_of_flight        ; recall ion's time of flight
   x<y exit                      ; exit if tof less than next pe update
   rcl PE_Update_each_usec       ; recall pe update increment
   + sto next_pe_update          ; add to tof and store as next pe update
   1 sto Update_PE_Surface       ; request a pe surface update



;---------------------------------------------------------------------
seg Terminate
         0 sto rerun_flym       ; turn off rerun mode
```

APPENDIX E

SIMIION supports user-written programs that allow programmatic access to and control over most properties of ions and fields, as well as timing and computational parameters. In this way time-varying electric fields, ion-neutral collisions, and randomization of initial ion properties are possible. This appendix outlines the specific algorithms used for the work presented here in specifying initial ion kinetic energies and positions, determining the outcome of ion-neutral collisions, and determining the number of collisions ions undergo. Note that SIMION treats all positions, velocities, etc. in Cartesian coordinates, so results in polar notation are converted to Cartesian in the program. In the following, the z-axis is the axis of approximate cylindrical symmetry of the trap.

E.1 Initial Ion Velocities

In determining initial ion velocities we assume that the ionization process does not change the kinetic energy or trajectory of the species being ionized, and we further assume that it was in thermal equilibrium prior to, and immediately upon ionization. The velocity distribution of ions under such conditions is a Maxwell, or spherical normal distribution, in which components in (x, y, z) represent independent normal distributions with common variance and mean zero. Thus the Cartesian velocity components are represented by three independent Gaussian distribution functions of the form

$$f\left(v_u\right) = ae^{-bv_u^2} \tag{E.1}$$

where u designates x, y, or z; where b is half the inverse of the variance, and has a value

$$b = \frac{m}{2k_bT} \tag{E.2}$$

and where normalization of the distribution function yields a with value

$$a = \sqrt{\frac{b}{\pi}} = \sqrt{\frac{m}{2\pi k_bT}} \tag{E.3}$$

Implementing these results into a computational algorithm involves randomly generating values for v_x, v_y, and v_z for each ion in such a way that the probability distribution function for each velocity component is Gaussian with the calculated variance. Standard computer random number generators, including that used in SIMION, produce random numbers (X) with a flat probability distribution, and a range of 0-1, thus the normalized distribution function is $f(x) = 1$. The mean of X is $\mu = ½$. The variance, σ^2, is defined as the value of the second central moment, and is calculated using

$$\sigma^2 \equiv E\left[\left(X-\mu\right)^2\right] = \int_0^1 x^2\left(f\left(x\right)-\mu\right)^2 dx = \frac{1}{4}\int_0^1 x^2 dx = \frac{1}{12} \tag{E.4}$$

According to the Central Limit Theorem, the sum (Y_n) of a large number (n) of such random numbers has an approximately Gaussian probability distribution centered at $n/2$. Because variances of uncorrelated random variables are additive, the variance of Y_n is $n/12$. Visual inspection of such distributions shows that $n = 5$ suffices for the purposes of this program. We define the scaling function $g(Y_n) = cY_n$ where c is used to set the variance of $g(Y_n)$ equal to the variance of the desired velocity distributions of ions. The value of c is determined by:

$$\frac{k_b T}{m} = \frac{n}{12} c \qquad \text{(E.5)}$$

and finally the velocity component is calculated using the relation

$$v_u = \left(Y_n - \frac{n}{2} \right) \sqrt{c} \qquad \text{(E.6)}$$

E.2 Initial Ion Positions

Ions originate within a cylindrical volume of radius R and length L, which are entered at the start of each simulation. For each ion, the radial position, r, is determined using the square root of a single random number, scaled by the radius of the desired cylinder, $r = R\sqrt{X}$. The ion is then assigned a random angle, ϕ, with range 0-2π. The x and y coordinates of the ion are then determined using $r\sin\phi$ and $r\cos\phi$, respectively. The z component of the ion is simply a random number scaled by L. The resulting distribution is equivalent to that made by taking a flat distribution within a rectangular solid and explicitly excluding those ions that fall outside of an inscribed cylinder, which is the method used by the program ITSIM.

E.3 Collision Mechanics

Once the program determines that a collision takes place (using the probability function given in Section 2), the program uses the following procedure to determine the velocity components of the ion after the collision. The velocity components of the neutral species prior to impact are determined using the same method as that used for initial ion properties (Section A.1). Following that, the ion trajectory (before collision) is put into the reference frame of the neutral species, with the orientations of the x, y, and z axes remaining the same as the SIMION workbench. The neutral species (which is now at rest) is assumed to be a sphere with radius r_n. The ion approaches the neutral at an angle, β, which SIMION treats as a combination of elevational (el) and azimuthal (az) angles. At the moment of impact, momentum is transferred from the ion to the neutral in the direction normal to the surface of the sphere at the point of impact. Because the neutral is stationary prior to impact, the direction with which momentum is transferred becomes the direction of motion for the neutral after the collision. Let this angle be called α, defined as the angle between the pre-collision ion motion and the post-collision neutral motion. Figure 13 diagrams the collision from two angles: the top schematic (a) shows the plane containing both the center of the neutral and the line containing the trajectory of the ion prior to collision, while the bottom schematic (b) shows the neutral as seen from the approaching ion (the ion is out of the page). The point of impact is represented by an asterisk (*). The radial

distribution of the impact point is $r_n\sqrt{X}$, while the angular distribution, θ, is randomized through 2π angles (determined using θ = 2π*X*). Note that $\sin\alpha = r_n\sqrt{X}$. The elevational and azimuthal components of the neutral motion are determined using the relations:

$$\begin{aligned} \text{el} &= \beta + \alpha\sin\theta \\ \text{az} &= \beta + \alpha\cos\theta \end{aligned} \qquad \text{(E.7)}$$

which angles are then converted into ratios v_x/v_y and v_y/v_z for the neutral. The reference for angle θ is arbitrary, but cancels out since θ spans 2π. Also, the orientation of the components sinθ and cosθ with respect to the SIMION coordinate system is arbitrary, but cancels out, so a rigorous transformation is not needed.

This calculation can be approached in a much simpler fashion, while still producing the same distribution of scattering angles and velocities. The probability distribution of the sine of a random number (*Y* = *sin*(*X*)) is identical to the distribution of forward/backward scattering angles for ions after a collision. Thus, after conversion to the frame of reference of the neutral at rest, the forward scattering angle can be found by scaling the sine of a random number to the maximum scattering angle, θ_{max}, which is $\theta_{max} = m_{neutral}/m_{ion}$ if the ion is more massive than the neutral, and $\theta_{max} = \pi$ in all other cases. This alternate algorithm was realized after the present studies commenced, and so was not used.

For two-body elastic collisions, conservation of momentum and energy provide four constraints on the six variables (three velocity components for the ion, three for the neutral). The randomized values v_x/v_y and v_y/v_z of the neutral species provide the other two constraints. Solving these equations gives the following for the changes in the ion velocity components upon collision:

$$\Delta v_{x_i} = \left(\frac{m_n}{m_i}\right)\left(\frac{-2\left(v_{x_i} + v_{z_i}U + v_{y_i}W\right)}{\left(\frac{m_n}{m_i}+1\right)\left(U^2+W^2+1\right)}\right) \qquad \text{(E.8)}$$

$$\Delta v_{y_i} = \left(\frac{Wm_n}{m_i}\right)\left(\frac{-2\left(v_{x_i} + v_{z_i}U + v_{y_i}W\right)}{\left(\frac{m_n}{m_i}+1\right)\left(U^2+W^2+1\right)}\right) \qquad \text{(E.9)}$$

$$\Delta v_{z_i} = \left(\frac{Um_n}{m_i}\right)\left(\frac{-2\left(v_{x_i} + v_{z_i}U + v_{y_i}W\right)}{\left(\frac{m_n}{m_i}+1\right)\left(U^2+W^2+1\right)}\right) \qquad \text{(E.10)}$$

where m_n and m_i are the mass of neutral and ion, respectively, and U and W are the ratios of post-collision neutral velocities defined as:

$$U = \frac{v_{z_n}}{v_{x_n}} \tag{E.11}$$

$$W = \frac{v_{y_n}}{v_{x_n}} \tag{E.12}$$

Subsequently, the ion velocity components are restored to the lab frame of reference. In this computer program the ion color also changed upon each collision, allowing visual observations of collisions.

E.4 Collision Counting

SIMION is unable to export information other than the values of reserved variables (e.g., ion properties) at given points in time, so the collision count had to piggyback on a reserved variable. The number of collisions each ion experienced was tracked in the following manner: each time an ion collided with a neutral, the mass of the ion was incremented by 10^{-9} amu. At the end of each simulation the mass of each ion was recorded. The outcomes of simulations did not appear to be affected by this small increase in mass.

APPENDIX F

Table F-1. DC resistance measurements for wafer JF45601C-W11.

Dice	Array	S12 Collector	S12 Ring	Shorted	Null
44	1.00E+04	5.75	5.03	4.20	Open
	1.00E+05	6.98	6.98	3.95	Open
45	1.00E+04	5.80	4.5	3.30	Open
	1.00E+05	5.60	6.25	3.80	Open
46	1.00E+04	21.99	5.07	3.92	Open
	1.00E+05	5.88	6.15	3.68	Open
51	1.00E+04	5.49	4.63	3.60	Open
	1.00E+05	5.91	6.49	3.78	Open
52	1.00E+04	5.26	4.53	3.35	Open
	1.00E+05	5.83	6.90	3.25	Open
53	1.00E+04	5.34	4.62	3.54	Open
	1.00E+05	5.61	6.11	3.74	Open
54	1.00E+04	6.04	4.59	3.75	Open
	1.00E+05	5.88	6.31	3.53	Open

Table F-2. DC measurements using an hp3478a multimeter for the r_0=1μm large sized array.

WAFER	JF45601C-W12 Q3 RELEASE ID 4641					
Dice no.	Coll/BEC	Coll/Ring	Coll/ TEC	BEC/Ring	BEC/TEC	Ring/TEC
1	OPEN	OPEN	OPEN	OPEN	OPEN	OPEN
2	OPEN	OPEN	OPEN	OPEN	OPEN	OPEN
3	OPEN			14 MΩ		1.1 MΩ
4	PARTICLES					0.5 MΩ
5			OPEN			5.0 MΩ
6						4.7 MΩ
7	OPEN	OPEN	OPEN	OPEN	OPEN	OPEN
	WAFER JF45601C-W12 Q4 RELEASE ID 4641					
9	OPEN	OPEN	OPEN	OPEN	OPEN	OPEN
10	OPEN	OPEN	OPEN	OPEN	OPEN	OPEN
11						0.6 MΩ
12	OPEN	OPEN	OPEN	OPEN	OPEN	OPEN
13						2.8 KΩ
14						8.1 MΩ
15	OPEN	OPEN	OPEN	OPEN	OPEN	OPEN
16	OPEN	OPEN	OPEN	OPEN	OPEN	OPEN
17						5.6 MΩ

Table F-3. DC measurements using an hp3478a multimeter for the r_0=5μm medium sized array.

WAFER	JF45602B-W08 r_0=5μm medium sized array RELEASE ID 4932					
Dice no.	Coll/BEC	Coll/Ring	Coll/ TEC	BEC/Ring	BEC/TEC	Ring/TEC
1						1.25 Ω
2	OPEN	OPEN	OPEN	OPEN	OPEN	OPEN
3		OPEN			OPEN	0.33 KΩ
4	OPEN	OPEN	OPEN	OPEN	OPEN	OPEN
5		OPEN		7.6 MΩ	OPEN	OPEN
6	OPEN	OPEN	OPEN	OPEN	OPEN	OPEN
7	OPEN	OPEN	OPEN	OPEN	OPEN	OPEN
8	OPEN	OPEN	OPEN	OPEN	OPEN	OPEN
9			DISCOLORED			0.6 KΩ
10	OPEN	OPEN	OPEN	OPEN	OPEN	OPEN
11	OPEN	OPEN	OPEN	OPEN	OPEN	OPEN
12	OPEN	OPEN	OPEN	OPEN	OPEN	OPEN
13		OPEN			OPEN	63 KΩ
14	OPEN	OPEN	OPEN	OPEN	OPEN	OPEN
15	OPEN	OPEN	OPEN	OPEN	OPEN	OPEN
16	OPEN	OPEN	OPEN	OPEN	OPEN	OPEN
17	OPEN	OPEN	OPEN	OPEN	OPEN	OPEN
18		PROBE INTO ARRAY BY MISTAKE				OPEN
19	OPEN	OPEN	OPEN	OPEN	OPEN	OPEN
20		OPEN			OPEN	0.28 KΩ

Table F-4. DC measurements using an Fluke 179 multimeter for the r_0=2μm medium sized packaged array.

WAFER	JF45602A-W12 r_0=2μm medium sized array RELEASE ID 4932					
Dice no.	Coll/BEC	Coll/Ring	Coll/ TEC	BEC/Ring	BEC/TEC	Ring/TEC
1	OPEN	OPEN	OPEN	OPEN	OPEN	OPEN
2	0.4 KΩ	15 Ω	3 KΩ	95 Ω	28 KΩ	2.7 KΩ
3	OPEN	OPEN	OPEN	OPEN	OPEN	OPEN
4				OPEN		53 Ω
5	OPEN	OPEN	OPEN	OPEN	OPEN	28 MΩ
6	OPEN	OPEN	OPEN	OPEN	OPEN	OPEN
7	OPEN	0.5 KΩ	OPEN	OPEN	OPEN	OPEN
8	OPEN	OPEN	OPEN	OPEN	OPEN	OPEN
9	OPEN	OPEN	OPEN	5.4 MΩ	0.5 KΩ	OPEN
10	OPEN	OPEN	OPEN	OPEN	OPEN	230 Ω
11	OPEN	OPEN	OPEN	OPEN	OPEN	OPEN
12	OPEN	OPEN	OPEN	OPEN	OPEN	OPEN

Table F-5. DC measurements using an Fluke 179 multimeter for the r_0=5μm medium sized packaged array.

WAFER	JF45602B-W08 r_0=5μm medium sized array RELEASE ID 4932					
Dice no.	Coll/BEC	Coll/Ring	Coll/ TEC	BEC/Ring	BEC/TEC	Ring/TEC
1	OPEN	OPEN	OPEN	OPEN	OPEN	OPEN
2	OPEN	OPEN	OPEN	OPEN	OPEN	OPEN
3	OPEN	OPEN	OPEN	OPEN	OPEN	OPEN
4	OPEN	OPEN	OPEN	OPEN	OPEN	OPEN
5	OPEN	OPEN	OPEN	OPEN	OPEN	OPEN
6	OPEN	OPEN	OPEN	OPEN	OPEN	OPEN
7	OPEN	0.5 KΩ	OPEN	OPEN	OPEN	7.2 KΩ
8	OPEN	OPEN	OPEN	OPEN	OPEN	11 MΩ
9	OPEN	OPEN	OPEN	OPEN	OPEN	OPEN
10	OPEN	OPEN	OPEN	OPEN	OPEN	OPEN
11	OPEN	OPEN	OPEN	OPEN	OPEN	19.6 Ω
12	OPEN	OPEN	OPEN	OPEN	OPEN	108.9 Ω
13	OPEN	OPEN	OPEN	OPEN	OPEN	OPEN
14	OPEN	OPEN	OPEN	OPEN	OPEN	OPEN
15	OPEN	OPEN	OPEN	OPEN	OPEN	0.75 KΩ

APPENDIX G

Table G-1. Capacitance measurements made with an HP4284A LCR meter.

Measurement	r_0 (μm)	Structure	Array Size	C (pF)	G_p (μS) 10KHz	G_p (μS) 100KHz
BEC:RE	1	S11	1E5	71.74	0.006	0.30
TEC:RE	1	S11	1E5	76.5	0.003	0.06
BEC:RE	1	S11	1E5	70.4	0.003	0.05
TEC:RE	1	S11	1E5	75.4	0.003	0.09
BEC:RE	1	S11	1E5	69.1	0.003	0.045
TEC:RE	1	S11	1E5	74.8	0.003	0.09
BEC:RE	1	S11	1E5	71.2	0.003	0.07
TEC:RE	1	S11	1E5	75.7	0.003	0.09
BEC:RE	1	S11	1E5	72.8	0.006	0.34
TEC:RE	1	S11	1E5	77.1	0.003	0.08
BEC:RE	1	S11	1E5	71.7	0.003	0.07
TEC:RE	1	S11	1E5	76.1	0.003	0.09
RE:ALL (BEC PAD)	1	S12	1E5	120.1	0.015	0.98
RE:ALL (TEC PAD)	1	S12	1E5	120.1	0.007	0.19
RE:ALL (BEC PAD)	1	S12	1E5	124.7	0.007	0.17
RE:ALL (TEC PAD)	1	S12	1E5	124.6	0.008	0.33
RE:ALL (BEC PAD)	1	S12	1E5	121.4	0.006	0.23
RE:ALL (TEC PAD)	1	S12	1E5	121.3	0.005	0.17
RE:ALL (BEC PAD)	1	S12	1E5	122.7	0.004	2.8
RE:ALL (TEC PAD)	1	S12	1E5	122.7	0.005	0.19
RE:ALL (BEC PAD)	1	S12	1E5	121.7	0.009	0.19
RE:ALL (TEC PAD)	1	S12	1E5	121.7	0.009	0.19
RE:ALL (BEC PAD)	1	S12	1E5	122	0.05	0.20
RE:ALL (TEC PAD)	1	S12	1E5	121.9	0.05	0.22

BIBLIOGRAPHY

Abian, J. (1999). "The coupling of gas and liquid chromatography with mass spectrometry." Journal of Mass Spectrometry **34**(3): 157-168.

Abraham, G. T., A. Chatterjee, et al. (2004). "Escape velocity and resonant ion dynamics in Paul trap mass spectrometers." International Journal of Mass Spectrometry **231**(1): 1-16.

Agilent (2005). Agilent Website (http://www.agilent.com).

Andricacos, P. C., C. Uzoh, et al. (1998). "Damascene copper electroplating for chip interconnections." IBM Journal of Research and Development **42**(5): 567-573.

Badman, E. R. and R. G. Cooks (2000). "Cylindrical Ion Trap Array with Mass Selection by Variation in Trap Dimensions." Analytical Chemistry **72**: 5079-5086.

Badman, E. R. and R. G. Cooks (2000). "Miniature Mass analyzers." Journal of Mass Spectrometry **35**: 659-671.

Badman, E. R. and R. G. Cooks (2000). "A Parallel Miniature Cylindrical Ion Trap Array." Analytical Chemistry **72**(14): 3291-3297.

Badman, E. R. and R. G. Cooks (2000). "A Parallel Miniature Cylindrical Ion Trap Array." Analytical Chemistry **72**: 3291-3297.

Badman, E. R., R. C. Johnson, et al. (1998). "A Miniature Cylindrical Quadrupole Ion Trap: Simulation and Experiment." Analytical Chemistry **70**: 4896-4901.

Baril, M., R. Le, et al. (1990). "An improved and accurate method for the calculation of trajectories in quadrupole mass filters and ion traps using phase space dynamics." International Journal of Mass Spectrometry and Ion Processes **98**(1): 87-97.

Beaty, E. C. (1987). "Simple Electrodes for Quadrupole Ion Traps." Journal of Applied Physics **61**: 2118-2122.

Benenson, W., J. W. Harris, et al., Eds. (2002). Handbook of Physics. New York, Springer-Verlag.

Berkout, V. D., R. J. Cotter, et al. (2001). "Miniaturized EI/Q/oa TOF mass spectrometer." Journal of the American Society of Mass Spectrometry **12**: 641-647.

Blain, M. G., L. S. Riter, et al. (2004). "Towards the hand-held mass spectrometer: design considerations, simulation and fabrication of micrometer-scaled cylindrical ion traps." International Journal of Mass Spectrometry **236**: 91-104.

Borst, C. L., W. N. Gill, et al. (2002). Chemical-Mechanical Polishing of Low Dielectric Constant Polymers and Organosilicate Glasses: Fundamental Mechanisms and Application to IC Interconnect Technology. New York, Springer.

Boumsellek, S. and R. J. Ferran (2001). "Trade-offs in miniature quadrupole designs." Journal of the American Society of Mass Spectrometry **12**(6): 633-640.

Brebbia, C. A. (1992). Boundary Elements: An Introductory Course. New York, McGraw-Hill.

Brewer, R. G., R. G. DeVoe, et al. (1992). "Planar ion microtraps." Physical Review A **46**(11): R6781-R6784.

Bui, H. A. and R. G. Cooks (1998). "Windows Version of the Ion Trap Simulation Program ITSIM: a Powerful Heuristic and Predictive Tool in Ion Trap Mass Spectrometry." Journal of Mass Spectrometry **33**: 297-304.

Cadien, K. C. and D. L. Losee (1984). "A method for eliminating hillocks in integrated-circuit metallizations." Journal of Vacuum Science and Technology B **2**(1): 82-83.

Casalnuovo, S. A., G. C. Frye-Mason, et al. (1999). Gas phase chemical detection with an integrated chemical analysis system. Joint Meeting EFTF-IEEE IFCS, Bensacon, France, IEEE.

Chen, K. and Y.-E. Wu (2000). "Thermal analysis and simulation of the microchannel flow in miniature thermal conductivity detectors." Sensors and Actuators **79**: 211-218.

Cirac, J. I. and P. Zoller (1995). "Quantum Computations with Cold Trapped Ions." Physical Review Letters **74**(20): 4091-4094.

Ciucanu, I. and A. Chriac (2002). "Membrane and trap system for continuous monitoring of volatile organic compounds using a portable gas chromatograph with thermal conductivity detector." Journal of Separation Science **25**: 447-452.

Cooper, R. K., M. T. Menzel, et al. (1987). New Documentation from the Los Alamos Accelerator Code Group. IEEE Particle Accelerator Conference.

Cooperberg, D. J., V. Vahedi, et al. (2002). "Semiempirical profile simulation of aluminum etching in a Cl2/BCl3 plasma." Journal of Vacuum Science and Technology A **20**(5): 1536-1556.

Cruz, D., J. P. Chang, et al. (2005). "Field-Emission Characteristics of a tungsten Microelectromechanical System Device" Applied Physics Letters **86**(15): 3502.

Dahl, D. A. (2000). SimIon 6.0 and 7.0 ed., Idaho National Engineering and Environmental Laboratory: Idaho Falls, ID.

Dawson, P. H., Ed. (1976). Quadrupole Mass Spectrometry and its applications. Amsterdam, Elsevier.

Daynes, H. A. (1933). Gas Analysis by Measurement of Thermal Conductivity. Cambridge, Great Britain, Cambridge University Press.

Dehmelt, H. G. (1967). "Radiofrequency Spectroscopy of Stored Ions I: Storage." Advance Atomic Molecular Physics **3**: 53-72.

Dehmelt, H. G. (1969). "Radiofrequency Spectroscopy of Stored Ions II: Spectroscopy." Advance Atomic Molecular Physics **5**: 109-154.

Denn, M. (1980). Process Fluid Mechanics. Englewood Cliffs, NJ, Prentice Hall, Inc.

DeVoe, R. G. and C. Kurtsiefer (2002). "Experimental study of anomalous heating and trap instabilities in a microscopic 137Ba ion trap." Physical Review A **65**: 063407-1:063407-8.

Diaz, J. A., C. F. Giese, et al. (2001). "Portable double-focusing mass-spectrometer system for field gas monitoring." Field Analytical Chemistry & Technology **5**(3): 156-167.

Diaz, J. A., C. F. Giese, et al. (2001). "Sub-miniature ExB sector-field mass spectrometer." Journal of the American Society of Mass Spectrometry **12**(6): 619-632.

Diaz, J. A., C. F. Giese, et al. (2002). "Mass spectrometry for in-situ volcanic gas monitoring." TrAC Trends in Analytical Chemistry **21**(8): 498-514.

Ding, L., M. Sudakov, et al. (2002). "A simulation study of the digital ion trap mass spectrometer." International Journal of Mass Spectrometry **221**(2): 117-138.

Dobkin, D. M. and M. K. Zuraw, Eds. (2003). Principles of Chemical Vapor Deposition What's Going on Inside the Reactor. New York, Kluwer Academic Publishers.

Driskill-Smith, A. A. G., D. G. Hasko, et al. (1997). "Nanoscale field emission structures for ultra-low voltage operation at atmospheric pressure." Applied Physics Letters **71**(24): 3159-3161.

Durr, W., U. Erben, et al. (1998). "Investigation of microstrip and coplanar transmission lines on lossy silicon substrates without backside metallization." IEEE Transactions on Microwave Theory and Techniques **46**(5): 712-715.

Dziuban, J. A., J. Mroz, et al. (2004). "Portable gas chromatograph with integrated components." Sensors and Actuators A **115**: 318-330.

Facer, G. R., D. A. Notterman, et al. (2001). "Dielectric spectroscopy for bioanalysis: From 40 Hz to 26.5 GHz in a microfabricated wave guide." Applied Physics Letters **78**: 996.

Ferran, R. J. and S. Boumsellek (1996). "High-pressure effects in miniature arrays of quadrupole analyzers for residual gas analysis from 10^-9 to 10^-2 Torr." Journal of Vacuum Science and Technology A **14**(3): 1258-1265.

Fischer, A. J., K. D. Choquette, et al. (2001). "High single-mode power observed from a coupled-resonator vertical-cavity laser diode." Applied Physics Letters **79**: 4079.

Fisk, P. T. H. (1997). Reports on Progressive Physics **60**: 761.

Fleming, J. G., S. Y. Lin, et al. (2002). "All-metallic three-dimensional photonic crystals with a large infrared badgap." Nature **417**: 52-55.

Fleming, J. G., E. Roherty-Osmun, et al. (1995). Growth and Properties of W, B, N Based Diffusion Barriers Deposited by Chemical Vapor Deposition. Advanced Metalization and Interconnect Systems for ULSI application in 1995., Portland, OR.

Frangsmyr, T., Ed. (1990). Les Prix Nobel. The Nobel Prizes 1989. Stockholm, Nobel Foundation.

Frye-Mason, G. C., R. P. Manginell, et al. (1999). Microfabricated Gas Phase Chemical Analysis System. International Microprocesses and Nanotechnology Conference, Tokyo, Japan.

Fursey, G. N., D. N. Novikov, et al. (2003). "The field emission from carbon nanotubes." Applied Surface Science **215**: 135-140.

Gajda, M. A. and H. Ahmed (1995). "Applications of thermal silicon sensors on membranes." Sensors and Actuators A **49**(1): 1-9.

Goldstein, J. I., D. E. Newbury, et al., Eds. (1992). Scanning Electron Microscopy and X-Ray Microanalysis A text for Biologist, Mareials Scientists, and Geologist. New York, Plenum Press.

Gomer, R. (1961). Field Emission and Field Ionization. Cambridge, MA, Harvard University Press.

Grob, R. L., Ed. (1995). Modern Practice of Gas Chromatography. New York, Wiley Interscience.

Hao, C. and R. E. March (2001). "A survey of recent research activity in quadrupole ion trap mass spectrometry." International Journal of Mass Spectrometry **212**: 337-357.

Hebner, G. A., M. G. Blain, et al. (1999). "Influence of surface material on the boron chloride density in inductively coupled discharges." Journal of Vacuum Science and Technology A **17**(6): 3218-3224.

Hebner, G. A., M. G. Blain, et al. (1999). "Surface dependent electron and negative ion density in inductively coupled discharges." Journal of Vacuum Science and Technology A **17**(6): 3172-3178.

Henry, C. M. (1999). "The Incredible Shrinking Mass Spectrometers." Analytical Chemistry News and Features: 264A-268A.

Herman, D. S., M. A. Schuster, et al. (1971). "Hillock Growth on Vacuum Deposited Aluminum Films." Journal of Vacuum Science and Technology **9**(1): 515-519.

Ho, P., J. E. Johannes, et al. (2001). "Modeling the plasma chemistry of C2F6 and CHF3 etching of silicon dioxide, with comparisons to etch rate and diagnostic data." Journal of Vacuum Science and Technology A **19**(5): 2344-2367.

Horvath, G. Z. K., R. C. Thompson, et al. (1997). "Fundamental physics with trapped ions." Contemporary Physics **38**(1): 25-48.

Itoh, J., K. Tsuburaya, et al. (1992). "Low-Operation-Voltage Comb-Shaped Field Emitter Array." Japanese Journal of Applied Physics **31**: L884-L886.

Jaeger, R. S. (1993). Introduction to Microelectronic Fabrication. New York, Addison-Wesley Publishing Company.

Jansen, F. (1998). Plasma-Enhanced Chemical Vapor Deposition (AVS monograph series). New York, American Vacuum Society.

Jerman, J. H. (1981). A miniature thin-film thermal conductivity detector for an integrated gas chromatograph. Stanford, Ca, Stanford University. **Ph.D.**

JMP (2005). JMP: The Statistical Discovery Software (http://www.jmp.com).

Jones, W. (1980). "Earnshaw's Theorem and the Stability of Matter." European Journal of Physics **1**: 85-88.

Kawamura, Y. (2001). "Development of a micro gas chromatograph for the analysis of hydrogen isotope gas mixtures in the fusion fuel cycle." Fusion Engineering and Design **58-59**: 389-394.

Kim, D.-k., B. Heiland, et al. (2000). "Microstructure of thermal hillocks on blanket Al thin films." Thin Solid Films **371**: 278-282.

Kim, Y.-K., K. K. Irikura, et al. (2005). NIST: Electron-Impact Cross sections for Ionization and Excitation (http://physics.nist.gov/PhysRefData/Ionization).

Kim, Y.-M., W.-S. Kim, et al. (2005). "A Numerical Study of the Thermal entrance Effect in Miniature Thermal Conductivity Detectors." Heat Transfer Engineering **26**(4): 65-72.

Kimura, M., J. Manaka, et al. (1995). "Application of the air-bridge microheater to gas detection." Sensors and Actuators B **25**: 857-860.

Kornienko, O., P. T. A. Reilly, et al. (1999). "Electron impact ionization in a microion trap mass spectrometer." Review of Scientific Instruments **70**(10): 3907-3909.

Kornienko, O., P. T. A. Reilly, et al. (1999). "Micro Ion Trap Mass Spectrometry." Rapid Communications in Mass Spectrometry
13: 50-53.

Kovacs, G. T. A. (1998). Micromachined Transducers Sourcebook. San Francisco, McGraw-Hill.

Langmuir, D. B., R. V. Langmuir, et al. (1962). Containment Device. United States. **3,065,640:** 23.

Langmuir, R. V. (1957). Mass Spectrometer. U. S. P. Office. US, General Electric Company. **2806955:** 15.

Laugere, F., G. W. Lubking, et al. (2001). "Downscaling aspets of a conductivity detector for application in on-chip capillary electrophoresis." Sensors and Actuators A **92**: 109-114.

Lee, W.-W., S.-K. Min, et al. (2003). "Stability of ion motion in the quadrupole ion trap driven by rectangular waveform voltages." International Journal of Mass Spectrometry **230**(1): 65-70.

Lee, W.-W., C.-H. Oh, et al. (2003). "Characteristics of cylindrical ion trap." International Journal of Mass Spectrometry **230**: 25-31.

Lide, D. R., Ed. (2004). CRC Handbook of Chemistry and Physics. Boca Raton, Fl., CRC Press.

Lieberman, M. A. and A. J. Lichtenberg (1994). Principles of Plasma Discharges and Materials Processing. New York, John Wiley & Sons, Inc.

Liebfried, D., R. Blatt, et al. (2003). "Quantum dynamics of single trapped ions." Review of Modern Physics **281**.

Londry, F. A., R. L. Alfred, et al. (1993). "Computer simulation of single-ion trajectories in Paul-type ion traps." Journal of the American Society for Mass Spectrometry **4**(9): 687-705.

Lujan, R. D., J. G. Fleming, et al. (1994). New Novel Cleaning Technique for Extending Mean Time Between Mechanical Cleans in a Genus Tungsten CVD Reactor. Ceramics and Advanced Materials Symposia, Albuquerque, NM.

Lysko, J. M., M. Gorska, et al. (2003). Silicon thermal conductivity detector (TCD) with the Pt resistors. SPIE.

Madou, M. (1997). Fundamentals of Microfabrication. New York, CRC Press LLC.

Malyshev, M. V., V. M. Donnelly, et al. (2000). "Diagnostic studies of aluminum etching in an inductively coupled plasma system: Determination of electron temperatures and connections to plasma-induced damage." Journal of Vacuum Science and Technology A **18**(3): 849-859.

Manginell, R. P., P. R. Lewis, et al. (2004). Recent Advancements in the Gas-Phase MicroChemLab(TM). Lab-on-a-Chip: Platforms, Devices, and Applications.

March, R. E., Ed. (1989). Quadrupole Storage Mass Spectrometry. New York, Wiley Interscience.

March, R. E. (1997). "An Introduction to Quadrupole Ion Trap Mass Spectrometry." Journal of Mass Spectrometry **32**(4): 351-369.

March, R. E. (2000). "Quadrupole ion trap mass spectrometry: a view at the turn of the century." International Journal of Mass Spectrometry **200**: 285-312.

March, R. E., F. A. Londry, et al. (1992). "Mass-selective isolation of ions stored in a quadrupole ion trap. A simulation study." International Journal of Mass Spectrometry and Ion Processes **112**(2-3): 247-271.

March, R. E. and J. J. Todd, Eds. (1995). Practical Aspects of Ion Trap Mass Spectrometry. Boca Raton, FL, CRC Press.

March, R. E. and J. J. Todd, Eds. (1995). Practical Aspects of Ion Trap Mass Spectrometry. Boca Raton, FL., CRC Press.

Mark, T. D. and G. H. Dunn, Eds. (1985). Electron Impact Ionization. New York, Springer-Verlag Wien.

Martin, B. C., C. J. Tracy, et al. (1995). "A comparative study of hillock formation in aluminum films." Thin Solid Films **271**(64-68).

Martin, S. J., M. A. Butler, et al. (1998). "Flexural plate wave resonator excited with Lorentz forces." Journal of Applied Physics **83**(9): 4589-4601.

Martin, S. J., M. A. Butler, et al. (1998). "Magnetically-excited flexural plate wave resonator." IEEE Transactions on Ultrasonics, Ferroelectrics, and Frequency Control **45**(5): 1381-1387.

Martin, S. J., G. C. Frye-Mason, et al. (1996). Gas Sensing with Acoustic Devices. IEEE Ultrasonics Symposium, IEEE.

McGuire, G. E., Ed. (1988). Semiconductor Materials and Process Technology Handbook. New York, William Andrew Publishing/Noyes.

McLahlan, N. W. (1947). Theory and Applications of Mathieu Functions. Oxford, Clarendon.

Merkle, P. B. and T. L. Myers (1998). End-point process development for low-volume, high reliability tungsten CMP. VLSI Multilevel Interconnection Conference CMP, Santa Clara, CA.

Milanovic, V., L. Doherty, et al. (2001). "Micromachining technology for lateral field emission devices." IEEE Transactions on Electron Devices **48**(1): 166-173.

Milanovic, V., M. Ozgur, et al. (1998). "Characterization of Broad-Band Transmission for Coplanar Waveguides on CMOS Silicon Substrates." IEEE Transactions on Microwave Theory and Techniques **46**(5): 632-640.

Moorman, M., R. P. Manginell, et al. (2003). Microcumbustor array and micro-flame ionization detector fo hydrocarbon detection. MEMS Components and Applications for Industry, Automobiles, Aerospace, and Communication.

Mowry, C. D., R. J. Kottenstette, et al. (2002). Sixth International Symposium on Micro Total Analysis Systems, Nara Japan, Kluwer Academic Publishers.

Muhle, R., M. Dobeli, et al. (1999). "A time-of-flight spectrometer for investigations on liquid metal ion sources." Journal of Physics D: Applied Physics **32**: 161-167.

Muto, H., Y. Kajio, et al. (1998). Thermal conductivity measuring device. United States, Yamatake-Honeywell Co., Ltd. **5,756,878**.

Naguib, H. M., R. A. Bond, et al. (1983). "Planar plasma etching of chromium." Vacuum **33**(5): 285-290.

Nappi, M., C. Weil, et al. (1997). "Visual representations of simulated three-dimensional ion trajectories in an ion trap mass spectrometer." International Journal of Mass Spectrometry and Ion Processes **161**(1-3): 77-85.

Nasby, R. D., J. J. Sniegowski, et al. (1996). Application of Chemical-Mechanical Polishing to Planarization of surface-micromachined Devices. 1996 Solid-State and actuator Workshop, Hilton Head Island, NC.

NIST (2005). NIST Chemistry Webbook (http://webbook.nist.gov).

Orient, O. J. and A. Chutjian (2002). "A compact, high-resolution Paul ion trap mass spectrometer with electron-impact ionization." Review of Scientific Instruments **73**: 2157-2160.

Orient, O. J., A. Chutjian, et al. (1997). "Miniature, high-resolution, quadrupole mass-spectrometer array." Review of Scientific Instruments **68**(3): 1393-1397.

Patterson, G. E., A. J. Guymon, et al. (2002). "Miniature Cylindrical Ion Trap Mass Spectrometer." Analytical Chemistry **74**(24): 6145-6162.

Paul, W. (1990). "Electromagnetic traps for charged and neutral particles." Review of Modern Physics **62**(3): 531-540.

Paul, W. and H. Z. Steinwedel (1953). "A new mass spectrometer without a magnetic field." Naturforsch **8a**: 448-450.

Perrier, P., T. Nguema, et al. (1997). "New operating mode of a quadrupole ion trap in mass spectrometry 4. Simulation studies." International Journal of Mass Spectrometry and Ion Processes **171**(1): 19-29.

Peterson, K., S. Rhode, et al. (2003). Novel LTCC Fabrication Techniques Applied to a Rolled Micro Ion Mobility Spectrometer. 204th Meeting of the Electrochemical Society, Orlando, FL.

Pierson, H. O. (1999). Handbook of Chemical Vapor Deposition Principles, Technology and Applications. New York, Noyes Publications.

Plass, W. R., H. Li, et al. (2003). "Theory, simulation and measurement of chemical mass shifts in RF quadrupole ion traps." International Journal of Mass Spectrometry **228**(2-3): 237-267.

Puttlitz, A. F., J. G. Ryan, et al. (1989). "Semiconductor Interlevel Shorts Caused by Hillock Formation in Al-Cu Metallization." IEEE Transactions on Compoents, Hybrids and Manufacturing Technology **12**(4): 619-626.

Rao, N. N. (1994). Elements of Engineering Electromagnetics. Englewood Cliffs, NJ, Prentice Hall.

Reiser, H.-P., R. K. Julian, et al. (1992). "A versatile method of simulation of the operation of ion trap mass spectrometers." International Journal of Mass Spectrometry and Ion Processes **121**(1-2): 49-63.

Reyna, L. G. and J. R. Sobehart (1994). "Dynamics of confined ions driven by light beams: A singular perturbation approach." Physical Review A **49**(3): 1629-1636.

Riter, L. S., B. C. Laughlin, et al. (2002). "Direct analysis of volatile organic compounds in human breath using a miniaturized cylindrical ion trap mass spectrometer with a membrane inlet." Rapid Communications in Mass Spectrometry **16**: 2370-2373.

Riter, L. S., Y. Peng, et al. (2002). "Analytical performance of a miniature cylindrical ion trap mass spectrometer." Analytical Chemistry **74**(24): 6154-6162.

Rocke, M. and M. Schneegans (1988). "Titanium nitride for antireflection control and hillock suppression on aluminum silicon metallization." Journal of Vacuum Science and Technology B **6**(4): 1113-1115.

Rudolph (1986). Rudolph Technologies, Inc. Corporate Headquarters. One Rudolph Road, Fladers, NJ 07836, U.S.A.

S.White, L., R. Blumenthal, et al. (1990). Tungsten and Other Advanced Metals for ULSI Applications in 1990. Pittsburg, PA.

Schmitz, J. E. J. (1992). Chemical Vapor Deposition of Tungsten and Tungsten Silicides. Park Ridge, NJ, Noyes Publications.

Serkland, D. K., K. D. Choquette, et al. (1999). "Two-element phased array of antiguided vertical-cavity lasers." Applied Physics Letters **75**: 3754.

Serkland, D. K., G. R. Hadley, et al. (2000). "Modal frequencies of vertical-cavity lasers determined by an effective-index model." Applied Physics Letters **77**: 22.

Sewell, H. (1978). "Control of pattern dimensions in electron lithography." Journal of Vacuum Science and Technology **15**(3): 927-930.

Sha, L. and J. P. Chang (2004). "Plasma etching of high dielectric constant materials on silicon in halogen chemistries." Journal of Vacuum Science and Technology A **22**(1): 88-95.

Sheretov, E. P., I. V. Philippov, et al. (2002). "Some properties of ion trajectories in the radial plane of an axially symmetric ion trap." Rapid Communications in Mass Spectrometry **16**(17): 1658-1667.

Simon, I. and M. Arndt (2002). "Thermal and gas-sensing properties of a micromachined thermal conductivity sensor for the detection of hydrogen in automotive applications." Sensors and Actuators A **97-98**: 104-108.

Singh, A. (1985). "A simple technique for eliminating hillocks in integrated circuit metallization." Journal of Vacuum Science and Technology B **3**(3): 923-924.

Sittler, F. C. and J. H. Crabtree (1990). Fluid flow detector. United States, Rosemount Inc. **4,909,078**.

Smith, P. H. (2000). Electronic applications of the smith chart in waveguide, circuit and component analysis. Atlanta, GA, Noble Publishing Corporation.

Smith, P. M., J. G. Fleming, et al. (1993). Chemical Vapor Deposition and characterization of tungsten boron alloy films. Advanced Metalization for ULSI Applications, San Diego, CA.

Sorge, S. and T. Pechstein (1997). "Fully integrated thermal conductivity sensor for gas chromatography without dead volume." Sensors and Actuators A **63**(3): 191-195.

Spindt, C. A., I. Brodie, et al. (1976). "Physical properties of thin-film field emission cathodes with molybdenum cones." Journal of Applied Physics **47**(12): 5248-5263.

Steane, A. (1997). "The ion trap quantum information processor." Applied Physics B **64**: 623-642.

Stein, D. J., T. R. Guilinger, et al. (1996). Polishing Slurries and Electrochemistry of Tungsten in Tungsten CMP. Chemical Mechanical Polishing Users Group, San Jose, CA.

Stein, D. J. and R. Y. S. Her (2000). Role of Alumina Phase and Size in Tungsten CMP. CMP-MIC 2000, Santa Clara, CA.

Stratedge (2005). "StratEdge Corporation (http://www.stratedge.com)."

Syage, J. A., B. Nies, J., et al. (2001). "Field-Portable, High Speed GC/TOFMS." Journal of the American Society of Mass Spectrometry **12**: 648-645.

Tabert, A. M., J. Griep-Raming, et al. (2003). "High Throughput miniature cylindrical ion trap array mass spectrometer." Analytical Chemistry **75**(21): 5656-5664.

Taylor, S., J. J. Tunstall, et al. (1998). "Initial results for a quadrupole mass spectrometer with silicon micromachined mass filter." Electronics Letters **34**(6): 546-547.

Terry, S. C., J. H. Jerman, et al. (1979). "A gas chromatograph air analyzer fabricated on a silicon wafer." IEEE Transactions on Electron Devices **26**: 1880-1886.

Todd, J. J., R. M. Waldren, et al. (1980). "The quadrupole ion store (QUISTOR) part VIII. The theoretical estimation of ion kinetic energies: A comparative survey of the field." International Journal of Mass Spectrometry and Ion Physics **34**: 17-36.

Tompkins, H. G. (1993). A User's Guide to Ellipsometry. San Diego, Academic Press, Inc.

Tondare, V. N., N. Pradeep, et al. (2001). "Field emission from diamond coated tungsten tips." Solid-State Electronics **45**: 957-962.

Tunstall, J. J., S. Taylor, et al. (1998). Silicon micromachined mass filter for a low power, low cost quadrupole mass spectrometer. IEEE Workshop on MEMS, Heidelberg, Germany.

Varian (2005). Varian Website (http://www.varianinc.com/image/vimage/docs/csb/products/gc3800ds.pdf).

Walker, P. and W. H. Tarn, Eds. (1991). CRC Handbook of Etchants for Metals and Metallic Compounds. CRC Press LLC, Boca Raton, FL.

Wang, Y. and J. Franzen (1994). "The non-linear ion trap. Part 3. Multipole components in three types of practical ion trap." International Journal of Mass Spectrometry and Ion Processes **132**: 155-172.

Warns, C., W. Menzel, et al. (1998). "Transmission lines and passive elements for multilayer coplanar circuits on silicon." IEEE Transactions on Microwave Theory and Techniques **46**(5): 616-622.

Wells, J. M., E. R. Badman, et al. (1998). "A Quadrupole Ion Trap of Cylindrical Geometry Operated in the Mass Selective Instability Mode." Analytical Chemistry **20**(3): 438-444.

Wu, Y. E., K. Chen, et al. (2002). "Fabrication and characterization of thermal conductivity detectors (TCDs) of different flow channel and heater designs." Sensors and Actuators A **100**: 37-45.

Wuerker, R. F., H. Shelton, et al. (1959). "Electrodynamic Containment of Charged Particles." Journal of Applied Physics **30**(3): 342-349.

Yang, M., W. B. Whitten, et al. (1995). "Quadrupole trap control circuit for laser desorption mass spectrometry." Review of Scientific Instruments **66**(11): 5222-5225.

Yoshinari, K. (2000). "Theoretical and numerical analysis of the behavior of ions injected into a quadrupole ion trap mass spectrometer." Rapid Communications in Mass Spectrometry **14**(4): 215-223.

Yu-Rong, J., F. Mang, et al. (2001). "Micro-Motion effect of a trapped ultra-cold ion in a standing-wave laser." Chinese Physics **10**(3): 202-205.

Yuasa, K., A. Shimoi, et al. (2002). "Modified Fowler-Nordheim field emission formulae from a nonplanar emitter model." Surface Science **520**: 18-28.

Zaborowski, M. and P. Dumania (2000). "Kinetics of hillock growth in Al and Al-alloys." Microelectronic Engineering **50**: 301-309.

Zheng, O., E. R. Badman, et al. (1999). "Characterization of a serial array of miniature cylindrical ion trap mass analyzers." Rapid Communications in Mass Spectrometry **13**(24): 2444-2449.

DISTRIBUTION

1	MS0123	LDRD Office, 1030
3	MS0603	M. G. Blain, 1722
1	MS0603	C. P. Tigges, 1742
1	MS0603	M. A. Mangan, 1713
1	MS0603	J. J. Hudgens, 1713
1	MS0782	K. L. Linker, 6418
1	MS0892	R. W. Cernosek, 1722
1	MS0892	C. D. Mowry, 1722
1	MS1071	J. F. Jakubczak, 1710
1	MS1077	T. E. Zipperian, 1740
1	MS1080	J. G. Fleming, 1749
1	MS1080	H. D. Stewart, 1749
1	MS1078	S. J. Martin, 1720
2	9018	Central Technical Files, 8944
2	0899	Technical Library, 4536